NATURAL FRACTURE CHARACTERIZATION BY SOURCE MECHANISM ESTIMATION AND SEMI-STOCHASTIC GENERATION OF DISCRETE FRACTURE NETWORKS USING MICROSEISMIC AND CORE DATA

A Thesis

by

EDITH SOTELO GAMBOA

Submitted to the Office of Graduate and Professional Studies of
Texas A&M University
in partial fulfillment of the requirements for the degree of

MASTER OF SCIENCE

Chair of Committee,	David S. Schechter
Co-Chair of Committee,	Richard L. Gibson, Jr.
Committee Member,	Akhil Datta-Gupta
Head of Department,	A. Daniel Hill

December 2014

Major Subject: Petroleum Engineering

ABSTRACT

The overall goal of this study is to generate discrete fracture networks using microseismic and core data from a natural fractured reservoir that has been hydraulically stimulated. To improve fracture characterization, a methodology based on source mechanisms estimations is developed with the aim to distinguish the two natural fracture sets present in the reservoir. Source mechanisms estimation is a geophysical processing technique that can provide orientation and rupture mode of seismic events. An intermediate step, moment tensor inversion, is however needed. The main challenge is that one element of the moment tensor is completely undetermined by the limited azimuthal acquisition coverage; thus, some kind of assumption needs to be considered to complete the missing element. In this work, it is assumed that the microseisms occur mainly as consequence of the natural fractures reactivation, thus source dip and strike are known. For the discrete fracture generation, a semi-stochastic technique is proposed, which combines information from the source mechanisms estimations, the microseismic report and the core analysis report.

The two main contributions of this work are that a methodology to improve natural fracture characterization is proposed, which incorporates micro seismic data to distinguish the fracture sets known to be present, and that a semi-stochastic technique to generate discrete fracture networks, which combines microseismic information and core data, is proposed and implemented as well.

DEDICATION

This dissertation is dedicated to my beloved family:

My father, Marcelino Sotelo who rests in peace

My mother, Fara Gamboa, my role model

My sisters, Lourdes and Janet, my sources of encouragement

ACKNOWLEDGEMENTS

I am grateful to the Department of Petroleum Engineering at Texas A&M for funding my entire master's research through the Crisman Institute for Petroleum Research. My participation in this institute allowed me to be involved in research related activities such as writing and presenting research progress reports, for which I am thankful.

I also want to thank Dr. Schechter, my principal advisor, for keeping my funding through his Crisman sponsored project, Natural Fractures Characterization, and, more importantly, for giving me the freedom to try my ideas. I deem this freedom a priceless commodity that helped me to grow as a researcher.

In the same way, I also want to thank Dr. Gibson, my co-advisor and professor at the Department of Geology and Geophysics, for providing his invaluable scientific insight to improve the implementation of my work. I also appreciate the advisory time he allotted to discuss my research progress.

I am also thankful for the technical support provided by Joel Le Calvez from Schlumberger, which helped me to understand particular details of the microseismic data. I am also thankful for the suggestions he provided for the review paper I wrote.

I would also like to acknowledge the sage advice to improve my writing habits and my time management offered by Dr. Goodson, a professor at the Department of Health and Kinesiology whom I met in a more informal setting. I cannot be more than thankful as well for the marvelous book she gave me, *One Thousands Gifts*, which I am currently reading and which constantly reminds me that *everything* is a gift that comes from God.

My graduate experience would be far from complete without my school peers. The time spent with them has increased my international awareness and my appreciation for culture diversity. It was a privilege to have had the opportunity to meet them: Aymen, from Saudi Arabia, who is the record holder of the lengthiest master dissertation – 300 plus pages, simply unbeatable. Indeed, his passion and enthusiasm are unwavering (and unmatchable). Ali, from Saudi Arabia as well, who is such a positive and optimistic person and whose good mood is more than contagious. Sunny, from China, who is such an outgoing person and a good friend with whom I shared not only the flat but also some good adventures. Zuhair, from Saudi Arabia, who is the sharp student with whom I could always have insightful conversations. Mohammed, form Saudi Arabia as well, who is the experiments dreamer, and who is always in the search for the *ultimate experiment*. Francisco and Johannes, both from Venezuela, who are undoubtedly, and *without bias*, the coolest *panas* (guys) that one could ever meet. Jianlei, from China, who is the fiercest programming tiger; Sangyup, from South Korea, whom I consider the living example of tenacity; and Weirong, from China, who is the group bonding element. To all of you, thank you.

I am also thankful to have had the opportunity to build ties outside school. The International Christian Fellowship (ICF)became my second home. I met so many passionate and friendly people there. I thank the Marshalls, Kent and Judy, for their constant care. I also thank the Roberts, Bill and Bel, for their open hearts. I cannot be more than thankful for the Parulians as well, Anthony and Lini, for the unforgettable Christmas parties. I thank to all my ICF friends with whom I share the same Christian faith: Monet,

Sichun, Tibi and Maggie, Charlotte, Vish, Chen, Mao, Sean and Vivian, Nannan, Hangtian, Josh and Lea, Sandeep, Simon, Adam, Xiaohua and Brittany, Silvia, Troy, Dmitri, Alex and Yenpo. All of you have made my international experience a cherished one.

This undertaking would not have been possible without the unconditional support of my family. Thank you Mom and sisters. Thank you Dad as well, I know you are in a better life.

Finally, I want to thank *the One* who is the source of every blessing, God.

TABLE OF CONTENTS

Page

Page

LIST OF FIGURES

FIGURE Page

FIGURE Page

FIGURE Page

FIGURE Page

FIGURE Page

FIGURE Page

FIGURE Page

FIGURE Page

FIGURE Page

FIGURE Page

FIGURE Page

FIGURE Page

FIGURE Page

FIGURE Page

FIGURE Page

LIST OF TABLES

TABLE Page

TABLE Page

1. INTRODUCTION

1.1 Motivation: Discrete Fracture Networks From Microseismicity

Microseismic monitoring is a widely used technique in the oil and gas industry to record induced rock failure occurring during hydraulic fracturing treatments (Phillips et al. 1998, Rutledge et al. 2004, Sleefe et al. 1995) to assess the generated fracture network and the created stimulated reservoir volume. Event locations and magnitudes are the basic processing outputs from the recorded waveforms. From the cloud of located events, a general interpretation of the fracture network can be derived. However, additional information such as source mechanisms can be extracted to improve fracture characterization (Maxwell and Urbancic 2005).

Source mechanisms can provide information about failure modes: shear, tensile or mixed shear tensile, and fracture orientation (Udias 1999). Thus, in principle it is possible to associate each located event with a fracture mechanism. Furthermore, in analogy to the cloud of located events, the spatial distribution of source mechanisms can, potentially, provide information of fracture connectivity and offer a more precise picture of the induced fracture network. Therefore, potential additional applications include the generation of more realistic discrete fracture models which can be used in reservoir simulations for production forecast (Cipolla et al. 2011, Williams-Stroud and Eisner 2010) . On the other hand, fracture orientation and fracture mode from source mechanisms can also provide more rigorous constraints for history matching and stimulated reservoir volume evaluation (Xie et al. 2012).

1.2 Thesis Objective and Organization

The overall goal of the present work is to generate discrete fracture networks from microseismic data recorded during a hydraulic fracture treatment. In this case study, the reservoir is naturally fractured and, according to the core analysis report, two fracture sets are present. To be able to relate microseismicity and these natural fracture sets, the assumption that the microseisms occur mainly as consequence of natural fractures reactivation is made. Source mechanisms estimations, a geophysical technique that can provide information about the rupture mode and orientation of the failing planes, are performed from selected microseismic events to improve the characterization of the natural fractures. Finally, Information from source mechanisms and the core analysis report are combined to generate semi-stochastically the corresponding discrete fracture network for a particular stage.

The organization of the present thesis work is as follows:

Section 1, the introductory and current section, explains the motivation of the work as well as the main goal and the organization of the thesis.

Section 2, The Literature Review, provides concepts related to source mechanisms and explains the most common technique for their estimations from recorded seismograms, namely moment tensor inversion. In this section, it is also discussed the main limitation for complete moment tensor inversion affecting reliable source mechanisms estimations: the widely used acquisition geometry using a single vertical array of receivers. Finally, the most accepted mechanical interpretation of microseismic occurance, reactivation of plane of weaknesses, is explained.

Section 3, provides background information about the fractured reservoir considered in this case study, The Spraberry formation. A general information of the hydraulic fracture stimulation job to be analyzed in the present work is also presented.

Section 4, presents a stability analysis on the two fracture sets under the influence of perturbed stress fields. The main goal is to learn whether the fracture planes will slip as consequence of the stress field disturbance caused by two main mechanisms: induced stress created by the propagating hydraulic fracture and effective stress decrease caused by the fracturing fluid leak off.

In section 5, an analysis of the accuracy in the source mechanisms solutions under different types of constraints is performed. Since the main issue to determine source mechanisms is the impossibility to find complete moment tensors from seismograms recorded from a single vertical array of receivers, it is necessary to provide some constraints or assumptions to find solutions. In this section three types of constraints are studied: deviatoric constraint, strike constraint and a combination of strike and dip constraints.

Section 6, offers an analysis of microseismic data from selected events. First, the analysis of a perforation shot is performed to test if the assumption of a homogenous, whole space medium is reasonable for our case study. Then the processing technique to find source mechanisms is shown using a selected event. The solutions are found by applying strike and dip constraints. Attenuation effects are also considered in the forward model. Finally the solutions for selected events for stage 5 and 7 of the hydraulic fracturing treatment are presented.

In Section 7, a semi-stochastic method to create discrete fracture networks, which combines the source mechanisms results and the core analysis report, is presented. A realization of the fracture network for stage 5 is shown.

In section 8 the concluding remarks of the present work are formulated.

2. LITERATURE REVIEW

2.1 Source Mechanisms and Dislocation Models

Microseismicity is produced by the sudden rupture of rock elements. Thus these fracturing events are the "seismic sources" that generate the elastic waves which are ultimately recorded at the monitoring stations. From the recorded waveforms not only the source locations can be estimated but also the "source mechanisms" (Baig and Urbancic 2010). Source mechanisms consists in describing the source in terms of the fracture mode and the fracture plane orientation that can best predict the recorded seismograms (Udias 1999). Source mechanism is a concept developed in the field of seismology (Aki and Richards 2002) to describe earthquake seismicity. Since most earthquakes are considered to be shear displacements across planar faults (Lay and Wallace 1995, Shearer 2009), the fracture mode is generally restrained to shear slip. Estimation of source mechanisms of shear faulting focuses on finding the orientation of the fault plane and the direction of the slip. The fault plane orientation is determined by the strike (ϕ) and dip (δ) angles (**Fig. 1 A**). The strike is the azimuth of the fault intersection with the horizontal plane; the dip is the angle measured from the horizontal plane to the fault surface. The slip direction is determined by the rake (λ) (**Fig. 1 A**) which is the angle between slip vector (**f**) and a parallel to the strike on the fault surface. The slip vector indicates the direction of relative displacement of the fault planes: the hanging wall respect to the foot wall. Thus, source mechanisms for shear faulting are completely described by the strike, dip and rake angles. In Seismology fractures are denoted as "dislocations" because this term emphasizes the discontinuity in displacement across the fracture plane (Udias 1999). For instance shear

faulting can also be referred as shear dislocation and the assumption of pure shear slip could be referred as the shear dislocation model.

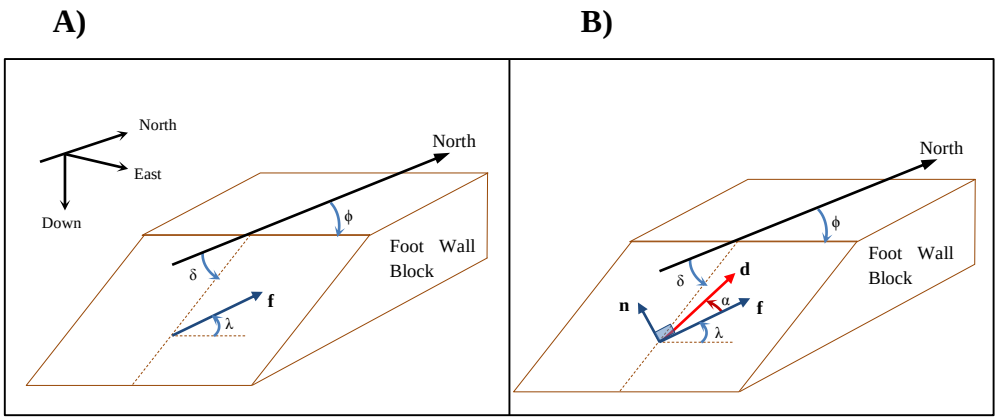

Fig. 1 - Representation of fracture models. A) Shear slip fracture model. The fault orientation is defined by the strike (ϕ) and dip (δ) angles. The rake (λ) defines the direction of the slip vector (f). The vector f is on the fault plane. B) General dislocation model. The slope (α) defines the direction of the dislocation vector (d). The dislocation vector has shear slip (f) and tensile (n) components. The vector n is parallel to the fault normal. Modified after Stein and Wysession (2003).

Since there is evidence that earthquakes of volcanic and geothermal origin can present opening components along with shear displacements (Julian et al. 1998, Miller et al. 1998), the "general dislocation model" has been proposed (Ou 2008, Vavryčuk 2001,2011). This model allows sources to exhibit mixed mechanisms with both shear and tensile components at the same time, where the tensile part refers to fracture opening or closing. The description of a mixed source is completed by adding the slope angle (α) to the original shear dislocation model (**Fig. 1 B**). The slope angle defines the direction of the dislocation vector (**d**) and is measured from the fault plane. The dislocation vector

determines the relative movement of the fracture planes. Since the dislocation vector (**d**) has to account for both shear and tensile displacements, it has two components. One component is the slip vector (**f**) which lies on the fault plane and defines the direction of the shear slip. The other component is parallel to the normal vector of the fault plane (**n**) and defines the direction of the tensile motion. Pure shear or pure tensile fractures are special cases of the "general dislocation model". For the pure shear slip case, the slope angle (α) is zero and the dislocation vector (**d)** is equal to the slip vector (**f**), thus no tensile component is present. For the pure tensile case, the dislocation vector is parallel to the normal of the fault and no shear component is present. For crack opening ($\alpha = 90$), the normal vector is pointing outward from the fault plane, while for crack closing ($\alpha = -90$) the normal is pointing inward towards the fault plane. Other values of α describe hybrid sources: compressional shear($-90 < \alpha < 0$) or extensional shear ($0 < \alpha < 90$) (Vavryčuk 2011).

2.2 Equivalent Body forces and the Seismic Moment Tensor

Seismic sources can also be represented by force systems of internal origin. These force systems are known as "equivalent body forces" because they produce the same elastic wave field as the complex displacement of a fracturing event, thus they are "seismically equivalent" (Lay and Wallace 1995). By definition body forces act over a volume. However, sources with zero spatial extent can be assumed. The "point source" approximation is valid when observation distances and wave lengths are large compared to the source dimensions. Under this assumption, sources can be represented by a system

of forces acting at a point (Udias 1999). Equivalent force systems are represented by a combination of force couples and dipoles. A couple consist of two parallel forces that are equal in magnitude, opposite in direction and separated by a certain distance. A dipole is similar to a couple but the forces are collinear. In the next lines some important sources and their force system representation are reviewed. Shear slip sources are represented by two force couples perpendicular to each other (**Fig. 2 A**).Thus they are known as double couples (DC) sources. Moreover, one force couples is parallel to the slip direction and perpendicular to the second couple. This force system arrangement leads to an issue known as the "fault plane ambiguity". This means that without a priori knowledge it is not possible to identify the couple parallel to the actual slip direction which leads to two possible fault plane solutions. An explosive source is described by three force dipoles all perpendicular to each other (**Fig. 2 B**). An explosion is an isotropic (ISO) source since it involves a net volume change. A pure tensile source is a combination of isotropic (ISO) and compensated linear vector dipole (CLVD) force systems (Vavryčuk 2001) (**Fig. 2 C**). A CLVD force system is represented by three orthogonal force dipoles with one dipole with double strength and opposite direction than the other two (**Fig. 2 C**). For a pure tensile source, the largest dipole of the CLVD is parallel to the direction of tensile displacement (Julian et al. 1998).

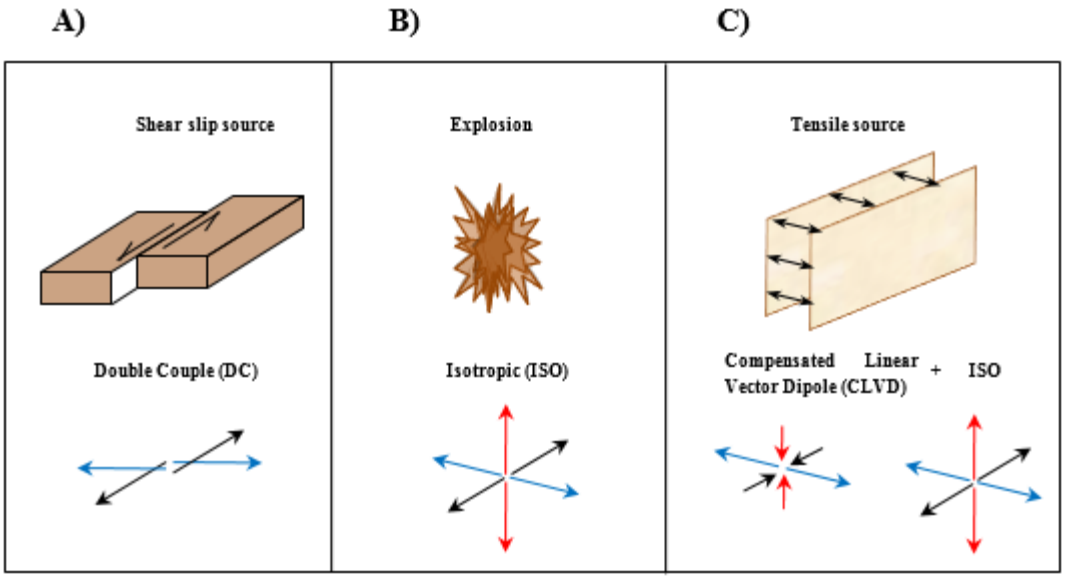

Fig. 2 - Sources and their equivalent forces. A) Shear slip is represented by a double couple (DC) with one couple parallel to the slip direction. B) An explosive source is represented by an isotropic (ISO) force system defined by three dipoles all perpendicular to each other. C) A tensile source is represented by the sum of ISO and CLVD force systems. The major dipole of the CLVD is parallel to the direction of tensile opening.

The generalized arrangement of force systems representing any source is defined as the seismic moment tensor (Jost and Herrmann 1989). The moment tensor $\boldsymbol{M}$ is a 3 by 3 symmetric matrix arrangement. Thus, it only has six independent elements out of the nine:

$$\boldsymbol{M} = \begin{bmatrix} M_{11} & M_{12} & M_{13} \\ M_{21} & M_{22} & M_{23} \\ M_{31} & M_{32} & M_{33} \end{bmatrix} \quad \textbf{(1)}$$

And

$$M_{12} = M_{21}, M_{13} = M_{31}, M_{23} = M_{31} \quad \textbf{(2)}$$

Each element M_{ij} represents the moment produced by either force couples or dipoles. The off-diagonal elements ($i \neq j$) correspond to force couples and the diagonal elements ($i = j$) to the force dipoles. The forces are pointing parallel to the *i* direction and are separated in the j direction (**Fig. 3**).The separation distance in each case is infinitesimal since forces are acting at a point.

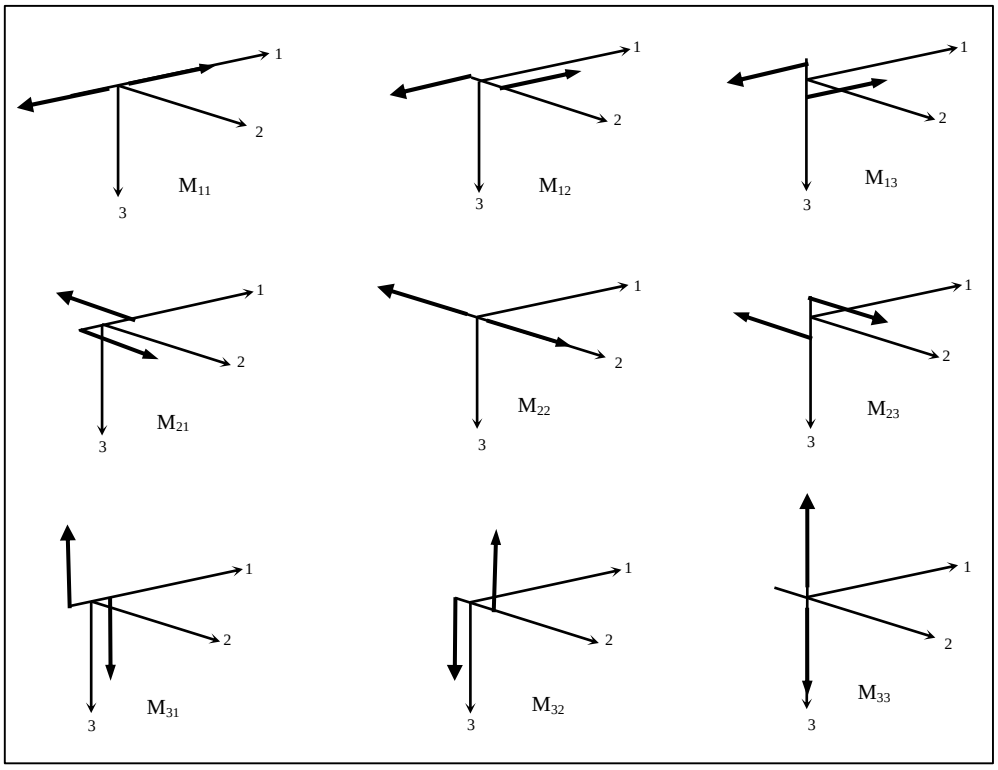

Fig. 3 - Nine elements of the seismic moment tensor in a Cartesian coordinate system with axes 1,2,3. Modified after Aki and Richards (2002).

In many cases it is useful to describe the moment tensor in terms of the contribution of known force systems. In general, $\boldsymbol{M}$ can be decomposed into an isotropic and deviatoric part:

$$\boldsymbol{M} = \boldsymbol{M}^{ISO} + \boldsymbol{M}^{DEVI} \quad \textbf{(3)}$$

Commonly, $\boldsymbol{M}^{DEVI}$ is decomposed into a double couple DC and CLVD (Godano et al. 2009, Sílený et al. 2009, Song and Toksöz 2011, Vavryčuk 2001):

$$\boldsymbol{M}^{\boldsymbol{D}EVI} = \boldsymbol{M}^{DC} + \boldsymbol{M}^{CLVD} \quad \textbf{(4)}$$

Even though other decompositions of the deviatoric part are possible, the separation into DC and CLVD plus the ISO component have a direct interpretation for fractures with shear and tensile components since the shear motion is related to the DC component and the tensile to a combination of ISO and CLVD as depicted in **Fig. 2**.

Recorded seismograms $\boldsymbol{U}$ can be regarded as the result of the linear combination of the moment tensor $\boldsymbol{M}$ and the spatial derivative $\boldsymbol{G}$ of a time and space dependent function known as " the Green's function" which is convolved with a time dependent function s(t) known as "the source time function" (Jost and Herrmann 1989, Stump and Johnson 1977) as shown :

$$\boldsymbol{U} = [\boldsymbol{G} * s(t)\,]\boldsymbol{M} \quad \textbf{(5)}$$

The source time function represents the slip dependence with time. Each element of $\boldsymbol{G}$ is a wave equation solution. Each particular solution represents the elastic displacement at a given receiver produced by a given impulse force couple or dipole applied at the source location. Once the matrix $\boldsymbol{G}$ is constructed, it can be used together with the recorded seismograms $\boldsymbol{U}$ to retrieve the moment tensor $\boldsymbol{M}$. The estimation of $\boldsymbol{M}$

is normally done through inversion techniques. In general these techniques seek to determine the moment tensor that can best fit the data $\boldsymbol{U}$.

For linear problems as the one defined by equation **Eq. (5)**, it is possible to examine the stability of the inversion by evaluating the eigenvalues of $\boldsymbol{G^T G}$ matrix:

$$k = \left|\frac{\lambda_{max}}{\lambda_{min}}\right| \quad \textbf{(6)}$$

Where k is the condition number defined as the ratio in absolute sense of the maximum to the minimum eigenvalue of $\boldsymbol{G^T G}$. A large condition number means that the matrix $\boldsymbol{G^T G}$ is unstable and the inversion is not reliable.

Once the moment tensor is estimated, it can be related to a source mechanism by means of a dislocation model. For instance the general dislocation model can be used as proposed by Vavryčuk (2001):

$$\boldsymbol{M} = A\, d\, \left[\left(\lambda\, \hat{\boldsymbol{d}}.\hat{\boldsymbol{n}}\, \boldsymbol{I}\right) + \mu(\, \hat{\boldsymbol{n}}\, \hat{\boldsymbol{d}} + \hat{\boldsymbol{d}}\, \hat{\boldsymbol{n}})\right] \quad \textbf{(7)}$$

$$\hat{\boldsymbol{d}} = \hat{\boldsymbol{n}}\ sin\,\alpha + \hat{\boldsymbol{f}}\ \ cos\,\alpha \quad \textbf{(8)}$$

Where $\hat{\boldsymbol{d}}, \hat{\boldsymbol{n}}$ and $\hat{\boldsymbol{f}}$ are the unit vectors of the dislocation (**d**), normal to the fault plane (**n**), and slip (**f**) vectors respectively (**Fig. 1** B) $\boldsymbol{I}$ is the 3 by 3 identity matrix; μ and λ are the Lame parameters in the fracture zone. A is the fault area; d is the dislocation vector magnitude and α is the slope angle, which is the angle between the fault plane and the dislocation vector.

2.3 Monitoring Coverage and Constrained Inversions

All the six independent elements of the moment tensor are needed to estimate general source mechanisms. In that sense, the recording coverage of microseismic events from different azimuths is a major limiting factor for complete moment tensor inversion. (Eaton and Forouhideh 2011). Nolen-Hoeksema and Ruff (2001) processed micro seismic data recorded by a single vertical array of three-component receivers and found that one of the eigenvalues of G^TG matrix associated with the isotropic moment tensor component was zero. Thus, he concluded that it is not possible to retrieve all six independent elements of the moment tensor but only five from this acquisition configuration. Vavryčuk (2007) proved theoretically that from a single azimuth data set (as a single vertical monitoring array), the dipole perpendicular to the plane formed by the vertical monitoring array and the event location cannot be resolved. For instance, assuming a vertical monitoring array and a source in the plane x1-x3, the unresolvable moment tensor element is the dipole in the x2 direction (M_{22} in **Fig. 3**). M_{22} cannot be determined because it is inducing wave components that are traveling off the x1-x3 plane, thus the seismograms recorded in the single monitoring array carry no information coming from this particular moment tensor element (Jechumtálová and Eisner 2008). Vavryčuk (2007) also indicated that to determine complete moment tensors it is necessary at least P and S amplitudes from two vertical arrays of three-component receivers or only P amplitudes coming from at least three vertical arrays of three-component receivers.

Microseismic monitoring with a single vertical array of receivers is a common practice in the oil industry. As discussed, with this acquisition geometry it is not possible

to recover complete moment tensors since one dipole is completely undetermined by the data. An alternative method is to complete the missing element by incorporating assumptions or "constraints". Since the undetermined dipole is associated with the isotropic part of the moment tensor element (Nolen-Hoeksema and Ruff 2001), then a common approach is to assume that the moment tensor presents only deviatoric components: DC and CLVD (Nolen-Hoeksema and Ruff 2001, Patton and Aki 1979, Strelitz 1978). Thus this type of constraint is known as "deviatoric" and it is achieved by setting to zero the trace of the moment tensor. In practice, applying this constraint means restricting the fracture mode to shear slip since normally only the DC part is considered in the estimation of source mechanisms (Jost and Herrmann 1989). However, Imposing a deviatoric constraint when the actual source mechanism has a high tensile component can yield to significantly biased estimations in terms of fracture orientation and fracture mode (Vavryčuk 2007). As consequence, the deviatoric constraint is valid when the actual mechanism is pure shear slip. This is equivalent to a moment tensor with only DC components. Hence, non-negligible CLVD in a deviatoric constrained solution may suggest that the actual source mechanism deviates from pure shear failure (Vavryčuk 2001).

The application of other constraints has also been studied in recent investigations. Jechumtálová and Eisner (2008) proposed a method to find possible source mechanisms constrained by the data. They tried different values of the unknown moment tensor element in a systematic way and estimated the corresponding source mechanisms. They observed that it is possible to determine if a specific solution such as the pure shear slip

can be among the probable source mechanisms. They also applied this methodology to microseismic field data recorded with a single vertical array of receivers and they found that many of the analyzed events were not consistent with pure shear failure. Song and Toksöz (2011) extended Jechumtálová and Eisner (2008) methodology. They included a priori information of expected source mechanisms as additional constraints: knowledge of either fracture strike and dip range, or exact strike value or maximization of the double couple component. They implemented synthetic analyses to test the accuracy of the inversion of a known source for each type of constraint. They found that the errors in the inversion are acceptable even with a reasonable amount of noise in the synthetic data and with errors in the velocity model and in the source location. Additionally, they applied the strike and dip range constraint to microseismic field data recorded with a single vertical array of receivers. They assumed a range of values for the strike considering the general trend of the microseismicty and a range of dip values considering subvertical to vertical fractures. They found that the resulting moment tensors indicated the existence of both DC and non-DC components in the source.

2.4 Microseismic Source Mechanisms From Field Observations

Currently, the understanding of rupture mechanisms of microseismic events is still an area of active research that is advancing as the monitoring coverage is improving and as the general seismic dislocation model is being implemented. Early studies commonly interpreted the induced microseismicity as the result of pure shear slippage along pre-existing fractures. For instance, Pearson (1981) analyzed data from a hydraulic fracture

injection in granitic rock where a single three-component receiver was deployed downhole. He concluded that the fracture mechanism of the detected events must be shear because of the high shear to compressional amplitude ratios observed. He reached this conclusion after comparing his observations against experimental results from Savage and Mansinha (1963) where the observed shear to compressional amplitude ratios for tensile fractures were much lower. Moreover, he suggested that the shear events were caused by the raised of pore pressure along the pre-existing joints. Sasaki (1998) also arrived to similar conclusions after studying microseismicity in a hot dry rock, where two injection experiments were conducted with a network of three-component receivers deployed in ten boreholes surrounding the injection site. For the first experiment, he observed that the seismic events clustered in the same plane of a pre-existing fault, thus he concluded that the faulting zone was reactivated by shear failure. For the second experiment, he estimated source mechanisms of twelve events assuming shear fracturing and using a grid search algorithm to find the optimum fracture plane. Finally, he reported that in average the mechanisms agreed with the expected maximum horizontal principal stress concluding that they were induced by shear slippage due to increased pore pressure. Rutledge et al. (2004) analyzed microseismicity induced in a sedimentary rock of interbedded sands and shales where two injection treatments were completed. The first stimulation was monitored by two vertical arrays of three-component receivers deployed in two different wells. The second stimulation was monitored with a single downhole vertical array of three-component receivers. The located events from both experiments were lumped together and regrouped based on waveform similarity and location proximity. Finally,

composite source mechanisms were estimated using a shear constrained inversion algorithm (Snoke 2003) by fitting amplitude ratios and first motion polarities. Most of the events presented strike-slip dislocations with fracture planes striking parallel to a pre-existing vertical fracture system trending close to the maximum horizontal stress direction. Some other events, although also displayed strike-slip mechanisms, were striking at an angle with respect to the natural fracture orientation. The events striking parallel to the natural fracture were interpreted as induced by the shear reactivation of the natural fracture planes, while the events trending at an angle were explained as induced by slippage of bend or jogs in the natural fracture system.

In more recent studies, inversion of complete moment tensors provides evidence of tensile components in microseismic events. Sílený et al. (2009) reprocessed selected events from microseismic data analyzed by Rutledge et al. (2004). These events were monitored by a dual vertical array of receivers. Following the original grouping scheme, composite source mechanisms were re-estimated by performing complete moment tensor inversions of P and S amplitudes applying a least square minimization technique. In general, the resulting moment tensors presented high non-DC components (ISO and CLVD), but differences in the relative proportions of ISO and CLVD and the orientation of CLVD eigenvectors suggested that the events could be clustered in two different types of fracture mechanisms. The first mechanism was considered to be consistent with crack opening in near vertical fractures striking subparallel to the maximum horizontal stress. The second mechanism was interpreted as a combination of fracture extension accommodated by strike slip faulting. Baig and Urbancic (2010) processed 147

microseismic events from a hydraulic fracture treatment recorded by three vertical arrays of receivers. They performed complete moment tensor inversions and found that events presented both DC and non-DC components. Thus, they concluded that these events could not be considered pure shear ruptures. Song et al. (2014) analyzed forty two microseismic events from Barnett shale recorded by two monitoring vertical arrays of receivers. He inverted for complete moment tensors by minimizing the square of the misfit using a grid search method with a full waveform fitting approach (Song and Toksöz 2011). Source mechanisms were estimated using the general dislocation model as proposed by Vavryčuk (2011). The results indicated that most events have both tensile and shear components. According to their strikes the events were interpreted as either reactivation of the pre-existing natural fractures (Gale et al. 2007) or predominantly opening mode failures on hydraulic fractures.

2.5 Rock Mechanics of Triggered Microseismicity

Reactivation of plane of weaknesses such as natural fractures has been suggested as the main source of microseismicity during hydraulic fracture treatments (Maxwell and Cipolla 2011, Rothert and Shapiro 2003, Warpinski et al. 2004). Moreover, the presence of natural fractures in many unconventional reservoirs has been confirmed by several geological studies (Curtis 2002, Gale and Holder 2010, Lorenz et al. 2002). According to Warpinski et al. (2013) there are two main mechanisms inducing the reactivation of natural fractures: local stress perturbation caused by the tip of the propagating hydraulic fracture and increased pore pressure due to fracturing fluid leak off along the hydraulic

fracture open planes. Thus, the suggested two possible zones of induced microseismicity are as depicted in **Fig. 4**: The area close to the fracture tip (zone 1) and the wide region normal to the fracture surface (zone 2). The interaction in zone 1 can be explained as a two-step process (Gu et al. 2012). First, a pure mechanical interaction occurs slightly ahead of the fracture tip. In this stage the influence of the fracturing fluid is not considered due to lag that its front experiences respect to the advancing crack tip (Garagash and Detournay 1999, Groenenboom et al. 2001). Then the second stage happens when the fluid front reaches the pre-existing discontinuity. Induced microseismicity can occur during the mechanical interaction if the local stress perturbation is sufficient to overcome the shear strength of the plane of weakness (Renshaw and Pollard 1995, Weng et al. 2011). Otherwise other two outcomes are possible: momentary arrest of the hydraulic fracture or the hydraulic fracture tip crossing the natural fracture. Once the fluid reaches the intersection point, it may divert into the natural fracture with the possibility of natural fracture dilation (Warpinski and Teufel 1987). Hydraulic fracture re-initiation can also be induced given the fluid pressure can overcome the tensile strength at the opposite face of the natural fracture (Potluri et al. 2005). It is also possible that the hydraulic fracture continue its original propagating path once its tip has crossed the natural fracture.

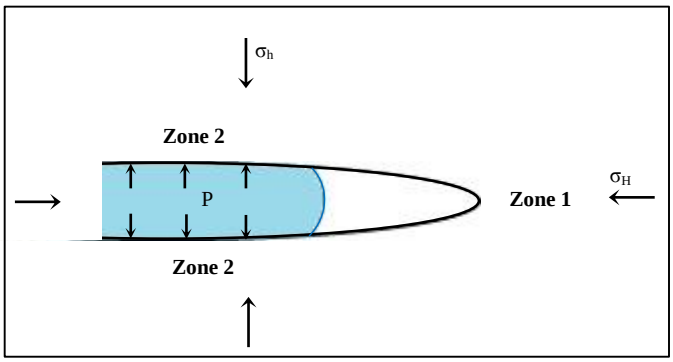

Fig. 4 - Possible zones of induced seismicity. Zone 1: slightly ahead of the hydraulic fracture tip. Zone 2: broad area along the hydraulic fracture faces. Modified after Song et al. (2014).

On the other hand, analytical and numerical models suggest that induced microseismicty by reactivation of plane of weaknesses occurs in zone 2 mainly as consequence of increased pore pressure due to fluid leak off along the hydraulic fracture faces. Since pore pressure decreases the effective normal stresses, shear slippage may take place when the normal stress on the natural fracture plane falls below a threshold at which it cannot longer prevent shear reactivation. Warpinski et al. (2004) used the analytical solution of a pressurized crack after Sneddon (1946) to calculate induced stresses caused by the presence of the hydraulic fracture, and pressure correlations to estimate the pore pressure distribution around the hydraulic fracture caused by leak off. They concluded that stress perturbation caused by increased pore pressure is more significant than hydraulic fracture induced stresses and that it is the main reason for reactivation of favorable oriented plane of weaknesses. In a more recent study, Ghassemi et al. (2013) performed rock fracture strength analysis around a hydraulic fracture in which stress and pore pressure distributions are calculated through numerical methods, by solving a coupled

problem of fluid flow in the hydraulic fracture and poroelastic deformation in the matrix surrounding the open fracture planes. They concluded that there is a potential for shear slippage away from the hydraulic fracture face since in the near vicinity the dominant rupture mode is tensile.

Warpinski et al. (2004) argue that it is unlikely that fracture planes fail in pure shear slip but some extensional or compressional motion must be involved. This idea agrees with the general dislocation model (Ou 2008, Vavryčuk 2001,2011) since this model allows source mechanisms solutions with both shear and tensile components at the same time. From a mechanical perspective the most accepted and studied brittle fractures are extensional and shear as independent and not overlapping rupture modes (Fossen 2010, Jaeger et al. 2007). However, in a recent work, Fischer and Guest (2011) extended this classification including two additional fracture modes according to stress intervals (**Table 1** and **Fig. 5**): compressional shear and extensional shear. Extensional shear fractures are the least known and studied from this classification (Engelder 1999). From a theoretical viewpoint, The Griffith failure criterion (Griffith 1924) provides the adequate basis to support their occurrence under mixed tensile and compressive stress.

Slope angle (α, deg) (Vavryčuk 2011)	Resolved normal (σ_n) and shear tractions (τ_s) on a fracture plane (Fischer and Guest 2011)	Fracture mode Modified from Fischer and Guest (2011)
$\alpha = 0$	$\sigma_n = 0$, $\lvert\tau_s\rvert > 0$	Pure shear
$\alpha = 90$	$\sigma_n < 0$, $\tau_s = 0$	Extensional (crack opening)
$-90 < \alpha < 0$	$\sigma_n > 0$, $\lvert\tau_s\rvert > 0$	Compressional shear
$0 < \alpha < 90$	$\sigma_n < 0$, $\lvert\tau_s\rvert > 0$	Extensional shear

Table 1 - Fracture mode classification according to slope angles of the general dislocation model and corresponding normal and shear tractions resolved on a fracture plane.

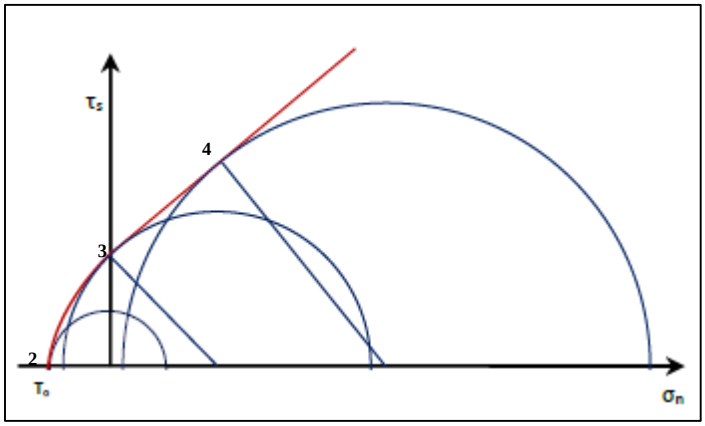

Fig. 5 - Prediction of extensional (2), pure shear (3) and compressional shear (4) fractures at different intersection points with the Griffith-Coulomb failure envelope. See Table 1 for ranges of shear and normal tractions resolved on the respective planes. Compared to Table 6A, the angle of intersection for extensional shear (1) is intermediate between extensional (2) and pure shear (3) fractures. Modified after Sibson (1996).

A failure criterion relates the normal traction (σ_n) to the expected shear traction (τ_s) on a plane at which fracture initiates. Thus if the actual shear traction on a plane is equal or greater than the calculated by the failure criterion, then the plane will fail in shear. Griffith criterion is of a parabolic form and is given by:

$$\tau_s{}^2 = 4\,T_o\,\sigma_n + 4\,T_o{}^2 \quad \textbf{(9)}$$

Where T_o is the uniaxial tensile strength of the rock. Griffith criterion is normally combined with the Coulomb failure criterion since it is deemed more suitable for the compressive regime ($\sigma_n > 0$). The Coulomb criterion is of a linear form and given by:

$$\tau_s = S_o + \mu\,\sigma_n \quad \textbf{(10)}$$

Where S_o represents the cohesion of the rock, μ is the coefficient of internal friction and it is an empirical parameter that represents the slope of the Coulomb failure line. Commonly a failure criterion is drawn in a Mohr-diagram. The Mohr-diagram is a graphical representation of the state of stress. In the 2D case, the state of stress is represented by a circle which intersects the horizontal axes at the minimum (σ_3) and maximum (σ_1) principal stresses (**Fig. 6 A**). The convention assumed is that compressive stresses are positive and extensional are negative. The horizontal and vertical axes represent the normal (σ_n) and shear tractions (τ_s) respectively on planes at different orientations represented by different points around the Mohr circumference. Plane orientations are described by the angle θ measured from σ_1. The angle θ in the Mohr circle is doubled to 2θ. Brittle failure will occur when the Mohr circle intersects the failure envelope. Half of the angle 2θ at the point of intersection represents the orientation of the failure plane from σ_1 (**Fig. 6 B)**. For an extensional shear fracture to take place, a mixed compressive ($\sigma_1 > 0$) and tensile ($\sigma_3 < 0$) state of stress is needed and a sufficient low differential stress ($\sigma_1 - \sigma_3$) so that the corresponding Mohr circle intersects the failure envelope in the negative side of the horizontal axis (**Fig. 6 B**), ensuring that the normal traction resolved on the fracture plane is extensional (Fischer and Guest 2011) with a non-zero shear traction.

Furthermore, the predicted fracture angle (θ) is intermediate between the uniaxial tensile ($\sigma_1 = 0$ and $\sigma_3 < 0$) and the compressive shear fractures ($\sigma_3 \geq 0$ and $\sigma_1 > \sigma_3$).

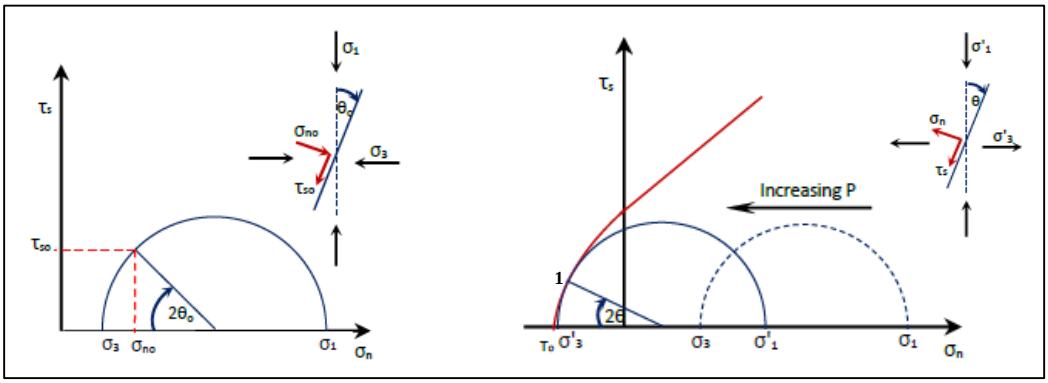

Fig. 6 - A) 2D State of stress represented in a Mohr diagram: σ_1 and σ_3 are the principal stresses, θo is the angle from σ1 of an arbitrary plane and represented by 2θo on the Mohr circumference, σ_{no} and τ_{so} are the normal and shear tractions resolved on this plane. B) Extensional shear fracture prediction: Increased pore pressure P shifts the Mohr circle to the left. Extensional shear fracture will occur if the Mohr circle intersects the Griffith-Coulomb failure envelope (red curve) when σn < 0 and $|\tau s| > 0$. The intersection point is indicated by 1. Modified after Fischer and Guest (2011).

In the experimental side, the laboratory tests by Ramsey and Chester (2004) provided the first convincing evidence for the occurrence of extensional shear fractures. They performed triaxial extension experiments on Carrara Marble at different confining pressures and they observed a continuous transition from pure extensional to shear fracture with increase of compressive stress. This transition was evident by the progressive change in morphology of fracture surfaces. They also noted that extensional shear fractures

formed under mixed state of stress at acute angles from σ_1, and that these angles were intermediate between pure extensional and shear fractures.

At reservoir scale underground rocks are commonly subjected to compressive stress rather than extensional. This compressive state of stress, assuming no tectonic stress influence, is produced by the overburden and the contact with contiguous rock masses (Fossen 2010). Nonetheless, there are possible mechanisms which may allow the development of a mixed tensile-compressive state of stress that can induce extensional shear fractures. Fischer and Guest (2011) indicated that raise in pore pressure due to the diffusion of injected fluids can shift the initial compressive state of stress to a mixed state of stress. This effect is possible because the pore pressure P acts against the absolute stress decreasing the effective stress ($\sigma'_1 = \sigma_1 - P, \sigma'_2 = \sigma_2 - P, \sigma'_3 = \sigma_3 - P$) (**Fig. 6 B**). Furthermore in overpressured formations there is a higher probability of hybrid crack opening due to the existence of low differential ($\sigma_1 - \sigma_3$) and low effective stress. To analyze the occurrence of fractures with extensional components, Fischer and Guest (2011) derived relationships among the fracture orientation θ , the resolved normal (σ_n) and shear (τ_s) tractions on the fracture plane and the differential stress ($\sigma_1 - \sigma_3$) from the intersection of the Mohr circle with the Griffith failure envelope. They applied these relationships in the evaluation of two field examples of microseismicity induced by fluid injection. For both cases, the analysis was done in 2D with the maximum horizontal stress (S_H) as σ_1 and the minimum horizontal stress (S_h) as σ_3. The first data set analyzed was from Cotton Valley stimulation (Rutledge et al. 2004). The Mohr circle constructed with effective stresses revealed a mixed stress of state and intersected the Griffith – Coulomb failure envelope at

two different angles from σ_1, on the negative and positive regions of the horizontal axis σ_n respectively. The intersection in the negative side of σ_n was interpreted as the extensional shear reactivation of the preexisting natural fractures striking subparallel to the horizontal maximum stress. This interpretation agrees with the shear-tensile mechanisms found by Sílený et al. (2009) from complete moment tensors after reprocessing part of the Cotton Valley data. On the other hand, the intersection in the positive side of σ_n was interpreted as the compressive shear reactivation of a second set of preexisting natural striking within a greater angle from σ_1. This result agrees with the pure shear mechanisms found by Rutledge et al. (2004). The second data set analyzed was from a geothermal field (Horálek et al. 2010) . In this case, the effective state of stress was compressive with such a high differential stress that the Mohr circle intersected the failure envelope in the positive region of the horizontal axes σ_n. Thus, the microseismic events were interpreted as induced by compressive shear fractures which agrees with the pure shear mechanisms found by Horálek et al. (2010) from complete moment tensors.

In a more recent study, Song et al. (2014) extended Fischer and Guest (2011) approach by incorporating local stress perturbations induced by the hydraulic fracture tip. They examined microseismic data from Barnett Shale recorded with two vertical arrays of receivers. He used 3-D Mohr diagrams and the Griffith failure envelope in his mechanical analyses. They considered a normal stress regime: σ_1 corresponds to the overburden (σ_v), and σ_2 and σ_3 to the horizontal maximum (σ_H), and minimum (σ_h) stresses respectively (Fossen 2010). Song et al. (2014) alos analyzed the influence of increased pore pressure due to fluid leak off in the possible formation of new fractures in the intact

rock. They found that given the low differential and effective stresses in the reservoir, the Mohr diagram could not intersect with the failure envelope, Thus they concluded that it is not expected the formation of new fractures in the intact rock due to fracturing fluid leakage. However, after arguing that the existing and mineral filled natural fracture sets can act as plane of weakness, they constructed the Griffith failure envelope assuming a lower value of tensile strength and Mohr circles for two cases of state of stress: influenced by hydraulic fluid leakage and by the hydraulic fracture tip. For the situation of effective stresses influenced by the increased in pore pressure, they found that it is reasonable to expect both compressive and extensional shear fractures; while for the case of stress perturbed by the fracture tip, they found that only compressive shear fractures could be expected. Furthermore they used the fracture plane angle from σ_1 as a criterion to solve the fault plane ambiguity and choose the most likely mechanism solution. Thus higher dipping planes were picked for source mechanisms with extensional components and lower dipping planes for source mechanism with compressional components.

3. HYDRAULIC FRACTURING JOB IN LOWER SPRABERRY

3.1 Geological Description of Spraberry Formation

The Spraberry formation lies in the Midland Basin, a sub-basin of the larger Permian Basin in West Texas and it forms a an area of hydrocarbon accumulation of 75 (120 km) miles long and 10- 35 miles (16-56 km) wide (Montgomery et al. 2000) (**Fig. 7**). Spraberry clastics are considered a series of submarine fan systems of Permian age acting as stratigraphic traps. This fan complex contains an accumulation of more than 10 million barrels of oil in place. The formation is broadly divided in three units known as the Upper, Middle and Lower Spraberry. The Upper and Lower units are siltstone and sandstone rich intervals separated by the Middle unit which is an interbedded interval of calcareous terrigenous mudstones, argillaceous limestones, and lesser siltstones and sandstones (Tyler et al. 1997). The Upper Spraberry consists of the Floyd and Driver submarine fan systems, while Lower unit is encompassed by the Jo-Mill fan system. In addition, the main units are subdivided into a series of sub-units of siltstone and sandstones zones (**Fig. 8**). The major oil producing zones includes units 1U and 5U of the upper Spraberry and 1L and 2L in the lower Spraberry. The Spraberry reservoirs are characterized by an extensive natural fracture system that provides the main fluid conduit, a matrix porosity range from 5 to 18% and permeabilities ranging from 0.05 to 3.0 md. This study is focused in the lower 1L Spraberry unit (**Fig. 8**). This unit presents a sandstone proportion between 60 and 80% with thicknesses than can be greater than 30 ft.

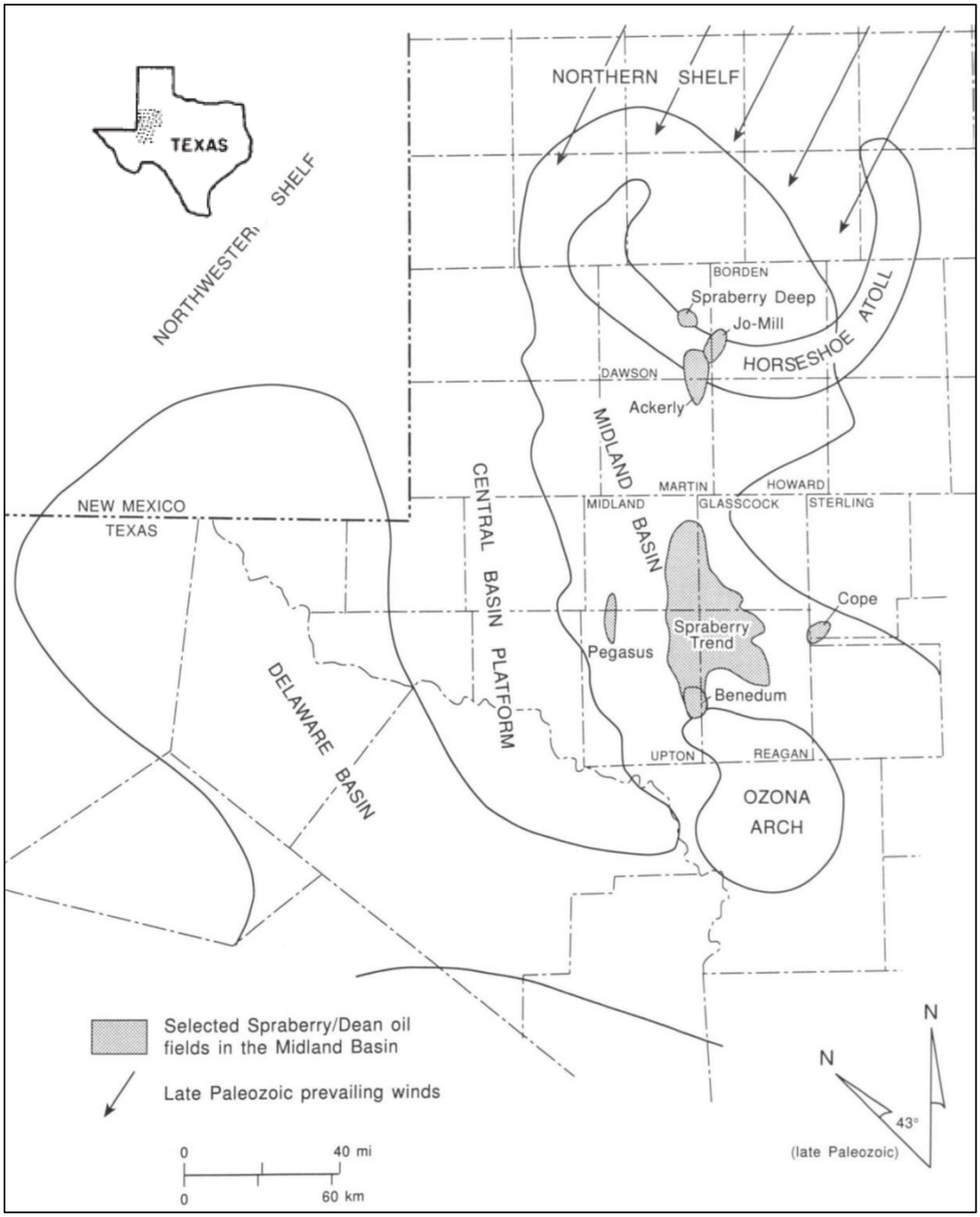

Fig. 7 - Structure of the Permian Basin and location of Spraberry field in the Midland Basing. Modified from Tyler et al. (1997). Modified after Tyler et al. (1997).

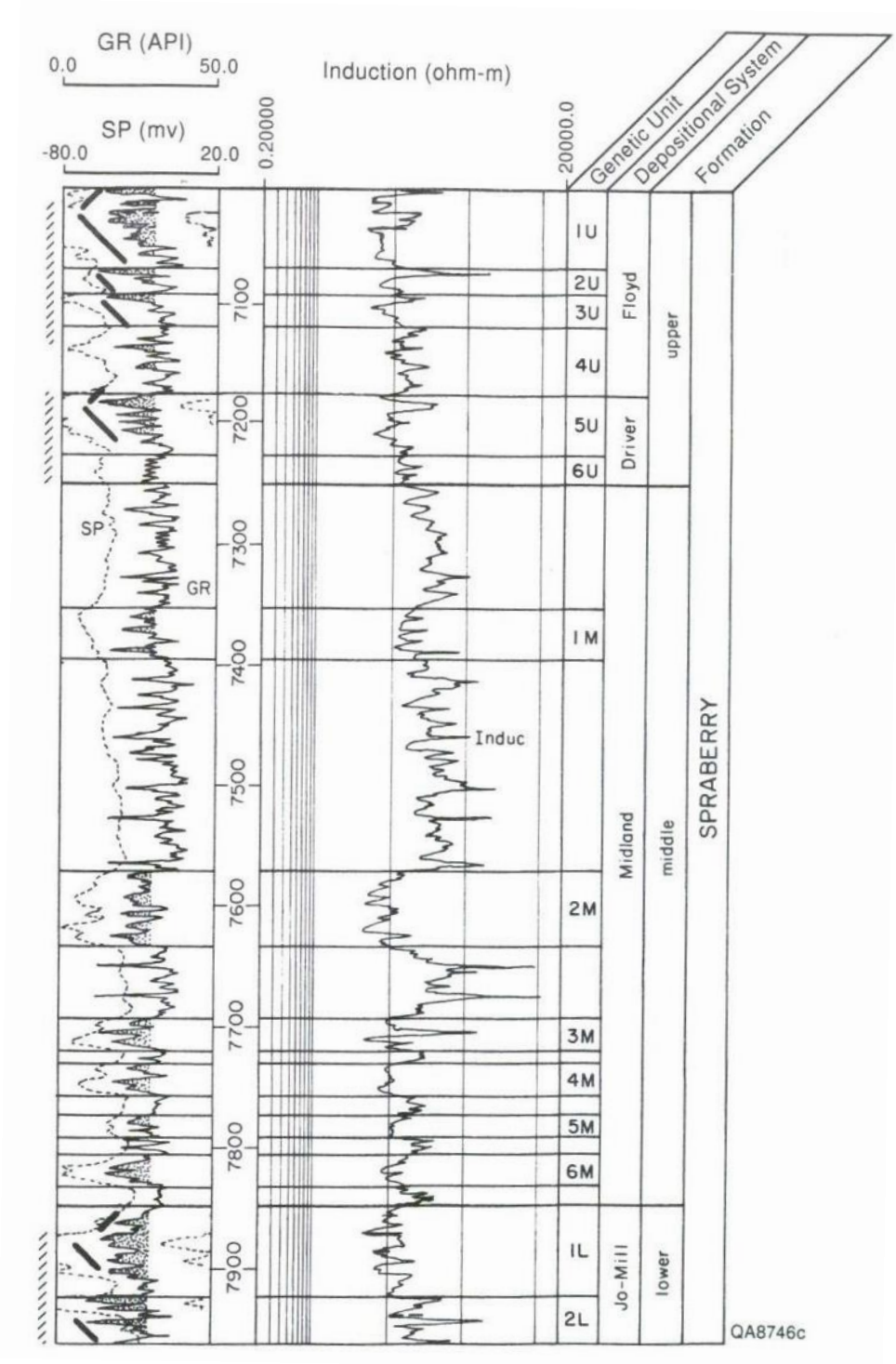

Fig. 8 - Type log and stratigraphic divisions of Spraberry Sandstone. Modified from Tyler et al. (1997).

3.2 Lower Spraberry Fracture System

Core samples Analysis from a horizontal well placed in the lower 1L Spraberry unit reveals that two types of natural fracture sets are present. Vertical to near vertical irregularly mineralized shear fracture striking NNE-SSW dominate the system; with a second much smaller fracture set composed of un-mineralized vertical extension fractures striking E-W (**Fig. 9**). The average spacing of the shear fracture system is 2 ft in average while the average spacing of the extensional fracture system is 20 ft.

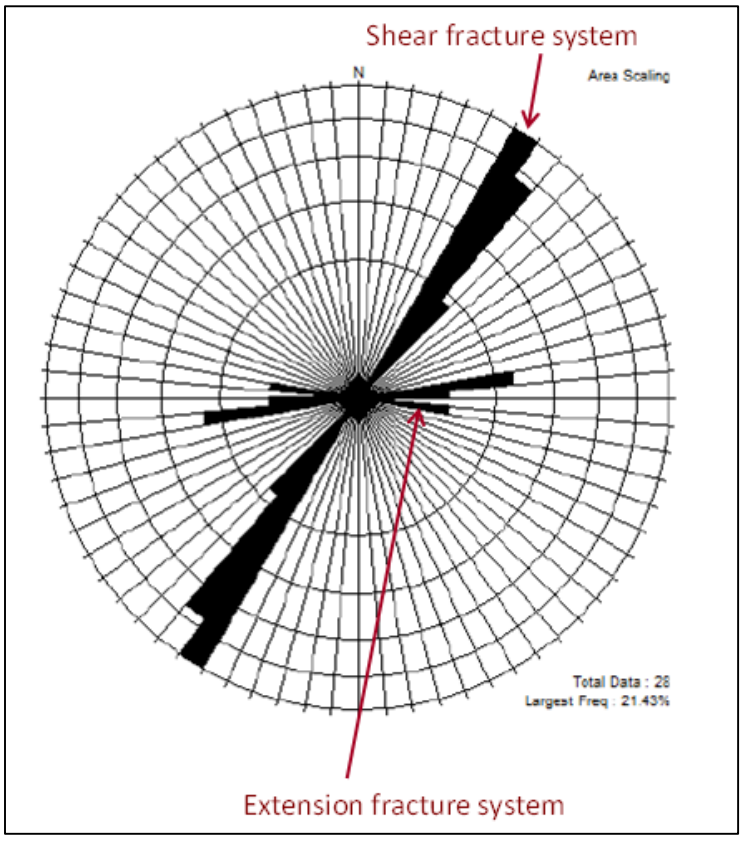

Fig. 9 - Rose diagram of the two fracture systems present in the lower 1L spraberry unit.

3.3 Microseismic Monitoring Field Setup

Microseismic data was acquired during the 15 stages of a hydraulic fracture stimulation treatment of a horizontal well drilled along the Jo Mill sandstone interval. The monitoring receiver array was deployed in a nearby vertical well and consisted of 12 shuttles of 3C geophone-accelerometer (GACD) spaced 30.5 m (100 ft.) apart with the top most shuttle at 1371.6 m (4500 ft.) measured depth from ground level.

Fig. 10 shows the rose diagram of the two natural fracture sets, together with the azimuth of the horizontal well and the average azimuth of the microseismic cloud of located events.

Fig. 11 and **Fig. 12** are the respective map and depth view of the located microseismic events color coded according the stages. The figure also shows the horizontal well. The vertical array of receivers is represented by the vertical aligned triangles in the side view and by the red dot in the map view.

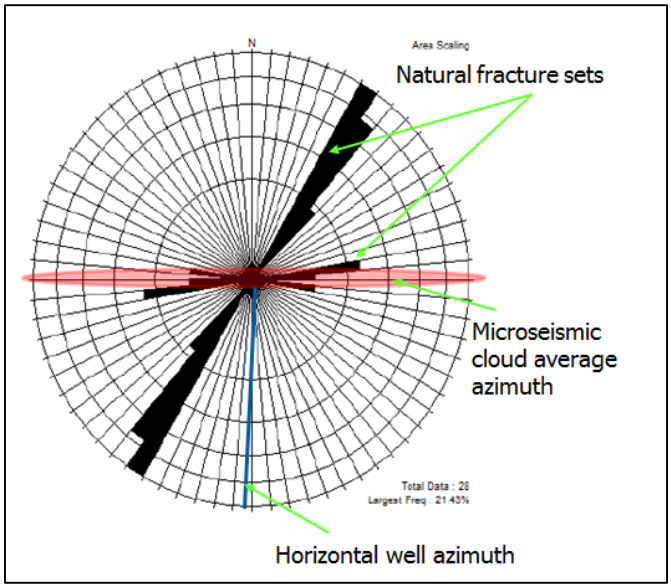

Fig. 10 - Rose diagram of the two fracture systems present in the lower 1L spraberry unit, the horizontal well azimuth and the average azimuth of the microseismic cloud of events.

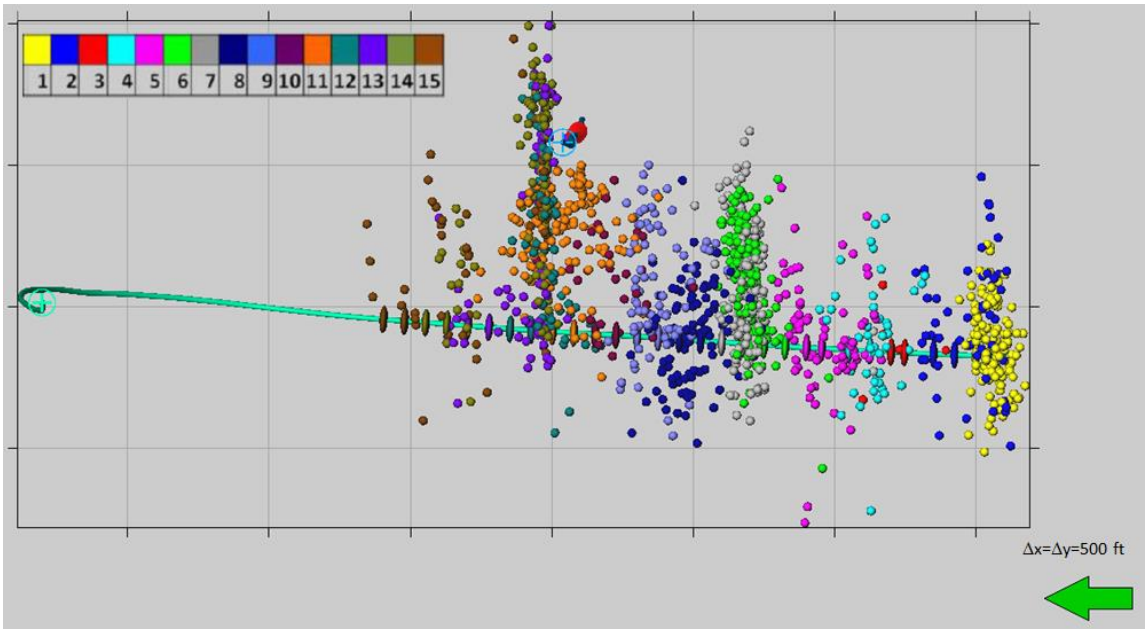

Fig. 11 - Map view of microseismic events.

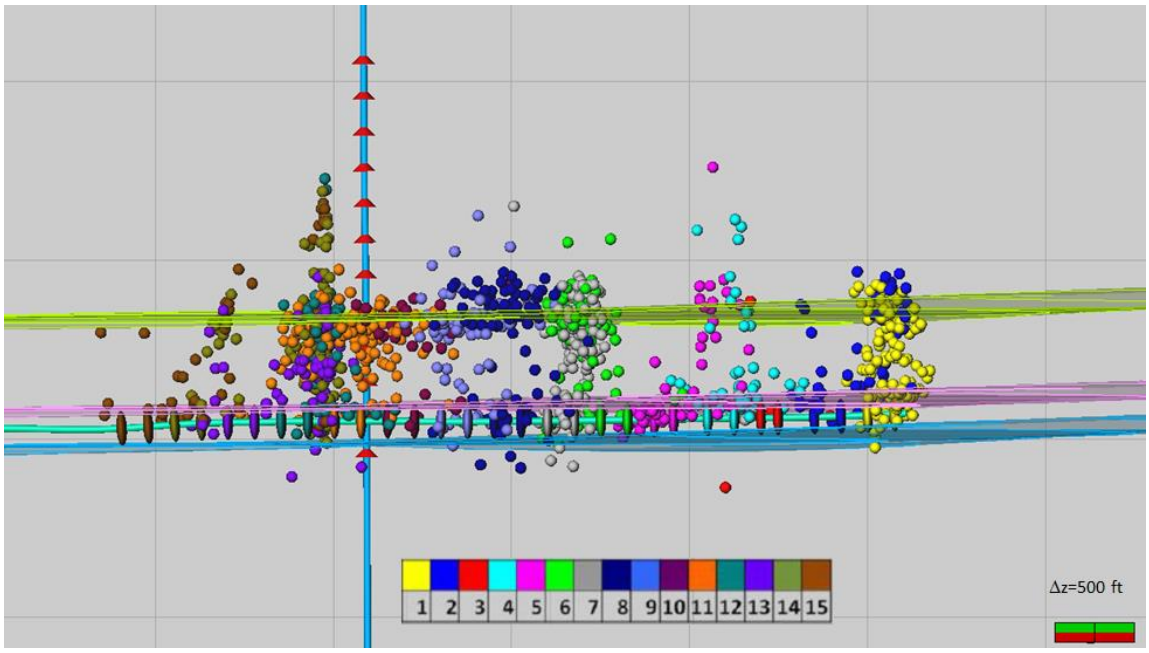

Fig. 12 - Depth view of microseismic events.

4. MECHANICAL ANALYSIS OF NATURAL AND HYDRAULIC FRACTURE INTERACTION

According to Warpinski et al. (2013) there are two main mechanisms inducing the reactivation of natural fractures: local stress perturbation caused by the tip of the propagating hydraulic fracture and increased pore pressure due to fracturing fluid leak off along the hydraulic fracture open planes. Thus, the suggested two possible zones of induced microseismicity **Fig. 4**: The area close to the fracture tip (zone 1) and the wide region normal to the fracture surface (zone 2).

The interaction in zone 1 can be explained as a two-step process (Gu et al. 2012). First, a pure mechanical interaction occurs slightly ahead of the fracture tip. In this stage the influence of the fracturing fluid is not considered due to lag that its front experiences respect to the advancing crack tip (Garagash and Detournay 1999, Groenenboom et al. 2001). Then the second stage happens when the fluid front reaches the pre-existing discontinuity. Induced microseismicity can occur during the mechanical interaction if the local stress perturbation is sufficient to overcome the shear strength of the plane of weakness (Renshaw and Pollard 1995, Weng et al. 2011).

On the other hand, analytical and numerical models suggest that induced microseismicty by reactivation of plane of weaknesses occurs in zone 2 mainly as consequence of increased pore pressure due to fluid leak off along the hydraulic fracture faces. Since pore pressure decreases the effective normal stresses, shear slippage may take place when the normal stress on the natural fracture plane falls below a threshold at which

it cannot longer prevent shear reactivation. Warpinski et al. (2004) used the analytical solution of a pressurized crack after Sneddon (1946) to calculate induced stresses caused by the presence of the hydraulic fracture, and pressure correlations to estimate the pore pressure distribution around the hydraulic fracture caused by leak off. They concluded that stress perturbation caused by increased pore pressure is more significant than hydraulic fracture induced stresses and that it is the main reason for reactivation of favorable oriented plane of weaknesses.

The mechanical analysis presented in this chapter consists of two parts. First, the possibility of reactivation of the two natural fracture sets will be assessed under the influence of the propagating hydraulic fracture tip. Then, their influence in natural fracture reactivation of the stress perturbation around the open hydraulic fracture plane and pore pressure increase due to fluid diffusion will be studied. For these analyses two sets of natural fracture will be considered, one striking 80 deg. from North, simulated the tensile set fracture sett and the other one striking 35 deg., simulating the shear fracture set. The medium will be considered as isotropic and homogenous in a 2-D space.

4.1 Interaction with the Hydraulic Fracture Tip

According to Linear Elastic Fracture Mechanics (LEFM), the stress components close to the fracture tip in opening mode for plane elasticity in a homogenous and isotropic material can be approximated in polar coordinates as (Sun and Jin 2012):

$$\sigma_{xx} = -\frac{K_{\mathrm{I}}}{\sqrt{2\pi r}}\cos\frac{\theta}{2}\left(1-\sin\frac{\theta}{2}\sin\frac{3\theta}{2}\right) \quad \textbf{(11)}$$

$$\sigma_{yy} = -\frac{K_{\mathrm{I}}}{\sqrt{2\pi r}}\cos\frac{\theta}{2}\left(1+\sin\frac{\theta}{2}\sin\frac{3\theta}{2}\right) \quad \textbf{(12)}$$

$$\tau_{xy} = -\frac{K_{\mathrm{I}}}{\sqrt{2\pi r}}\sin\frac{\theta}{2}\cos\frac{\theta}{2}\cos\frac{3\theta}{2} \quad \textbf{(13)}$$

Where K_I is the stress intensity factor and r and θ are the polar coordinates with origin at the fracture tip.

Considering a hydraulic fracture approaching a natural fracture with angle β in an infinite rectangular medium whose far field stresses are σ_H and σ_h with $\sigma_H > \sigma_h$ and with σ_H in the direction of the hydraulic fracture propagation (**Fig. 13**), and using the principle of superposition, the total stress can be expressed as:

$$\sigma'_{xx} = \sigma_H + \sigma_{xx} \quad \textbf{(14)}$$

$$\sigma'_{yy} = \sigma_h + \sigma_{yy} \quad \textbf{(15)}$$

$$\tau'_{xy} = \tau_{xy} \quad \textbf{(16)}$$

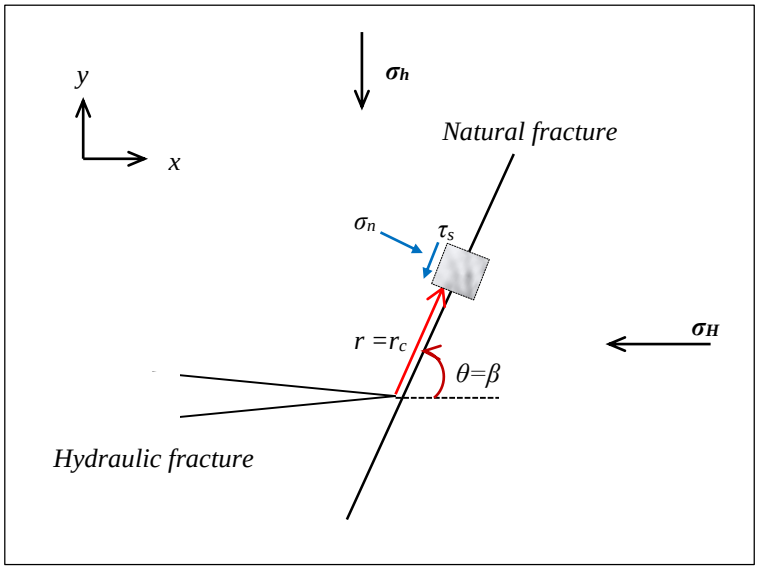

Fig. 13 - Hydraulic fracture approaching a natural fracture. Modified after H.Gu and X.Weng (2010).

It can be noticed from **Eq. (11) to Eq. (13)** that all stress components present a $1/\sqrt{r}$ factor and have an infinite value at the fracture tip (r = 0). However, no material can bear an infinite stress and it will deform plastically at a finite stress value. Then, it can be assumed that there is a distance r_c from the fracture tip beyond which the aforementioned equations are valid (Renshaw and Pollard 1995).

For the natural fracture to slip, the Coulomb criterion must be satisfied:

$$|\tau_s| \geq S_o + \mu\,\sigma_n \qquad \textbf{(17)}$$

Where τ_s and σ_n are the shear and normal stress on the natural fracture plane respectively, S_o is the cohesion of the fracture plane and μ is the coefficient of friction.

Stresses on the natural fracture plane are calculated by rotating the total stress field by the angle between the natural and hydraulic fracture (β) as follows:

$$\tau_s = -\frac{1}{2}\left(\sigma'_{xx} - \sigma'_{yy}\right)\sin 2\beta + \tau'_{xy}\cos 2\beta \quad \textbf{(18)}$$

$$\sigma_n = \frac{1}{2}\left(\sigma'_{xx} + \sigma'_{yy}\right) - \frac{1}{2}\left(\sigma'_{xx} + \sigma'_{yy}\right)\cos 2\beta - \tau'_{xy}\sin 2\beta \quad \textbf{(19)}$$

The total stress field ($\sigma'_{xx}, \sigma'_{yy}, \tau'_{xy}$) is calculated using **Eq. (14) to Eq. (16)** with θ = β. K_I and r_c values still need to be calculated. K_I and r_c are lamped in a new variable K following the treatment of H.Gu and X.Weng (2010):

$$K = \frac{K_{\mathrm{I}}}{\sqrt{2\pi r_c}}\cos\frac{\theta}{2} \quad \textbf{(20)}$$

After replacing K in **Eq. (11) to Eq. (13)**, an additional equation is set up considering that for the hydraulic fracture to reinitiate on the opposite side of the natural fracture, the maximum principal stress σ_1 must reach the rock tensile strength T_o:

$$\sigma_1 = T_o \quad \textbf{(21)}$$

Where σ_1 is calculated as follows:

$$\sigma_1 = \frac{1}{2}\left(\sigma'_{xx} + \sigma'_{yy}\right) + \sqrt{\left(\frac{\sigma'_{xx}+\sigma'_{yy}}{2}\right)^2 - {\tau'_{xy}}^2} \quad \textbf{(22)}$$

Finally, **Eq.(21)** becomes a quadratic equation in K and the solution giving $\sigma_1 = T_o$ is picked.

Table 2 shows the parameters used for the stress analysis close to the propagating fracture tip.

$\boldsymbol{\sigma_h}$	2700 psi (18.6 MPa)
$\boldsymbol{\sigma_H}$	1.3 σh
$\boldsymbol{T_o}$	- 150 psi (- 1.0 MPa)
$\boldsymbol{S_o}$	0 psi (0 MPa)
$\boldsymbol{\mu}$	0.6

Table 2 - Values for stress analysis induced on the natural fracture by the hydraulic fracture tip.

Fig. 14 and **Fig. 15** show the plots for normal and shear stress components on the natural fracture plane vs σ_H / σ_h ratio calculated using **Eqs. (18) and (19)** for the two different fracture sets: one intersecting the natural fracture at β = 10 deg. and the other one intersecting the natural fracture at β = 55 deg. The red horizontal dashed line marks the assumed σ_H / σ_h ratio equal to 1.3 (Farrington 1955).

According to **Fig. 14**, for the lower angle of interserction β = 10 deg, the normal stress component is lower than the shear stress on the fracture plane for every σ_H / σ_h ratio considered in the plot. For the assumed σ_H / σ_h ratio at the reservoir, the actual values are: σ_n = 10.6 psi (0.1 MPa), τ_s = 375.9 psi (2.6 MPa) which accommodates for a high probability for shear slip.

On the other hand, for the higher angle of intersection at β = 55 deg (**Fig. 15**), the shear stress component resolved on the fracture plane is always greater than the normal stress component. The actual values of tensile and shear components are: σ_n = 1708.2 psi (11.8 MPa), τ_s = 1179.8 psi (8.13 MPa) which decreases the possibility of shear reactivation.

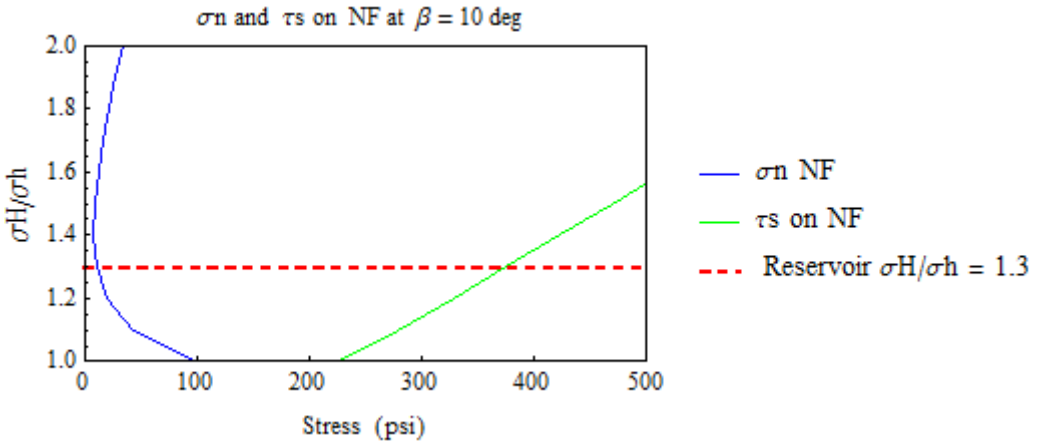

Fig. 14 - Normal and shear stress on the natural fracture plane vs σ_H / σ_h ratio for a natural fracture intersecting at 10 deg. the hydraulic fracture. The red dashed line is the assumed stress ratio at the reservoir.

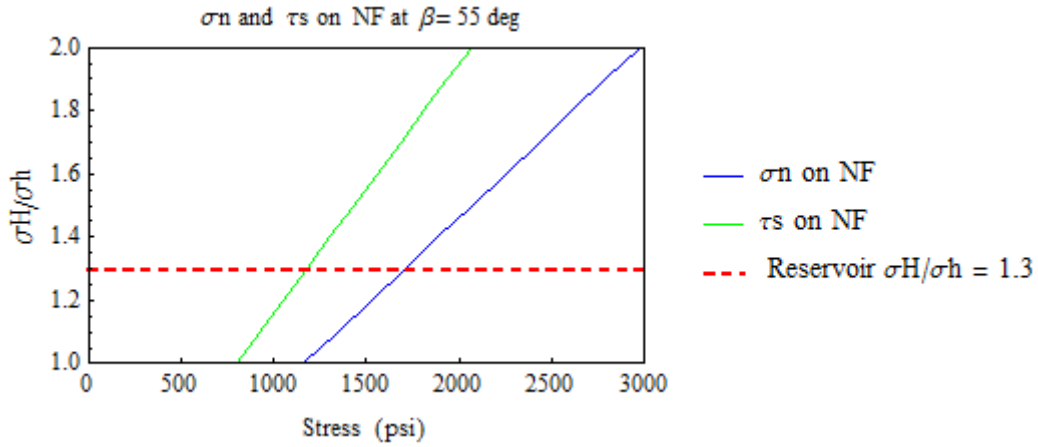

Fig. 15 - Normal and shear stress on the natural fracture plane vs σ_H / σ_h ratio for a natural fracture intersecting at 10 deg. the hydraulic fracture. The red dashed line is the assumed stress ratio at the reservoir.

For both angles of interaction, the normal stress on the fracture planes is never negative. Thus, the type of rupture expected is compressional shear, however normal stress values close to zero for β = 10 deg. suggest that pure shear rupture mode can also be expected.

For the slip criterion, a slight modification of **Eq. (17)** is used as follows:

$$\mu \leq \frac{(|\tau_s| - S_o)}{\sigma_n} \qquad \textbf{(23)}$$

Furthermore, shear and normal stresses (τ_s and σ_n) on the fracture plane are expressed in terms of σ_H / σ_h ratio.

Fig. 16 and **Fig. 17** show the criterion curves for a hydraulic fracture crossing a natural fracture at β = 10 deg. Crossing occurs in the zone below the curves. The red dashed line marks the assumed σ_H / σ_h ratio at the reservoir (1.3), the vertical black dashed is the assumed natural fracture friction coefficient (0.6). The intersection of both lines determines the assumed state at the reservoir.

Fig. 16 shows the criterion for two for two different values of fracture cohesion (S_o). Notice that the reservoir state at the assumed values of σ_H / σ_h ratio and natural fracture friction coefficient (0.6) is above both curves meaning that the natural fracture will slip at this condition. However, notice the effect of the natural fracture cohesion (S_o). The higher this value is, the closer it gets to crossing at the assumed σ_H / σ_h and friction coefficient at the reservoir.

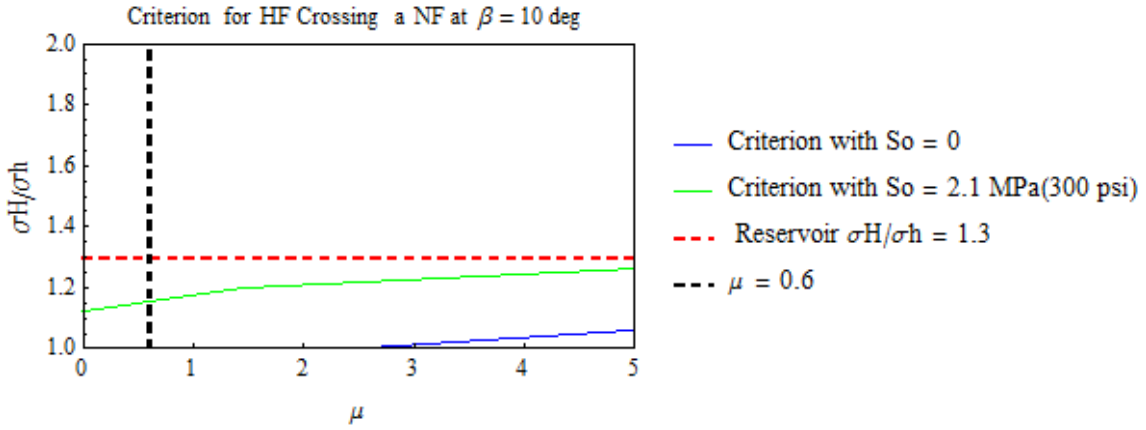

Fig. 16 - Criterion for a hydraulic fracture crossing a natural fracture at an angle of 10 deg. and for two different values of fracture cohesion (So). Crossing occurs in the zone below the curves. The red dashed line marks the assumed σ_H / σ_h ratio at the reservoir (1.3), the vertical black dashed is the assumed natural fracture friction coefficient (0.6). The intersection of both lines determines the assumed state at the reservoir. This point is above both curves meaning that the natural fracture will slip at this condition.

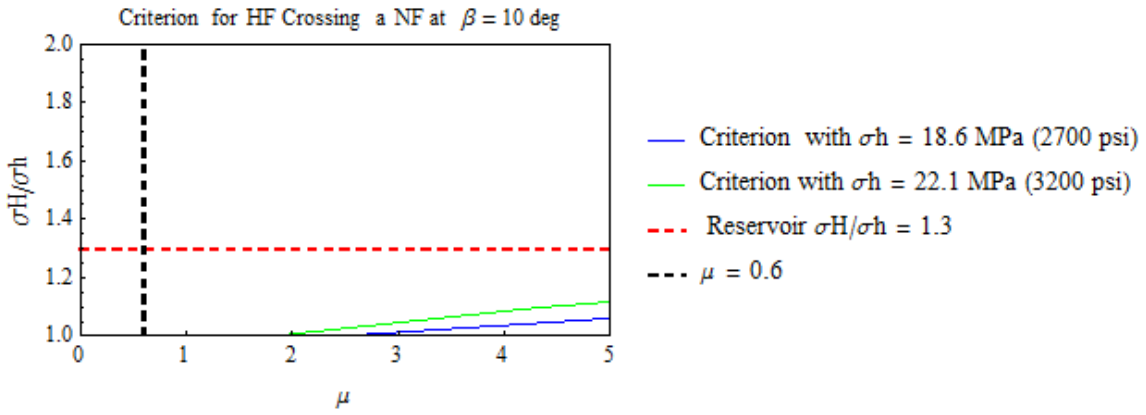

Fig. 17 - Criterion for a hydraulic fracture crossing a natural fracture at an angle of 10 deg. and for two different σ_h .Crossing occurs in the zone below the curves. The red dashed line marks the assumed σ_H / σ_h ratio at the reservoir (1.3), the vertical black dashed is the assumed natural fracture friction coefficient (0.6). The intersection of both lines determines the assumed state at the reservoir. This point is above both curves meaning that the natural fracture will slip at this condition.

Fig. 17 shows the criterion for two for two different values of σ_h. At reservoir conditions, marked by the intersection of the vertical and horizontal dashed lines, the natural fracture will slip since the reservoir state is at above both curves. The effect of increasing σ_h is similar to the effect of increasing S_o, in the sense that the criterion curve gets closer to the reservoir state but in this case the variation is less stronger.

Fig. 18 and **Fig. 19** shows the criterion curves for a hydraulic fracture crossing a natural fracture at β = 55 deg. Crossing occurs in the zone to the right of the curves. The red dashed line marks the assumed σ_H / σ_h ratio at the reservoir (1.3), the vertical black dashed is the assumed natural fracture friction coefficient (0.6). The intersection of both lines determines the assumed state at the reservoir.

Fig. 18 shows the criterion for two for two different values of fracture cohesion (S_o). For this case, notice that for the assumed σ_H / σ_h ratio at the reservoir (1.3), and the natural fracture friction coefficient (μ = 0.6), natural fracture slippage will occur for the case of S_o =0 but hydraulic fracture crossing will occur for S_o =300 psi.

Fig. 19 shows the criterion fro two different values of the reservoir rock tensile strenght (T_o). For both curves S_o =300 psi. For the assumed σ_H / σ_h ratio at the reservoir (1.3) and the natural fracture friction coefficient (μ = 0.6), natural fracture slippage will occur for T_o = -750 psi but hydraulic fracture crossing will occur for T_o =-150 psi. Notice that decreasing the value of the rock tensile strength move the criterion curve to the right increasing the probability of natural fracture slippage.

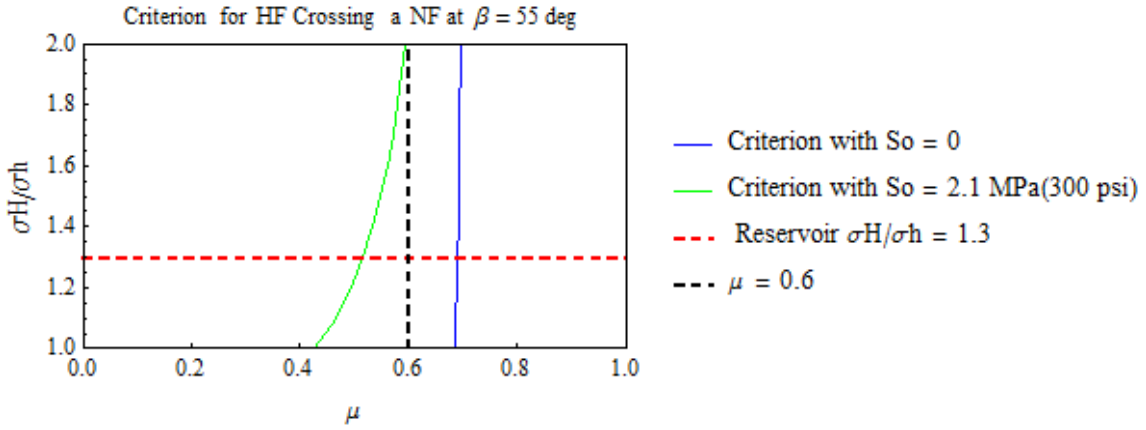

Fig. 18 - Criterion for a hydraulic fracture crossing a natural fracture at an angle of 55 deg. and for two different values of fracture cohesion (So) .Crossing occurs in the zone to the right of the curves. The red dashed line marks the assumed σ_H/σ_h ratio at the reservoir (1.3), the vertical black dashed is the assumed natural fracture friction coefficient (0.6). The intersection of both lines determines the assumed state at the reservoir. This point is to the left of the curve when So =0 and to the right when So = 300 psi. Slip of the natural fracture plane will occur in the first case and crossing of the hydraulic fracture in the second case.

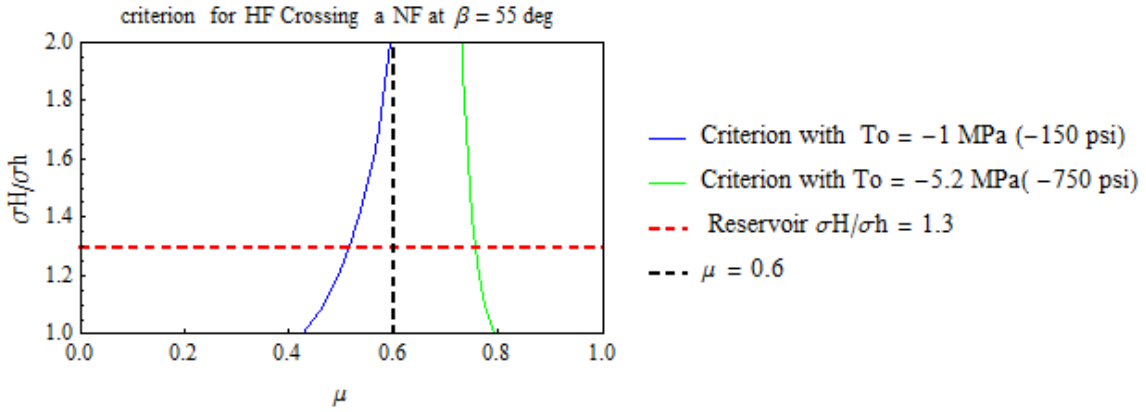

Fig. 19 - Criterion for a hydraulic fracture crossing a natural fracture at an angle of 55 deg. and for two different values of *To* .Crossing occurs in the zone to the right of the curves. The red dashed line marks the assumed $\sigma H/\sigma_h$ ratio at the reservoir (1.3), the vertical black dashed is the assumed natural fracture friction coefficient (0.6). The intersection of both lines determines the assumed state at the reservoir. This point is to the right of the curve when To = -150 psi and to the left when To = -750 psi. Crossing of the hydraulic fracture will occur in the first case and slip of the natural fracture in the second case

From these analyses we conclude that:

- The lower the angle of interaction (β), the greater the opportunity of natural fracture slippage.

- The greater the fracture cohesion (S_o,), the lower the opportunity of slippage on the natural fracture.

- The greater the differential stress (σ_h), the lower the opportunity of slippage on the natural fracture, but this effect is less pronounced compared to the effect of increasing fracture cohesion.

- The lower the tensile strength of the reservoir rock (T_o), the higher the opportunity of slippage on the natural fracture.

Finally, for the two natural fracture sets considered, and for the parameters used as in Table 2**,** both fractures will slip in shear. However if a certain value of cohesion exists on the natural fractures such as S_o = 300 psi, only the set with a lower angle (β = 10 deg.) will slip, unless the reservoir rock presents a lower value of tensile strenght. For a rock tensile stress equal to -750 psi, both sets will slip in shear.

4.2 Interaction Along the Hydraulic Fracture Open Planes

For this analysis, stress perturbations coming from two sources are considered. First, induced stresses due to the open hydraulic fracture planes are calculated for at 2-D model. Then, the pore pressure increase to induce shear slippage on both of the fracture sets is estimated together with the time needed to reach the necessary pore pressure at a certain distance from the hydraulic fracture open planes.

To calculate the stress field induced by the open hydraulic fracture planes, the equations as proposed by Sneddon (1946) for a 2-D model pressurized elliptical crack are used:

$$\sigma_{xx} = p_0 \left(\frac{r}{r_1^{\frac{1}{2}} r_2^{\frac{1}{2}}} \cos\left(\theta - \frac{1}{2}\theta_1 - \frac{1}{2}\theta_2\right) - 1 - \frac{c^2 r}{r_1^{\frac{3}{2}} r_2^{\frac{3}{2}}} \sin\theta \ \sin\frac{3}{2}(\theta_1 + \theta_2) \right) \quad \textbf{(24)}$$

$$\sigma_{yy} = p_0 \left(\frac{r}{r_1^{\frac{1}{2}} r_2^{\frac{1}{2}}} \cos\left(\theta - \frac{1}{2}\theta_1 - \frac{1}{2}\theta_2\right) - 1 + \frac{c^2 r}{r_1^{\frac{3}{2}} r_2^{\frac{3}{2}}} \sin\theta \ \sin\frac{3}{2}(\theta_1 + \theta_2) \right) \quad \textbf{(25)}$$

$$\tau_{xy} = p_0 \frac{c^2 r}{r_1^{\frac{3}{2}} r_2^{\frac{3}{2}}} \sin\theta \ \cos\frac{3}{2}(\theta_1 + \theta_2) \quad \textbf{(26)}$$

Where *po* is the effective internal pressure inside the crack; *c* is the half-length of the crack; r, r_1, r_2, θ, θ_1, θ_2 are the components of the polar coordinates around the fracture planes as shown in **Fig. 20**.

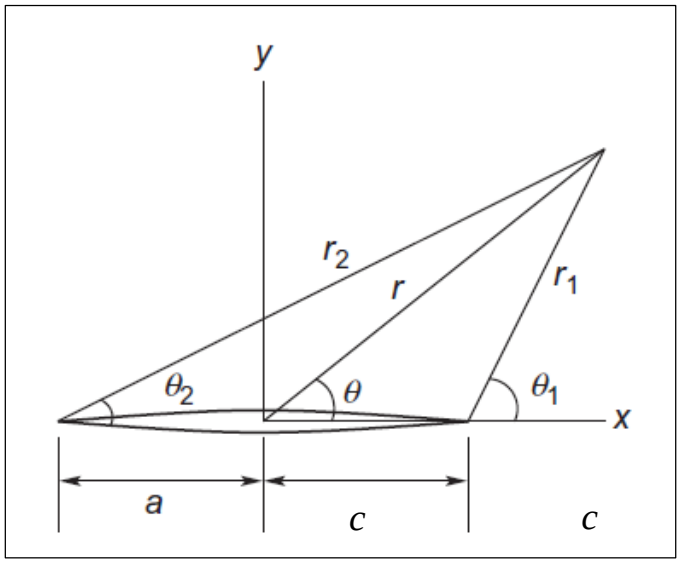

Fig. 20 - Pressurized crack with half-length equal to *c* in polar coordinates. Modified after Sun and Jin (2012).

The maximum displacement occurs at the origin of the coordinate system in the *y* direction and it is equal to:

$$\omega = \frac{2\,(1-\sigma^2)\,p_0\;c}{E} \qquad \textbf{(27)}$$

Where σ, E are the Poisson's ratio and Young's modulus of the rock.

Table 3 shows the reference values used for the calculation of stresses around the hydraulic fracture plane and maximum displacement in the *y* direction

c	500 ft (152.4 m)
po	100 psi (0.7 MPa)
E	5.08 .10^6 psi (35.0 GPa)
σ	0.23

Table 3 - Values for stress analysis to estimate stress around the hydraulic fracture tip.

According to **Eq. (23)** and using the values of Table 3, the maximum displacement in the *y* direction of the proposed hydraulic fracture is ω = 0.22 in. (0.57 cm).

Fig. 21 shows one quarter of the elliptic hydraulic fracture and **Fig. 22** to **Fig. 24** shows the stress field induced by the presence of the open planes of the hydraulic fracture.

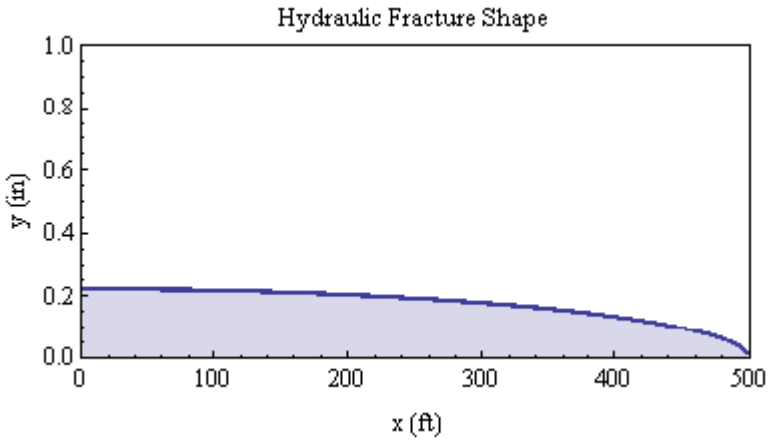

Fig. 21 - Hydraulic fracture shape.

The horizontal component of stress σ_{xx} (**Fig. 22**) is mainly tensile and around -100 psi (0.7 MPa) very close to the fracture plane (y = 0 ft) and gradually decreases to 0 psi as the normal distance from the fracture plane increases. However, close to the fracture tip the behavior is different since σ_{xx} is compressive, increases as the normal distance from the fracture plane increases.

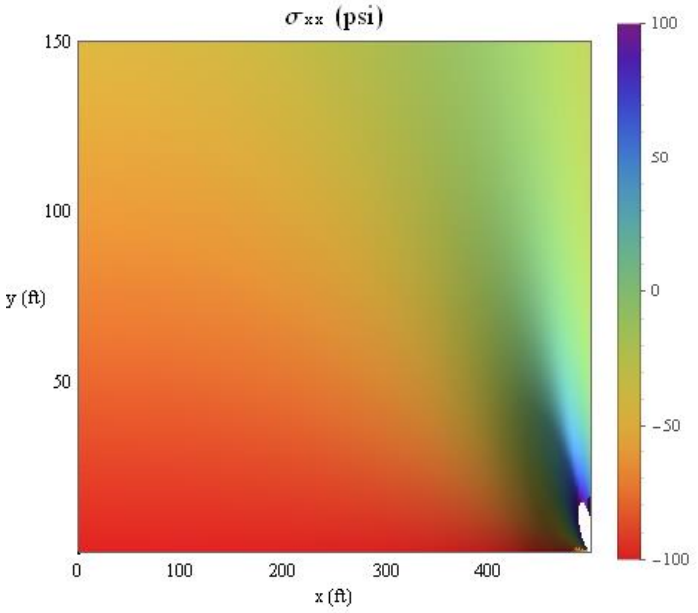

Fig. 22 - Horizontal component of stress induced due to the presence of the hydraulic fracture. The vertical coordinates *y* is the normal distance from the fracture plane and the horizontal coordinate *x* is parallel to the fracture plane.

In a similar way, the vertical component of stress σ_{yy} (**Fig. 23**) is mainly tensile and around -100 psi (0.7 MPa) for most of the shown area. Close to the fracture tip, the vertical component is compressive.

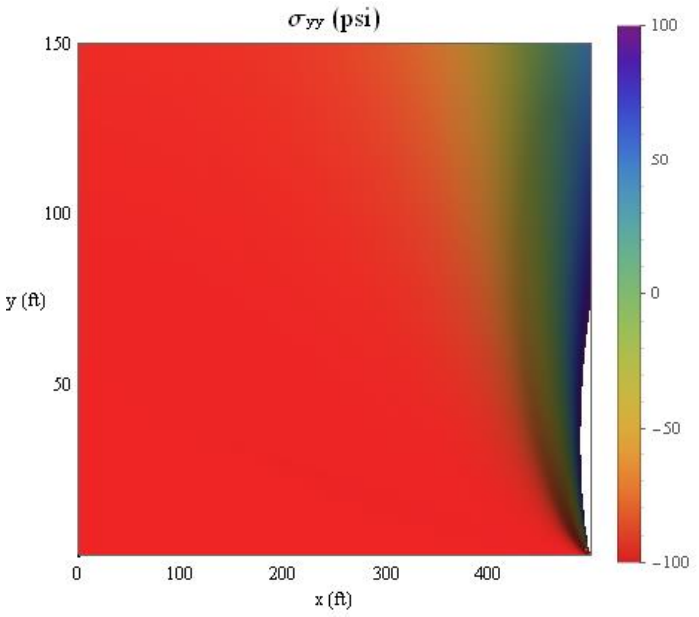

Fig. 23 - Vertical component of stress induced due to the presence of the hydraulic fracture. The vertical coordinates *y* is the normal distance from the fracture plane and the horizontal coordinate *x* is parallel to the fracture plane.

The shear component of stress σ_{xy} (**Fig. 24**) is close to zero for most of the area showed in the graphic except the band parallel to the *y* coordinate, close to the fracture tip where it becomes tensile.

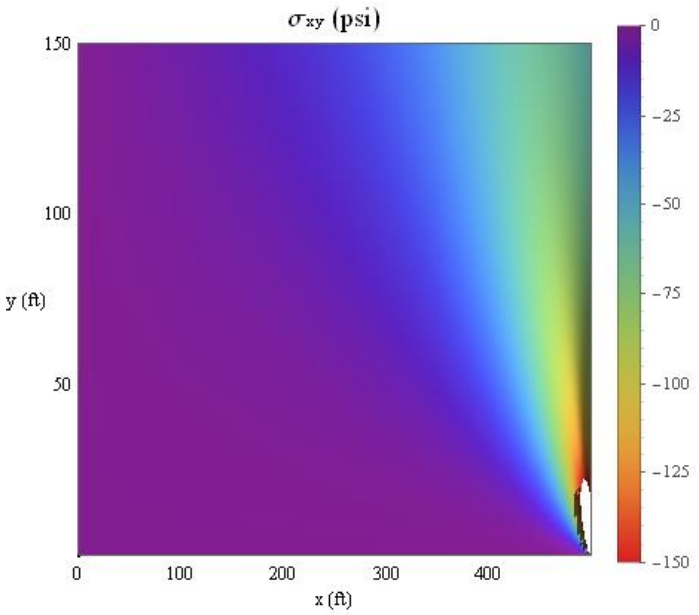

Fig. 24 - Shear component of stress induced due to the presence of the hydraulic fracture. The vertical coordinates *y* is the normal distance from the fracture plane and the horizontal coordinate *x* is parallel to the fracture plane.

To find the possibility of shear failure on any of the sets of the natural fractures, the perturbed stress due to the hydraulic fracture at x = 250 ft (76.2 m) and y = 8.7 ft (2.7 m) are calculated and added to the far field stress σ_H (Maximum Horizontal Stress) σ_h (Minimum Horizontal Stress) whose values are specified in Table 2. Then, the respective Mohr circle will be constructed as well as the Griffith-Coulomb failure envelope following **Eq.(9)** and **Eq.(10)** using the parameters from **Table 2**. The Griffith envelope is constructed for negative normal stresses while the Coulomb envelope is used for positive normal stresses.

The perturbed stress due to the hydraulic fracture at x = 250 ft (76.2 m) and y = 8.7 ft (2.7 m) are: σ_{xx} = - 95 psi (- 0.65 MPa), σ_{yy} = -100 psi (-0.65 MPa) and σ_{xy} = 0 psi (0 MPa).

By the principal of superposition, the total stress field at this point is the sum of the far field stress and the perturbed stress: σ'_{xx} = 3415.4 psi (23.5 MPa), σ'_{yy} = 2600.0 psi (17.9 MPa) and σ'_{xy} = 0 psi (0 MPa)

The Mohr circle is constructed with the maximum principal stress equal to the horizontal stress component ($\sigma_1 = \sigma'_{xx}$) and the minimum principal stress equal to the vertical stress component ($\sigma_3 = \sigma'_{yy}$). For either natural fracture set to slip, the Griffith-Coulomb failure envelope must intersect the Mohr circle at the corresponding angles. However, according to **Fig. 25** the proposed failure envelope does not intersect the Mohr circle at this state of stress.

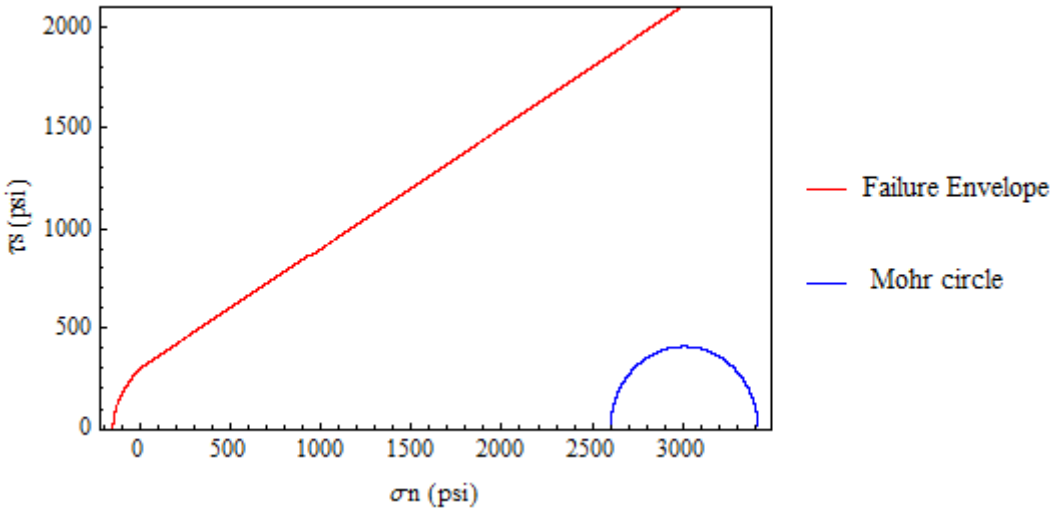

Fig. 25 - Mohr diagram and failure envelope. The Mohr diagram is constructed considering the influence of the perturbed stress due to the presence of the hydraulic fracture at x = 250 ft (76.2 m) and y = 8.7 ft (2.7 m) and the far field reservoir stress σ_H and σ_h.

Pore pressure increase due to hydraulic fracture fluid diffusion can shift the Mohr circle to the left and induce shear slippage on preferred oriented natural fractures. For this study, two types of intersections of the Mohr circle with the failure envelope due to pore pressure increase are considered. For the first case, the Mohr circle intersects tangentially the failure envelope. For the second case, intersection is considered when the least principal stress is equal to the tensile strength of the weakened rock. For both cases, the necessary pore pressure increase will be calculated, as well as the angle of the rupture plane respect to the maximum principal stress.

When the Mohr circle intersects tangentially the failure envelope, the angle of the plane of rupture from the Maximum Principal Stress is:

$$\beta = \frac{\pi}{4} - \frac{1}{2}\tan^{-1}\mu \qquad \textbf{(28)}$$

Table 4 shows the necessary pressure drop (ΔP) to shift the Mohr circle to the left to intersect tangentially the failure envelope and the corresponding angle of the rupture plane (β) from the maximum principal stress (σ_1). The final values of maximum (σ_1) and minimum (σ_3) principal stresses are also shown, as well as the normal (σ_n) and shear (τ_s) stress on the natural fracture plane. **Fig. 26** shows graphically the intersection of the Mohr diagram with the failure envelope.

For this case, none of the natural fracture sets proposed (β =10 deg or β =55 deg.). will slip in shear since according to **Fig. 26** the angle of the plane of rupture is unique and has intermediate value (β =29.5 deg) compared to the angles of the two expected natural fracture sets.

ΔP	2715.3 psi (18.7 MPa)
β	29.5 deg
σ_1	700 psi (4.8 MPa)
σ_3	-115.3 psi (-0.8 MPa)
σ_n	82.6 psi (0.6 MPa)
τ_s	349.6 psi (2.4 MPa)

Table 4 - Solution for the case when the Morh circle intersects tangentially the failure envelope.

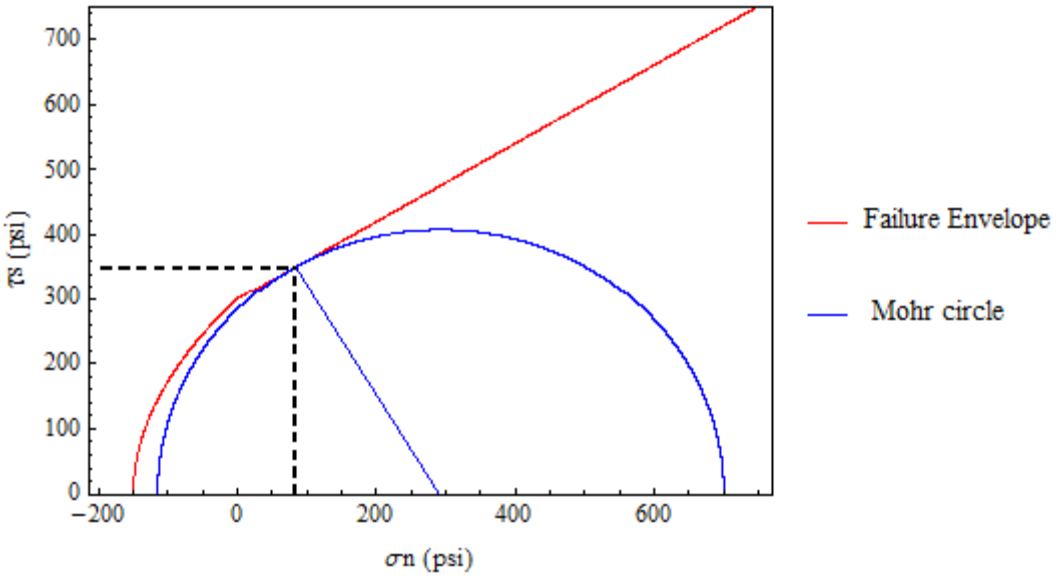

Fig. 26 - Mohr diagram intersecting tangentially the failure envelope.

Considering the case when the minimum principal stress (σ_3) equals the tensile strength of the natural fracture plane (*To*), the pore pressure increase *(ΔP)* needed to shift the Mohr circle is 2700 psi (19 Mpa) as shown in **Table 5**. For this case, the Morh circle intersects the failure envelope at two points (**Fig. 27** and **Table 5)**. The left most point of intersection is at the tensile strength of the natural fracture (- 150 psi) and the rupture mode is pure opening with no shear component. The angle of the rupture plane (β_1) from the maximum principal stress (σ_1) is 0 deg. The second point of intersection occurs for a rupture plane forming an angle (β_2) of 38 deg from the maximum principal stress (σ_1). The shear and normal stress components on the plane of rupture are shown in **Table 5** and marked by the dashed black lines in **Fig. 27**.

ΔP	2750 psi (19 MPa)
β_1	0 deg
β_2	38 deg
β_3	10 deg
σ_1	665.4 psi (4.6 MPa)
σ_3	-150.0 psi (-1.0 MPa)
$\sigma_n^{\beta 1}$	-150 psi (-1.0 MPa)
$\tau_s^{\beta 1}$	0 psi (0 MPa)
$\sigma_n^{\beta 2}$	159.5 psi (1.1 MPa)
$\tau_s^{\beta 2}$	395.7 psi (2.7 MPa)
$\sigma_n^{\beta 3}$	-118.7 psi (-0.8 MPa)
$\tau_s^{\beta 3}$	137.0 psi (0.9 MPa)

Table 5 - Solution for the case when the Minimum principal stress (σ_3) is equal to the tensile strength (*To* = -150 psi)

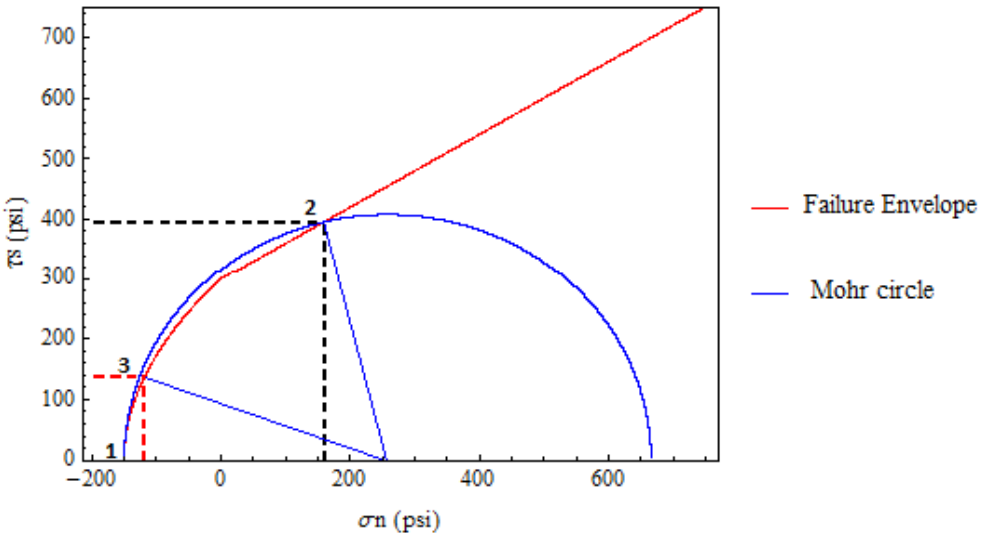

Fig. 27 - Mohr diagram with the minimum principal stress (σ_3) equal to the weak zone tensile strength (*To*= -150 psi). Points 1 and 2 are the intersections with the failure envelope. Point 3 marks the failure point for the fracture set forming an angle of 10 deg. with σ_1. For details see Table 5.

Between the two points of intersection, the Mohr circle is above the failure envelope which means that natural fractures forming angles between 0 and 38 deg. from the maximum principal stress will reactivate. The rupture mode will depend on the sign of the normal stress. For negative values of normal stress, the fracture plane will reactivate in extensional shear, while for positive values of normal stress; the fracture plane will fail in compressional shear. Pure shear will happen when the normal stress is 0 psi (0 MPa) at a fracture plane forming an angle of 24.7 deg. from the maximum principal stress. Thus, only the first natural fracture set (β_3 =10 deg.) considered may reactivate under these conditions since it is found between the two possible points of intersection of the Mohr diagram and the failure envelope (**Fig. 27**), and the expected rupture mode is extensional shear, since the normal stress is extensional (**Table 5**).

To find the possibility of reactivation for the fracture set forming an angle of 55 deg from the maximum principal stress, the parameters for constructing the failure envelope are modified. For this case we considered the tensile strength (T_o) of the weak zone equal to -105 psi (-0.72 MPa) and the friction coefficient value (μ) considered is 0.4. In **Fig. 28**, points 1 and 2 are the intersections of the Mohr envelope with the failure envelope. According to Table 6, the intersection at point 1 occurs at 0 deg from σ_1 (β_1) and the intersection at point 2 at 55 deg from σ_1 (β_3). Thus, for this case, the second natural fracture set forming an angle of 55 deg σ_1 may reactivate with a compressional shear rupture mode according to the values listed in Table 6. Point 3 marks the failure of the natural fracture set forming an angle of 10 deg from σ_1 (β_3) with an extensional shear rupture mode.

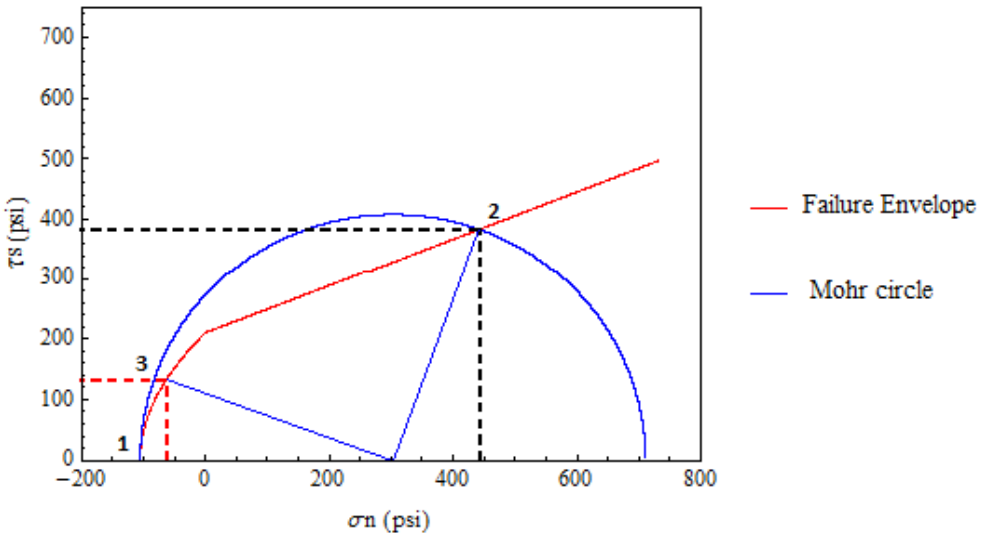

Fig. 28 - Mohr diagram with the minimum principal stress (σ_3) equal to the weak zone tensile strength (*To*= -150 psi). Points 1 and 2 are the intersections with the failure envelope. Point 3 marks the failure point for the fracture set forming an angle of 10 deg with σ_1. For details see Table 6.

ΔP	2705 psi (18.7 MPa)
β_1	0 deg
β_2	55 deg
β_3	10 deg
σ_1	710.4 psi (4.9 MPa)
σ_3	-105.0 psi (-0.7 MPa)
$\sigma_n^{\beta 1}$	-105 psi (-0.7 MPa)
$\tau_s^{\beta 1}$	0 psi (0 MPa)
$\sigma_n^{\beta 2}$	442.1 psi (3.0 MPa)
$\tau_s^{\beta 2}$	382.1 psi (2.6 MPa)
$\sigma_n^{\beta 3}$	- 62.9 psi (-0.4 MPa)
$\tau_s^{\beta 3}$	133.0 psi (0.9 MPa)

Table 6 - Solution for the case when the Minimum principal stress (σ_3) is equal to the tensile strength (To = -105 psi).

To estimate the time needed to reach the necessary pressure increase to reactivate the two sets of natural fractures, the solution of the diffusivity equation for linear flow in an infinite acting reservoir will be used. For this case, the hydraulic fracture is considered as a line source from where fluid is injected to an infinite reservoir at a constant rate. Considering a symmetric hydraulic fracture, only one fourth of the model will be considered. Additionally, only single phase flow of water in will be considered.

The diffusivity equation considered in dimensionless form is:

$$\frac{\partial^2 p_D}{\partial y_D^2} = \frac{\partial p_D}{\partial t_D} \qquad \textbf{(29)}$$

With initial condition:

$$p_D = 0 \ \ for\ t_D = 0 \ \ and\ y_D \geq 0 \quad \textbf{(30)}$$

And boundary conditions:

$$p_D = 0 \ \ for\ t_D > 0 \ \ and \ \ \ y_D \rightarrow \infty \quad \textbf{(31)}$$

$$\frac{\partial p_D}{\partial t_D} = -1 \ \ for\ t_D > and \ \ y_D = 0 \quad \textbf{(32)}$$

Where:

$$y_D = \frac{y}{y_e} \quad \textbf{(33)}$$

$$P_D = \frac{4\ k\ h\ c}{q\ \mu_w y_e}\ \Delta P \quad \textbf{(34)}$$

$$t_D = \frac{k}{\phi \mu_w c_t y_e^2}\ t \quad \textbf{(35)}$$

Where k is the rock permeability, y_e is the length of the reservoir, h is the height of the hydraulic fracture, c is the half-length of the hydraulic fracture, q is the total injected flow rate, μ_w is the viscosity of water, ϕ is the reservoir porosity and c_t is the total compressibility factor.

The solution of **Eq.(29)** under the specified conditions is:

$$p_D\ (y_D, t_D) = 2\sqrt{\frac{t_D}{\pi}} \exp\left(-\frac{y_D^2}{4t_D}\right) - \ y_D\ erfc\left(\frac{y_D}{2\sqrt{t_D}}\right) \quad \textbf{(36)}$$

Fig. 29 shows a cartoon of the assumed geometry for the fluid low solution and **Table 7** shows the parameters used for **Eq.(29)**. **Fig. 30** shows the pressure increase vs time at different distances from the fracture face and **Table 8** shows the time needed to reach a pressure increase of 2700 psi (18.6 MPa) at different distances from the fracture face.

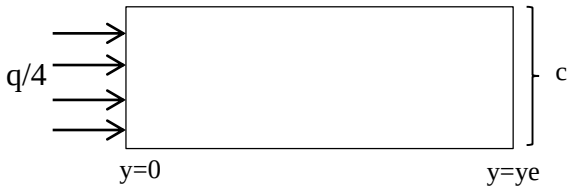

Fig. 29 - Plan view of the linear flow model for fluid diffusion from ¼ of a hydraulic fracture from where the fluid is injected at a constant rate.

c	500 ft (152.4 m)
h	560 ft (170.7 m)
y_e	100 c
q	50 bpm (0.13 m^3/s)
ϕ	0.08
k	0.1 md ($9.9.10^{-17}$ m^2)
μ_w	1.3 cp
c_w	3.10^6 psi^{-1} ($4.4.\ 10^{-10}$ Pa)
c_f	4.10^6 psi^{-1} ($5.8.\ 10^{-10}$ Pa)

Table 7 - Parameters for the estimation of pressure increase.

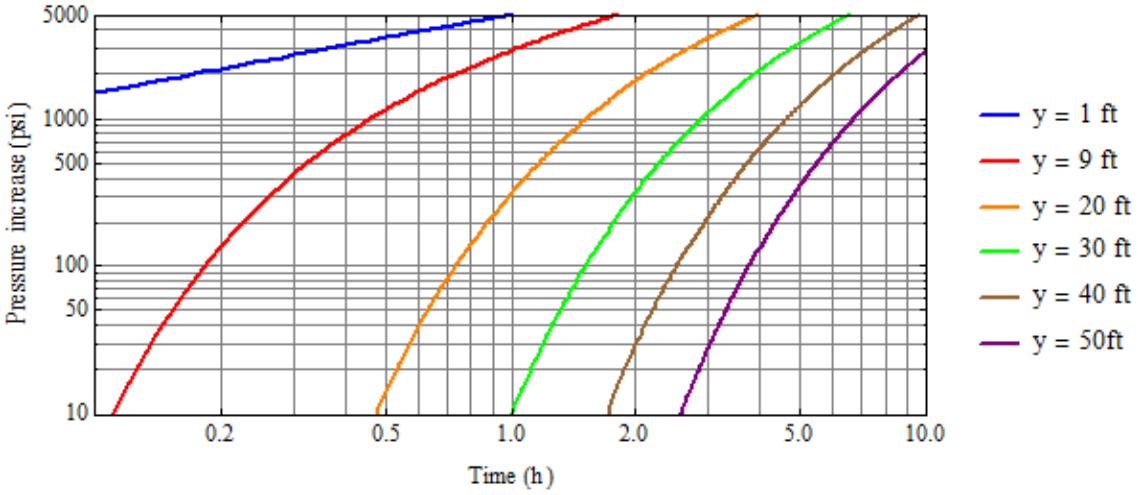

Fig. 30 - Pressure increase vs time at 6 different distances from the hydraulic fracture face.

Distance (ft)	Time (hr)
1	0.3
9	0.9
20	2.5
30	4.5
40	6.9
50	9.8

Table 8 - Time needed to reach a pressure increase of 2700 psi at different distances from the fracture face.

Microseismic events caused by pore increase are later in time since the fracturing fluid needs to diffuse from the hydraulic fracture face. Moreover, this time depends on the distance between the natural fracture and the hydraulic fracture face. Events caused by stress perturbation of the propagating fracture tip are earlier in time since they happen as the hydraulic fracture propagates.

The tensile natural fracture set is the most favorable oriented for reactivation by pressure decrease because of fracturing fluid leak off. The expected rupture mode is extensional shear. The reactivation of the shear set will be strongly controlled by its mechanical properties; in the case of reactivation, the expected rupture mode is compressional shear.

5. SIMULATION STUDIES OF SOURCE MECHANISMS ESTIMATIONS

For all the simulations, the medium is assumed to be an isotropic and homogenous whole space with compressional velocity (Vp) equal to 4361.6 m/s (14309.7 ft/s), shear velocity (Vs) equal to 2619.7 m/s (8594.8 ft/s) and with density (ρ) equal to 2584.4 Kg/m^3 (161.3 lb/ft^3). These medium properties are the same as the estimated for the Lower Spraberry Formation in Section 6, where a homogenous medium validation is also presented. The ratio k =λ/μ is equal to 0.77 which is calculated from the Vp and Vs relationship as follows:

$$\frac{\lambda}{\mu} = \left(\frac{V_p}{V_s}\right)^2 - 2 \qquad \textbf{(37)}$$

The location of the source is: East: 0 m (0 ft); North: 0 m (0 ft); Depth: 1539.2 m (5050 ft).

The recording system is assumed to be a vertical array of 11 receivers; each receiver has three mutually perpendicular recording directions with the following surface coordinates: East: 0 m (0 ft); North: 304.8 m (1000 ft).

Since the recording system is northward from the source epicenter, the radial direction (the direction from the source epicenter to the receiver surface coordinates) and the North coincide. Furthermore, the East coordinate becomes the transverse direction; and both the radial and transverse directions have their origin at the source epicenter (**Fig. 31 A**).

The receivers are separated vertically by a constant distance equal to 30.48 m (100 ft). The shallowest receiver depth is equal to 1402.08 m (4600 ft) and the deepest receiver depth is 1706.88 m (5600 ft).

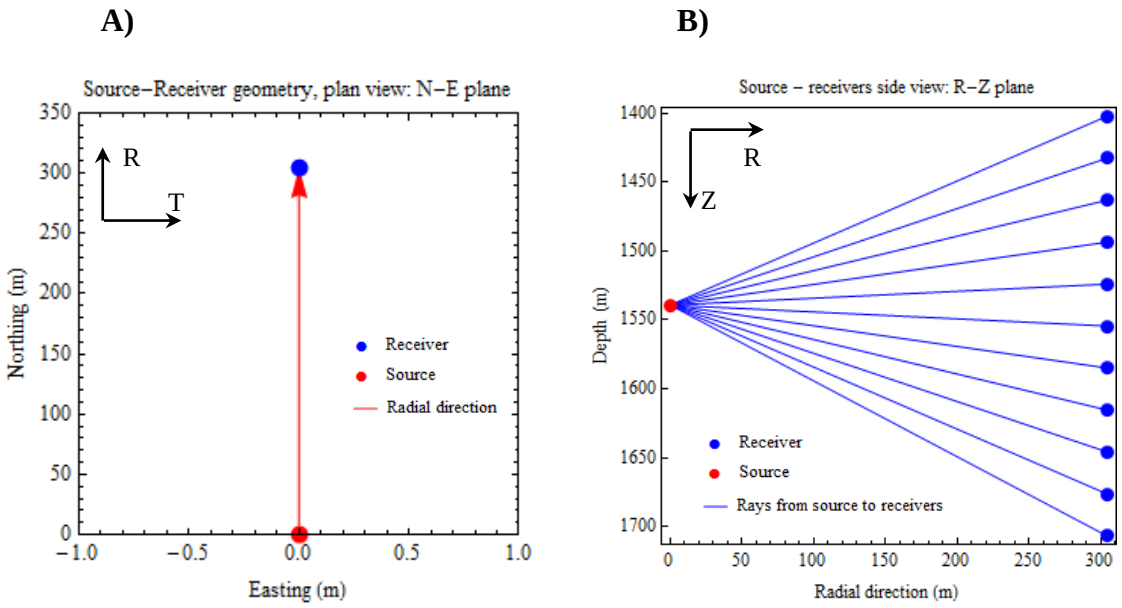

Fig. 31 - A) Plane view of the source and vertical array of receivers with the red arrow showing the radial direction. In the Top left corner, the radial (R) and transverse (T) directions are shown. B) Radial (R) – Depth (Z) view showing the source and the eleven receivers. In the top left corner the radial (R) and down (Z) directions are shown.

On the other hand, if the Radial (R) and Z directions are renamed as x1 and x3 respectively, then the missing moment tensor element is the dipole in the x2 direction (M_{22}) (**Fig. 3**) where x2 is the same as the transverse (T) direction.

5.1 Analysis of Constrained Solutions

Source mechanisms can be estimated from moment tensors, and moment tensors can be estimated by inversion of seismograms. However, Vavryčuk (2007) proved that, from a single recording azimuth, which is the common acquisition design in the oil industry, it is not possible to resolve the moment tensor element perpendicular to the plane formed by the source and the array of vertical receivers. Furthermore, with an incomplete moment tensor it is not possible to estimate the corresponding source mechanism unless some assumptions regarding the rupture event are made. However, if the assumptions defer significantly from the actual mechanism, the estimated source mechanism will be unreliable.

The goal of this section is to analyze the effect of different types of constraints in the reliability of source mechanism estimations. The types of constraints considered are:

- Deviatoric constraint
- Strike constraint
- Combination of strike and dip constraint

To be able to perform the analysis, first amplitude data will be simulated from proposed sources assuming a single vertical array of receivers, then an attempt to retrieve the initial sources will be done by constrained moment tensor inversion applying least squares minimization of amplitude data. In the following paragraphs the mathematical treatment for the forward and inverse modeling is presented.

Assuming that all components M_{kj} of the seismic moment tensor $\boldsymbol{M}$ have the same time dependence $s(t)$, the forward model to simulate displacement components $U_{\boldsymbol{i}}$ at an

arbitrary position $\boldsymbol{x}$ at time t can be written using indicial notation as (Jost and Herrmann 1989) :

$$U_{\boldsymbol{i}}\,(\boldsymbol{x}, t) = [G_{ik,j} * s(t)\,]M_{kj} \qquad \textbf{(38)}$$

Where $G_{ik,j}$ denotes the first spatial derivative of the Green's function and represents displacements due to couples or dipoles of impulsive forces, $s(t)$ is the source time function and represents the slip dependence on time, and * denotes convolution.

The moment tensor describes the properties of the source and the Green's function describes the properties of the medium in which the source is situated. Assuming that the medium is homogenous and isotropic, that $s(t)$ is a step function and that 3-component receivers are placed several wavelengths far from the source, amplitude components $A_{\boldsymbol{i}}$ observed at the 3-component receivers can be derived from **Eq. (38)** and expressed as (Vavryčuk 2007):

$$A_i^w = G_{ik,j}^w\, M_{kj} \qquad \textbf{(39)}$$

Where W refers to P or S phase and $G_{ik,j}^P$ and $G_{ik,j}^S$ are defined as:

$$G_{ik,j}^P = \frac{n_i\, n_k\, n_j}{4\pi\, \rho\, Vp^3\, r} \qquad \textbf{(40)}$$

$$G_{ik,j}^S = -\frac{(n_i\, n_k - \delta_{ik})n_j}{4\pi\, \rho\, Vs^3\, r} \qquad \textbf{(41)}$$

Where n_i, n_k and n_j are the components of the unit vector connecting the source to the ith- component receiver; δ_{ik} is the Kronecker delta; ρ is the density of the medium, Vp and Vs are the compressional and shear velocities of the medium respectively and r is the distance from the source to the receiver.

The moment tensor $\boldsymbol{M}$ for the forward model can be determined from proposed sources using a slight modification of **Eq. (7)**. After assuming that the product $A\,d\,\mu$ is equal to one:

$$\boldsymbol{M} = \frac{\lambda}{\mu}\left(\hat{\boldsymbol{d}}.\hat{\boldsymbol{n}}\,\boldsymbol{I}\right) + \left(\hat{\boldsymbol{n}}\,\hat{\boldsymbol{d}} + \hat{\boldsymbol{d}}\,\hat{\boldsymbol{n}}\right) \qquad \textbf{(42)}$$

The second order moment tensor $\boldsymbol{M}$ is symmetric, therefore it only has six independent components which can be written as the elements of a vector $\widehat{\boldsymbol{M}} = (M_{11}, M_{22}, M_{33}, M_{12}, M_{13}, M_{23})$. Then **Eq. (39)** becomes

$$\widehat{\boldsymbol{A}} = \widehat{\boldsymbol{G}}\widehat{\boldsymbol{M}} \qquad \textbf{(43)}$$

Where $\widehat{\boldsymbol{A}}$ is the vector composed of the amplitudes from all the 3-component receivers. $\widehat{\boldsymbol{G}}$ has as many rows as the number of elements in $\widehat{\boldsymbol{A}}$ and as many columns as moment vector components. The elements of $\widehat{\boldsymbol{G}}$ can still be computed using **Eq.(40)** and **Eq. (41)** according to the arrangement of $\widehat{\boldsymbol{M}}$, however the results have to be doubled for $\widehat{\boldsymbol{G}}$ elements corresponding to the off-diagonal moment tensor components considered in $\widehat{\boldsymbol{M}}$.

For the inverse problem, $\widehat{\boldsymbol{M}}$ can be estimated by least squares minimization:

$$\widehat{\boldsymbol{M}} = \left[\widehat{\boldsymbol{G}}^T\widehat{\boldsymbol{G}}\right]^{-1}\widehat{\boldsymbol{G}}^T\,\widehat{\boldsymbol{A}} \qquad \textbf{(44)}$$

Since for the present field case study, the amplitude data have been recorded from a single vertical array of receivers, one diagonal component of the moment tensor is complete undetermined (Vavryčuk 2007). Thus, only the five recoverable components of the moment tensor will be estimated by least squares inversion.

Once the five recoverable elements of the moment tensor are retrieved, the appropriate constraints can be applied to estimate the missing element. Finally, the

corresponding source mechanisms can be estimated following Vavryčuk (2011). According to him the unit normal vector $\hat{\boldsymbol{n}}$ of the fault plane and the dislocation vector $\hat{\boldsymbol{d}}$ are estimated from the eigenvalues and eigenvectors of the moment tensor as follows:

$$\hat{\boldsymbol{n}} = \sqrt{\frac{\mathbf{E_1}-\mathbf{E_2}}{\mathbf{E_1}-\mathbf{E_3}}}\,\hat{e}_1 + \sqrt{\frac{\mathbf{E_3}-\mathbf{E_2}}{\mathbf{E_3}-\mathbf{E_1}}}\,\hat{e}_3 \qquad \textbf{(45)}$$

$$\hat{\boldsymbol{d}} = \sqrt{\frac{\mathbf{E_1}-\mathbf{E_2}}{\mathbf{E_1}-\mathbf{E_3}}}\,\hat{e}_1 - \sqrt{\frac{\mathbf{E_3}-\mathbf{E_2}}{\mathbf{E_3}-\mathbf{E_1}}}\,\hat{e}_3 \qquad \textbf{(46)}$$

Where the eigenvalues of the moment tensor $\boldsymbol{M}$ are E1 ≥ E2 ≥ E3 and $\hat{\boldsymbol{e}}_{\mathbf{1}}$, $\hat{\boldsymbol{e}}_{\mathbf{1}}$, $\hat{\boldsymbol{e}}_{\mathbf{1}}$ are the corresponding eigenvectors.

It can be noticed in **Eq. (42)** that vectors $\hat{\boldsymbol{n}}$ and $\hat{\boldsymbol{d}}$ can be interchanged without affecting the moment tensor solution. This effect is known as the ambiguity of the fault plane solution. Therefore, the complementary plane can be found by interchanging $\hat{\boldsymbol{n}}$ and $\hat{\boldsymbol{d}}$ in **Eqs. (45)** and **(46)**.

The fault normal and the dislocation vector can be related to the orientation angles: strike (ϕ) and dip (δ); and the rupture angles: rake (λ) and slope (α) as follows:

$$\hat{\boldsymbol{n}} = (-\sin\delta\,\sin\phi\;,\;\sin\delta\,\cos\phi\;,-\cos\delta\,) \qquad \textbf{(47)}$$

$$\hat{\boldsymbol{d}} = \begin{bmatrix} (\cos\lambda\cos\phi + \cos\delta\,\sin\lambda\,\sin\phi\,)\,\cos\alpha - \sin\delta\,\sin\phi\,\sin\alpha\;, \\ (\cos\lambda\cos\phi - \cos\delta\,\sin\lambda\,\sin\phi\,)\,\cos\alpha + \sin\delta\,\sin\phi\,\sin\alpha\;, \\ -\sin\lambda\,\sin\delta\,\cos\alpha - \cos\delta\,\sin\alpha \end{bmatrix} \qquad \textbf{(48)}$$

$$\sin\alpha = \frac{E_1 + E_3 - 2E_2}{E_1 - E_3} \qquad \textbf{(49)}$$

Finally, it is possible to calculate the percentages of ISO, CLVD and DC components by following Vavryčuk (2011):

$$ISO\ \% = \frac{1}{3}\,\frac{Tr\,(\boldsymbol{M})}{|E_{max}|}\;x\;100 \qquad \textbf{(50)}$$

$$CLVD\ \% = 2\,\varepsilon\,(100 - |ISO\ \%|\,) \quad \textbf{(51)}$$

$$DC\ \% = \ (100 - |ISO\ \%| - \ |CLVD\ \%|) \quad \textbf{(52)}$$

Where $Tr\ (\boldsymbol{M})$ is the trace of the Moment tensor $\boldsymbol{M}$, E_{max} refers to the eigenvalue of $\boldsymbol{M}$ with the maximum absolute value and ε is defined as:

$$\varepsilon = \ -\frac{E^*_{min}}{|E^*_{max}|} \quad \textbf{(53)}$$

Where E^*_{min} and E^*_{max} are the eigenvalues of the deviatoric moment tensor $\boldsymbol{M^*}$ with the maximum and minimum absolute values respectively.

The deviatoric moment tensor $\boldsymbol{M^*}$ is calculated as follows:

$$\boldsymbol{M}^* = \boldsymbol{M} \ - \ \frac{1}{3}\,Tr\,(\boldsymbol{M})\,I \quad \textbf{(54)}$$

Where *I* is the identity matrix

The ratio λ/μ is also part of the inversion solution and can be found by applying the following equation:

$$\frac{\lambda}{\mu} = \frac{E_1 + E_3}{E_1 + E_3 - 2E_2} - 1 \quad \textbf{(55)}$$

Notice that when the source mechanism is pure shear, the dot product $\left(\,\widehat{\boldsymbol{d}}.\widehat{\boldsymbol{n}}\,\right)$ in **Eq. (42)** becomes zero since the vectors are perpendicular. Thus, for pure shear sources, the ratio λ/μ is no longer part of the inversion solution.

5.1.1 Deviatoric Constrained Solutions

Induced microseismicity by hydraulic fracturing is commonly interpreted as consequence of shear slippage of plane of weaknesses (Warpinski et al. 2013). Thus, in principle, there would not be a need to consider the isotropic component since this term

would be negligible for sources showing pure slip mechanisms. As consequence, a common assumption is to consider only the deviatoric component in the solution which is achieved my setting to zero the moment tensor trace:

$$M_{11} + M_{22} + M_{33} = 0 \quad \textbf{(56)}$$

If the coordinate system is set in such a way that the unresolvable tensor element is the central dipole M_{22}, then its value can be found from **Eq. (56)**:

$$M_{22} = -(M_{11} + M_{33}) \quad \textbf{(57)}$$

In this study, an analysis of the effect of velocity mismodeling, event mislocation and noisy data in the reliability of source estimations will be also performed for deviatoric constraint solutions.

For this analysis, the rupture mode of the sources are as detailed in Table 9.The moment tensors will be calculated for sources A and B using **Eq. (42)**. Then data will be simulated by calculating P and S amplitudes using **Eqs. (39) to (41)**. Inversion for the five recoverable moment tensor elements will be performed following **Eq. (44)**. Then the unrecoverable moment tensor element will be estimated by applying the deviatoric constraint as in **Eq. (57)**. Finally, source mechanisms will be calculated using **Eqs. (45)** to **(49)**. To be able to compare with the proposed sources, the plane solution with the least strike error from the proposed sources will be chosen. If the angular error is greater than 180, the complementary angle will be reported.

Source	Strike (deg)	Dip (deg)	Rake (deg)	Slope (deg)	k = λ/μ
A	35	75	0	0 - 90	0.77
B	75	85	0	0 - 90	0.77

Table 9 - Proposed sources to be used for the forward modeling.

The percentages of ISO, CLVD and DC for sources A and B are shown in **Fig. 32** and **Fig. 33** respectively. The resulting curves show that these percentages are the same for both sources. Vavryčuk (2001) demonstrated that the percentages of the moment tensor components depend on the slope angle and the ratio 'k', which are confirmed by the results obtained for these two sources which have the same slope angles and values of 'k'.

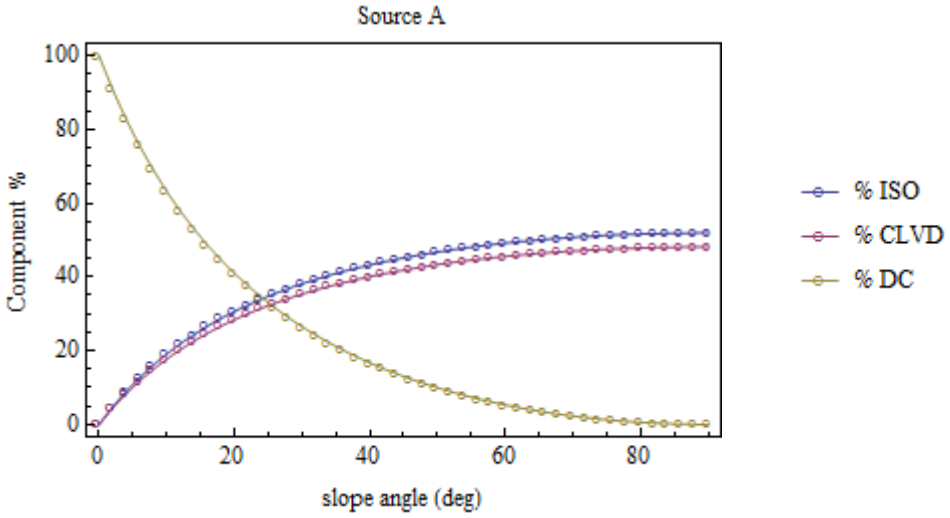

Fig. 32 - Percentages of Moment tensor components for Source A

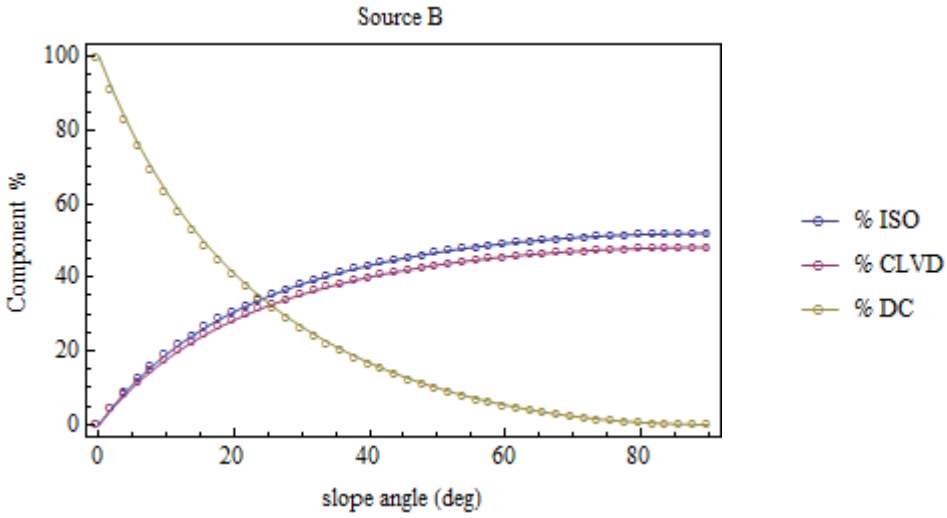

Fig. 33 - Percentages of Moment tensor components for Source B.

From **Fig. 32** and **Fig. 33**, notice that a zero slope angle corresponds to percentages of 100% DC and 0 % CLVD and ISO which is an expected result since a zero slope angle corresponds to a pure shear rupture mechanism which is represented by DC forces only.

Fig. 34 and **Fig. 35** show the results from the deviatoric constrained solutions and the corresponding errors for source A. **Fig. 36** and **Fig. 37** shows the percentages of the moment tensor components and corresponding percentage errors for the retrieved moment tensors for source A .

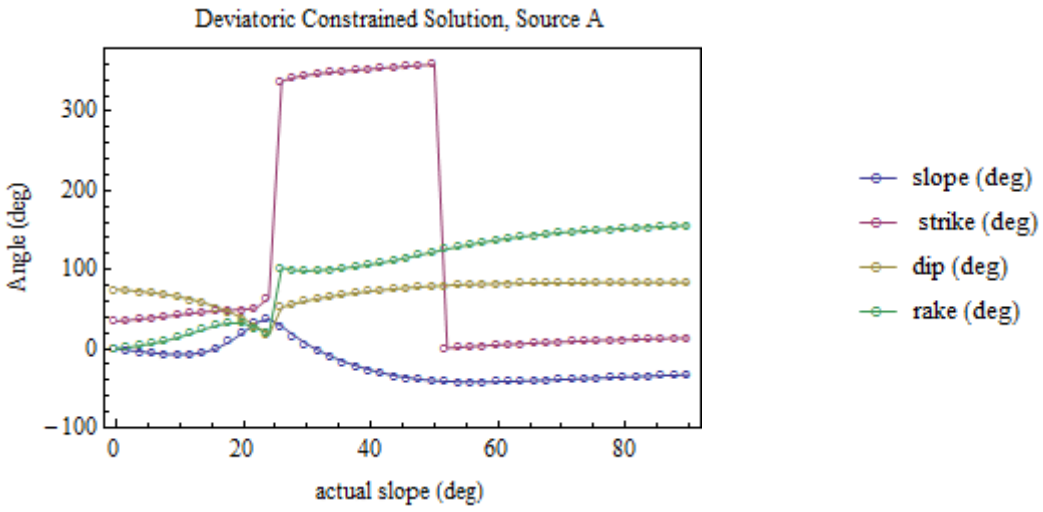

Fig. 34 - Deviatoric constrained fault plane solutions for source A.

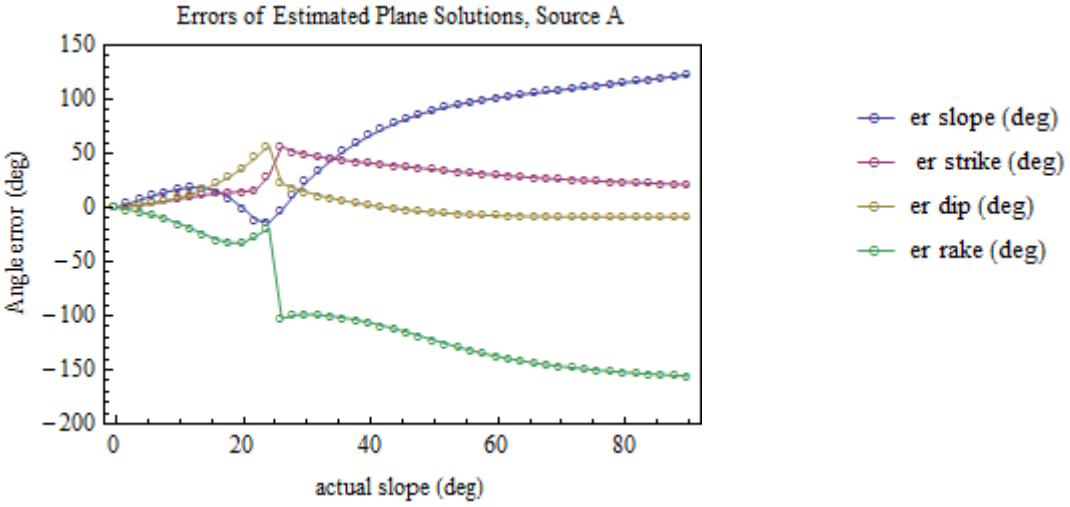

Fig. 35 - Errors in the deviatoric constrained fault plane solutions for source A.

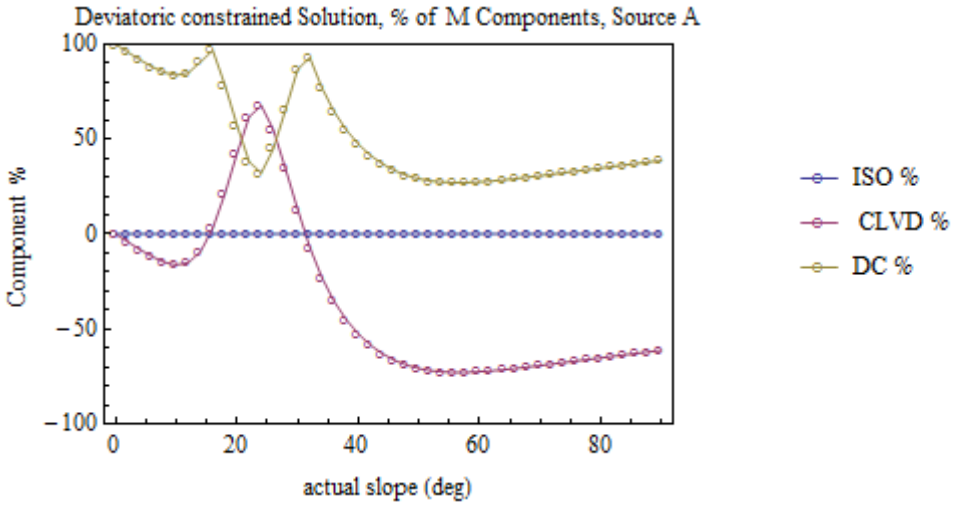

Fig. 36 - Percentage of the moment tensor components for the deviatoric constrained solutions for source A.

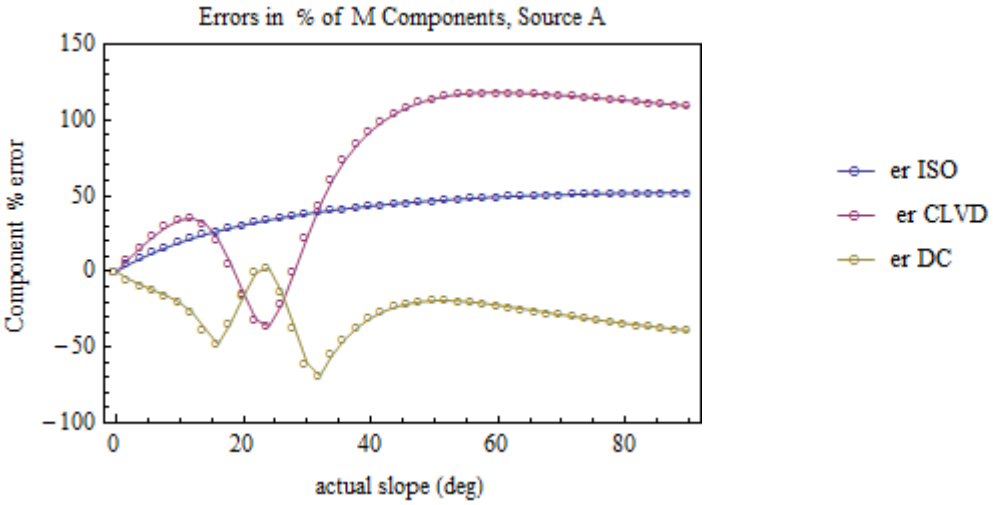

Fig. 37 - Errors in the percentage of the moment tensor components for the deviatoric constrained solutions for source A.

Fig. 38 and **Fig. 39** and show the results from the deviatoric constrained solutions and the corresponding errors for source B. **Fig. 40 a**nd **Fig. 41** shows the percentages of the moment tensor components after applying the deviatoric constrained inversion and the corresponding percentage errors for the retrieved moment tensors for source B.

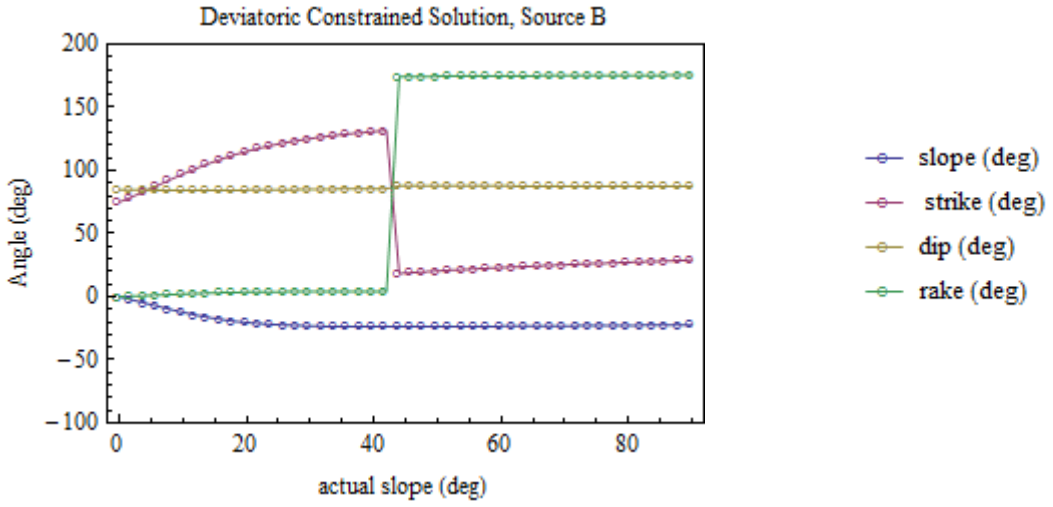

Fig. 38 - Deviatoric constrained fault plane solutions for source B.

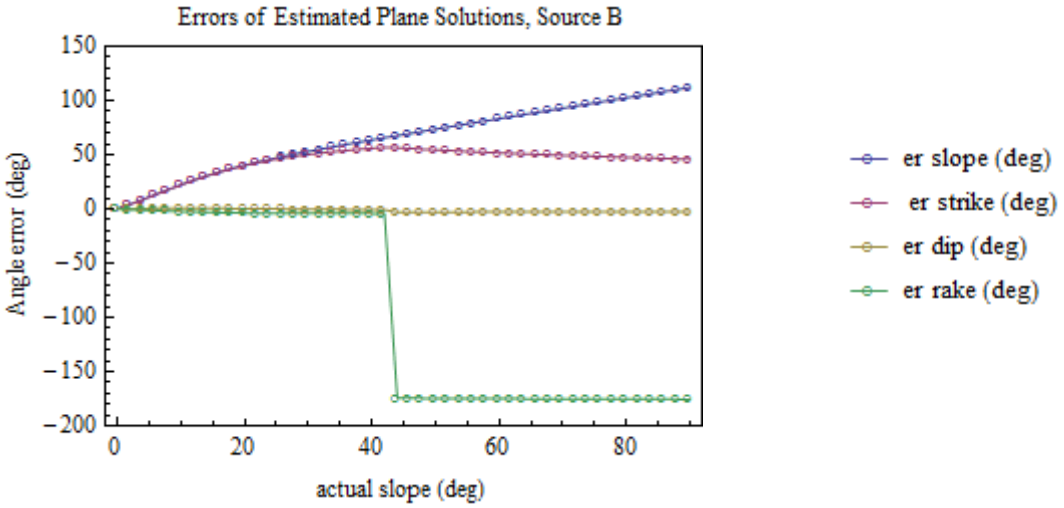

Fig. 39 - Errors in the deviatoric constrained fault plane solutions for source B.

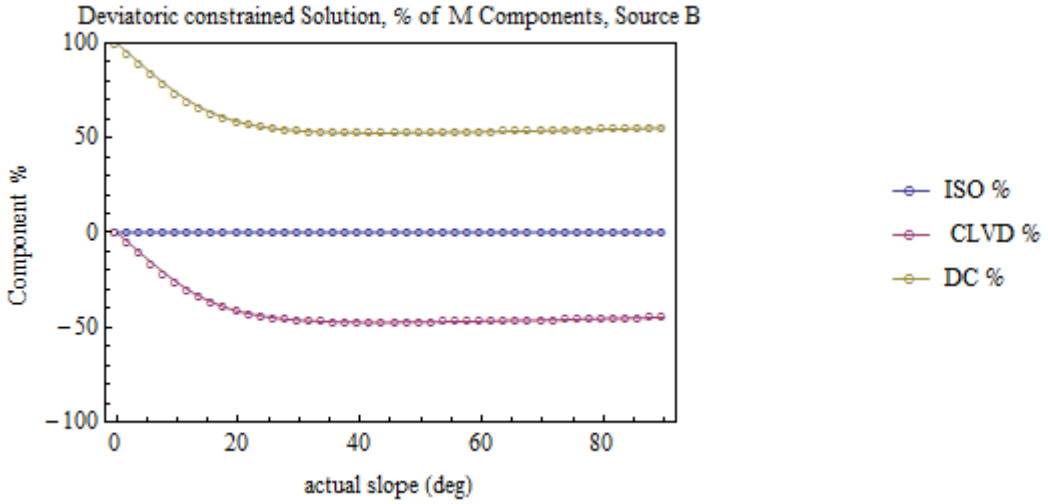

Fig. 40 - Percentage of the moment tensor components for the deviatoric constrained solutions for source B.

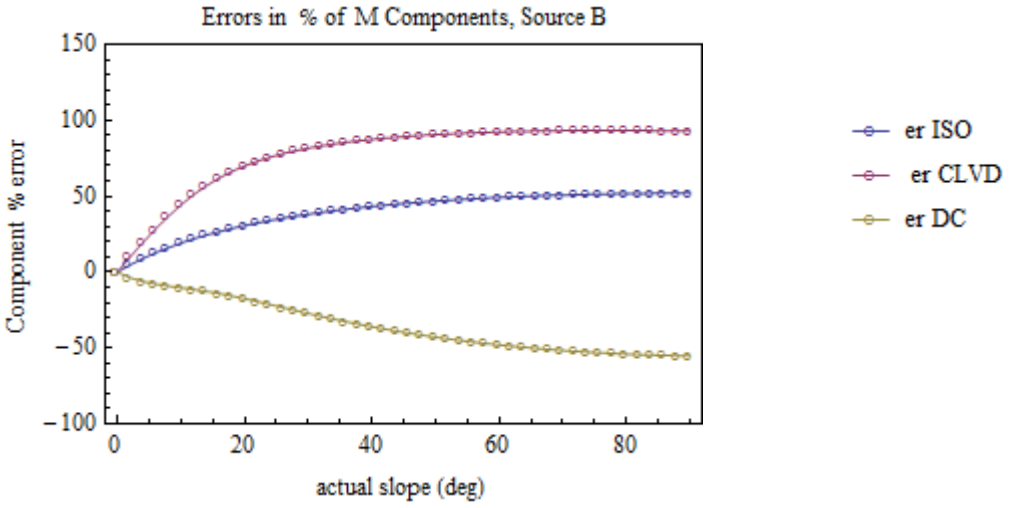

Fig. 41 - Errors in the percentage of the moment tensor components for the deviatoric constrained solutions for source B.

For both sources notice that the greatest errors in absolute for the mechanisms solutions to slope and rake angles which go beyond 50 deg (**Fig. 35** and **Fig. 39**). In a similar way, the greatest error in the moment tensor components (**Fig. 37** and **Fig. 41**) corresponds to CLVD % which also go beyond 50% in absolute values.

For source A notice that the slope error in the fault plane solution (**Fig. 35**) passes through zero two additional times, which corresponds to around 15 and 35 deg in the horizontal axis. A similar behavior is observed in the errors for the moment tensor components (**Fig. 37**) where CLVD and DC % errors decrease close to zero at the same actual slope angles. However, this unexpected behaviors do not indicate that the constrained solution match the actual solution since errors in the other fault plane angles are still significant as well errors in the ISO %.

Fig. 42 to **Fig. 48** show the density plot errors for deviatoric constrained moment tensor solutions as a function of the actual slope and strike of source A. For this case, it was assumed that strike values for source A varies from 0 to 180 degrees with dip, rake and slope angles values as shown in Table 9. For these plots, the errors are shown in absolute value.

Notice that for slope angles around 15 deg and strike values between 30 and 40 degrees, the errors in the slope, DC and CLVD components of the deviatoric constrained solutions go close to zero in a region forming a red ring. However, it is not found the same behavior in the other components of the solution. In fact, errors in dip angles are the highest in this zone.

On the other hand, in general, the highest errors in the deviatoric constrained fault plane solutions correspond to rake and slope angles while the least errors correspond to dip angles. Therefore, according to this simulation deviatoric constrained solutions have the highest uncertainties in the rupture mode (slope and rake angles).

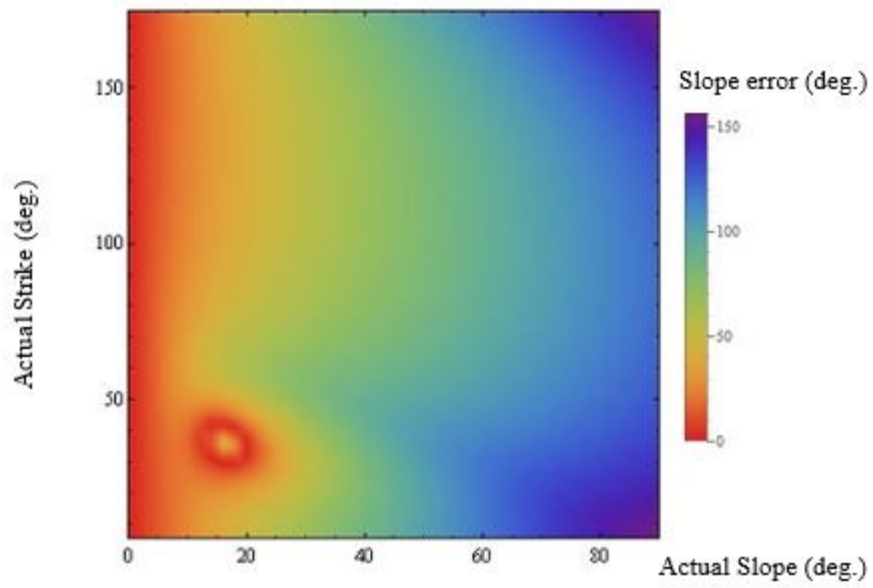

Fig. 42 - Density map showing slope errors for deviatoric constrained solutions as a function of the actual slope and strike of source A.

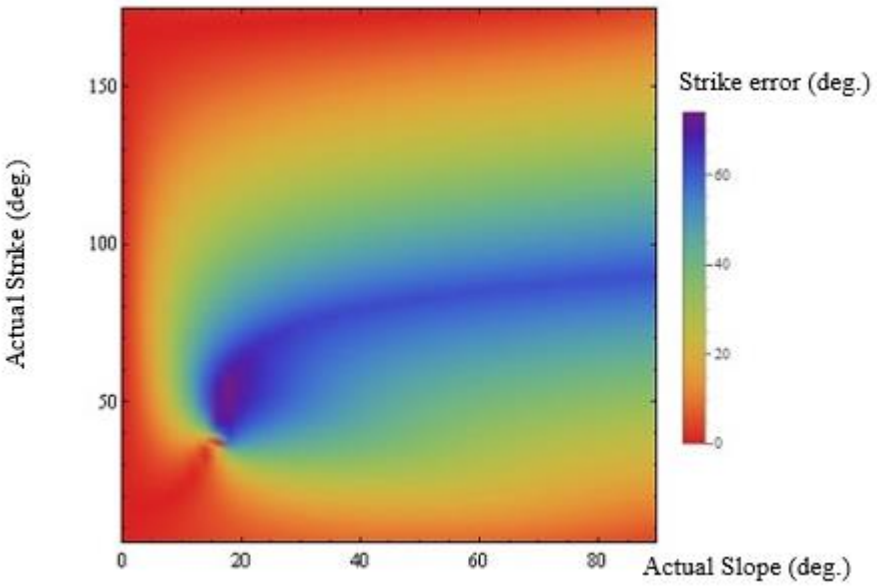

Fig. 43 - Density map showing strike errors for deviatoric constrained solutions as a function of the actual slope and strike of source A.

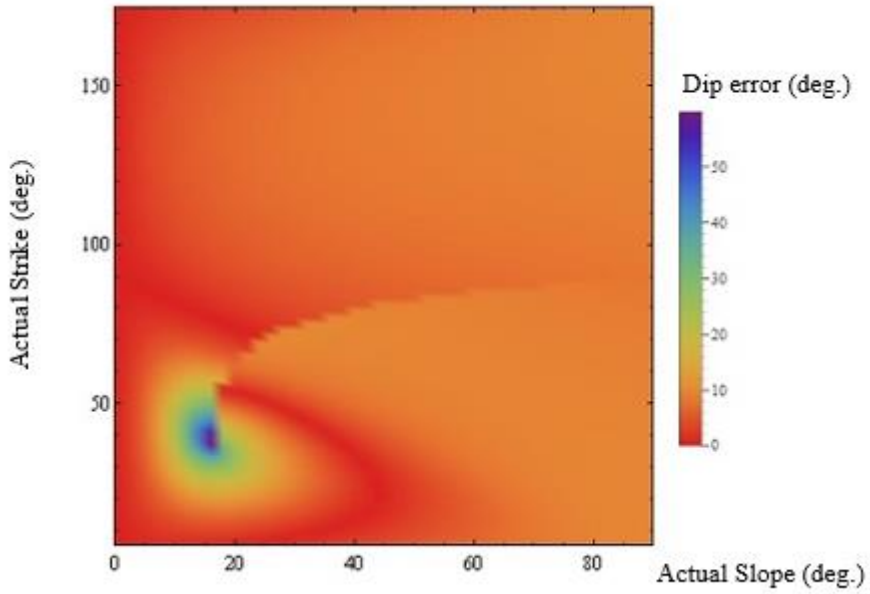

Fig. 44 - Density map showing dip errors for deviatoric constrained solutions as a function of the actual slope and strike of source A.

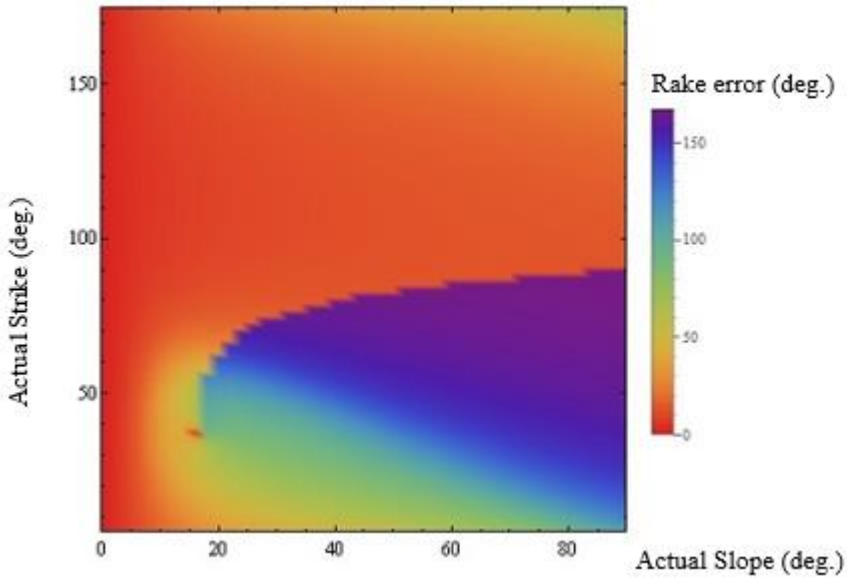

Fig. 45 - Density map showing rake errors for deviatoric constrained solutions as a function of the actual slope and strike of source A.

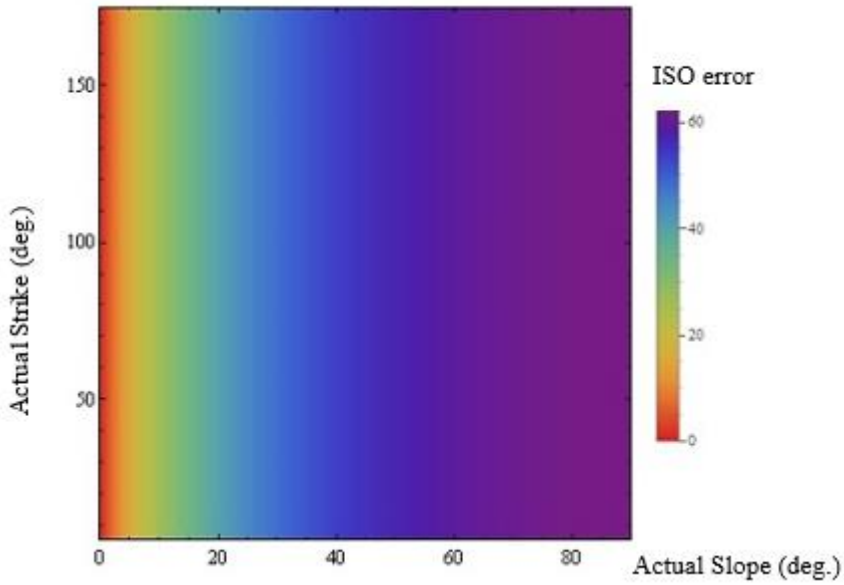

Fig. 46 - Density map showing ISO errors for deviatoric constrained moment tensor solutions as a function of the actual slope and strike of source A.

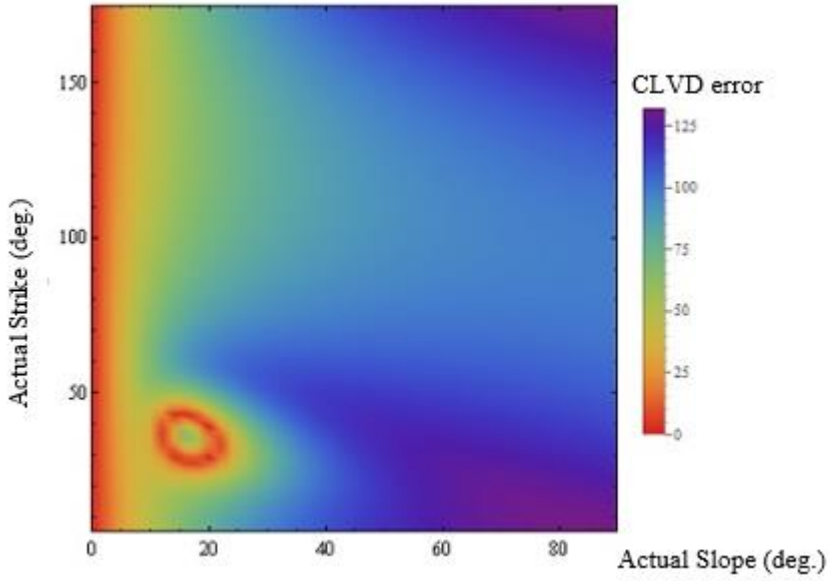

Fig. 47 - Density map showing CLVD errors for deviatoric constrained moment tensor solutions as a function of the actual slope and strike of source A.

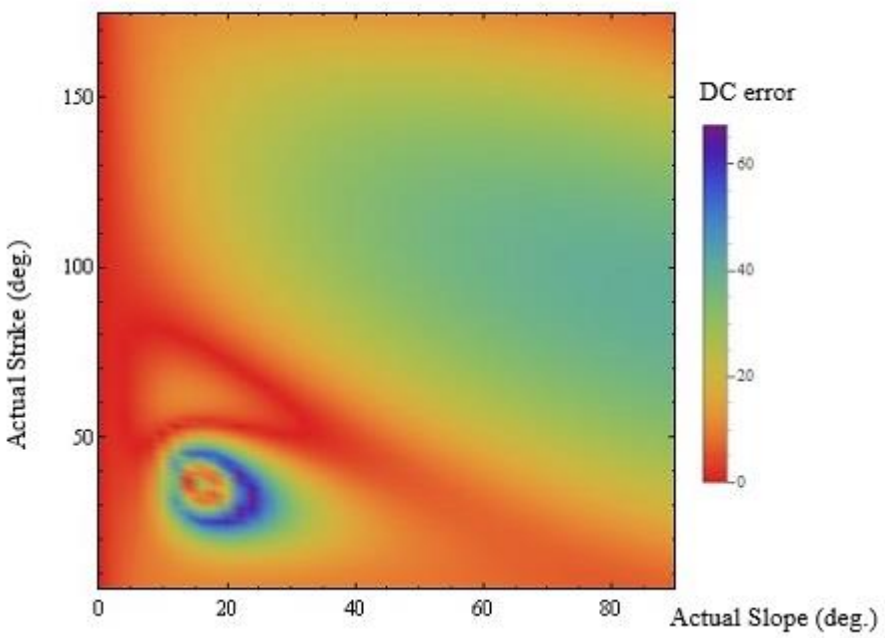

Fig. 48 - Density map showing DC errors for deviatoric constrained moment tensor solutions as a function of the actual slope and strike of source A.

5.1.2 Strike Constrained Solutions

Recent analysis of microseismic data using moment tensor inversion reveals that source mechanisms solutions have both, shear and tensile components (Sílený et al. 2009, Song et al. 2014). At the same time, the most accepted explanation of microseismcity occurrence is that reactivation of plane of weakness is the principal source of microseismic events. Thus, it can be expected that microseismicity will mainly occur on the natural fracture sets with a mixed shear-tensile rupture mode, as consequence it is reasonable to assume that dip and strike of the mechanisms solutions are known.

For the current simulation it will be assumed that only the strike of the source is known. To obtain the complete fault plane solution, a similar procedure proposed by

Jechumtálová and Eisner (2008) and Song and Toksöz (2011) will be followed. The five recoverable elements of the moment tensor will be retrieved first, and then the missing moment tensor element (M_{22}) will be completed by testing values from -5 to 5. For each tested value the fault plane solutions will be calculated, the solution with the least strike error in absolute value will be picked from the two possible solutions. Then, from the fault plane solutions for every M_{22}, the one with the least strike error in absolute value will be picked.

For this study we consider a source with a dip of 75 degrees and a rake of 0 degrees, the ratio $k = \lambda/\mu$ is equal to 0.77. Strike and slope values will vary and will be specified accordingly in the text. For the forward and inversion models, the exact location and velocities will be used to test the accuracy with which the solutions can be retrieved.

Fig. 49 and **Fig. 51** show density plots of strike errors (absolute deg.) of estimated solutions with M_{22} values from -5 to 5. The actual source slopes are 30 and 75 degrees for each respective figure. The actual source strike varies from 0 to 180 degrees. The true solutions are marked with the black dotted line. Areas with errors greater than 60 degrees have been clipped and shaded with a light pink color. **Fig. 50** and **Fig. 52** are the corresponding error density plots of k (λ/μ) (absolute %) of estimated solutions.

Notice that in both, **Fig. 49** and **Fig. 51**, there is more than a single M_{22} value for which the error is zero. This happens especially at strikes less than 50 degrees and higher than 100 degrees. The non-uniqueness of the solutions can also be observed for the *k* ratios in **Fig. 50** and Fig**. 52**. **Fig. 54** takes a slice of **Fig. 49** and shows the fault plane solution errors for an actual source strike equal to 30 degrees, while **Fig. 56** is a slice of **Fig. 51** and shows the fault plane solution errors for an actual source strike equal to 100 degrees. **Fig. 53** and **Fig. 55** show the corresponding fault plane solutions for **Fig. 54** and **Fig. 56** respectively.

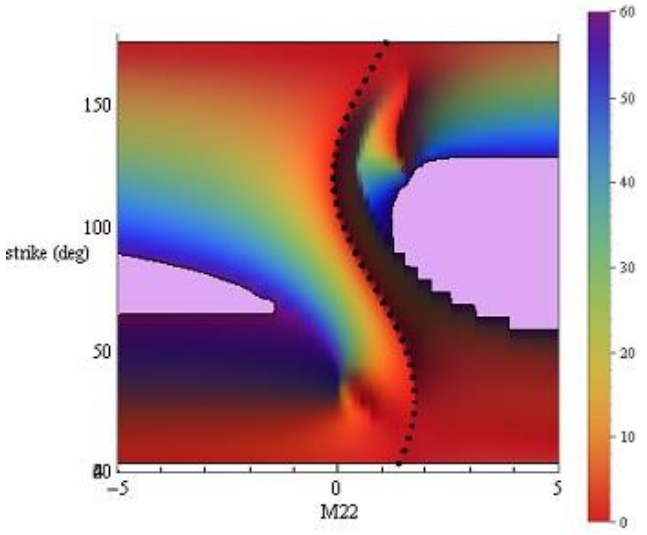

Fig. 49 - Strike error density plot (deg) of estimated solutions for different M_{22} for an actual source slope and dip equal to 30 and 75 degrees repectively, and for actual source strikes from 0 to 180 degrees. The true solutions are marked by the black dotted line. Areas with errors greaters than 60 degrees have been clipped and shaded with a light pink color.

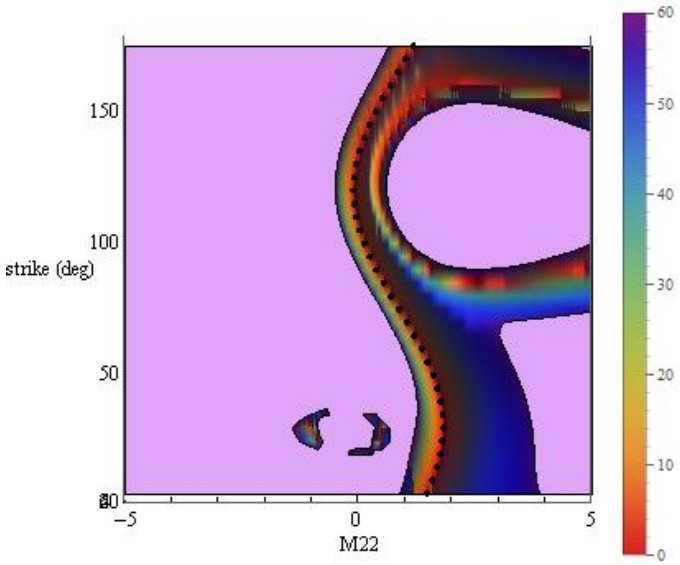

Fig. 50 - *k* (λ/ μ) error density plot (%) of estimated solutions for different M_{22} for an actual source slope and dip equal to 30 and 75 degrees repectively, and for actual source strikes from 0 to 180 degrees. The true solutions are marked by the black dotted line. Areas with errors greaters than 60 degrees have been clipped and shaded with a light pink color.

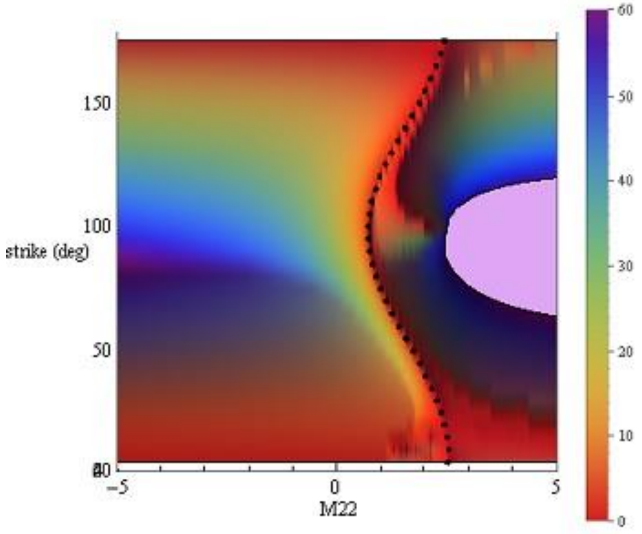

Fig. 51 - Strike errors density plot (deg) of estimated solutions for different M_{22} for an actual source slope and dip equal to 75 degrees and for actual source strikes from 0 to 180 degrees. The true solutions are marked by the black dotted line. Areas with errors greaters than 60 degrees have been clipped and shaded with a light pink color.

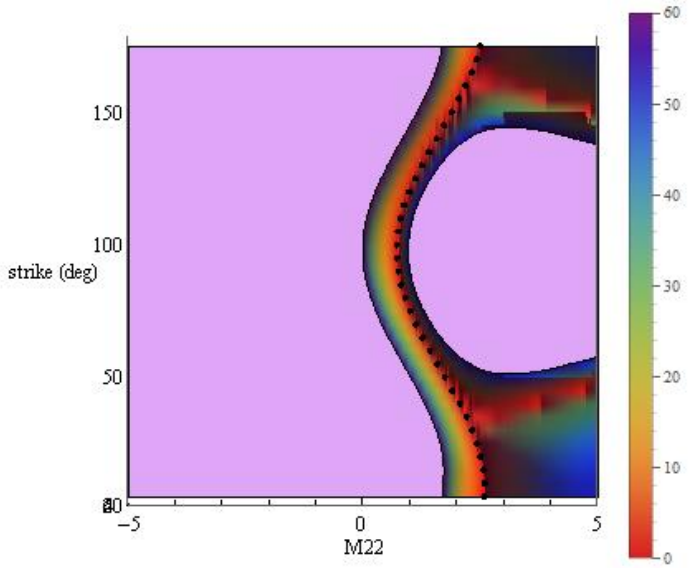

Fig. 52 - *k* (λ/ μ) error density plot (%) of estimated solutions for different M_{22} for a nd actual source slope and dip equal to 75 degrees, and for actual source strikes from 0 to 180 degrees. The true solutions are marked by the black dotted line. Areas with errors greaters than 60 degrees have been clipped and shaded with a light pink color.

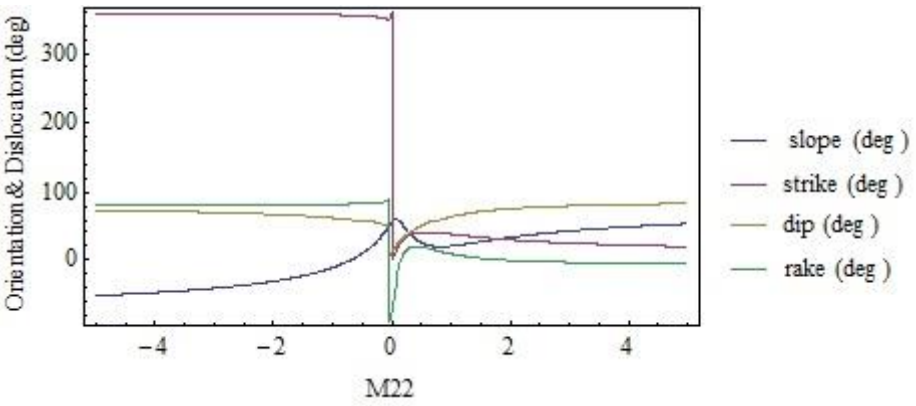

Fig. 53 - Fault plane solutions versus diferrent M_{22} for a source with actual strike and slope equal to 30 degrees.

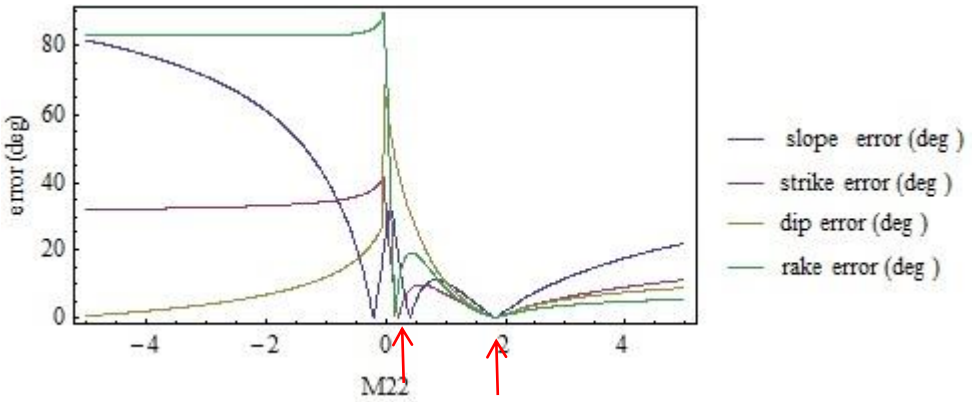

Fig. 54 - Fault plane solutions errors in absolute value versus diferrent M_{22} for a source with actual strike and slope equal to 30 degrees. The red vertical lines mark the values of M_{22} for which strike errors are zero.

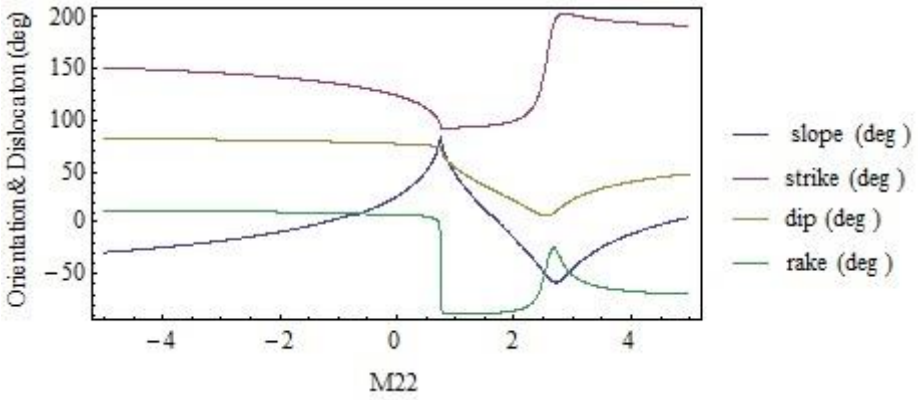

Fig. 55 - Fault plane solutions versus diferrent M_{22} for a source with actual strike equal to 100 degrees and slope equal to 75 degrees.

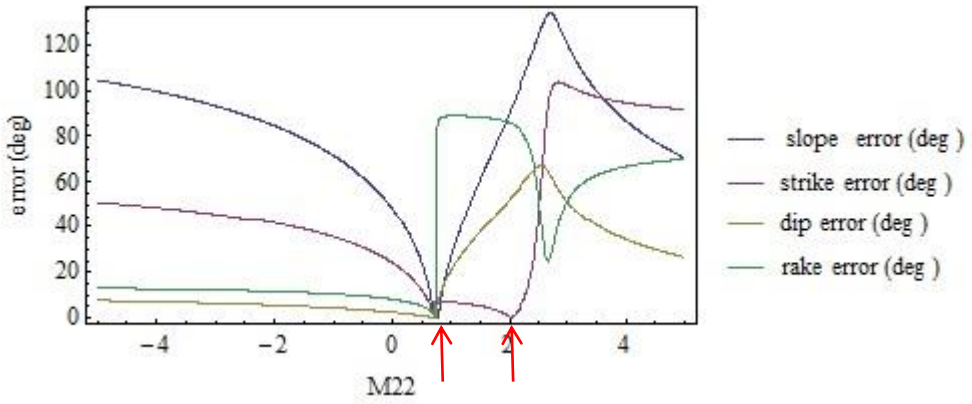

Fig. 56 - Fault plane solutions errors in absolute value versus diferrent M_{22} for a source with actual strike equal to 100 degrees and slope equal to 75 degrees. The red vertical lines mark the values of M_{22} for which strike errors are zero.

Notice that in both, **Fig. 54** and **Fig. 56**, there are two values of M_{22} for which the strike errors are zero. Thus based on strike information only, solutions could be non-unique. However, according to these figures there is a single M_{22} for which all errors of the fault plane solution are zero. Then, to be able to identify the solution in all cases it is necessary to impose and additional condition. Normally, dislocation angles as slope and rake are the least known, but the dipping angle of natural fractures can be characterized through core or image log analysis.

5.1.3 Strike and Dip Constrained Solutions

It has been shown that assuming a known strike value to constrain source mechanisms can lead to non-unique solutions. To be able to obtain a unique solution, an additional constraint such as a known dip angle will be considered. In conclusion, it will be assumed that the orientation of the source is known (strike and dip) and the dislocation

orientation (slope and rake) are the parameters to find. However instead of assuming exact values of strike and dip, we will assume a range of values to incorporate some uncertainty in the knowledge of these parameters.

We will use two sources for the forward model, one with strike and slope of 30 degrees and the other one with strike and slope of 100 and 75 degrees. Both sources have dip and rake angles of 75 and 0 degrees respectively. For each proposed source, we will also assume noisy amplitudes. The noise will be added on top of the amplitudes calculated with the exact location and velocity model. The noise will follow a Gaussian distribution with zero mean and standard deviation equal to 10 % of the maximum amplitude at each component receiver. One hundred inversions of noisy data will be performed with the $\widehat{\boldsymbol{G}}$ matrix constructed with perturbed location and velocity. The perturbed location is 40 m (131.2 ft) in East, North and Z directions respectively. Perturbations in velocity are 5.1% and - 4.9 % for Vp and Vs respectively. For the inversion of moment tensor components, first we will estimate the five recoverable elements and then we will find the corresponding fault plane solutions by completing M_{22} values from -5 to 5. In in order to get single fault plane estimation for each M_{22} value, we will calculate the mean values of strike, dip, rake and slope of the 100 inversions. The solution will be picked in such a way that the strike and dip plane solutions are within the interval of the assumed values. For the source striking 30 degrees, the assumed strike range is equal 30 +/- 20 degrees and for the source striking 100 degrees, the assumed strike range is 100 +/- 20 degrees, the dip range is the same for both and equal to 75 +/- 10 degrees.

The shaded area in **Fig. 57** marks the solution range picked according to the assumed strike range (30 +/- 20 deg.) and dip (75 +/- 10 deg.) for the actual source striking 30 deg. and with slope of 30 deg., and **Fig. 58** shows the respective solution errors **Table 10** shows the corresponding initial, final and mean values of the solution range.

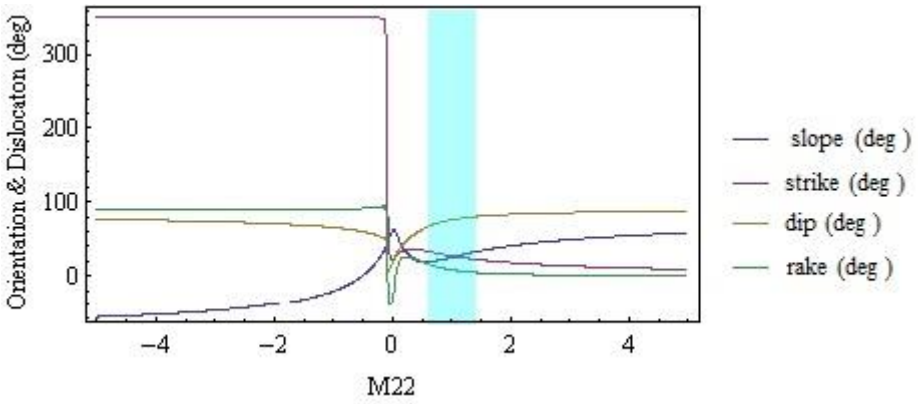

Fig. 57 - Solutions for different M_{22} values of an actual source with strike and slope of 30 deg. with dip equal 75 deg. and rake of 0 deg. The light blue shaded area corresponds to assumed strike and dip ranges from which the solution range is picked.

	slope (deg)	strike (deg)	dip (deg)	rake (deg)
initial	18.5219	33.6713	65.1613	17.3225
final	47.6552	14.1054	84.9835	1.29588
mean	35.1219	21.2768	79.7566	5.04452

Table 10 - Initial, final and mean values of the solution range picked according assumed strike and dip ranges for an actual source with strike and slope of 30 deg. with dip equal 75 deg. and rake of 0 deg.

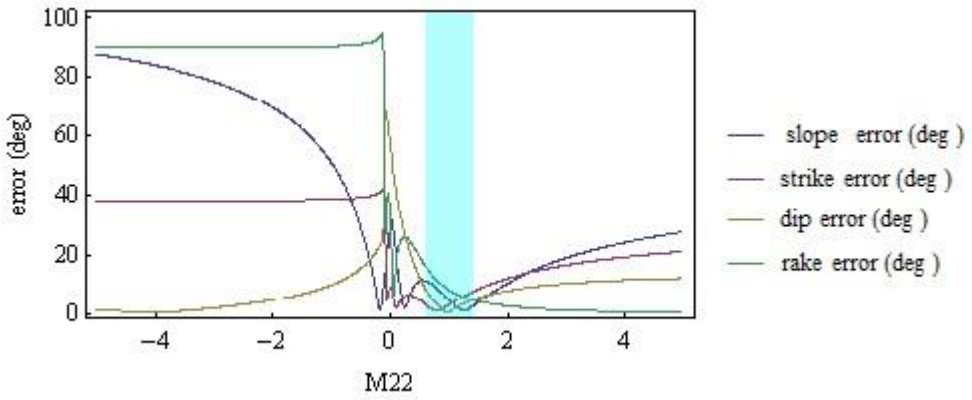

Fig. 58 - Solution errors for different M_{22} values of an actual source with strike and slope of 30 deg, with dip of 75 deg. and rake of 0 deg. The light blue shaded area corresponds to assumed strike and dip ranges from which the solution range is picked.

The shaded area in **Fig. 59** marks the solution range picked according to the assumed strike range (100 +/- 20 deg.) and dip (75 +/- 10 deg.) for the actual source striking 100 deg., and with slope of 75 deg. and **Fig. 60** shows the corresponding solution errors. **Table 11** shows the corresponding initial, final and mean values of the solution range.

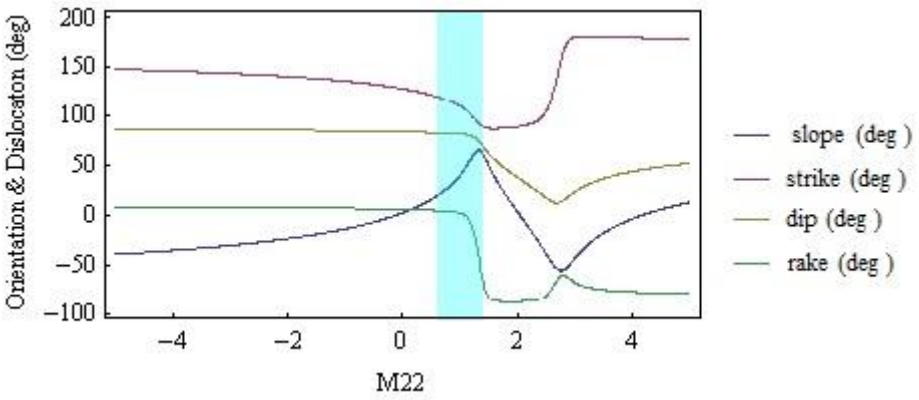

Fig. 59 - Solutions for different M_{22} values of an actual source with strike of 100 deg and slope of 75 deg. with dip of 75 deg. and rake of 0 deg. The light blue shaded area corresponds to assumed strike and dip ranges from which the solution range is picked.

	slope (deg)	strike (deg)	dip (deg)	rake (deg)
initial	19.1117	119.839	82.5225	4.66235
final	57.4903	87.8342	66.126	-74.2909
mean	42.3675	106.834	79.4191	-10.0274

Table 11 - Initial, final and mean values of the solution range picked according assumed strike and dip ranges for an actual source with strike of 100 deg. and slope of 75 deg. with dip equal 75 deg. and rake of 0 deg.

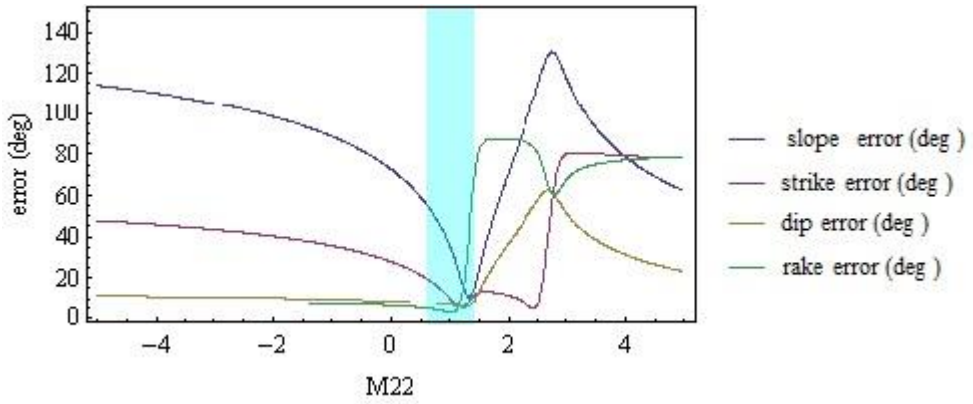

Fig. 60 - Solution errors for different M_{22} values of an actual source with strike of 100 deg and slope of 75 deg. with dip of 75 deg. and rake of 0 deg. The light blue shaded area corresponds to assumed strike and dip ranges from which the solution range is picked.

Notice from **Fig. 58** and **Fig. 60** the non-uniqueness of strike constrained solutions is solved. For the case of the source striking 30 deg. and with slope of 30 deg., the mean values of the solution range is very close to the actual source with errors no greater than 5 deg. However, for the source striking 100 deg. and with slope of 75 deg., the mean values of the solution range have the greatest error in the slope which is around 40 deg. followed by the rake which is around 10 deg. These results suggest that reliability of the dislocation angles (slope and rake) decreases as the slope of the actual source increases and this effect is greater in the retrieved slope angle.

5.2 Simulation of Uncertainties in Source Location, Velocity Model and Amplitude Data

The effects of location uncertainty, P and S velocity uncertainty and data amplitude uncertainty for deviatoric constrained solutions of pure shear sources (slope angle equal to zero) will be studied.

For this simulation, it is assumed that the source have zero slope which is equivalent to pure shear rupture, with strikes varying from 0 to 180 degrees as shown in Table 12. Thus, for this case, errors for assuming deviatoric moment tensors would not be an issue, since as shown by **Fig. 42** to **Fig. 48** solution errors are zero when the slope angle is zero.

Source	Strike (deg.)	Dip (deg.)	Rake (deg.)	Slope (deg.)
A	0-180	75	0	0

Table 12 - Proposed source to be used for the forward modeling.

To simulate uncertainty in location, East, North and Z coordinates will be varied in turns keeping the other coordinate components constant. These variations will be between -100 m (-328.1 ft) to 100 m (328.1 ft) in steps of 10 m (32.8 ft) from the actual location coordinates. As consequence of the assumed source and receivers' configuration (**Fig. 31**) only perturbations in the East coordinate affect the source azimuth respect to the receivers.

For the inversion, amplitudes data are calculated from the forward model with the exact location and velocities, then deviatoric constrained inversions are performed with the simulated data and with G functions constructed with the exact velocities but perturbed locations.

In the case of simulation of P- and S- velocities uncertainties, Vp/ Vs (vr) ratio will be varied between 1.4 and 2.2 in steps of 0.05. The actual Vp/Vs ratio is 1.66. Vp perturbed (Vpp) will be calculated as follows:

$$V_{pp} = V_s \; vr \tag{58}$$

Vs perturbed (Vsp) will be calculated as:

$$V_{sp} = V_p \; / \; vr \tag{59}$$

For the inversion, amplitude data are calculated from the forward model with the exact location and velocities, then deviatoric constrained inversions are performed with the simulated data and with G functions constructed with the exact location but perturbed velocities

For amplitude perturbation simulation, P- and S- amplitudes calculated with exact location and velocities will be perturbed by adding noise following a Gaussian distribution with zero mean and standard deviation equal to 10% of the maximum amplitude at each component receiver. After noise is added, deviatoric constrained solutions are calculated with G function with the exact location and velocity model. For this case one hundred amplitudes perturbations with different noise realizations are performed for each strike value.

Fig. 61 to **Fig. 64** to show the density error maps for the constrained solutions of pure shear sources as a function of errors in East coordinate location of the source and for different strike values. Errors are calculated as the difference from the actual fault plane in absolute value. In general, the errors in the fault plane solution are not significant, reaching to around 3 degrees as maximum, except for the strike errors which goes up to around 20 degrees. Notice as well the symmetry of the solution errors for positive and negative values of the horizontal coordinate.

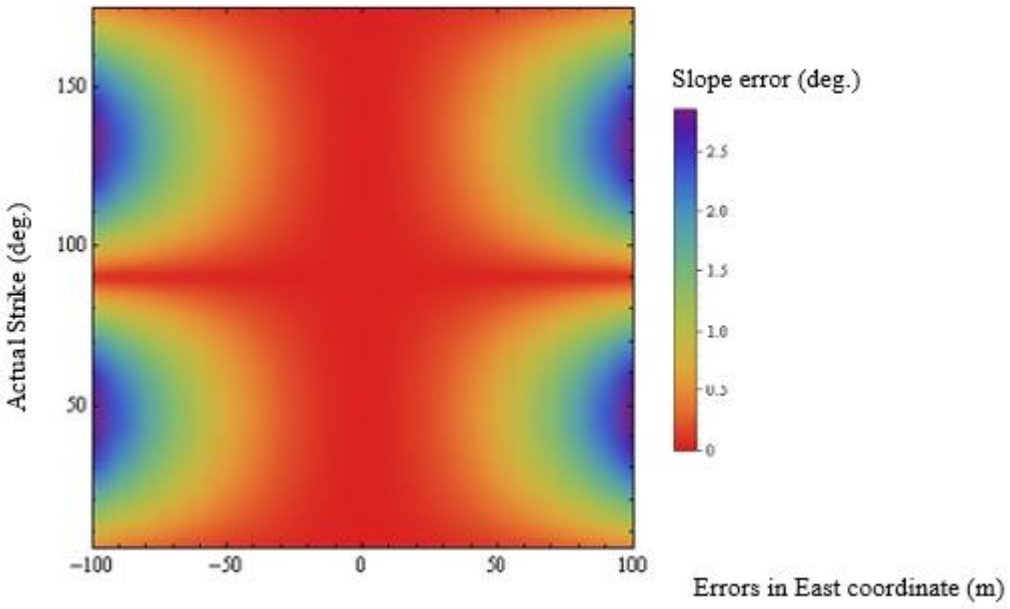

Fig. 61 - Density map showing slope errors for deviatoric constrained solutions as a function of errors in the East coordinate location and actual strike of source A.

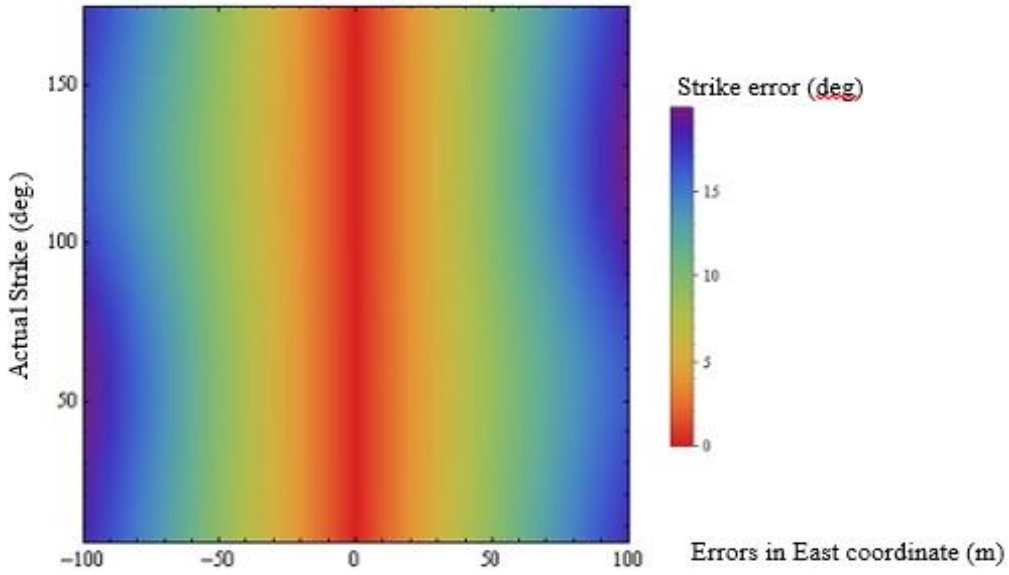

Fig. 62 - Density map showing strike errors for deviatoric constrained solutions as a function of errors in the East coordinate location and actual strike of source A.

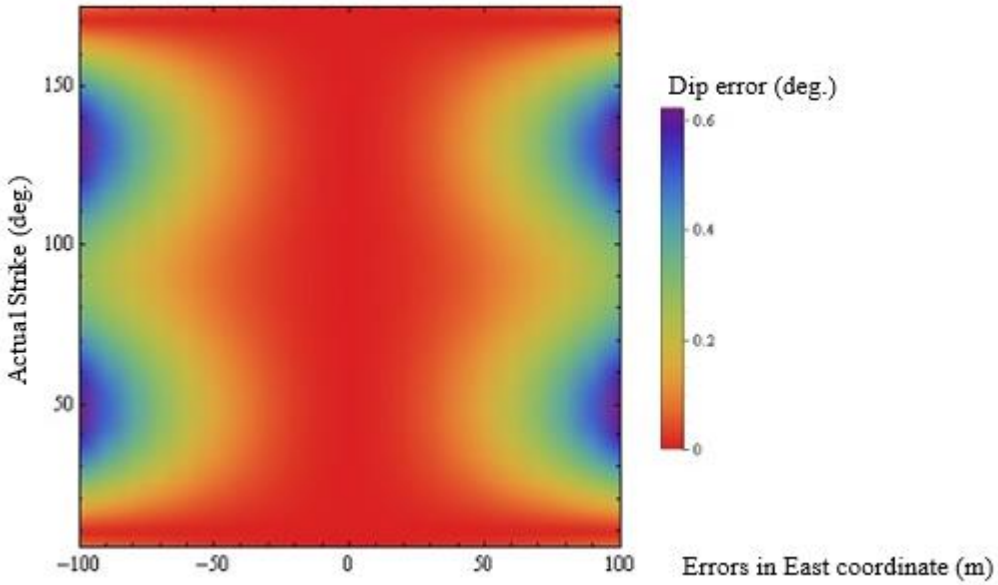

Fig. 63 - Density map showing dip errors for deviatoric constrained solutions as a function of errors in the East coordinate location and actual strike of source A.

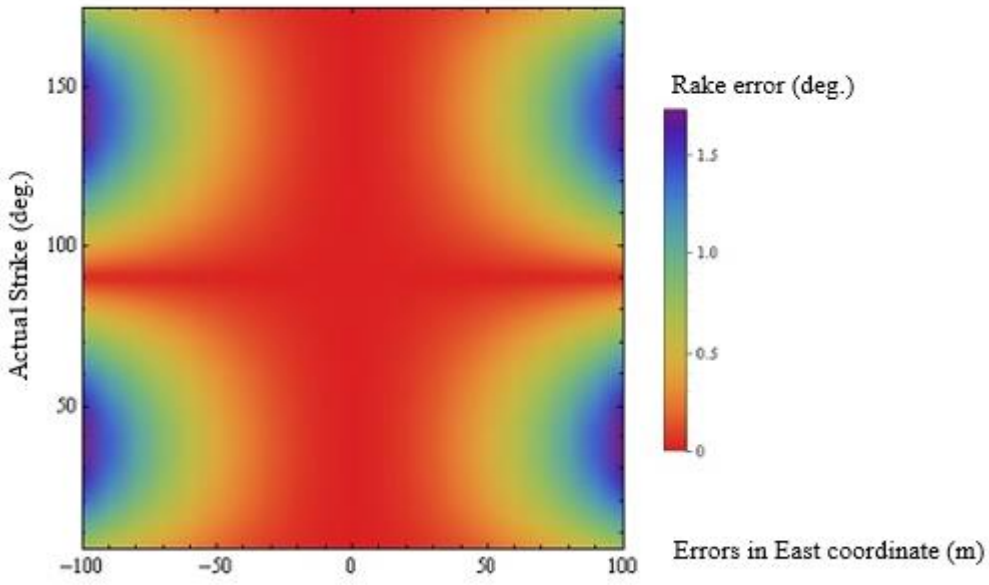

Fig. 64 - Density map showing rake errors for deviatoric constrained solutions as a function of errors in the East coordinate location and actual strike of source A.

Fig. 65 to **Fig. 68** show the density error maps for the constrained solutions of pure shear sources as a function of errors in North coordinate location of the source and for different strike values. Errors are calculated as the difference from the actual fault plane in absolute value. For this case, the least errors in the fault plane solution correspond to the dip angle error reaching values around 6 degrees and the greatest errors correspond to slope angles reaching values up to around 20 degrees.

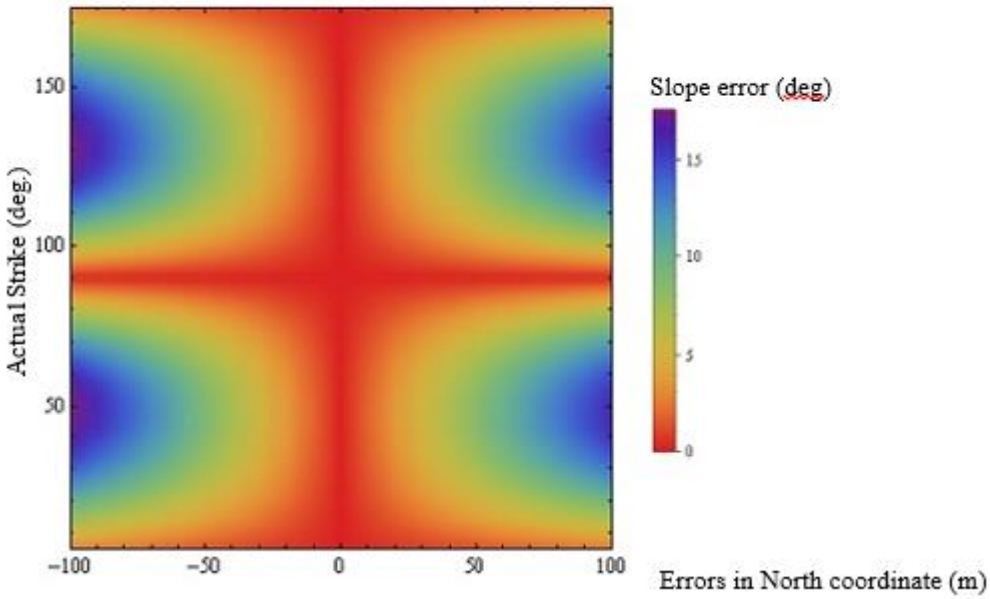

Fig. 65 - Density map showing slope errors for deviatoric constrained solutions as a function of errors in the North coordinate location and actual strike of source A.

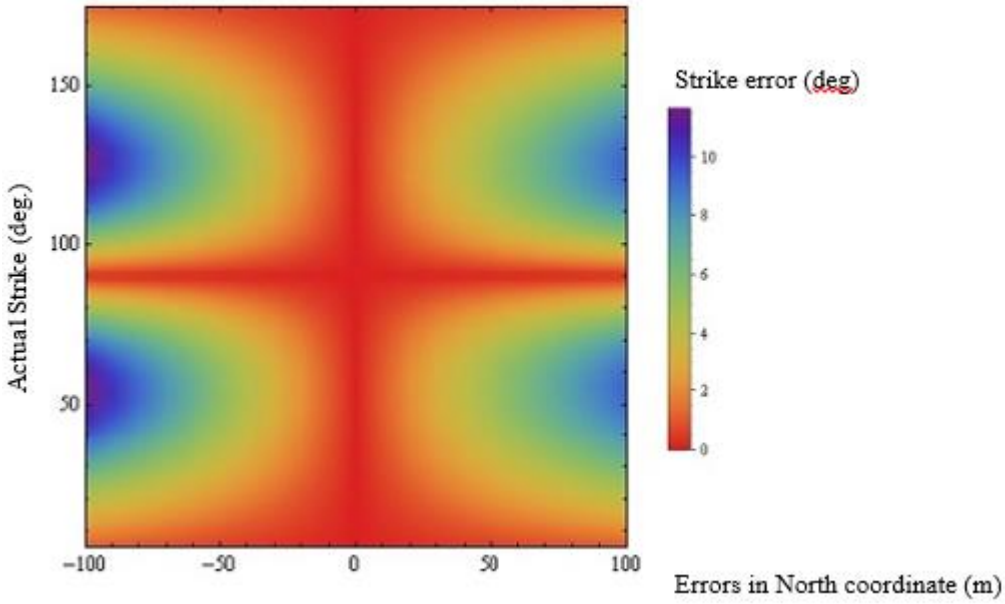

Fig. 66 - Density map showing strike errors for deviatoric constrained solutions as a function of errors in the North coordinate location and actual strike of source A.

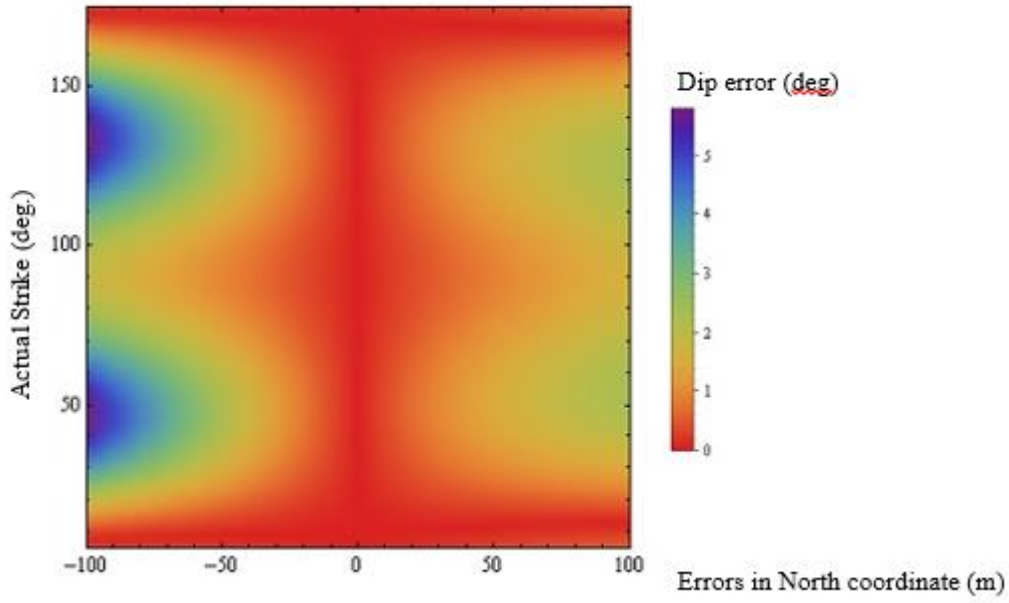

Fig. 67 - Density map showing dip errors for deviatoric constrained solutions as a function of errors in the North coordinate location and actual strike of source A.

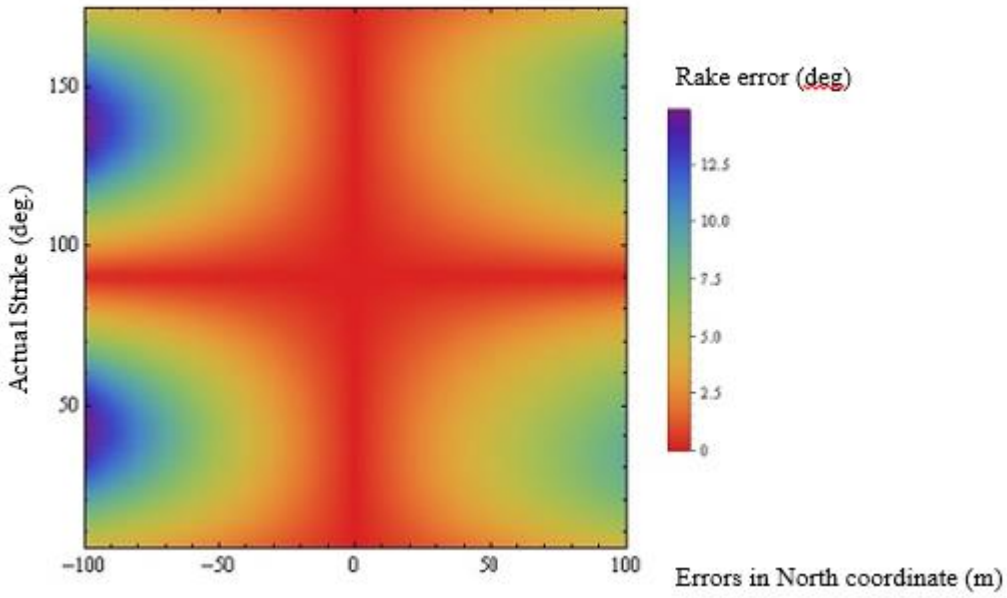

Fig. 68 - Density map showing rake errors for deviatoric constrained solutions as a function of errors in the North coordinate location and actual strike of source A.

Fig. 69 to **Fig. 72** show the error density maps for the constrained solutions of pure shear sources as a function of errors in Z coordinate location of the source and for different strike values. Errors are calculated as the difference from the actual fault plane in absolute value. For this case, the least errors in the fault plane solution correspond to the slope errors and strike angles reaching values around 5 degrees and the greatest errors correspond to dip and rake angle errors reaching values up to around 30 degrees.

In general, notice that fault plane solution angles present the highest errors close to the extremes of the horizontal coordinates which correspond to the highest errors in location either in East, North or Z. However in the interior; for values less than 50 m (164 ft) in the horizontal coordinates, the errors are fairly low reaching around 20 degrees in the worst cases. Notice that errors also depend on the actual source strike value, where for certain strike values errors in the fault plane solution are always zero independent of the errors in location.

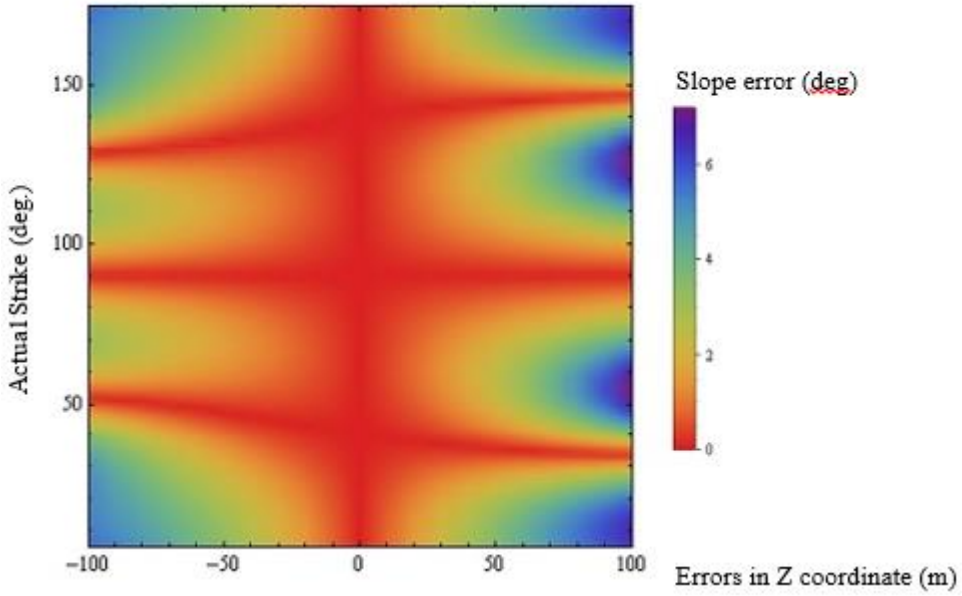

Fig. 69 - Density map showing slope errors for deviatoric constrained solutions as a function of errors in the Z coordinate location and actual strike of source A.

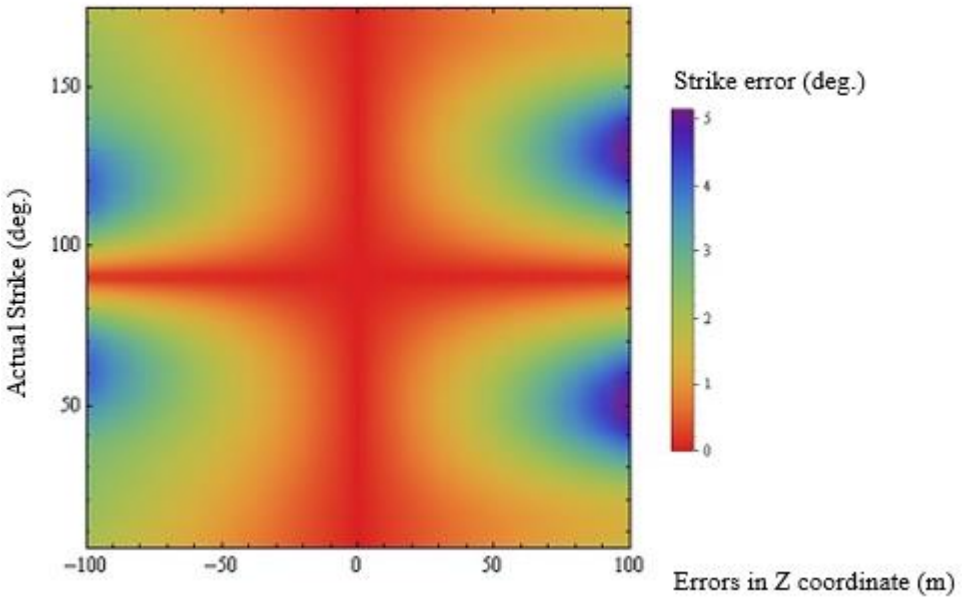

Fig. 70 - Density map showing strike errors for deviatoric constrained solutions as a function of errors in the Z coordinate location and actual strike of source A.

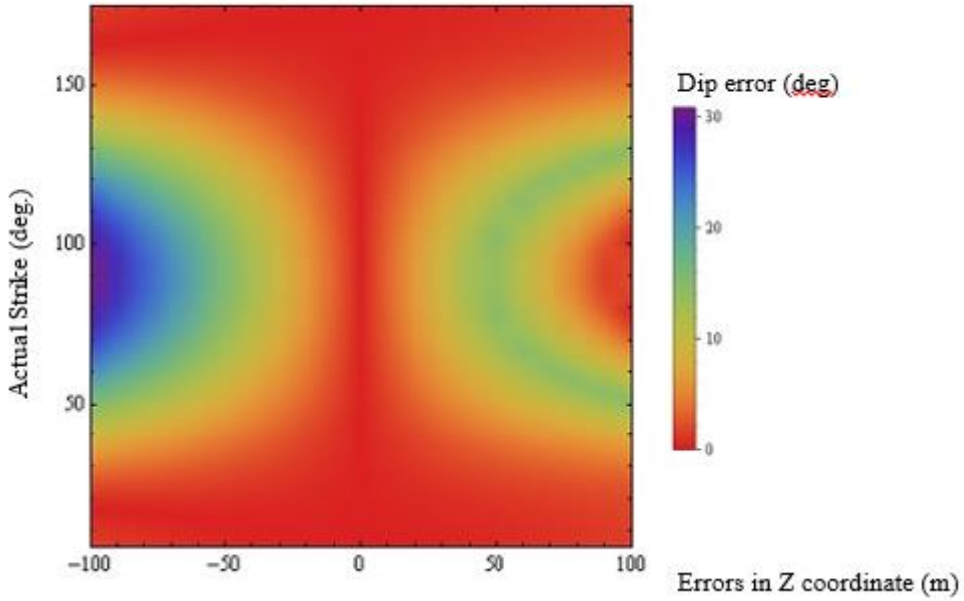

Fig. 71 - Density map showing dip errors for deviatoric constrained solutions as a function of errors in the Z coordinate location and actual strike of source A.

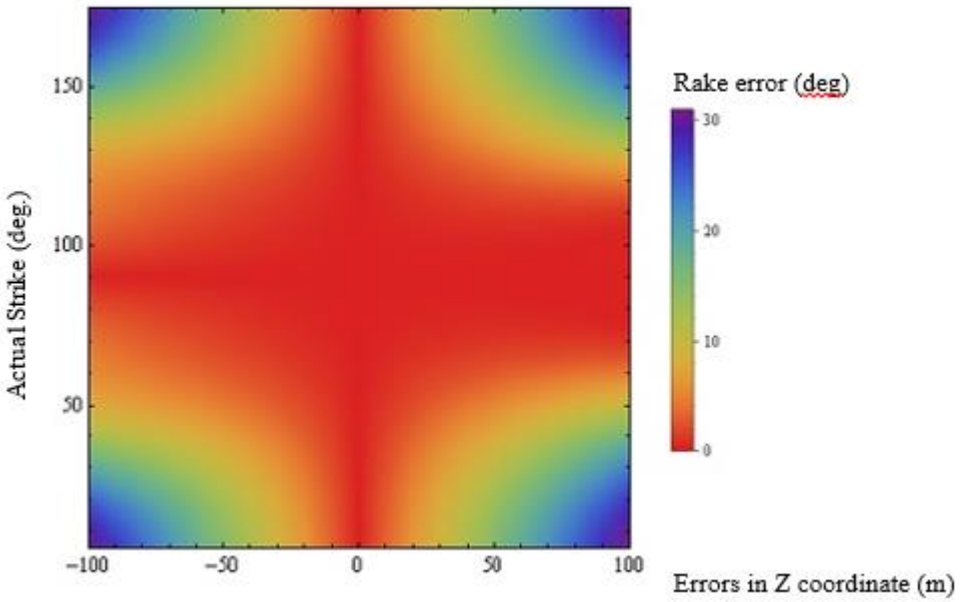

Fig. 72 - Density map showing rake errors for deviatoric constrained solutions as a function of errors in the Z coordinate location and actual strike of source A.

Fig. 73 to **Fig. 76** show the error density maps for the constrained solutions of pure shear sources as a function of % Vp errors for different strike values and **Fig. 77** to **Fig. 80** show the density error maps for the constrained solutions of pure shear sources as a function of % Vs errors for different strike values. Errors are calculated in absolute value. Notice that errors in the fault plane solution for errors in Vp and Vs are mirror image of each other. This is because Vp and Vs are related by the Vp/Vs ratio as shown in **Eq. (58)** and **Eq. (59)**. Notice that in general perturbations in velocities affect more to the errors in the fault plane solutions than location errors. The greatest errors correspond to rake angles reaching up to around 40 degrees, followed by slope errors and strike errors.

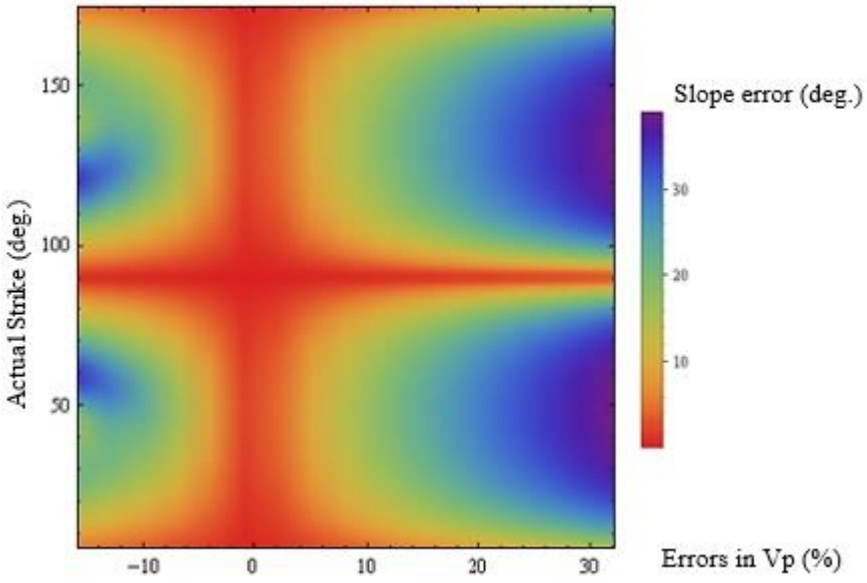

Fig. 73 - Density map showing slope errors for deviatoric constrained solutions as a function of % errors in Vp velocity and actual strike of source A.

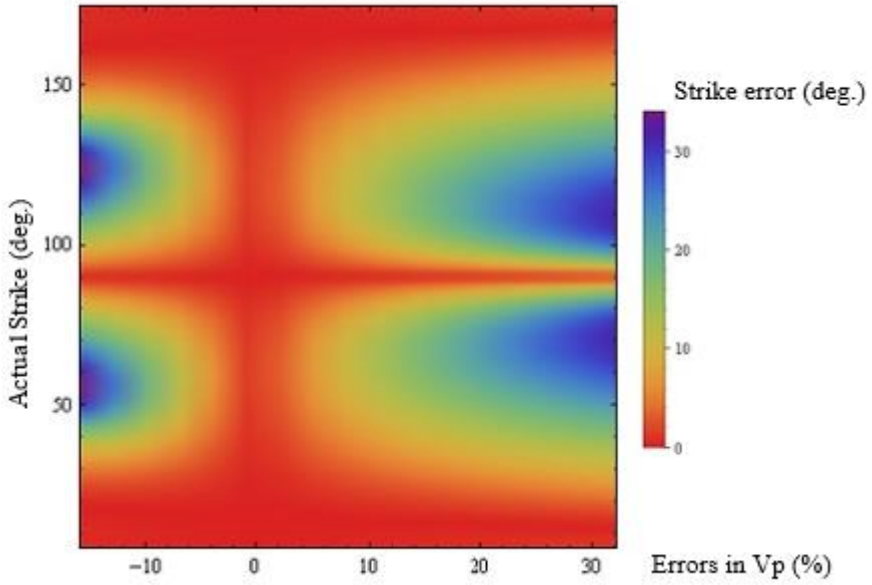

Fig. 74 - Density map showing strike errors for deviatoric constrained solutions as a function of % errors in Vp velocity and actual strike of source A.

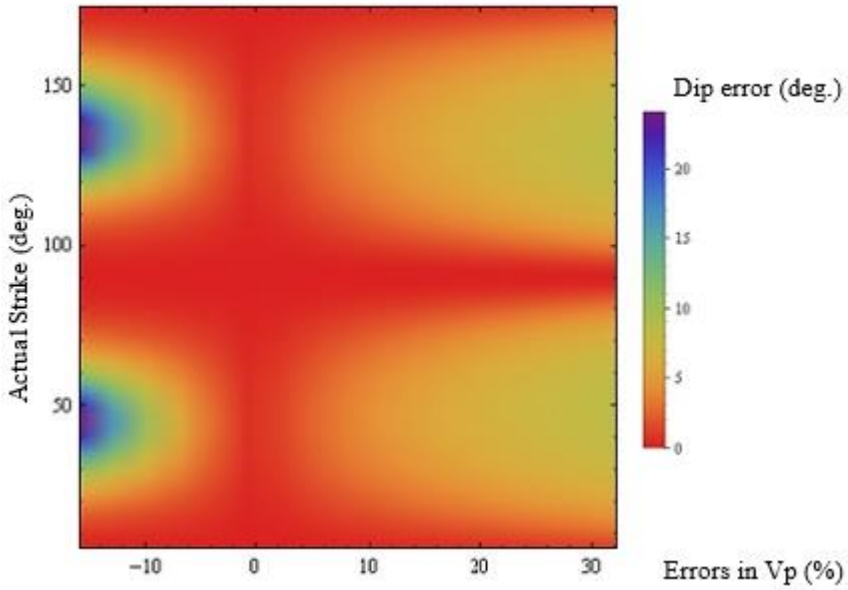

Fig. 75 - Density map showing dip errors for deviatoric constrained solutions as a function of % errors in Vp velocity and actual strike of source A.

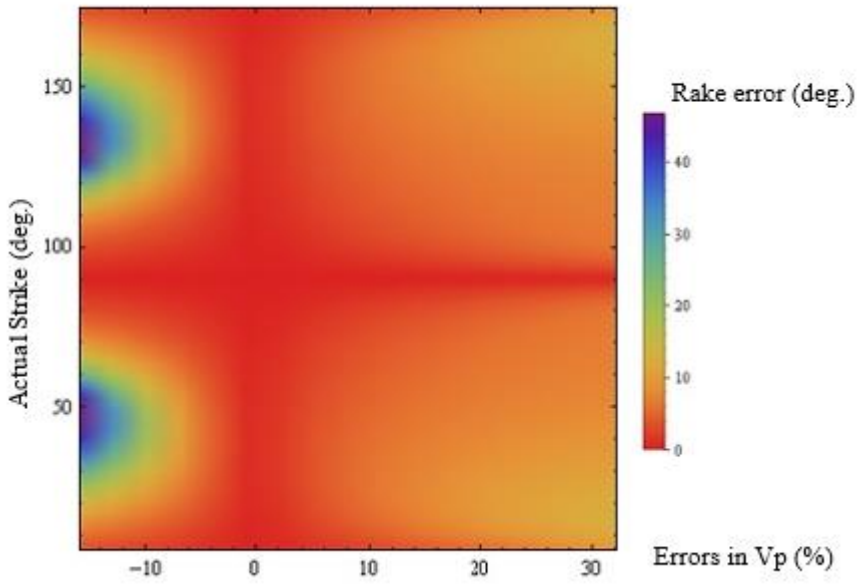

Fig. 76 - Density map showing rake errors for deviatoric constrained solutions as a function of % errors in Vp velocity and actual strike of source A.

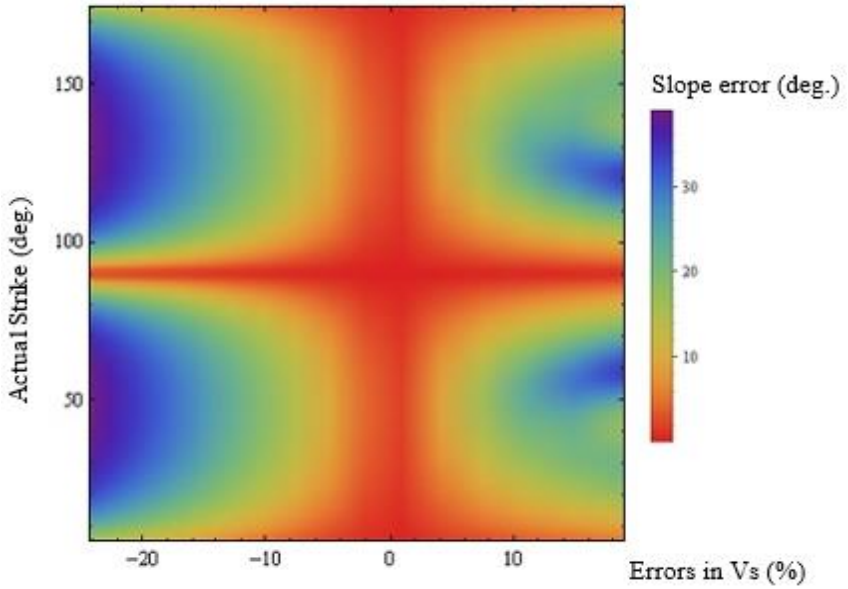

Fig. 77 - Density map showing slope errors for deviatoric constrained solutions as a function of % errors in Vs velocity and actual strike of source A.

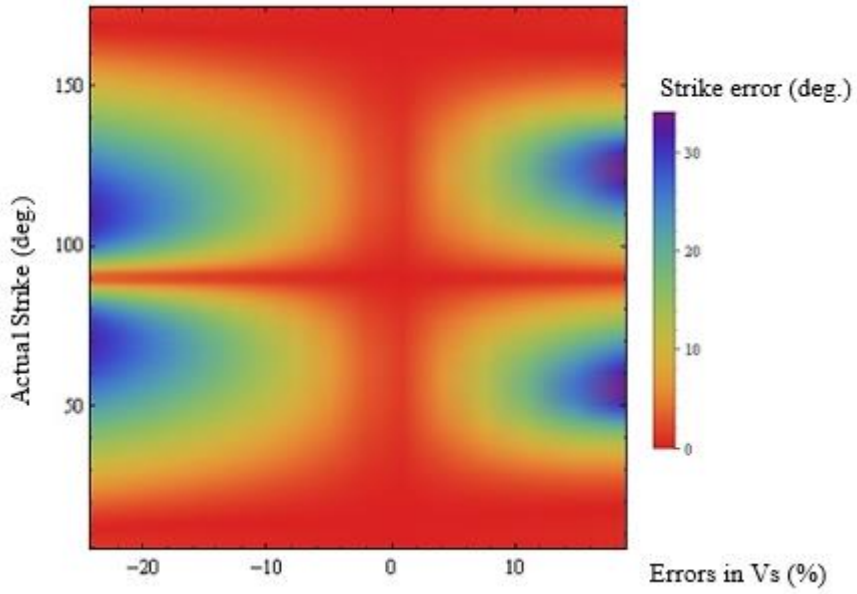

Fig. 78 - Density map showing strike errors for deviatoric constrained solutions as a function of % errors in Vs velocity and actual strike of source A.

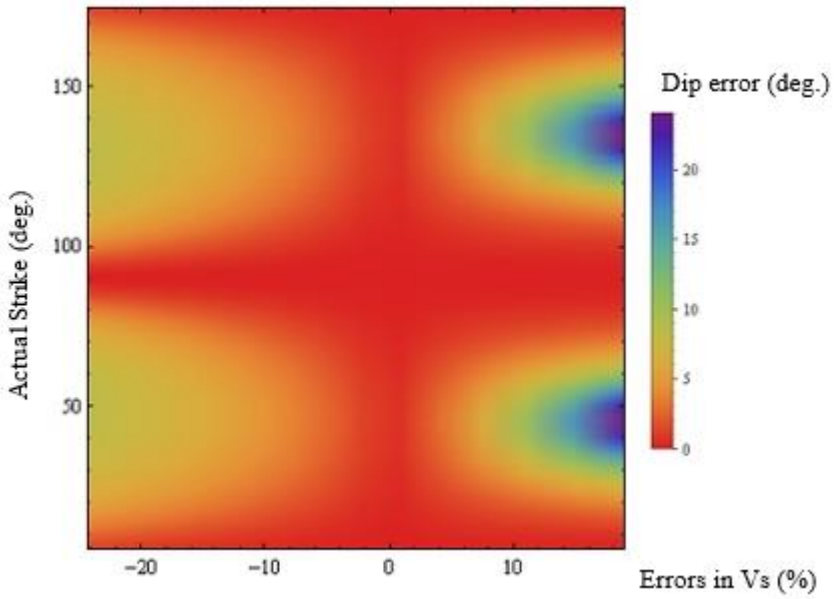

Fig. 79 - Density map showing dip errors for deviatoric constrained solutions as a function of % errors in Vs velocity and actual strike of source A.

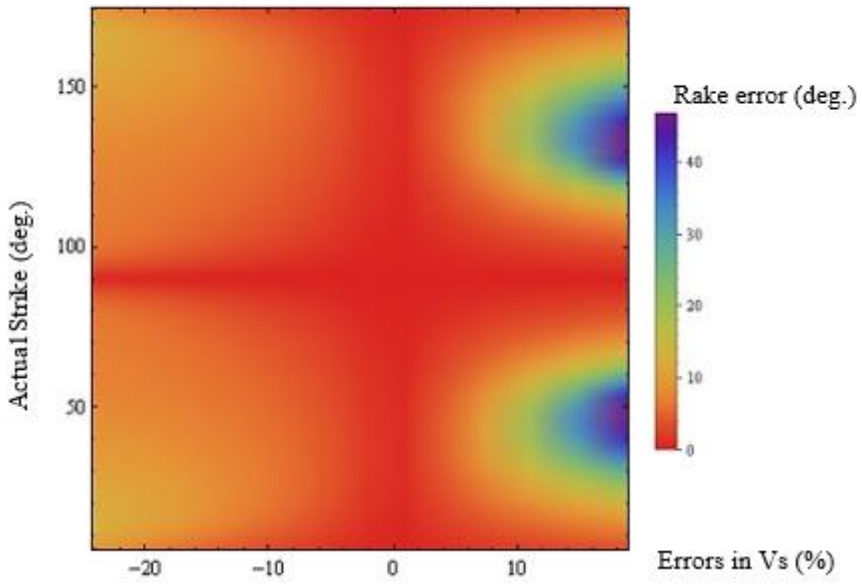

Fig. 80 - Density map showing rake errors for deviatoric constrained solutions as a function of % errors in Vs velocity and actual strike of source A.

Fig. 81 to **Fig. 86** show error plots for the constrained solutions of pure shear sources as a function of the actual source strike of 100 inversions of noisy data for each strike value. The noisy data was created with a Gaussian distribution with a standard deviation of 10% of the maximum amplitude in each given component. The red dashed lines are the mean value for each set of 100 inversions and the black dashed lines are the mean values plus or minus one standard deviation. Notice that in general the standard deviations for the fault plane solution errors do not go over 10 degrees in absolute value.

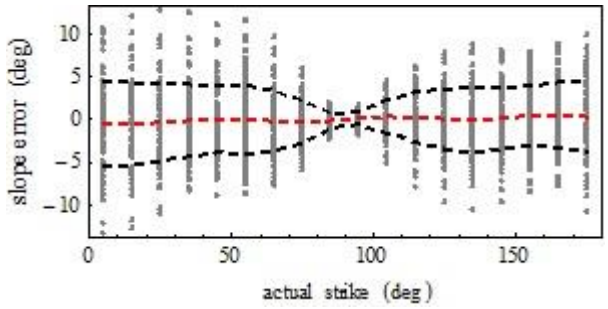

Fig. 81 - Plot showing slope errors for deviatoric constrianed solutions as a function of actual strike of source A, with 100 inversions of noisy data for each strike value.

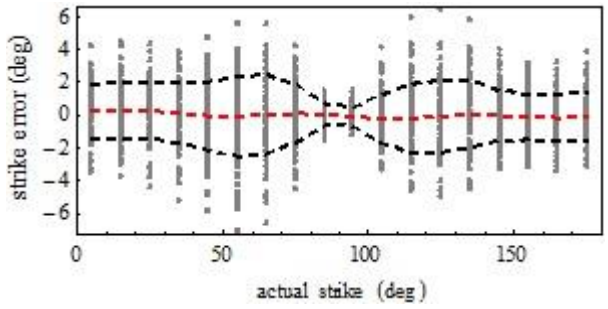

Fig. 82 - Plot showing strike errors for deviatoric constrianed solutions as a function of actual strike of source A with 100 inversions of noisy data for each strike value.

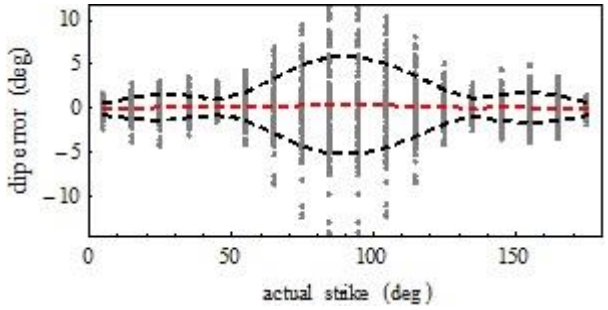

Fig. 83 - Plot showing dip errors for deviatoric constrianed solutions as a function of actual strike of source A with 100 inversions of noisy data for each strike value.

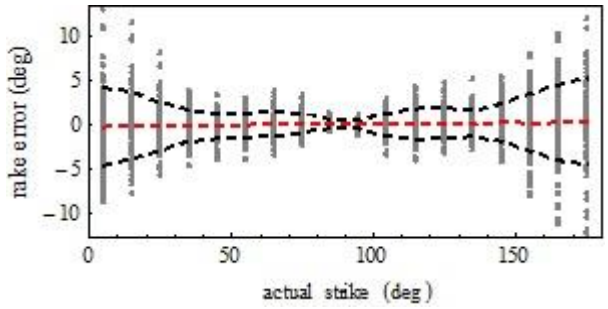

Fig. 84 - Plot showing rake errors for deviatoric constrianed solutions as a function of actual strike of source A with 100 inversions of noisy data for each strike value.

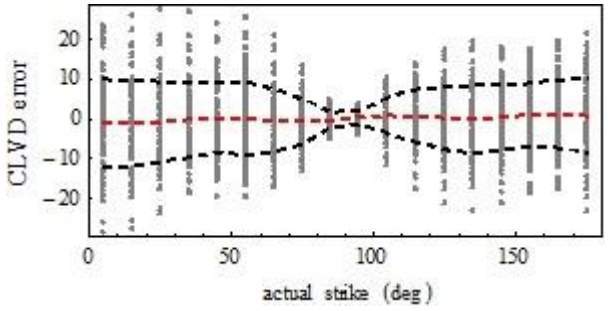

Fig. 85 - Plot showing CLVD errors for deviatoric constrianed solutions as a function of actual strike of source A with 100 inversions of noisy data for each strike value.

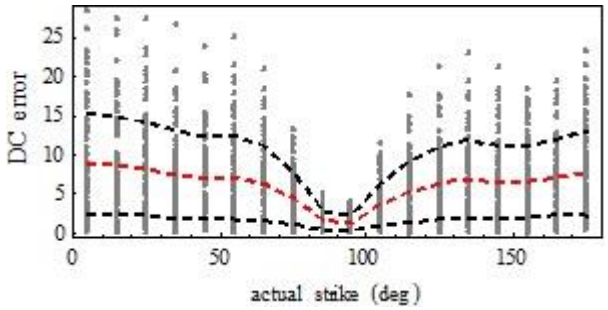

Fig. 86 - Plot showing DC errors for deviatoric constrianed solutions as a function of actual strike of source A with 100 inversions of noisy data for each strike value.

5.3 Simulation of Intrinsic Attenuation Effects

Amplitudes estimations according to **Eq (39)** through **Eq. (41)** assume a perfect elastic medium where amplitude reduction is mainly caused by geometrical spreading which is considered in the 1/r term in **Eqs. (40)** and **(41)**. However, in a deformable medium there is always a mechanical dissipation of energy due to internal friction which is responsible for additional amplitude attenuation of seismic waves (Udias 1999).

The energy loss per cycle of harmonic motion (ΔE) can be related to a quality factor Q as a function of frequency in the following way:

$$\frac{1}{Q(\omega)} = -\frac{\Delta E}{\boldsymbol{2\,\pi\,E}} \qquad \textbf{(60)}$$

Note that Q is inversely related to the energy loss. For seismic waves the energy loss per cycle is very small (Q >>1) an approximate relationship between amplitude reduction and Q factor can be derived:

$$A\,(x) = A_o\,\exp\left[-\frac{\omega\,x}{2\,c\,Q}\right] \qquad \textbf{(61)}$$

Where *x* is measured along the propagation direction and *c* is either *P* or *S* velocity. Different attenuation factors *Q* are used for P and S phases due to the difference in the direction in particle motion of these two phases.

Furthermore, a common relationship between Qp and Qs is:

$$\frac{1}{Q_p} = \frac{4}{3}\left(\frac{V_s}{V_p}\right)^2\,\frac{1}{Q_s} \qquad \textbf{(62)}$$

To show the effect of attenuation on amplitude, source and spreading effects will be neglected. First, the no attenuating case is presented assuming P and S unit impulse amplitudes departing from the source and arriving on one of the seismogram components

of the top most receiver as shown in **Fig. 87**. However, if attenuation is incorporated using **Eq. (61)** and **(62)**, then P and S unit impulse amplitudes departing from the source will decrease and broaden as they travel through the medium to finally reach the top most receiver as shown in **Fig. 88**.

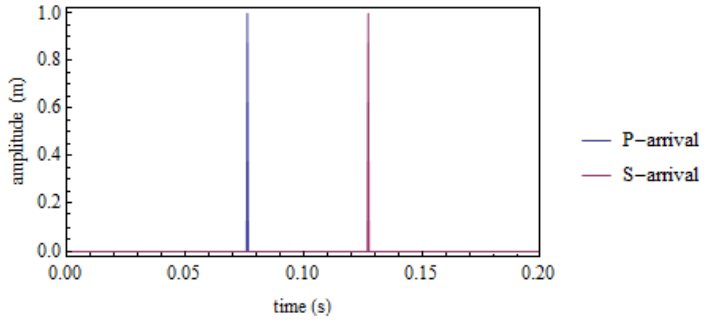

Fig. 87 - P and S impulse arrival in one of the receiver's components.

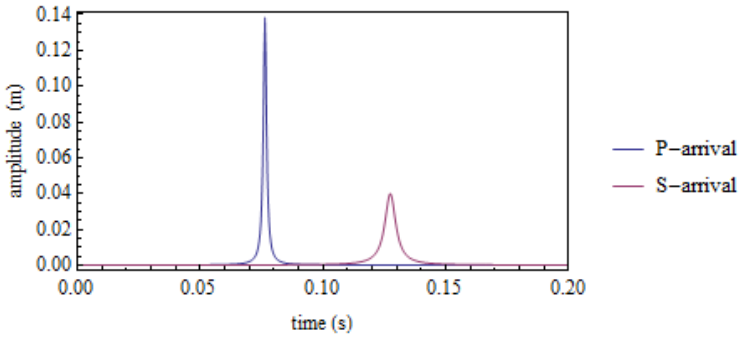

Fig. 88 - P and S non causal unit impulse attenuated arrival in one of the receiver's components. Calculations performed using data from Table 13.

Table 13 shows the data used for the attenuation calculation. Notice that the S arrival is more attenuated and broaden compared to the P arrival, as consequence of a lower Q value used for this phase. For the attenuation calculations velocity dispersion is also neglected.

Qp	50
Qs	24
f	1500 Hz
x	334.2 m (1096 ft.)
Vp	4361.6 m/s (14309.7 ft/s)
Vs	2619.7 m/s (8594.8 ft/s)

Table 13 - Data for attenuation calculation.

To show the effect of not considering attenuation of moment tensor inversion and estimation of source mechanisms, a simulation is performed where amplitudes are calculated considering an attenuating medium as in **Table 13**. However the inversion is performed with a $\widehat{\boldsymbol{G}}$ matrix without considering an attenuating medium. For the forward model, amplitudes are calculated assuming a pure shear source as shown in **Table 12**, including attenuation in the model by incorporating **Eq.(61)**. The Inversion is performed assuming a deviatoric constraint.

Fig. 89 shows the errors for deviatoric constrained solutions of pure shear sources with different strike values without considering attenuation in the inverse model. Notice that the highest errors correspond to slope angles reaching values up to around 40 degrees in absolute value. The least errors correspond to dip angles which are less than 10 degrees in absolute value. Notice that all angle errors become very close to zero for a source strike around 90 degrees.

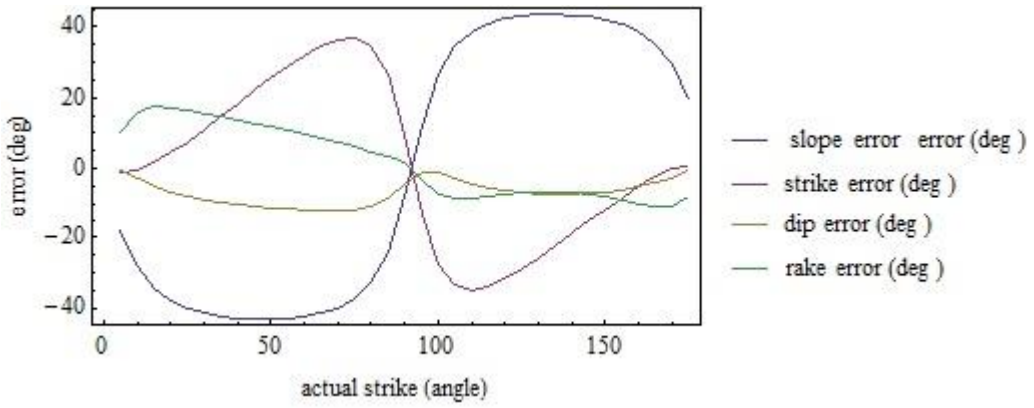

Fig. 89 - Plot showing the errors in the constrained fault plane solutions of pure shear sources without considering attenuation in the inverse model. Amplitudes data were calculated using Qp = 75 and Qs = 36.1.

5.4 Investigation of a Possible Joint Inversion for Moment Tensor and Attenuation Factors

The possibility of a joint inversion of moment tensor and attenuation factor is investigated by a simulation studies. First an inversion analysis considering an explosive source will be done to learn if it is possible to invert for attenuation factors using data from

a perforation shot, under the assumption that a perforation shot can be considered an explosive source. Then, an attempt to retrieve attenuation factors using an assumed source is performed to establish the possibility of a joint inversion from microseismic events.

The moment tensor of a perforation shot is as represented as follows:

$$\boldsymbol{M}_{exp} = \begin{bmatrix} 1 & 0 & 0 \\ 0 & 1 & 0 \\ 0 & 0 & 1 \end{bmatrix} \quad \textbf{(63)}$$

Simulated amplitudes can be generated with **Eq.(39)**. In addition, attenuation is incorporated using **Eq. (61)**. Since for an explosive source only P waves are radiated, then only Qp equal to 50 is used with a central frequency of 1500 Hz. In this case, the location of the explosive source is as shown in **Table 14**.

Event	Easting	Northing	Depth	Back Azimuth
Perfo 1 (stage 8)	-215.6 m (-707.5 ft)	-153.3 m (-502.8 ft)	1681 m (5514.7 ft)	234.6 deg

Table 14 - Location of perforation relative to the surface location of the receiver array.

For the inversion, the calculated amplitudes are the input data, while the $\widehat{\boldsymbol{G}}$ matrix is calculated with of Qp from 10 to 100 and without attenuation as well. Then the moment tensor is estimated by least squares minimization following **Eq.(44)**. Finally, the error fit for each case is calculated as:

$$e = \frac{\sum_{n=1}^{11}\sum_{k=1}^{3} Abs(A_{kn}^{f} - A_{kn}^{i})}{\sum_{n=1}^{11}\sum_{k=1}^{3} Abs(A_{kn}^{f})} * 100 \quad \textbf{(64)}$$

Where A_{kn}^{f} is the amplitude calculated using the forward model for the kth component of the nth receiver, A_{kn}^{i} is the amplitude calculated for the kth component of the nth receiver using the inverted moment tensor and the $\widehat{\boldsymbol{G}}$ matrix for the inverse model.

Table 15 shows the results of the inversions using Qp values from 10 to 100 and one additional inversion without attenuation. The retrieved elements of the moment tensors are very close with the expected values for an explosive source. All the corresponding errors are less than 1% except for the case of no attenuation for which the fit error is around 11%. However, the strength of the source (*Mo*) is different for every case. The highest value (close to 5 N m) corresponds to the lowest Qp, while the lowest strength (around 0.15 Nm) corresponds to the case of no attenuation in the medium. The strength is 1 Nm when the attenuation factor is the same as used in the forward model which completely coincides with the moment tensor proposed.

The inversion results suggest that attenuation affects only the strength of the explosive source but not the moment tensor because for an isotropic source as this, P-phase departs homogenously in all directions. Furthermore, the higher the attenuation (lower Qp value) the higher the strength of the source since a stronger source is needed to compensated for the amplitude loss.

Qp	Fit Error %	Mo (N m)	M_{11}	M_{12}	M_{13}	M_{23}	M_{33}
10	0.120	4.991	0.9994	0.0000	-0.0002	0.0000	1.0000
20	0.120	2.495	0.9994	0.0000	-0.0002	0.0000	1.0000
30	0.117	1.664	0.9994	0.0000	-0.0002	0.0000	1.0000
40	0.089	1.248	0.9996	0.0000	-0.0001	0.0000	1.0000
50	0.000	1.000	1.0000	0.0000	0.0000	0.0000	1.0000
60	0.171	0.837	1.0000	0.0000	0.0002	0.0000	0.9992
70	0.419	0.722	1.0000	0.0000	0.0006	0.0000	0.9980
80	0.725	0.638	1.0000	0.0000	0.0009	0.0000	0.9965
90	1.070	0.574	1.0000	0.0000	0.0013	0.0000	0.9948
100	1.437	0.524	1.0000	0.0000	0.0017	0.0000	0.9932
∞	11.367	0.158	1.000	0.000	0.0020	0.0000	0.9944

Table 15 - Inversion solutions for different Qp values. The forward model for amplitude calculations assume an explosive source with Qp=50.

Fig. 90 shows the comparison between the amplitudes at each component receiver for the forward model with Qp =50 and the inversion without considering attenuation effects (Qp = ∞). Despite the error in misfit of around 11%, the moment tensor elements for the original explosive source are retrieved with good match but with very low strength as shown in **Table 15**.

In conclusion, a perforation shot for which an explosive model is assumed cannot be used for estimating attenuation factor by a joint inversion of moment tensor.

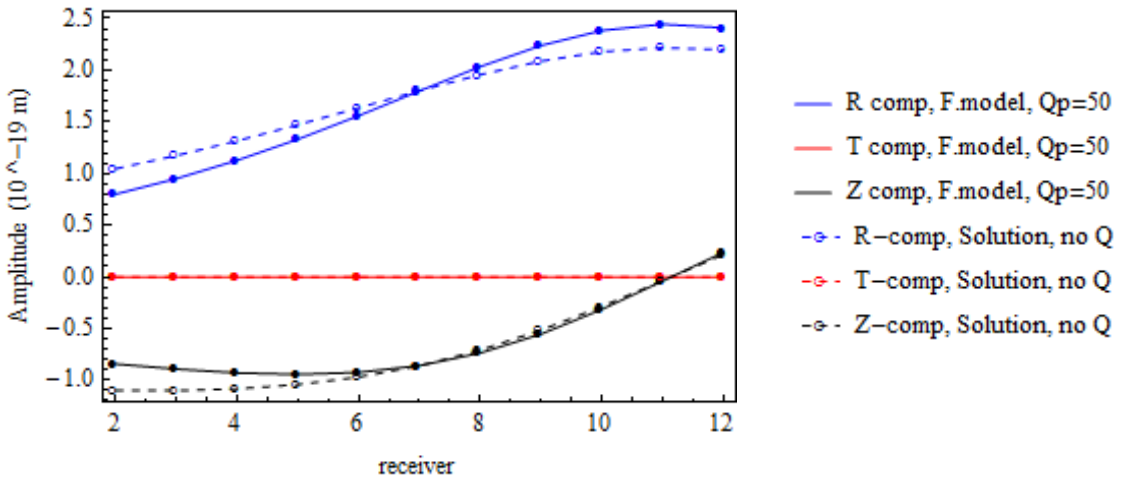

Fig. 90 - Comparison between amplitudes calculated from the forward model with an explosive source and Qp=50 and from the inversion solution without considering attenuation in the $\widehat{G}$ matrix .

To further investigate the effect of attenuation in shear waves, together with the possibility to perform joint inversion of moment tensor and attenuation factor, the joint inversion for attenuation factor and moment tensor is attempted using a pure shear source.

P and S amplitudes from a shear fracture are simulated including attenuation effects, then inversion is performed by applying the deviatoric constraint and considering different Qp attenuation factors. Qs factors are calculated using **Eq. (62),** which corresponds to a Qp/Qs ratio of 2.1. An inversion case without considering attenuation factor in the inverse model is also performed. Additional cases presented consider a Qp/Qs equal to 2.1 for the simulation of amplitude data and two other ratios (1.6 and 1.4) for the inverse model.

Table 16 shows the fracture model for this study and **Eq. (65)** is the respective moment tensor. For the forward model, Qp is equal to 50, Qs is 24.1 and the respective Qp/Qs ratio is 2.1, and the source location is as per **Table 14**.

$$M_{frac} = \begin{bmatrix} -0.908 & 0.33 & -0.212 \\ 0.33 & 0.908 & -0.148 \\ -0.212 & -0.148 & 0 \end{bmatrix} \quad \textbf{(65)}$$

Fig. 91 and **Fig. 92** show the radiation pattern for P and S respectively in the R-Z plane, the red dots are the angular position of the receivers respect to the source.

Slope (deg.)	0
Strike (deg.)	35
Dip (deg.)	75
Rake (deg.)	0

Table 16 - Fracture model for the forward simulation.

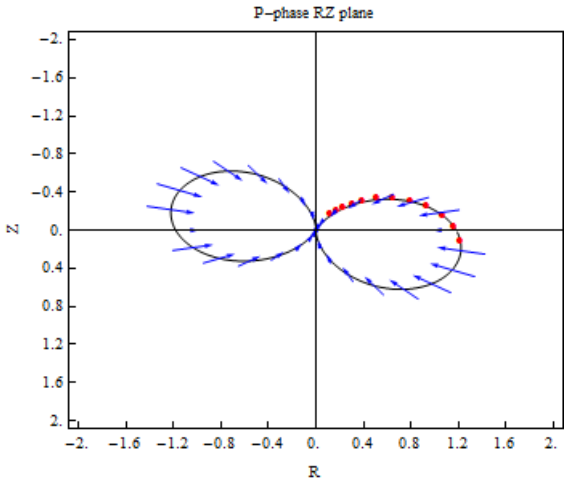

Fig. 91 - P radiation pattern in the radial-Z plane for the fracture model plane proposed in Table 16. The red dots are the angular positions of the receivers.

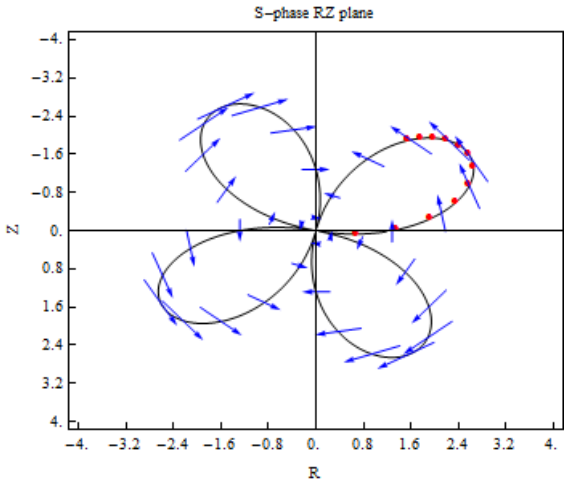

Fig. 92 - S radiation pattern in the radial-Z plane for the fracture model plane proposed in Table 16. The red dots are the angular positions of the receivers.

Table 17 shows the results of the inversion under the deviatoric constraint assumption for different Qp values and with Qp/Qs ratio equal to 2.1. The fitting errors are zero for practical purposes and the corresponding fracture plane is retrieved with negligible error as well. The only difference among the solutions is the strength of the source (*Mo*), which coincides with the proposed source when the attenuation factor is the same as the proposed in the forward model. **Table 17** also shows the result for the case when attenuation in not considered in the inverse model. For this case, the fitting error is around 17% and the plane solution errors are also appreciable.

Fig. 93 and **Fig. 94** show the amplitudes for all receiver components for the forward model constructed with Qp = 50 and Qs = 24.1 and the amplitudes from the inversion results without considering attenuation.

Qp	Fit error %	Mo (Nm)	slope (deg.)	Strike (deg.)	Dip (deg.)	Rake (deg.)
10	0.081	4.989	-0.094	35.026	74.975	0.052
20	0.083	2.495	-0.100	35.028	74.973	0.057
30	0.082	1.663	-0.099	35.028	74.973	0.057
40	0.063	1.248	-0.078	35.022	74.979	0.045
50	0.000	1.000	0.000	35.000	75.000	0.000
60	0.129	0.836	0.172	34.950	75.047	-0.097
70	0.327	0.721	0.457	34.866	75.126	-0.253
80	0.590	0.636	0.856	34.747	75.236	-0.466
90	0.904	0.571	1.361	34.596	75.374	-0.727
100	1.258	0.520	1.955	34.416	75.535	-1.026
average	**0.352**		**0.443**	**34.868**	**75.122**	**-0.236**
∞	**17.055**	**0.130**	**45.692**	**18.267**	**85.543**	**-14.979**

Table 17 - Inversion results using the amplitude data generated with the fracture model from Table 16 and Qp =50 and Qs=24.1 or Qp/Qs =2.1. The inversion is done applying the deviatoric constraint for different values of Qp and with Qp/Qs =2.1, including a model without attenuation (Qp = ∞).

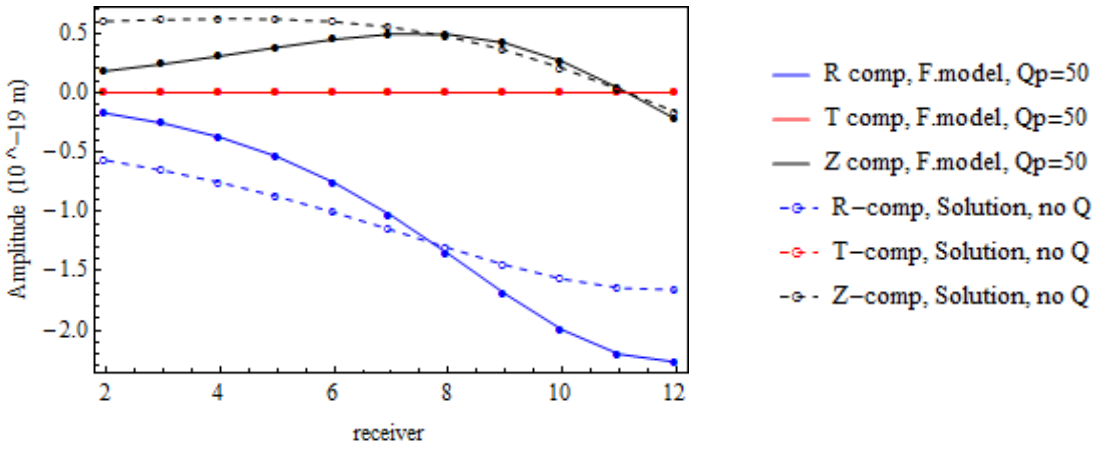

Fig. 93 - P amplitudes from the forward model and the estimated by the inversion without considered attenuation and using the forward model amplitudes as input data.

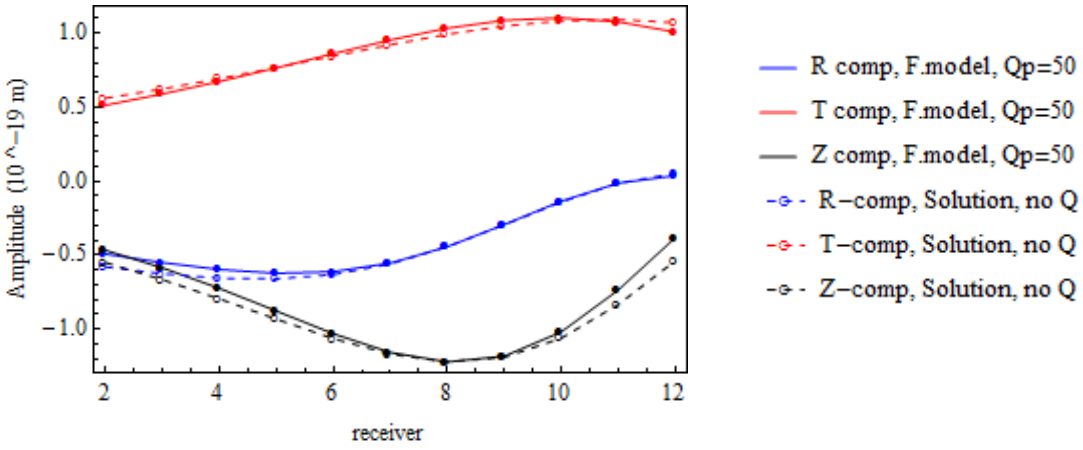

Fig. 94 - S amplitudes from theforward model and the estimated by the inversion without considered attenuation and using the forward model amplitudes as input data.

To test the effect of Qp/Qs ratio, inversions are performed using Qp = 75 and different values of Qp/Qs ratios in the inverse model. The amplitude data are calculated with Qp =50 and Qp/Qs =2.1 (Qs =23.8).

Table 18 shows the inversion results for Qp/Qs ratios ranging from 0.9 to 3.1. According to **Fig. 95** and **Fig. 96** the fitting errors and plane solution errors are appreciable with a minimum for Qp/Qs = 2.1, at which the errors are practically zero and which correspond to the forward model Qp/Qs ratio. The highest fitting error is around 10% and corresponds to Qp/Qs =0.9. **Fig. 97** shows the comparison of fitting and plane solution errors for three different Qp/Qs ratios and the case for no attenuation in the inverse model. The errors for the case with no attenuation in the inverse model are always higher.

Qp/Qs	Fit error %	Mo (Nm)	slope (deg.)	Strike (deg.)	Dip (deg.)	Rake (deg.)
0.900	9.587	0.584	33.739	23.550	82.125	-9.464
1.100	8.218	0.601	27.063	25.955	80.949	-8.375
1.300	6.765	0.617	20.880	28.122	79.787	-7.139
1.500	5.245	0.632	15.153	30.079	78.634	-5.732
1.700	3.675	0.647	9.865	31.843	77.482	-4.137
1.900	2.072	0.662	5.021	33.421	76.330	-2.344
2.100	0.454	0.676	0.640	34.812	75.177	-0.352
2.300	1.167	0.688	-3.255	36.015	74.027	1.828
2.500	2.776	0.700	-6.638	37.024	72.888	4.173
2.700	4.362	0.712	-9.492	37.835	71.774	6.640
2.900	5.917	0.722	-11.815	38.448	70.698	9.171
3.100	7.431	0.731	-13.624	38.866	69.680	11.699

Table 18 - Inversion results using the amplitude data generated with the fracture model from Table 16 and Qp =50 and Qs=23.8, (Qp/Qs =2.1). The inversion is done applying the deviatoric constraint for Qp=75 and different values of Qp/Qs.

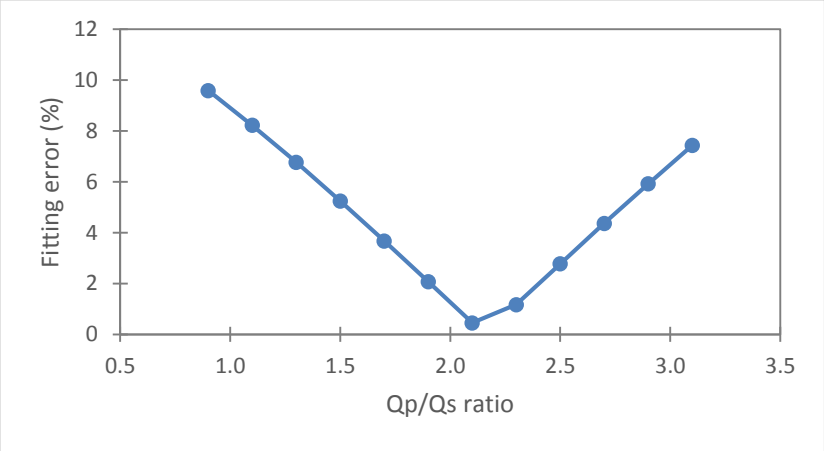

Fig. 95 - Inversion Fitting error for different Qp/Qs cases in the inverse model. All inversions performed applying the deviatoric constraint with Qp=75. Forward model with Qp=50 and Qp/Qs =2.1.

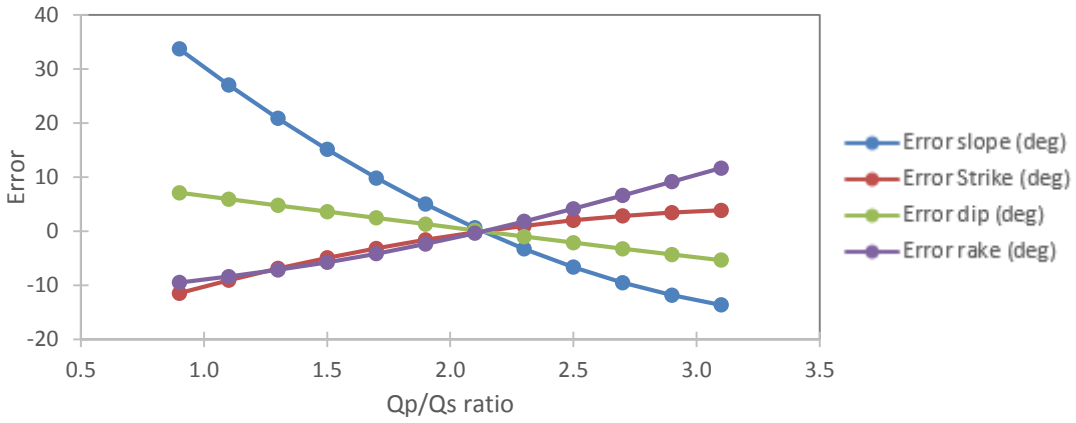

Fig. 96 - Fracture plane error for different Qp/Qs cases in the inverse model. All inversions performed applying the deviatoric constraint with Qp=75. Forward model with Qp=50 and Qp/Qs =2.1.

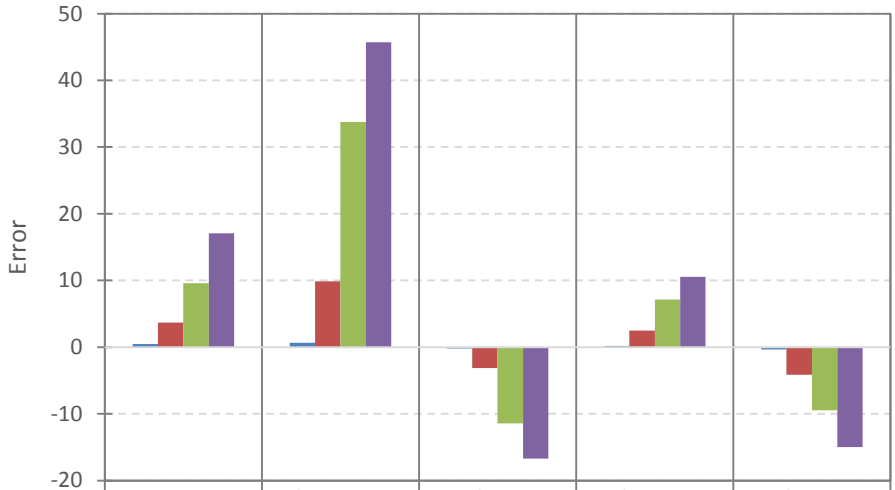

	fit error %	slope error (deg)	strike error (deg)	dip error (deg)	rake error (deg)
Qp/Qs =2.1	0.454	0.640	-0.188	0.177	-0.352
Qp/Qs =1.7	3.675	9.865	-3.157	2.482	-4.137
Qp/Qs =0.9	9.587	33.739	-11.450	7.125	-9.464
Q = ∞	17.055	45.692	-16.733	10.543	-14.979

Fig. 97 - Inversion Fitting error and fracture plane error for different Qp/Qs cases for Qp=75 in the nverse model including a case without attenution. All inversions performed applying the deviatoric constraint. Forward model with Qp=50 and Qp/Qs =2.1.

In principal and according to the results presented, it is possible to perform the joint inversion for moment tensor and Qp/Qs ratio that best fit the amplitude data. However, it is not possible to find the actual strength of the source since it depends on the absolute value of Qp which has to be estimated by other means.

6. ANALYSIS OF MICROSEISMIC DATA

In this section, the analysis of micrososeismic data for selected events will be done. However, a perforation shot analsis will be performed first to establish the absolute orientation of each 3C component receiver and to find the attenuation coefficient that best matches the observed amplitudes assuming an explosive moment tensor model.

6.1 Absolute Orientation of Receivers' Components

To be able to process microseismic data, it is necessary to know the absolute orientation of each of the 3 components (x, y, z) of the downhole receivers respect to the geographical North. In a vertical well, the z component coincides with the vertical direction, and the convention that will be followed is that the z component is positive in the down direction. However, the x and y components of the 3C receivers are oriented randomly downhole and their components not necessarily coincide with the cardinal directions. Then, the goal is to find the rotation angle needed to align the x direction with the geographical North.

The first step is to find the radial and transverse directions using particle motion diagram for the P-arrival which is the strongest phase for perforation events. This step is completed by rotating the *y* component until the P- amplitude is close to zero, so that the *y* component is aligned with the transverse direction. However, there will be an ambiguity of 180 deg. and as consequence the polarity of the first motion cannot be established. To establish absolute orientation of the radial and transverse directions a comparison against

the expected first motion polarity for an explosive moment tensor model will be done. Once the absolute orientation of the radial and transverse directions are estimated, the alignment of the *x* and y components with North and East direction respectively is done by using the back azimuth angle which can be estimated from the perforation shot location.

The first perforation from stage 8 whose location is marked with a red dot in **Fig. 98** will be analyzed. **Table 14** presents the location of the perforation shot relative to the receiver array and its respective back azimuth, and **Fig. 99** shows the side view from the plane R-Z, where the arrow points to the 9th receiver (the first receiver is the top most one), and whose 3-C raw seismogram is displayed in **Fig. 100**. The red circle in **Fig. 100** encloses the P-arrival. **Fig. 101 A** and **B** show the zoom in around the P arrival and the x-y particle motion diagram.

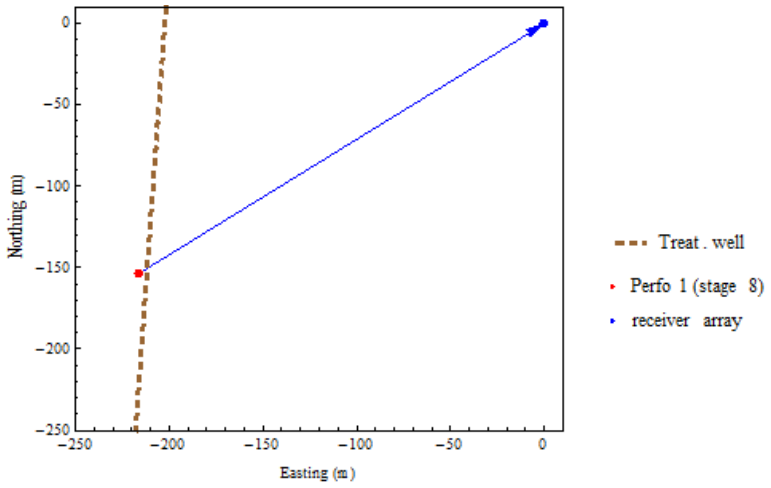

Fig. 98 - Plan view of selected perforation shot, receiver array and treatment well. The blue line represents the transverse direction.

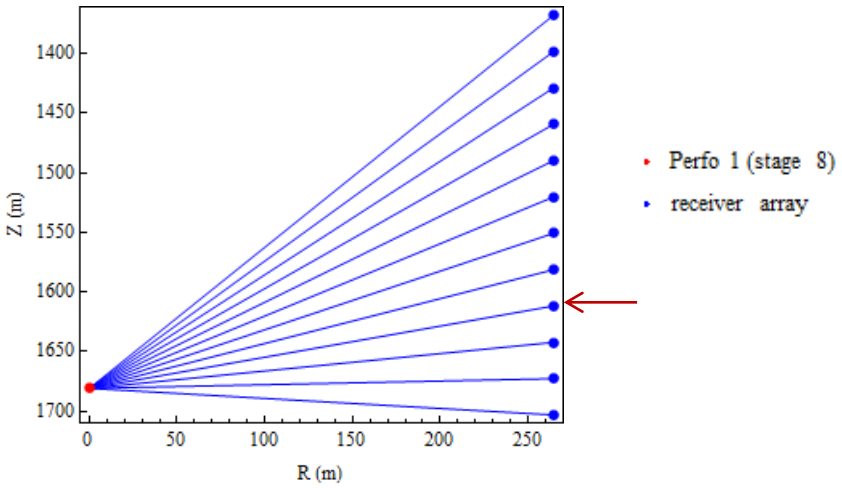

Fig. 99 - Side view (R-Z) of selected perforation shot and receiver. The blue lines represent the ray propagation path from the source to the receiver assuming a homogeneous medium. The red arrow is pointing to the 9th receiver.

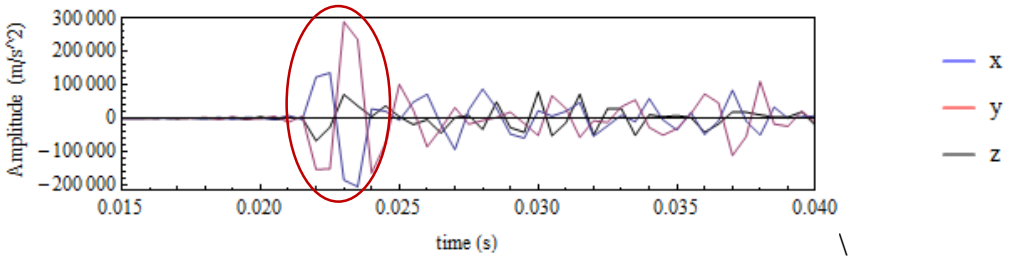

Fig. 100 - 3C raw seismogram data from the 9th rceiver . The red circle is enclosing the P-arrival.

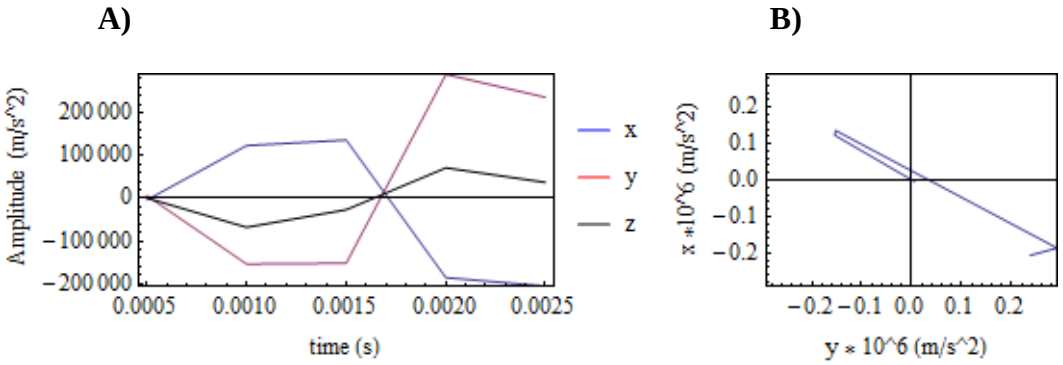

Fig. 101 - A) Zoom in of P-arrival at the 9th receiver. B) Particle motion plot of the y and x components of the P arrival.

Since the P arrival should not present a transverse component in rotated seismograms, the x-y seismogram components will be rotated until aligning the *y* component with the T direction. This search will be done by finding the angle that yields the minimum amplitude in the y seismogram component. **Fig. 102 A and B** present the result of the rotated seismogram into the R-T direction and the x-y (R-T) particle motion respectively. This procedure is repeated to find the respective rotation angles for the other 11 receivers. However, there is an ambiguity of the R-T direction, since a rotation of θ or $\theta + \pi$ will yield similar R-T particle motions. This ambiguity affects the polarity of the P-arrival in the R component. As Shown in **Fig. 98** and **Fig. 99** the R direction is considered to be pointing outwards from the source towards the receiver array. To be able to determine if the R-T directions found by minimization of the y- component amplitude coincides with the proposed R-T direction, the radiation pattern for an explosive moment tensor model will be used.

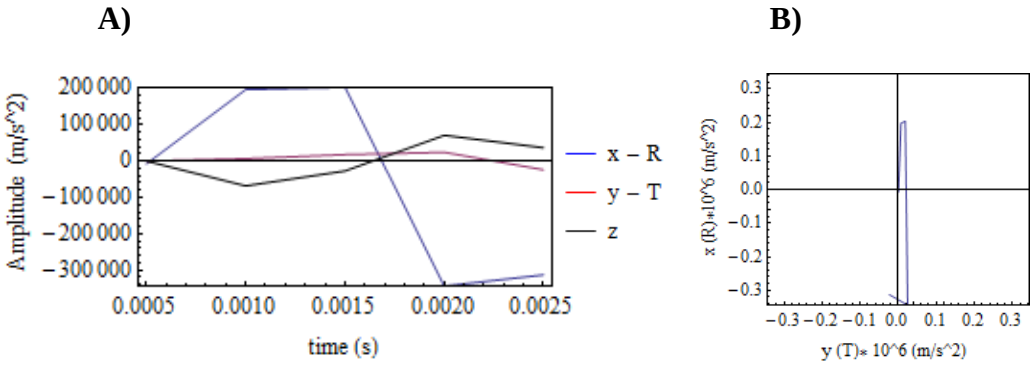

Fig. 102 - Rotated seismogram (x-R, y-T). A) Zoom in of P-arrival at the 9th receiver. B) Particle motion plot of the y (T) and x (R) components of the P arrival.

To plot the radiation pattern for the assumed explosive source, first P- amplitudes in the R and Z components are calculated around the source using **Eq. (39)** to **(41)** in which the moment tensor for an explosive model is used as described by **Eq. (63)**

Then, a vector plot is drawn in the R-Z direction using the module of the calculated R-Z amplitudes with R as the horizontal component and Z as the vertical one. The vectors are plotted around a circle as shown in **Fig. 103**, where each vector shows the first motion of the P-wave departing from the source. The red dots show the angular position of the 12 receivers respect to the source. For all the receivers, the corresponding vectors have positive R components. Thus, under the assumption of a homogenous medium, the picked amplitudes in the seismogram should have positive radial components. Even though, the radiation pattern as calculated from **Eq. (39)** to **(41)** show the first motion of amplitude displacement, while the seismogram recordings are particle acceleration, the first motion polarity does not vary due to the different types motion recordings. To demonstrate it, a Gaussian time dependent function is used as shown in **Fig. 104 A**. The upward first motion

of the Gaussian function does not vary after the second derivative is applied even though the amplitudes are different **(Fig. 104 B)**.

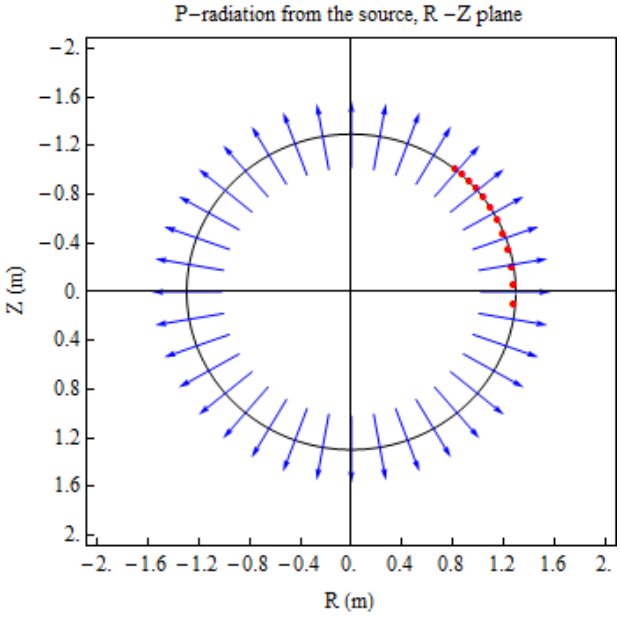

Fig. 103 - Radiation pattern for the explosive model assumed for the perforation shot. The vectors show the first motion direction of R-Z components. The red dots represent the angular direction of the 12 receivers; in these directions all the respective P- vectors have positive R components.

Fig. 105 shows the P amplitudes picked at each seismogram with their corresponding polarity after rotating the seismograms and **Fig. 106** shows the corrected amplitude polarity in the R - component after comparing with the radiation pattern of an explosive source.

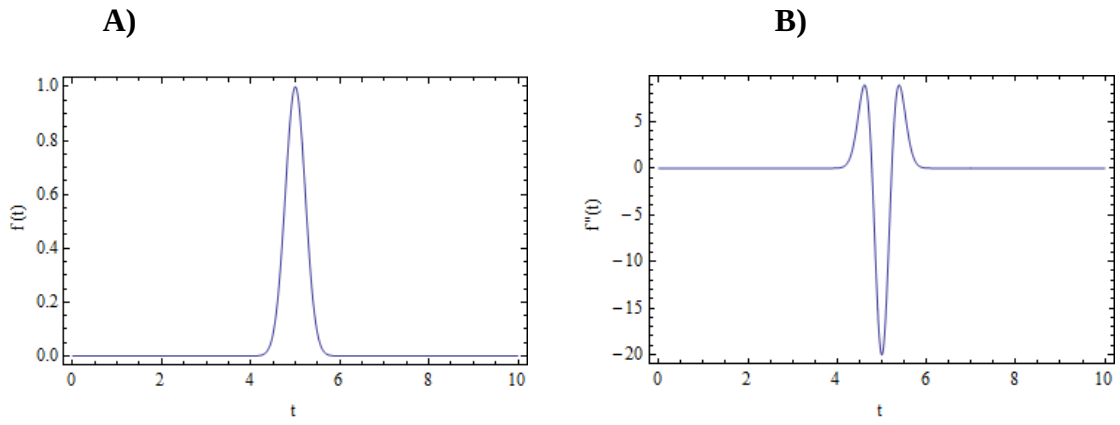

Fig. 104 - A) Gaussian as a function of time B) Second time derivative of the Gaussian function shown in A.

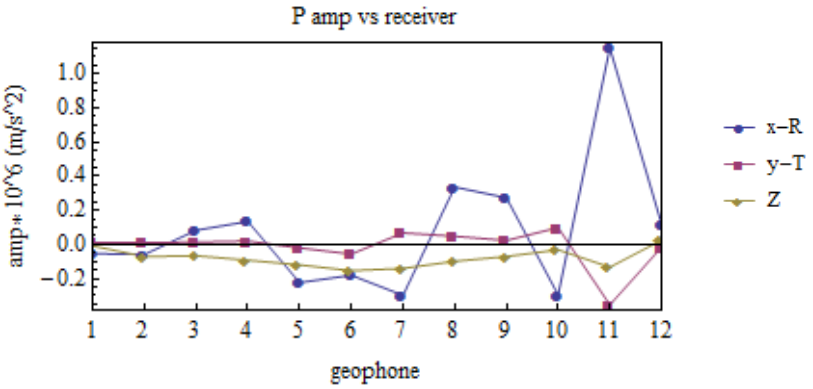

Fig. 105 - Picked P amplitudes in the R, T and Z seismogram components after finding the rotation angle that minimizes the amplitude in the y-component.

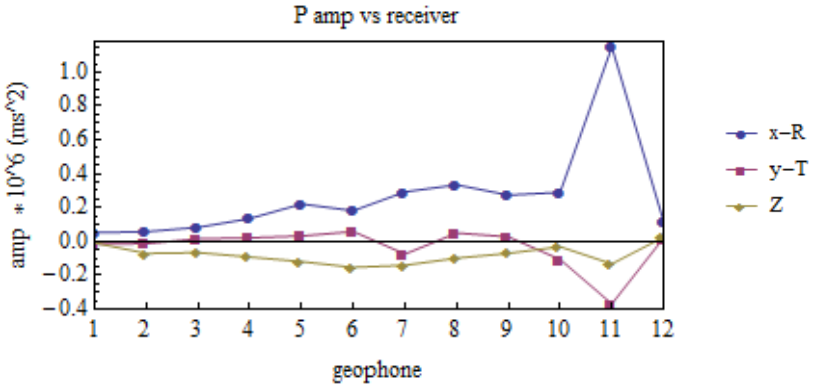

Fig. 106 - Corrected polarity of picked amplitudes in the R seismogram component after comparison with the radiation pattern of an explosive source (Fig. 103).

Finally, to align the x seismogram component with the geographical North, the back azimuth angle is used and the final rotation angle is calculated as:

$$\theta_n = \theta_R - B_{Az} + 180 \quad \textbf{(66)}$$

Where θ_n is the rotation angle needed to align the seismogram x component with the geographical North, θ_R is the rotation angle needed to align the x seismogram component with the radial direction and B_{Az} is the back azimuth angle of the perforation location respect the vertical receiver array. Clockwise rotation angles are positive.

Table 19 shows the estimated rotation angles needed to align the x component of each receiver to the geographical North.

Receiver	θ_n (deg)
1	141.9
2	108.7
3	29.9
4	-31.0
5	189.8
6	156.9
7	68.6
8	-109.3
9	-107.9
10	124.4
11	-123.6
12	18.4

Table 19 - Corrresponding rotation angle needed to align the seimogram x component with the geographical North at each receiver. Clockwise rotation is positive.

6.2 Homogeneous Medium Validation

In a homogenous medium, ray vectors from source to receivers are straight lines as depicted in **Fig. 99**. Then to verify if the homogenous assumption is a good approximation for Spraberry Formation, the ray vector angle will be compared with the angle of incidence estimated from a P –particle motion plot from Z-R components for all receivers. The angle of incidence is estimated by fitting a straight line in the Z-R particle motion plot as shown in **Fig. 107 B**, where the red line is the best fitted straight line for the P- particle motion plot with Z-R components for receiver 9.

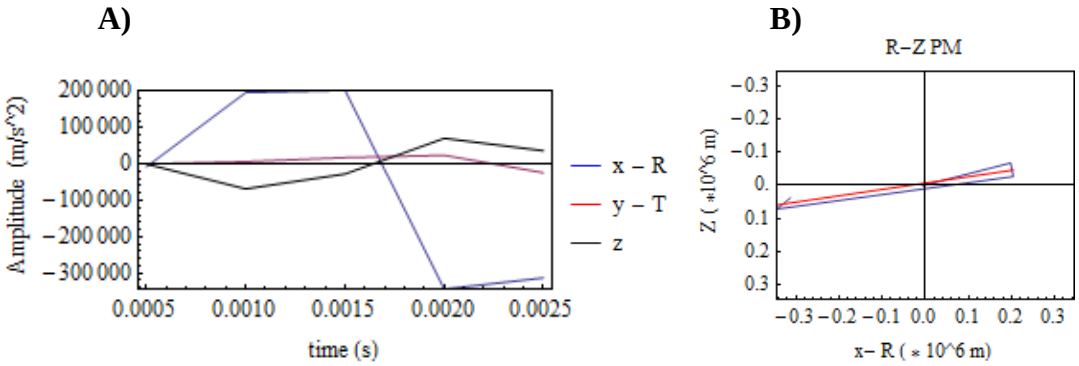

Fig. 107 - Rotated seismogram (x-R, y-T). A) Zoom in of P-arrival at the 9th receiver. B) The blue curve is the particle motion plot of the Z and x (R) components of the P arrival and the red line is the best fitted straight line.

Table 19 shows the calculated source receiver ray vector angle assuming a homogenous medium, the estimated angle of incidence from the P- particle motion plot with the respective error for the straight line fit and the difference between the straight ray vector and the estimated angle of incidence for the 12 receivers. These estimated errors are around 10 deg. or less for most of the receivers except for the top most for which the error is around 40 deg.

Receiver	Ray vector angle (deg.)	Incidence angle - PM (deg.)	PM straight line fit error	Difference Ray v. and PM (deg.)
1	49.8	8.6	0.8	41.2
2	46.9	45.9	0.9	1.0
3	43.6	38.9	0.7	4.7
4	39.9	35.6	1.0	4.3
5	35.8	30.1	0.9	5.7
6	31.2	36.2	0.9	5.0
7	26.2	15.6	0.5	10.6
8	20.6	11.0	0.5	9.6
9	14.6	10.9	0.9	3.8
10	8.3	-2.7	0.2	11.0
11	1.8	-2.9	0.2	4.7
12	-4.8	-5.9	0.3	1.1

Table 20 - Comparison between a sources –receiver straight ray vector and the incidence angle.

According to the velocity model in **Fig. 108 A**, there is a considerable reduction of Vp and Vs at the depth of the top most receiver. If the top most receiver is not considered, the velocities tend to be more homogenous across the entire receivers depth as shown in **Fig. 108 B**, and with a lower standard deviation as calculated in **Table 21**. Thus, for this case the homogenous model is a good approximation if the top most receiver is not considered. Then Vp and Vs velocities are estimated from the velocity model as the average along the vertical distance covering the remaining 11 receivers. Finally the calculated average Vp and Vs velocities for the homogenous model together with the average density are shown in **Table 22**.

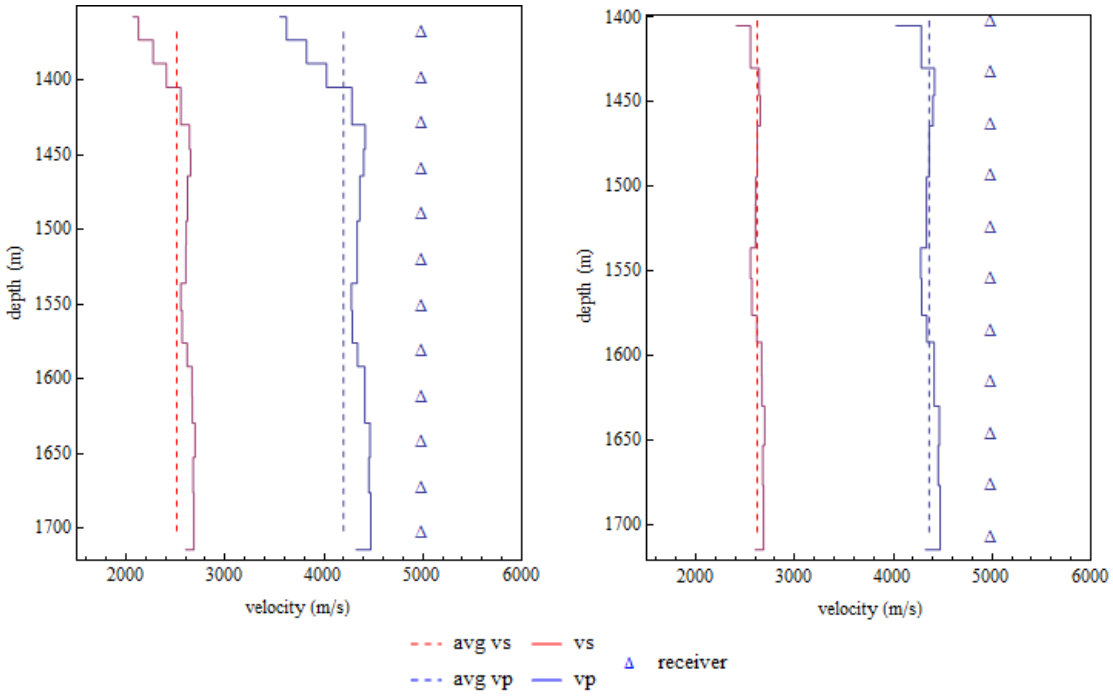

Fig. 108 - Velocity model for the medium with all 12 receivers and with bottom 11 receivers only.

	Vp Standard Deviation (m/s)	Vs Standard Deviation (m/s)
All 12 receivers	256.5 m/s (871 ft/s)	171.3 m/s (562 ft/s)
Bottom 11 receivers	90.9 m/s (298.2 ft/s)	61.5 m/s (201.7 ft/s)

Table 21 - Vp and Vs Standard deviation for all 12 receivers and bottom 11 receivers.

Vp	4361.6 m/s (14309.7 ft/s)
Vs	2619.7 m/s (8594.8 ft/s)
ρ	2584.4 kg/m^3 (161.4 lb/ft^3)

Table 22 - Medium properties as the average along the the bottom 11 receivers depth represinting an homogenous medium.

6.3 Microseismic Events Analysis

The analysis of a single microseismic event is presented in detail as an example, and the processing steps are repeated in the analysis of other events.

6.3.1 Analysis of a Selected Microseismic Event

Table 23 shows the location of the selected event relative to the receiver array. **Fig. 109** and **Fig. 110** show the North -East plan view and the Radial-Depth side view of the selected event respectively. The properties of the medium are as per **Table 22**

Event	Easting	Northing	Depth	Back Azimuth
Stg 7, Ev 14	-212.3 m (-696.5 ft.)	-195.1 m (-640.1 ft.)	1,680.0 m (5511.7 ft.)	227.4 deg.

Table 23 - Location of an example event relative to the surface location of the receiver array

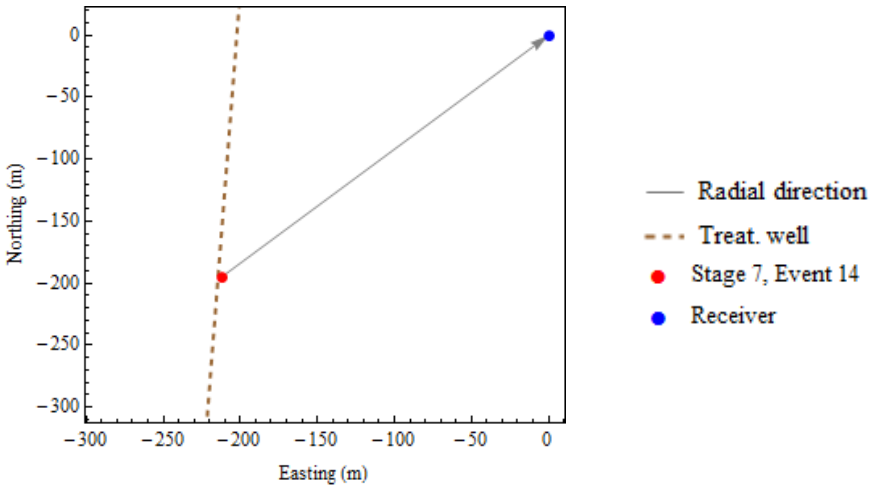

Fig. 109 - Plan view of selected microseismic event, receiver array and treatment well. The gray line represents the transverse direction.

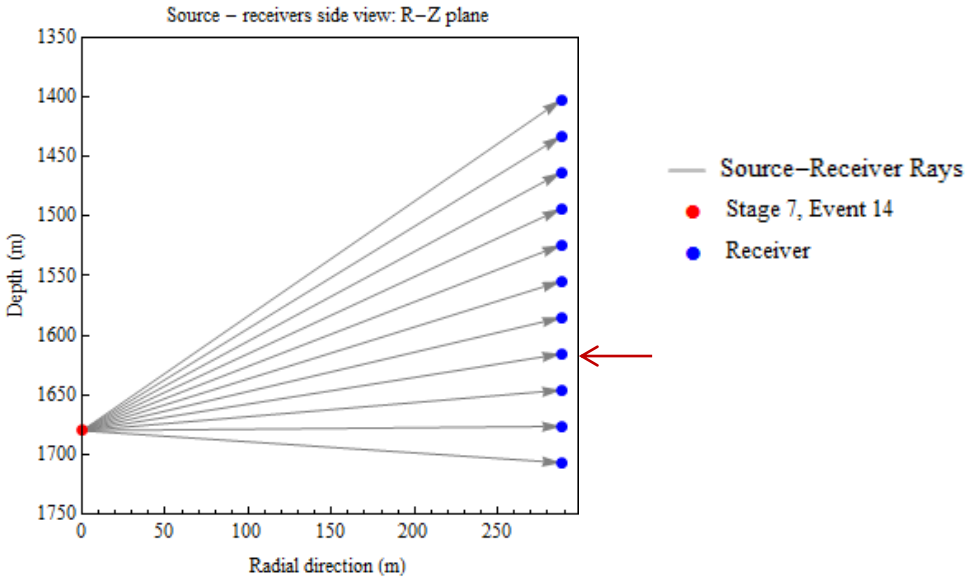

Fig. 110 - Side view (R-Z plane) of selected microseimic evetn and receiver array. The gray lines represent the ray propagation path from the source to the receiver assuming a homogeneous medium. The arrow points to receiver 9.

Since the recorded seismograms are particle acceleration, but the inverse model as proposed in **Eq. (40)**, **Eq. (41)**, and **Eq. (33)** is for particle displacement, the rotated seismograms at each component receiver need to be integrated twice to get displacement data. The top most receiver will be neglected to conform to the homogenous model assumption as analyzed in section 6.2.

The integration is done in frequency domain. After performing the discrete Fourier transform for each seismogram component, displacement can found by double integration in frequency domain as follows:

$$xi_k = -\frac{1}{{w_k}^2} x_k \qquad \textbf{(67)}$$

Where x_k is the input discrete signal, $xi_k$is the output signal and w_k is the discrete angular frequency.

However, direct double integration as in **Eq. (67)** creates a low frequency drift in the seismograms, shifting randomly the signal from the baseline. This is an expected effect after applying the double integration because the frequency is decreased by the square of its value and as consequence low frequency errors are enhanced. According to Chiu (1997) low frequency errors affecting the base line of integrated signals have diverse origins such as instrument and background noise, initial value and manipulation errors.

One of the methods proposed to remove low frequency base line errors is to filter the input signal at different stages of the integration processing (Hwang et al. 2012). Then, the general processing steps for the integration are:

- Filter of the original signal
- First Integration

- Filter of the signal after first integration
- Second integration
- Filter of the signal after the second integration

The filters applied are FIR and could be either bandpass or low pass. At each step, the same filter parameters are applied for all receivers' seismograms. For this event, the original acceleration data was filtered using a bandpass filter within 40-580 Hz and after each integration step, the signal was again bandpass filtered within 30-580 Hz.

Fig. 111 shows the particle displacement seismograms from the 11 receivers for the selected event.

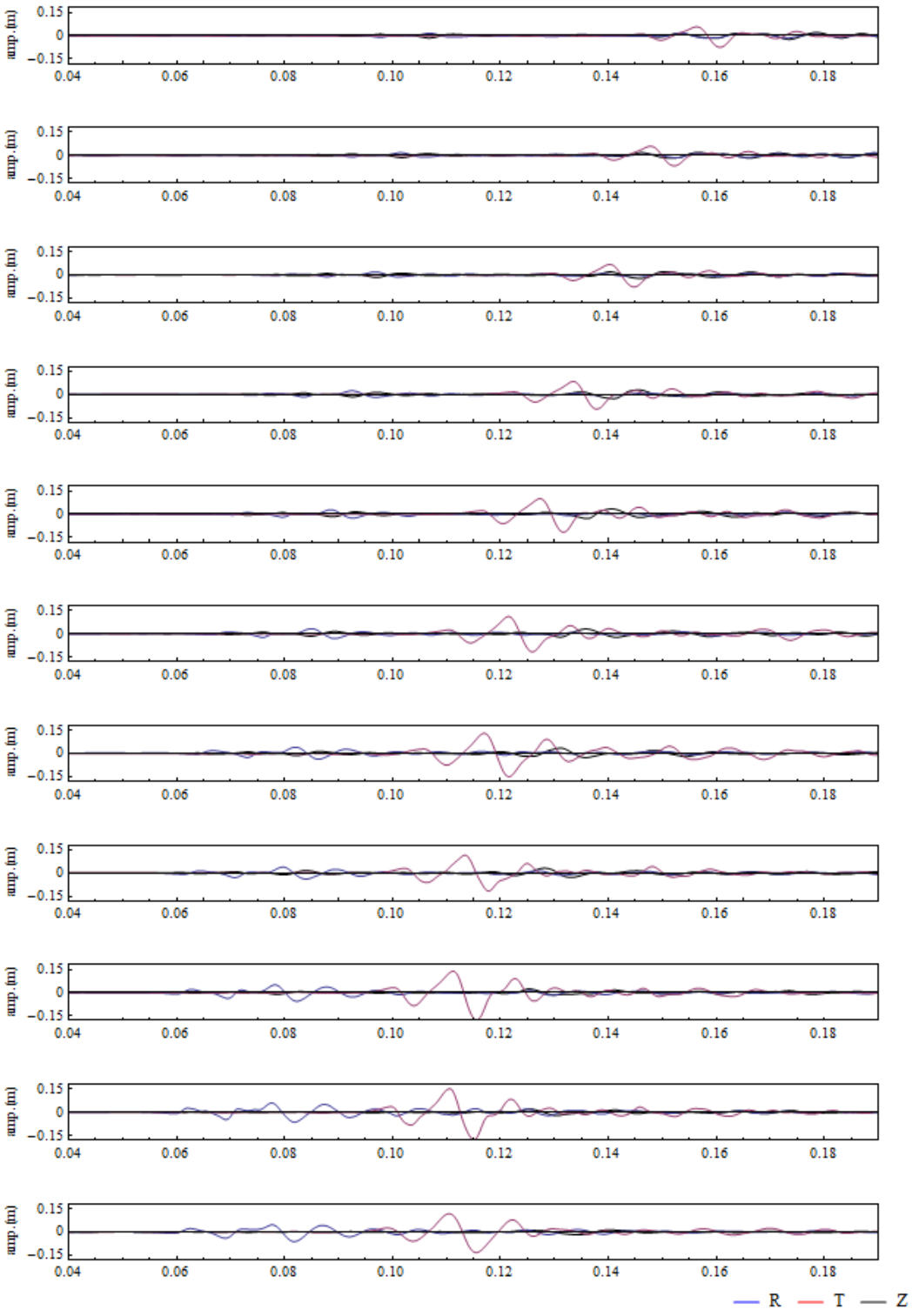

Fig. 111 - rotated seismograms of particle displacement from the 11 bottom receivers for the selected event.

6.3.1.1 Analysis of plane solution errors

The effect of two types of errors in the plane solution will be analyzed:

- Location errors
- Velocity errors

For both analysis, the plane solution errors will be found by looking up in the simulation results of section 5.2

For the analysis of location error effects, the largest axis of the error ellipsoid reported for the event location is picked, which corresponds to 11.4 m (37.6 ft). The errors in plane solutions reported in **Table 24** corresponds to the case when the location error in one coordinate axes is equal to 11.4 m while the errors in the other two coordinates are assumed to be zero.

Max Location Error	Max slope error (deg.)	Max strike error (deg.)	Max dip error (deg.)	Max rake error (deg.)
East =11.4 m (37.6 ft)	0.03	1.90	0.01	0.02
North =11.4 m (37.6 ft)	1.76	1.00	0.35	0.96
Z =11.4 m (37.6 ft)	0.74	0.18	0.02	3.07

Table 24 - Maximum planes solution errors acoording to coordinates errors in the location.

To consider the effects of Vp and Vs velocity errors in the plane solutions, P and S time difference arrivals are analyzed. They are obtained in two different ways: by calculation using the medium velocity model together with the source-receiver distance and by picking P and S time arrivals in particle displacement seismograms. Then the time

residual between these two methods is found by a simple subtraction. This time residual is assumed to be caused by errors in the velocity model. Vp and Vs errors are analyzed in turns; first the assumption that the time residual is due to errors in Vp only is made, and Vp errors are found for each receiver, the same procedure is repeated for Vs velocities. Since, the interest is in the maximum possible error in the plane solution, then the maximum Vp and Vs error are taken.

The P and S time difference arrival (Δt_c) are calculated from the medium velocities and the source- receivers' geometry as follows:

$$\Delta t_c = r_i \left(\frac{1}{V_S} - \frac{1}{V_P}\right) \quad \textbf{(68)}$$

Where *Vp* and *Vs* are the P and S medium velocities and ri is the distance from the source to the *i*-th receiver in the radial-Z plane as shown by the ray paths in Fig. 110.

Fig. 112 shows the radial, transverse and z seismogram components of the original acceleration data from receiver 9.The arrow in **Fig. 110** points to receiver 9. **Fig. 113** shows the seismogram components from the same receiver but for particle displacement data, which was obtained by double integration in frequency domain. P and S time arrivals were picked from the particle displacement seismograms in the radial and transverse components of each receiver respectively and the time difference (Δt_s) was calculated as well as follows:

$$\Delta t_s = t_S - t_P \quad \textbf{(69)}$$

Where t_s and t_p are the S and P time arrivals respectively.

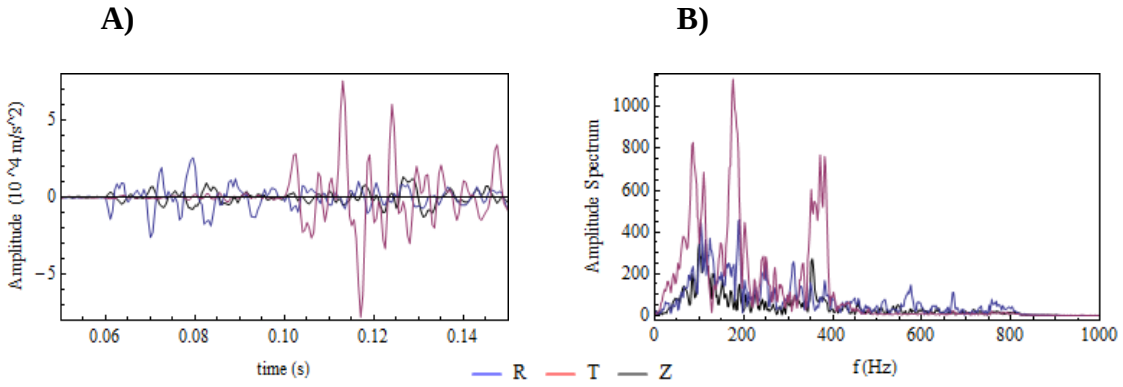

Fig. 112 - A) Radial, transverse and Z seismogram components of the original particle acceleration data from receiver 9. B) the corresponding amplitude spectrum.

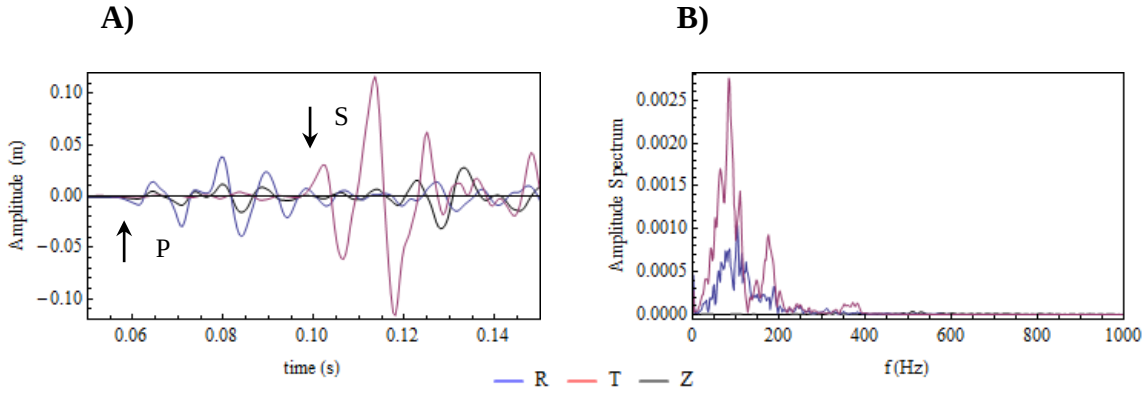

Fig. 113 - A) Radial, transverse and Z seismogram components of particle displacement data from receiver 9. B) the corresponding amplitude spectrum.

Fig. 114 shows the P-S time difference for each receiver calculated from the medium and source receivers' geometry (Δt_c) and estimated from P and S arrivals from particle displacement seismograms (Δt_s). The calculated time arrival difference is always greater than the picked in the seismograms; thus for the velocity error analysis, when one

of the velocities is kept constant, the other one has to increase to match the time difference from the seismograms. This increment in velocity (ΔV) for each receiver is calculated as:

$$\Delta V = \frac{1}{\frac{1}{V_m} - \frac{dt_r}{r_i}} - V_m \qquad \textbf{(70)}$$

Where V_m is either P or S current model velocity.

Finally the percentage error of either velocity at each receiver is calculated as:

$$\%\, V_{err} = \frac{\Delta V}{\Delta V + V_m}\ x\ 100 \qquad \textbf{(71)}$$

Fig. 115 shows the percentage error calculated for P and S velocities at each receiver, and **Table 25** shows the maximum possible errors in the plane solution from the simulation performed in section 5.2 for the maximum errors found for S and P velocities.

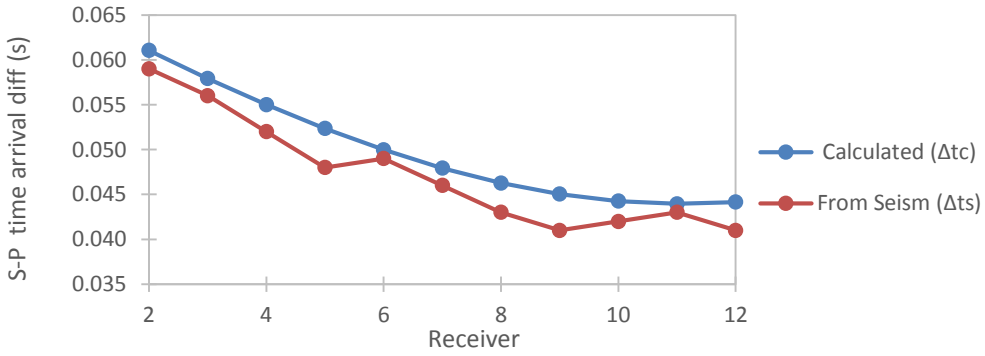

Fig. 114 - S-P time arrival difference for each receiver calculated from the medium velocities and source-receiver geometry (Δt_c) and estimated by pciking the P and S time arrivals in displacement seismograms (Δt_s).

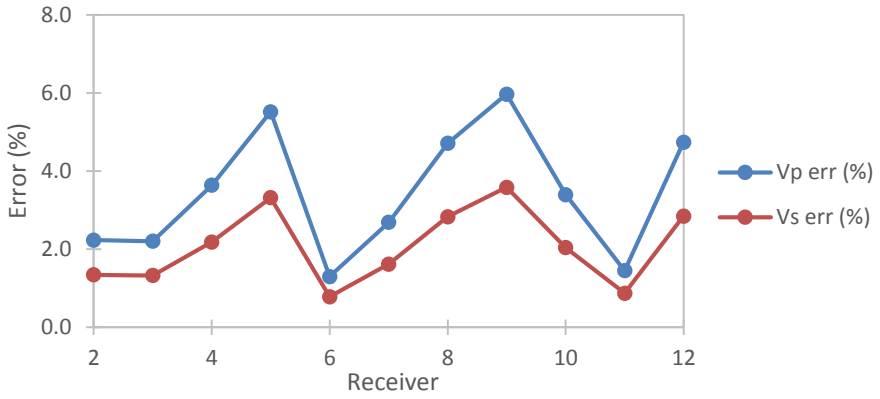

Fig. 115 - P and S Velocity errors (%) calculated for each receiver .

Max Velocity Error	Max slope error (deg)	Max strike error (deg)	Max dip error (deg)	Max rake error (deg)
Vp = 6%	9.49	6.37	2.39	2.98
Vs = 3.6%	8.80	5.57	2.71	4.25

Table 25 - Maximum expected plane solution errors based simulations performed in section 5.1.2 for the maximumVp and Vs velocity errors from Fig. 115.

6.3.1.2 Moment Tensor inversion and Source Mechanisms

To estimate moment tensors, P and S amplitudes are picked from rotated seismograms, then moment tensors are estimated by least squares minimization using **Eq. (44)** . Attenuation effects are included in the $\widehat{\boldsymbol{G}}$ matrix. Qp factor is assumed to be equal to 75 and different values of Qp/Qs are tried in the inversion with the goal of finding the Qp/QS that yields the minimum fitting error. After finding the moment tensor, the corresponding source mechanism is estimated by imposing strike and dip constraints. Since in the formation there are two possible fracture sets, two different strike values are

provided as strike constraints: 35 +/- 20 deg. (or 215 +/- 20 deg.) and 90 +/- 20 deg, (or 270 +/- 20 deg.) and a dip constraint of 80+/- 10 deg. To provide an additional constraint the value of the λ/μ ratio (*k*), which is also part of the inversion results, will be fixed to its theoretical value with a tolerance of +/-10%. The theoretical k value is calculated from Vp and Vs velocity models as:

$$k = \left(\frac{V_P}{V_S}\right)^2 - 2 \qquad \textbf{(72)}$$

The theoretical value of *k* is 0.77. An inversion without considering attenuation in the G matrix will also be performed.

Fig. 116 A and **B** show the time window for P and S arrivals for receiver 9. **Fig. 117 A** and **B** show the P and S picked amplitudes at each component of receiver 9

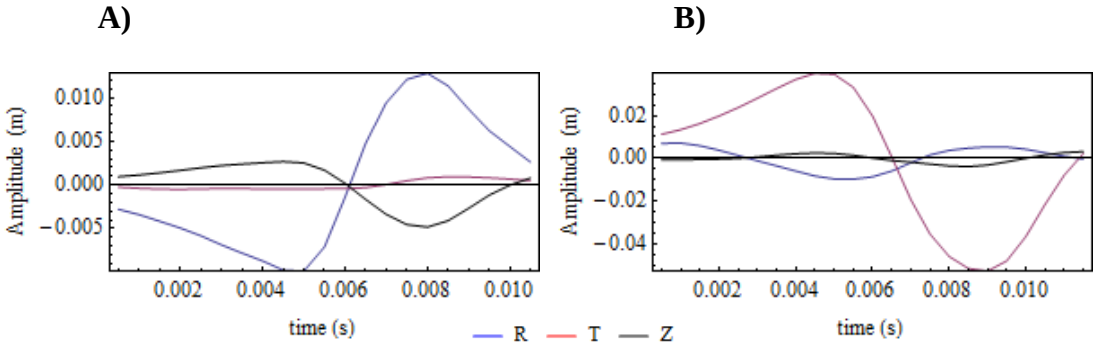

Fig. 116 - Receiver 9 time windows A) Time windwon for P arrival. B) time windwow for S arrival.

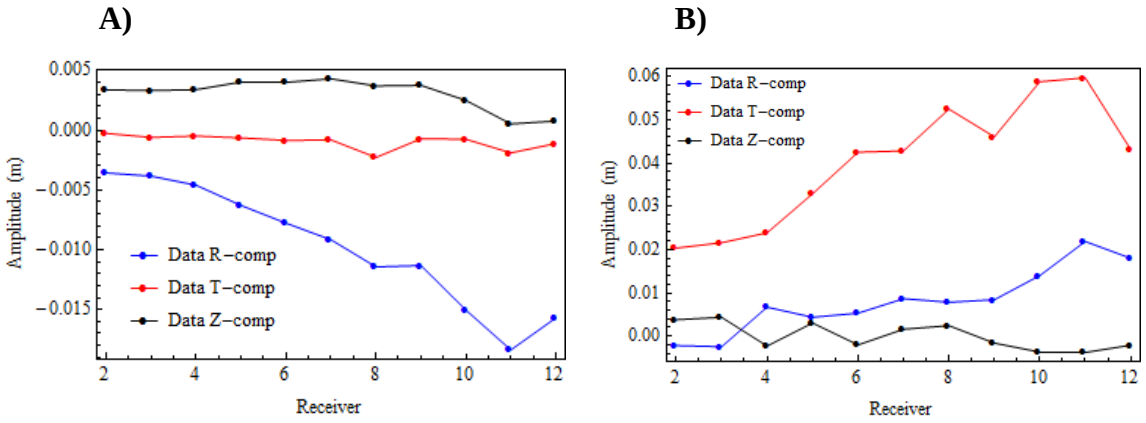

Fig. 117 - Picked ampilutes in each reciever component A) P amplitues B) S amplitudes.

Table 26 shows the five elements of the moment tensor retrieved for the different cases of Qp/Qs and for the case of no attenuation considered in the model. According to **Fig. 118**, there is not an observable minimum and a unique Qp/Qs ratio cannot be found from the inversion procedure. The fit error for the no attenuation case is also very close to the errors considering different Qp/Qs ratios.

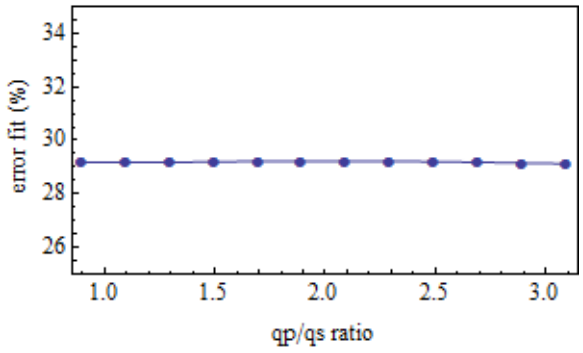

Fig. 118 - Error fit vs different Qp/Qs ratios.

Qp/Qs	Fit error %	Mo (N m)	M_{11}	M_{12}	M_{13}	M_{23}	M_{33}
0.90	29.19	3.17E+16	-0.797	0.986	-0.049	-0.040	-1.000
1.10	29.18	3.75E+16	-0.674	1.000	-0.052	-0.054	-0.878
1.30	29.18	4.39E+16	-0.577	1.000	-0.053	-0.061	-0.777
1.50	29.20	5.04E+16	-0.503	1.000	-0.054	-0.065	-0.700
1.70	29.22	5.70E+16	-0.446	1.000	-0.056	-0.067	-0.639
1.90	29.23	6.37E+16	-0.400	1.000	-0.057	-0.068	-0.589
2.10	29.23	7.03E+16	-0.364	1.000	-0.058	-0.068	-0.548
2.30	29.22	7.70E+16	-0.333	1.000	-0.059	-0.068	-0.514
2.50	29.21	8.37E+16	-0.308	1.000	-0.060	-0.068	-0.485
2.70	29.18	9.04E+16	-0.286	1.000	-0.061	-0.068	-0.459
2.90	29.16	9.71E+16	-0.268	1.000	-0.062	-0.069	-0.437
3.10	29.13	1.04E+17	-0.252	1.000	-0.063	-0.069	-0.417
No Q	31.11	1.09E+16	-0.858	0.847	-0.037	0.183	-1.000

Table 26 - Inversion results for different Qp/Qs ratio and for a model without considering attenuation.

Fig. 119 and **Fig. 120** show the P and S amplitude data and the amplitudes calculated from the estimated moment inversion and the $\widehat{\boldsymbol{G}}$ matrix without considering attenuation.

Fig. 121 and **Fig. 122** show the P and S amplitude data and the amplitudes calculated from the estimated moment inversion and the $\widehat{\boldsymbol{G}}$ matrix with Qp/Qs = 0.9.

Fig. 123 and **Fig. 124** show the P and S amplitude data and the amplitudes calculated from the estimated moment inversion and the $\widehat{\boldsymbol{G}}$ matrix with Qp/Qs = 3.1.

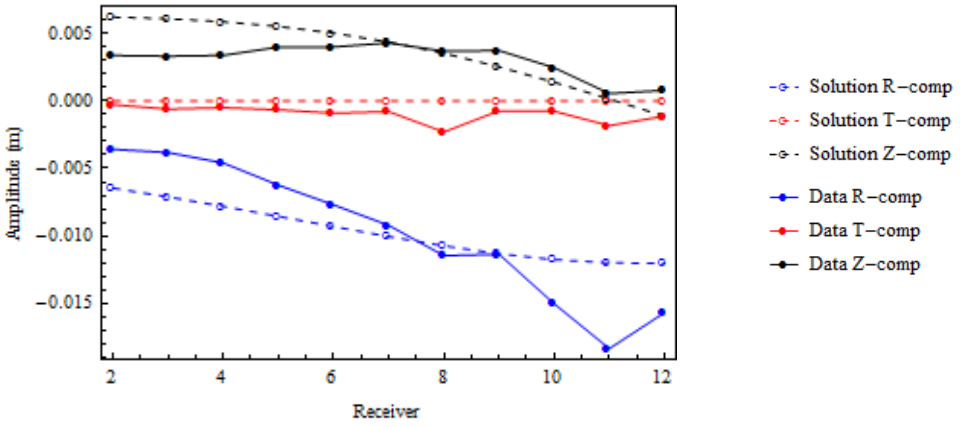

Fig. 119 - P amplitude data and P amplitudes calculated using the inverted moment tensor without considering attenuation in the model.

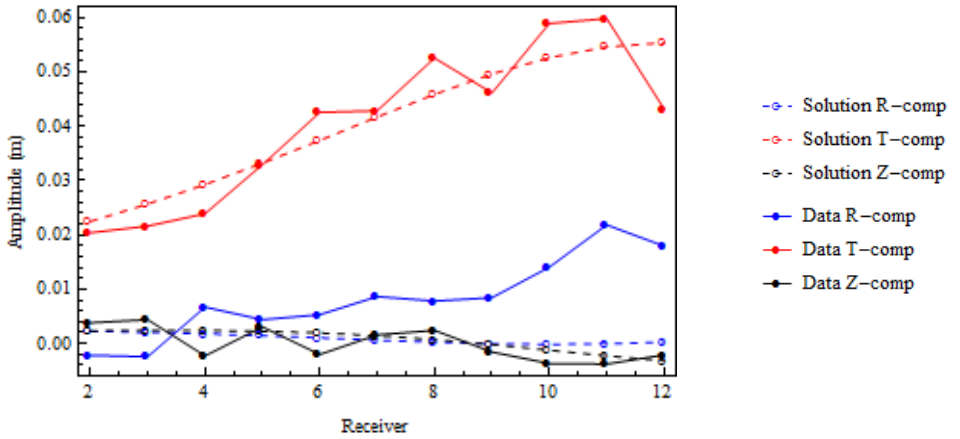

Fig. 120 - S amplitude data and S amplitudes calculated using the inverted moment tensor without considering attenuation in the model.

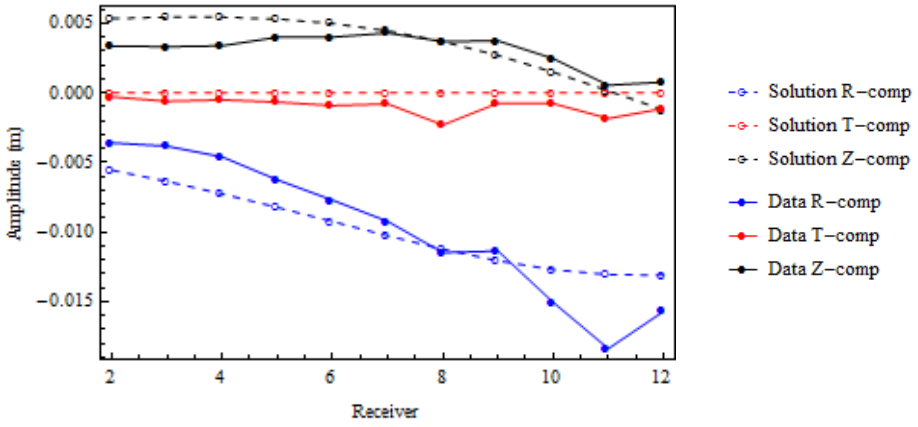

Fig. 121 - P amplitude data and P amplitudes calculated using the inverted moment tensor with Qp/Qs =0.9 in the model.

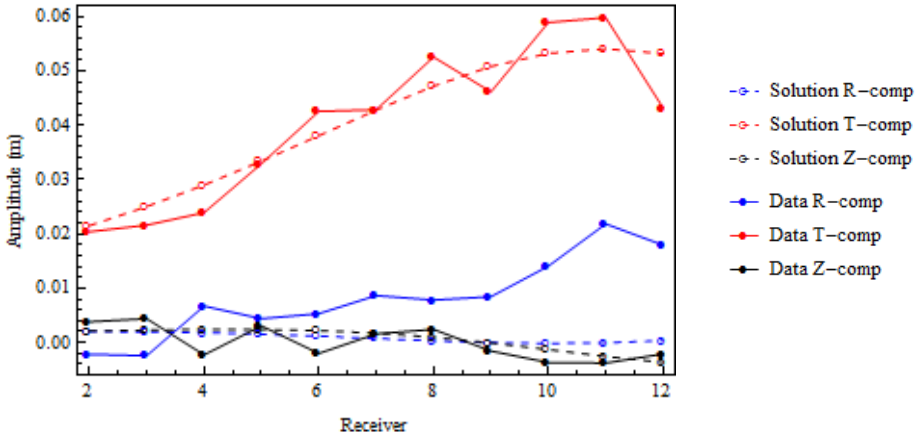

Fig. 122 - S amplitude data and S amplitudes calculated using the inverted moment tensor with Qp/Qs =0.9 in the model.

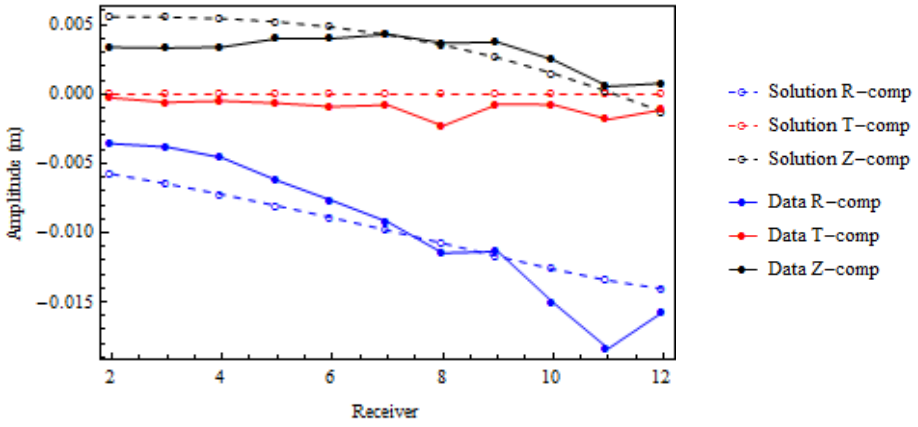

Fig. 123 - P amplitude data and P amplitudes calculated using the inverted moment tensor with Qp/Qs =3.1 in the model.

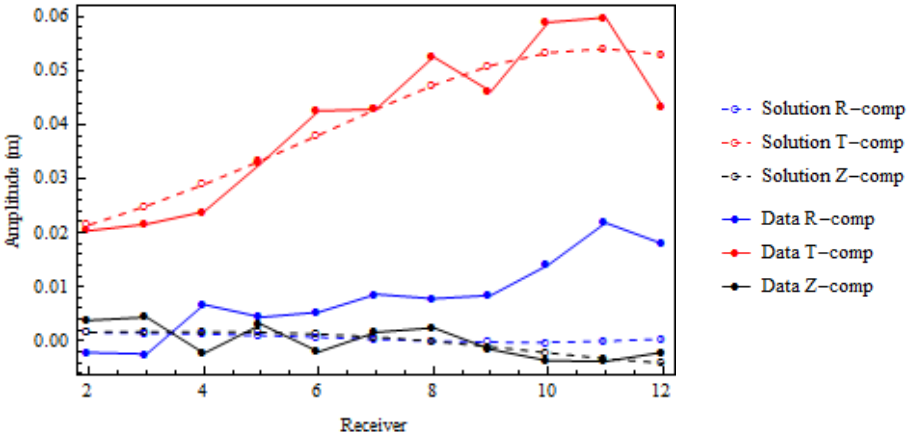

Fig. 124 - S amplitude data and S amplitudes calculated using the inverted moment tensor with Qp/Qs =3.1 in the model.

For each Qp/Qs ratio and for the inversion with no attenuation, a plane solution is found applying dip and strike constraints and providing the value of *k* for the medium. To find the plane solution, first the unknown moment tensor element M_{22} is completed by trying values from -10 to 10 in steps of 0.02. For each attempted value of M_{22}, the corresponding source mechanisms are calculated using the general model as per **Eq. (45)** to Eq. **(48)**. To choose from the two possible solutions, the sum of dip and strike error is calculated and the solution with the minimum error sum is picked. The reference values for strikes are 35 deg. and 90 deg. and for dip is 80 deg. Finally, solutions within +/-20 deg. for strike errors, +/- 10 deg. for dip errors and +/-10% for *k* values are chosen.

Fig. 125 to **Fig. 127** correspond to the plane solutions for a model without considering attenuation. **Fig. 126** shows the *k* value solutions vs M_{22}. The cyan band corresponds to theoretical value of *k* +/- 10%. **Fig. 127 A** shows the plane solutions vs M_{22} that have the least errors respect a reference strike and dip of 35 deg and 80 deg. **Fig. 126 B** shows the dip and strike errors and their corresponding error limits, with all errors in absolute value. **Fig. 127 A** shows the solution vs M_{22} f that have the least errors respect a reference strike and dip of 90 and 80 deg. respectively. **Fig. 127 B** shows the dip and strike errors and their corresponding error limits, with all errors in absolute value**.** Notice that in **Fig. 127** and **Fig. 127**, the cyan bands correspond to the constrained plane solutions since dips and strikes are within the prescribed error limits and within the theoretical *k* value. In addition, it is observed that both strike solutions, 35 ad 90 deg., are possible.

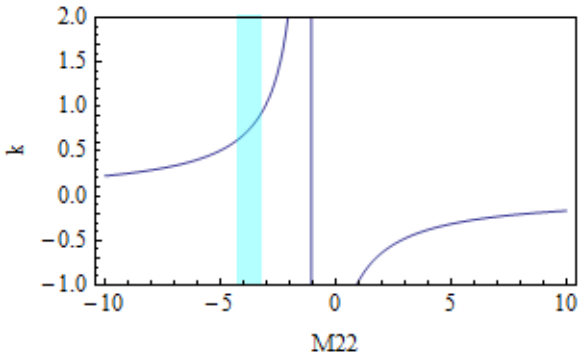

Fig. 125 - Inverted *k* parameters vs M_{22} values for the case of no attenuation in the model. The cyan band correspond to the theoretical value of *k* +/- 10%.

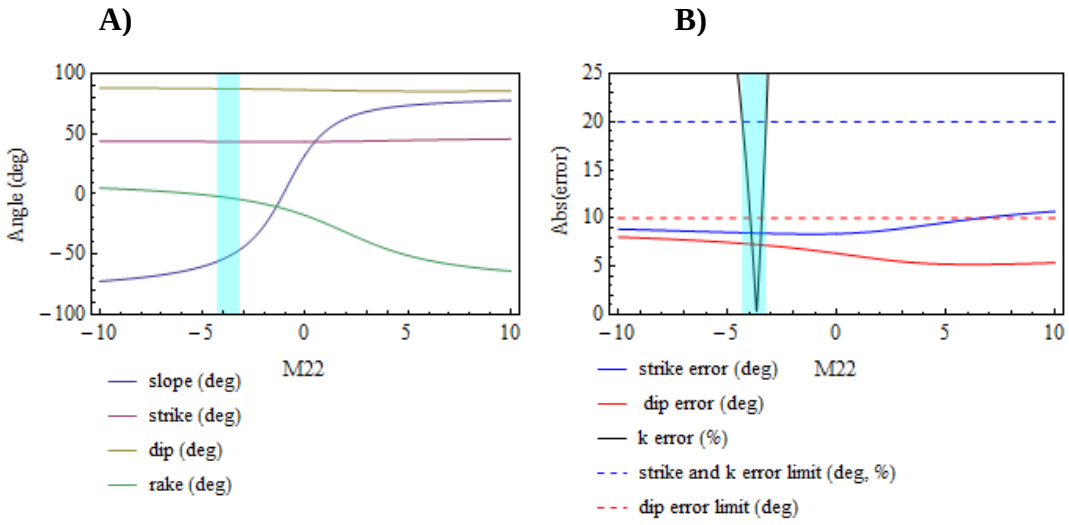

Fig. 126 - A) Fault plane solutions vs M_{22} values for a model without attenuation and for a reference strike =35 deg and reference dip = 80 deg. B) Strike and dip errors respect the referece values and the corresponding error limits. The cyan band correspond to the theoretical value of *k* +/- 10%.

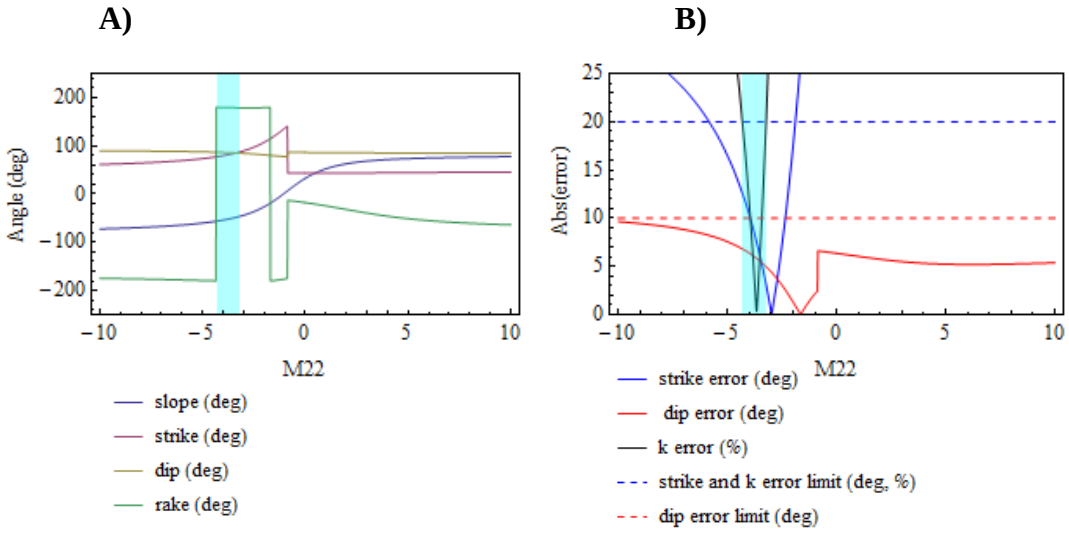

Fig. 127 - A) Fault plane solutions vs M_{22} values for a model without attenuation and for a reference strike =90 deg and reference dip = 80 deg. B) Strike and dip errors respect the referece values and the corresponding error limits. The cyan band correspond to the theoretical value of *k* +/- 10%.

Fig. 128 to **Fig. 130** correspond to the plane solutions for a model with Qp/Qs = 0.9 and **Fig. 131** to **Fig. 133** correspond to the plane solutions for a model with Qp/Qs = 3.1.The details for the figures are similar to the case for no attenuation in the model. However, notice that **Fig. 130** and **Fig. 133** are showing the results for a strike constraint of 270 +/- 20 deg. instead of 90 +/- 20 deg. Since no results within the strike tolerance were found for a strike constraint of 90 deg., the supplementary angle was used instead. It also can be observed that both strike solutions, 35 and 270 deg., are possible.

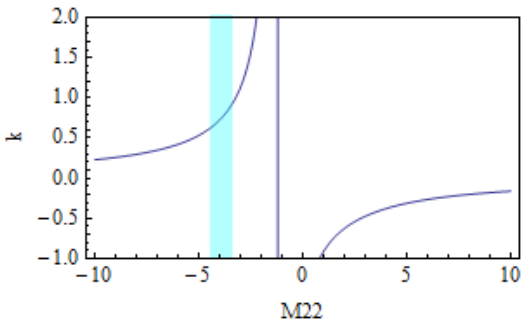

Fig. 128 - Inverted *k* parameters vs M_{22} values for the case when Qp/Qs =0.9 in the model. The cyan band correspond to the theoretical value of *k* +/- 10%.

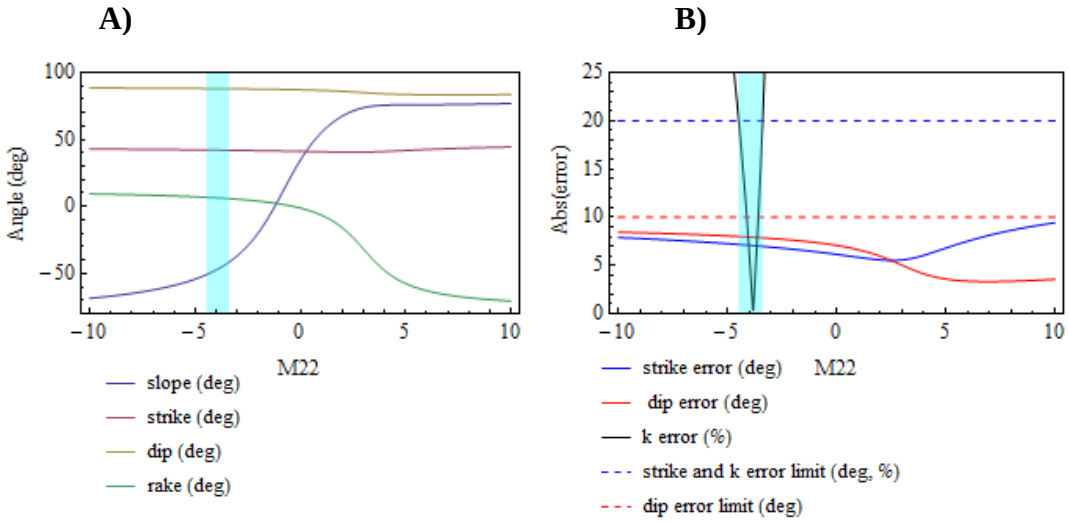

Fig. 129 - A) Fault plane solutions vs M_{22} values for the case when Qp/Qs =0.9 in the model and for a reference strike =35 deg and reference dip = 80 deg. B) Strike and dip errors respect the referece values and the corresponding error limits. The cyan band correspond to the theoretical value of *k* +/- 10%.

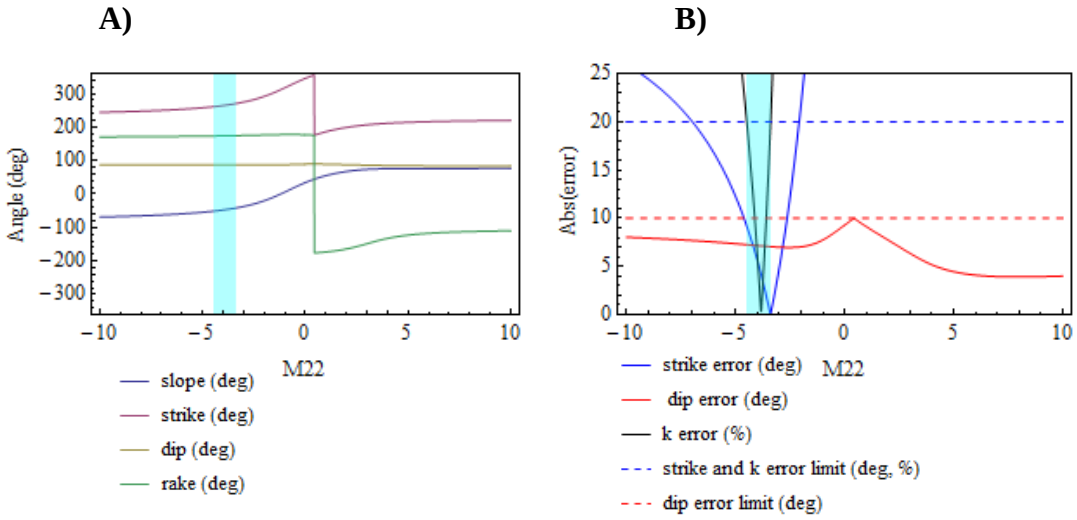

Fig. 130 - A) Fault plane solutions vs M_{22} values for the case when Qp/Qs =0.9 in the model and for a reference strike = 270 deg and reference dip = 80 deg. B) Strike and dip errors respect the referece values and the corresponding error limits. The cyan band correspond to the theoretical value of *k* +/- 10%.

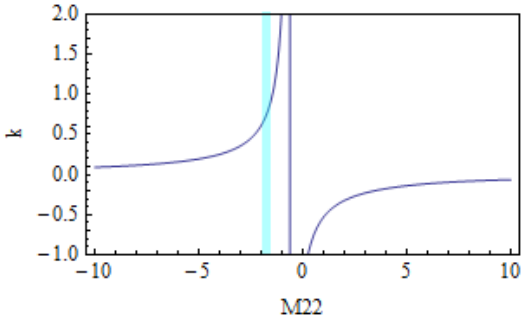

Fig. 131 - Inverted *k* parameters vs M_{22} values for the case when Qp/Qs =3.1 in the model. The cyan band correspond to the theoretical value of *k* +/- 10%.

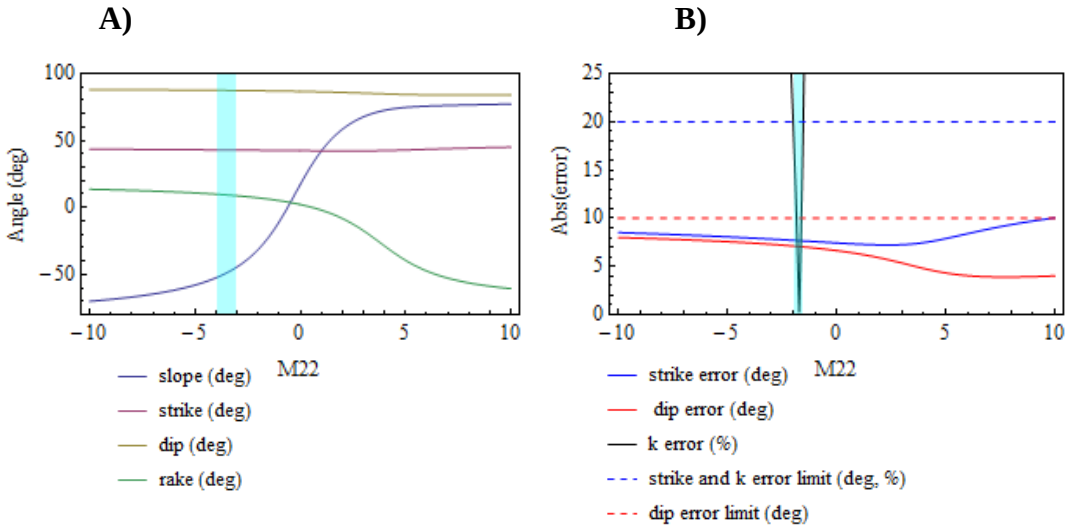

Fig. 132 - A) Fault plane solutions vs M_{22} values for the case when Qp/Qs =3.1 in the model and for a reference strike =35 deg and reference dip = 80 deg. B) Strike and dip errors respect the referece values and the corresponding error limits. The cyan band correspond to the theoretical value of *k* +/- 10%.

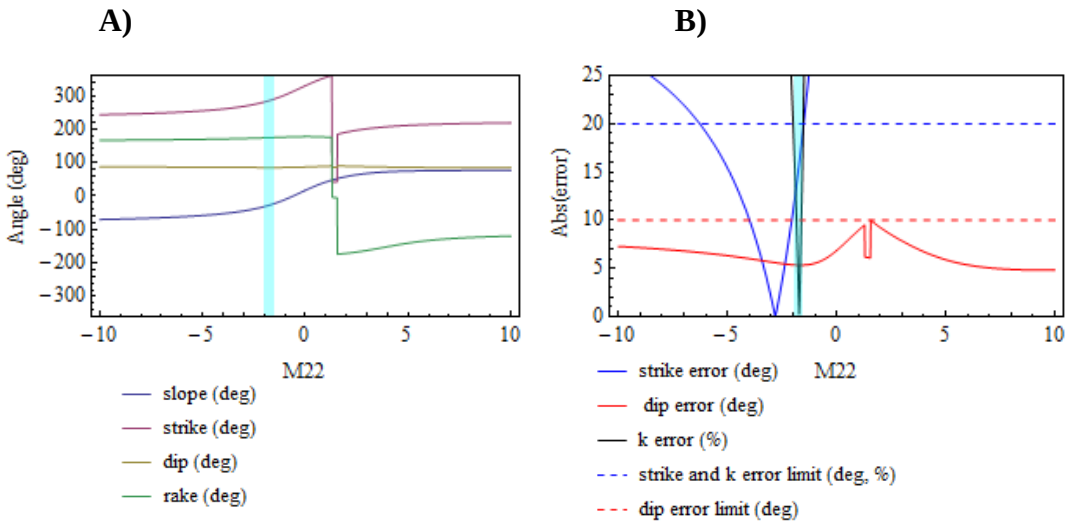

Fig. 133 - A) Fault plane solutions vs M_{22} values for the case when Qp/Qs =3.1 in the model and for a reference strike = 270 deg and reference dip = 80 deg. B) Strike and dip errors respect the referece values and the corresponding error limits. The cyan band correspond to the theoretical value of *k* +/- 10%.

Table 27 shows the plane solutions for a strike constraint of 35 +/20 deg. and **Table 28** shows the plane solutions for a strike constraint of 90 +/- 20 deg. or 270 +/- 20 deg. The solutions were recovered with the additional dip constraint of 80 +/- 10 deg. and within +/-10% of the theoretical *k* value for 3 different models: without considering attenuation, Qp/QS =0.9 and Qp/Qs =3.1. Notice that the plane solutions are very similar for the three different models for each strike constraint case, except for the slope angles. An important observation is that the slope angle is the same for both plane solutions, strike constraint of 35 and 90 (or 270) deg.

Model	k	Slope (deg.)	Strike (deg.)	Dip (deg.)	Rake (deg.)
No Q	0.75	-51.7	43.5	87.3	-3.0
Qp/Qs =0.9	0.75	-46.7	42.1	87.9	6.4
Qp/Qs =3.1	0.75	-27.1	42.7	87.1	6.7

Table 27 - Plane solutions for a reference strike of 35 deg. and for three different models: wihout attenuation, Qp/Qs =0.9 and Qp/Qs =3.1.

Model	k	Slope (deg.)	Strike (deg.)	Dip (deg.)	Rake (deg.)
No Q	0.75	-51.7	81.8	86.0	179.3
Qp/Qs =0.9	0.75	-46.7	265.1	87.2	173.9
Qp/Qs =3.1	0.75	-27.1	285.2	85.3	174.3

Table 28 - Plane solutions for a reference strike of 90 or 270 deg. and for three different models: wihout attenuation, Qp/Qs =0.9 and Qp/Qs =3.1.

Fig. 134 shows the solution for different Qp/Qs ratios used in the model and for the two different strike constraints (35 +/- 20 deg. and 270 +/- 20 deg.). Since both strike solutions are possible from the inversion, it is not possible to differentiate between the two natural fractures sets striking close to 35 and 90 deg. respectively. Notice that, for each strike constraint case, the solutions among every Qp/Qs are very similar with the only perceptible difference in the slope angle, which decreases in absolute value as the ratio Qp/Qs increases.

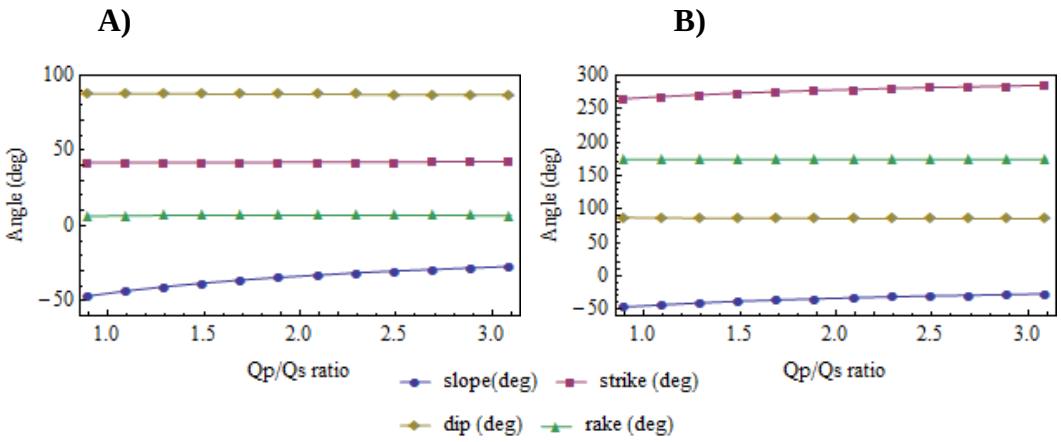

Fig. 134 - Plane solutions for different Qp/Qs in the model A) Plane solutions for a strike constraint of 35 +/- 20 deg. B) Plane solution for a strike constraint of 270 +/- 20 deg. The dip constriant is 80 +/- 10 deg. for both cases and solutions are within +/- 10% of *k* theoretical value.

The highest uncertainty in amplitude picking comes from the S arrival in the Radial and Z components. Indeed, notice that in **Fig. 116 B**, which is showing the time window for the S arrival, the onset in the transverse component can be easily distinguished since it produces a complete sinusoidal cycle; in contrast, the onset in the other two components

are ambiguous since there is a cycle and a half corresponding to the complete cycle for the transverse component.

According to the radiation pattern for P and S in an homogeneous and isotropic medium as derived by Vavryčuk (2007), the moment tensor elements relate to each amplitude components of rotated seismograms in the following way:

$$P^R = \begin{bmatrix} R = n_1^3 M_{11} + 2n_1^2 n_3 M_{13} + n_3^2 n_1 M_{33} \\ T = 0 \\ Z = n_1^2 n_3 M_{11} + 2n_3^2 n_1 M_{13} + n_3^3 M_{33} \end{bmatrix} \quad \textbf{(73)}$$

$$S^R = \begin{bmatrix} R = n_3^2 n_1 (M_{11} - M_{33}) + (n_3^2 - n_1^2) n_3 M_{13} \\ T = n_1 M_{12} + n_3 M_{23} \\ Z = n_1^2 n_3 (M_{33} - M_{11}) + (n_1^2 - n_3^2) n_1 M_{13} \end{bmatrix} \quad \textbf{(74)}$$

Where P^R and S^R are the radiation patterns for the P and S respectively; n_1, n_2, and n_3 are the components of the ray vector $\boldsymbol{n}$; and M_{ik} are the elements of the moment tensor $\boldsymbol{M}$.

From **Eq**. **(73)** and **Eq. (74)**, notice that moment tensor elements M_{11}, M_{13}, M_{33} are part of the radial and Z components of both P an S radiation functions while M_{12}, M_{23} are part only of the transverse component of the S phase. In principle, it is possible to neglect radial and Z amplitude components of the S phase, and still be able to retrieve five elements of the moment tensor.

To test the possibility of performing the inversion neglecting radial and Z amplitude components of the S phase , a simulation is run, in which the amplitude data is calculated by using the fracture model as per **Table 16** including attenuation with Qp =50 and Qp/Qs ratio is 2.1. For the inversion, amplitude data from radial and Z components from the S phase are neglected. The matrix G is constructed assuming Qp= 75 and

different values of Qp/Qs ratios. One case without considering attenuation effects is also included.

According to **Fig. 135**, the error fit for all the cases of Qp/Qs ratio considered are the practically the same and close to zero. However, this does not mean that the corresponding plane solutions are free from errors as shown in **Fig. 136**, where the errors fluctuate between +/-10 deg with the highest errors corresponding to the plane solution for Qp/Qs =0.9. Nonetheless, these errors are lower than the plane errors obtained when all S- amplitudes components are considered (**Fig. 96**).

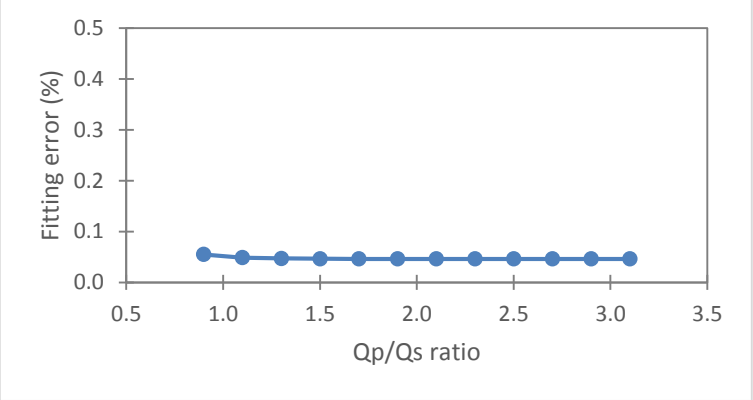

Fig. 135 - Inversion Fitting error for different Qp/Qs cases in the inverse model. All inversions performed applying the deviatoric constraint with Qp=75 and neglecting S amplitude data in radial and Z components. Forward model with Qp=50 and Qp/Qs =2.1.

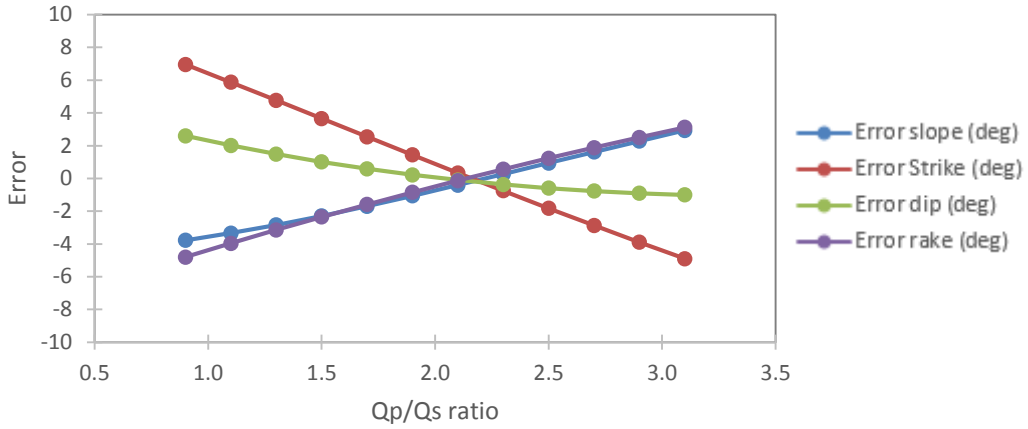

Fig. 136 - Fracture plane error for different Qp/Qs cases in the inverse model. All inversions performed applying the deviatoric constraint with Qp=75 and neglecting S amplitude data in radial and Z components. Forward model with Qp=50 and Qp/Qs =2.1.

On the other hand, fitting and plane solution errors when attenuation is not considered (Qp =∞) in the inversion model are greater than for any case with different Qp/Qs ratios. **Fig. 137** shows the fitting errors for the inversion case where attenuation is not considered and for Qp/Qs =0.9 which has the highest plane solution errors of all Qp/Qs ratios tested. **Fig. 138** and **Fig. 139** shows P and S amplitudes respectively from the forward model and from the inversion with Qp/Qs =0.9. Notice the perfect match for all amplitude components except for radial and z for S phase which were not use in the inversion.

In conclusion, neglecting S amplitude data from radial and Z components for the inversion of moment tensors, yields to lower errors in the plane solution, around +/- 10 deg. as maximum when attenuation is considered, as compared to the plane solution errors when including all S amplitude data components (up to 40 deg. when including attenuation). However, since the error fit is the same for every case of Qp/Qs, it is not possible to pick the optimum solution.

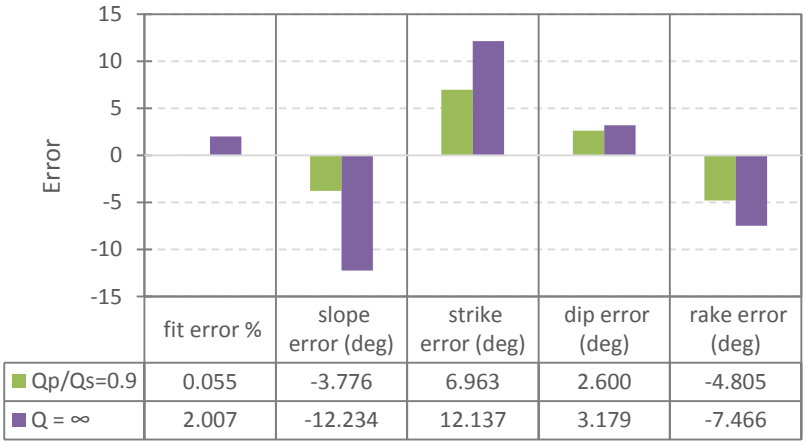

	fit error %	slope error (deg)	strike error (deg)	dip error (deg)	rake error (deg)
Qp/Qs=0.9	0.055	-3.776	6.963	2.600	-4.805
Q = ∞	2.007	-12.234	12.137	3.179	-7.466

Fig. 137 - Inversion Fitting error and fracture plane error for Qp/Qs =0.9 and Qp=75 in the inverse model including a case without attenuation. All inversions performed applying the deviatoric constraint and neglecting S amplitude data in radial and Z components. Forward model with Qp=50 and Qp/Qs =2.1.

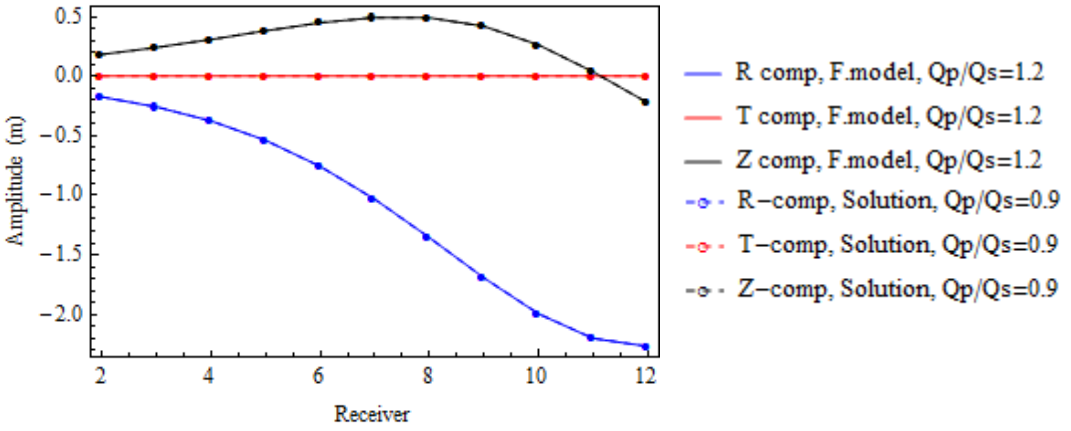

Fig. 138 - P amplitudes from the forward model and the estimated by the inversion with Qp/Qs =0.9.

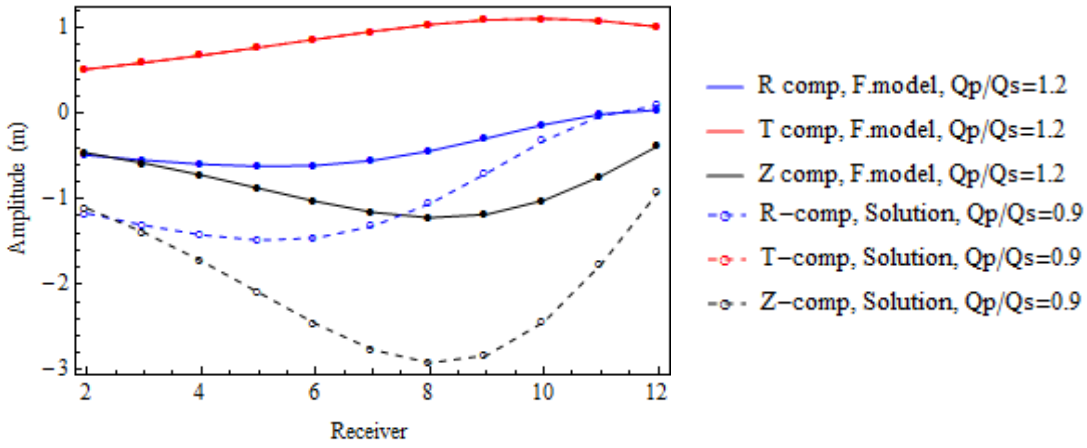

Fig. 139 - S amplitudes from the forward model and the estimated by the inversion with Qp/Qs =0.9.

The inversion is reprocessed neglecting S amplitude data from radial and Z components. **Table 29** shows the five elements of the moment tensor retrieved for the different cases of Qp/Qs and for the case of no attenuation considered in the model. **Fig. 140** shows the error fit for the different Qp/Qs ratios. Notice that error fit is around 10 % which is lower than for the inversion case where all S amplitude components were considered, around 29 % as per **Fig. 118**. In addition, the fit error for the case of no attenuation in the model also improves and is almost the same as the errors considering different Qp/Qs ratios.

Qp/Qs	Fit error %	Mo (N m)	M11	M12	M13	M23	M33
0.90	11.50	3.15E+16	-1.000	0.995	-0.270	-0.039	-0.499
1.10	11.46	3.75E+16	-0.838	1.000	-0.226	-0.052	-0.419
1.30	11.43	4.40E+16	-0.716	1.000	-0.193	-0.060	-0.358
1.50	11.42	5.05E+16	-0.623	1.000	-0.168	-0.063	-0.311
1.70	11.42	5.71E+16	-0.551	1.000	-0.149	-0.065	-0.275
1.90	11.42	6.38E+16	-0.494	1.000	-0.133	-0.066	-0.247
2.10	11.42	7.04E+16	-0.447	1.000	-0.121	-0.067	-0.223
2.30	11.42	7.71E+16	-0.408	1.000	-0.110	-0.067	-0.204
2.50	11.42	8.38E+16	-0.375	1.000	-0.101	-0.067	-0.188
2.70	11.42	9.05E+16	-0.348	1.000	-0.094	-0.067	-0.174
2.90	11.42	9.72E+16	-0.324	1.000	-0.087	-0.067	-0.162
3.10	11.42	1.04E+17	-0.303	1.000	-0.082	-0.067	-0.151
No Q	12.50	1.26E+16	-1.000	0.729	-0.286	0.158	-0.300

Table 29 - Inversion results for input data neglecting R and Z components of S amplitudes for different Qp/Qs ratio and for a model without considering attenuation.

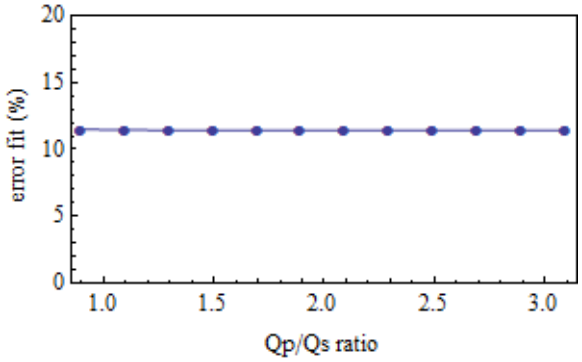

Fig. 140 - Error fit vs different Qp/Qs ratios. Inversion done neglecting S amplitude data from radial and Z components.

Fig. 141 and **Fig. 142** show the P and S amplitude data and the calculated ones from the inverted moment tensor without considering attenuation in the model. **Fig. 143** and **Fig. 144** show the P and S amplitude data and the calculated ones from the inverted moment tensor with Qp/Qs =0.9 in the model. Notice that for both cases, no attenuation in the model and a model with Qp/Qs =0.9, the fitting of P amplitudes have improved. However, notice as well that the estimated S amplitude data for the R and T components are different for these two cases.

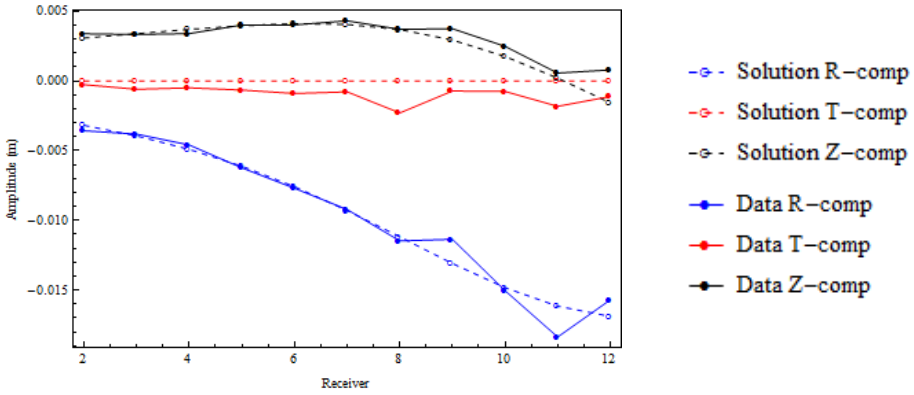

Fig. 141 - P amplitude data and P amplitudes calculated using the inverted moment tensor without considering attenuation in the model. For the inversion, S amplitude data from the R and Z components were neglected.

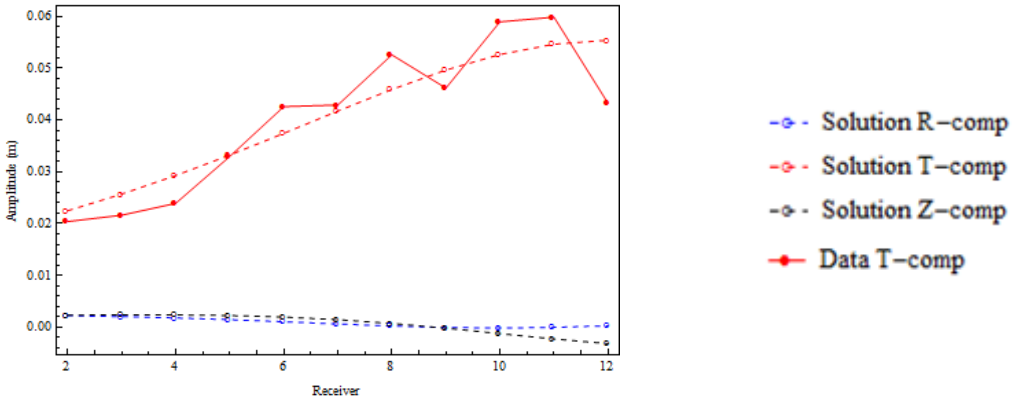

Fig. 142 - S amplitude data and S amplitudes calculated using the inverted moment tensor without considering attenuation in the model. For the inversion, S amplitude data from the R and Z components were neglected.

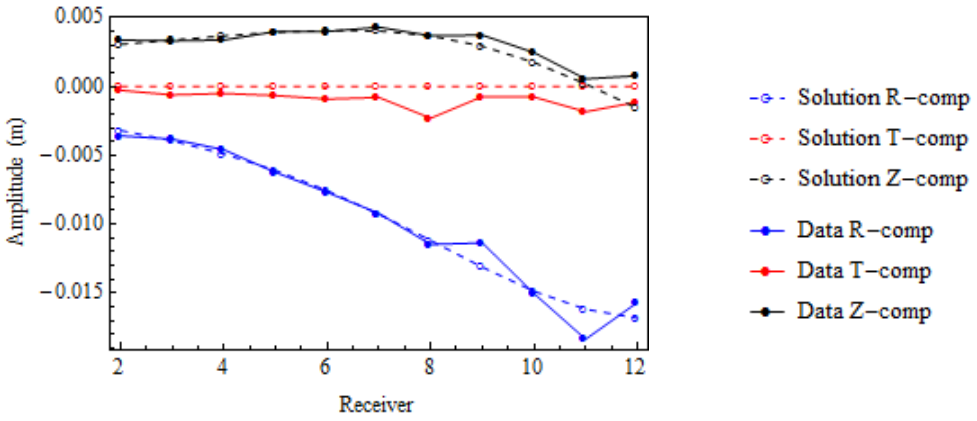

Fig. 143 - P amplitude data and P amplitudes calculated using the inverted moment tensor with Qp/Qs =0.9 in the model. For the inversion, S amplitude data from the R and Z components were neglected.

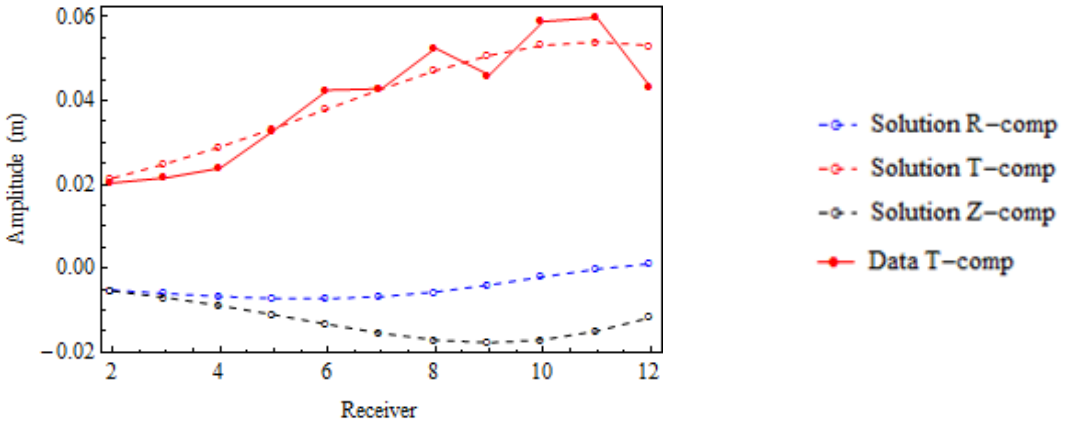

Fig. 144 - S amplitude data and S amplitudes calculated using the inverted moment tensor with Qp/Qs =0.9 in the model. For the inversion, S amplitude data from the R and Z components were neglected.

The plane solutions are estimated in the same way as in the case when all the S amplitude components were used. **Fig. 145** to **Fig. 147** correspond to the plane solutions for a model without considering attenuation. **Fig. 145** shows the *k* value solutions vs M_{22}. The horizontal red line shows that there are 3 different values corresponding to the theoretical *k* value. **Fig. 146 A** shows the plane solutions vs M_{22} that have the least errors respect a reference strike and dip of 35 deg. and 80 deg.; however from **Fig. 146 B**, it is noticed that when *k* is within its theoretical tolerance, dip and strike are not; thus no solution is found for a strike of 35 deg. The strike supplementary angle was also tried with similar results. **Fig. 147 A** shows the solution vs M_{22} f that have the least errors respect a reference strike and dip of 90 and 80 deg. respectively. Notice that in **Fig. 147** the cyan band corresponds to the constrained plane solutions since dips and strikes are within the prescribed error limits and within the theoretical *k* value

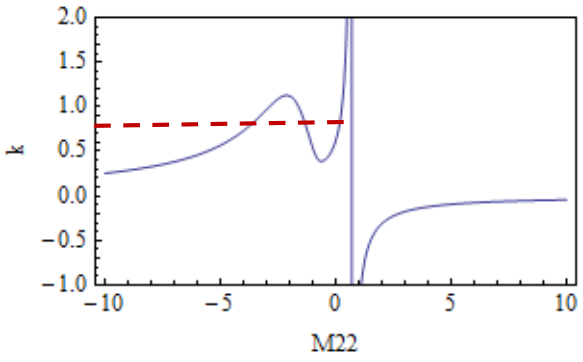

Fig. 145 - Inverted *k* parameters vs M_{22} values for the case of no attenuation in the model. The horizontal dashed line shows that for the theoretical *k* value there are 3 different values of possible M_{22} values. Inversion performed neglecting R and Z components of S-amplitude data.

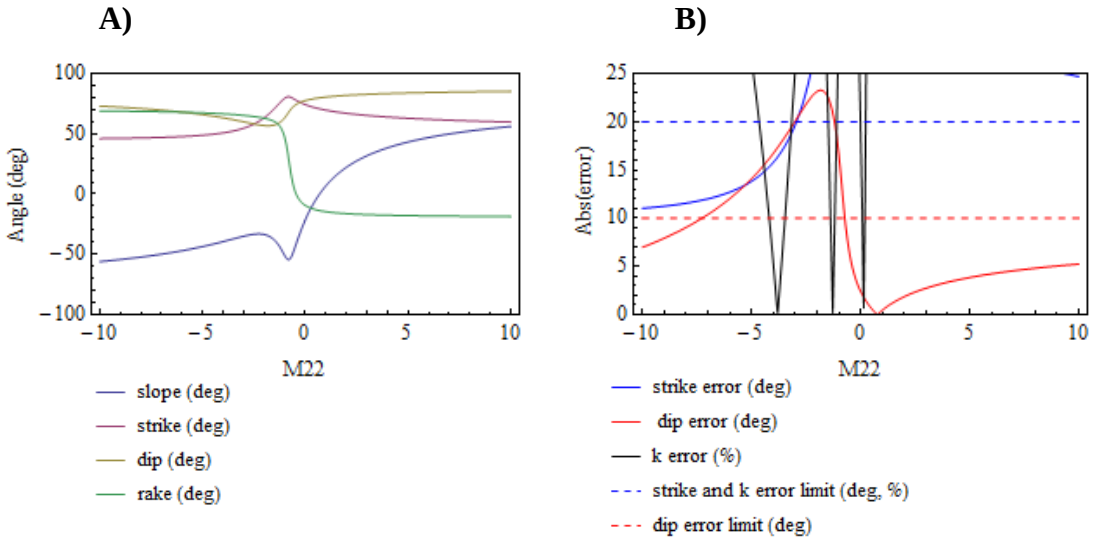

Fig. 146 - A) Fault plane solutions vs M_{22} values for a model without attenuation and for a reference strike =35 deg and reference dip = 80 deg. B) Strike and dip errors respect the referece values and the corresponding error limits. Inversion performed neglecting R and Z components of S-amplitude data.

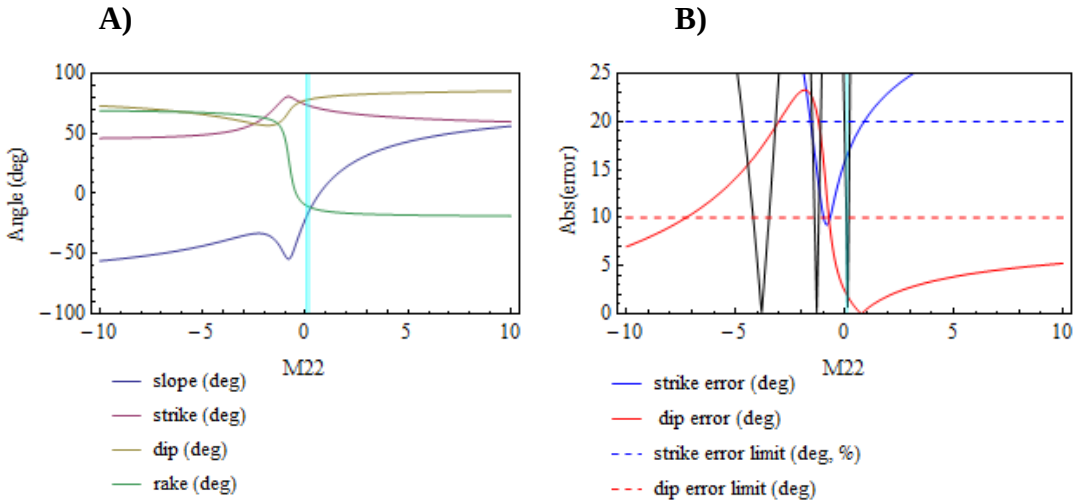

Fig. 147 - A) Fault plane solutions vs M_{22} values for a model without attenuation and for a reference strike =90 deg and reference dip = 80 deg. B) Strike and dip errors respect the referece values and the corresponding error limits. Inversion performed neglecting R and Z components of S-amplitude data.

Fig. 148 to **Fig. 150** correspond to the plane solutions for a model with Qp/Qs = 0.9 and for an inversion performed neglecting R and Z components of S-amplitude data Notice that the plane solutions are different for the case of no attenuation in the model (**Fig. 145** to **Fig. 147**). For this case, the corresponding M_{22} value for the theoretical *k* value is unique as shown in **Fig. 148**. In addition, both solutions, for strike 35 and 270 deg., exist as shown in **Fig. 149** and **Fig. 150**.

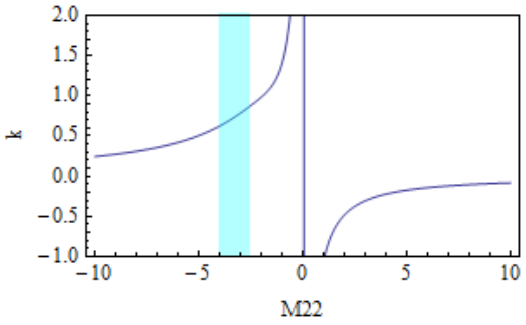

Fig. 148 - Inverted *k* parameters vs M_{22} values for the case when Qp/Qs =0.9 in the model. The cyan band correspond to the theoretical value of *k* +/- 10%. Inversion performed neglecting R and Z components of S-amplitude data.

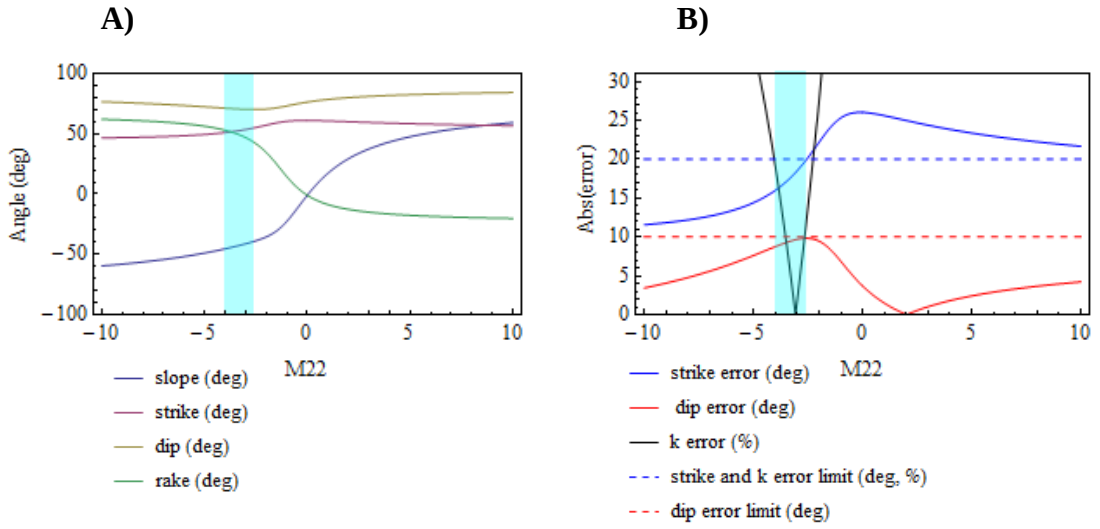

Fig. 149 - A) Fault plane solutions vs M_{22} values for the case when Qp/Qs =0.9 in the model and for a reference strike =35 deg and reference dip = 80 deg. B) Strike and dip errors respect the referece values and the corresponding error limits. The cyan band correspond to the theoretical value of *k* +/- 10%. Inversion performed neglecting R and Z components of S-amplitude data.

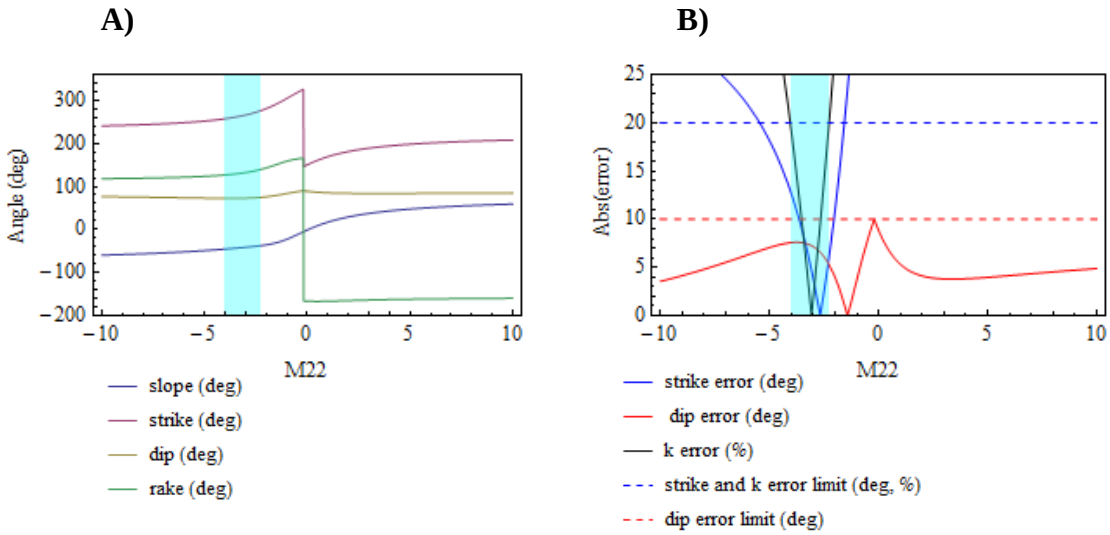

Fig. 150 - A) Fault plane solutions vs M_{22} values for the case when Qp/Qs =0.9 in the model and for a reference strike =35 deg and reference dip = 80 deg. B) Strike and dip errors respect the referece values and the corresponding error limits. The cyan band correspond to the theoretical value of *k* +/- 10%. Inversion performed neglecting R and Z components of S-amplitude data.

Table 30 shows the plane solutions for a strike constraint of 35 +/20 deg. For a model without attenuation no solution for this strike constraint is found. **Table 31** shows the plane solutions for a strike constraint of 90 +/- 20 deg. or 270 +/- 20 deg. Notice that for this strike constraint the rupture angles are different (slope and rake) for the two solutions.

Model	k	Slope (deg.)	Strike (deg.)	Dip (deg.)	Rake (deg.)
No Q	-	-	-	-	-
Qp/Qs =0.9	0.74	-42.5	52.7	70.6	48.8

Table 30 - Plane solutions for a reference strike of 35 deg. and for three different models: wihout attenuation and Qp/Qs =0.9. Inversion performed neglecting R and Z components of S-amplitude data.

Model	k	Slope (deg.)	Strike (deg.)	Dip (deg.)	Rake (deg.)
No Q	0.75	-17.1	73.5	78.1	-10.4
Qp/Qs =0.9	0.76	-42.5	265.2	73.0	131.8

Table 31 - Plane solutions for a reference strike of 270 deg. and for three different models: wihout attenuation and Qp/Qs =0.9. Inversion performed neglecting R and Z components of S-amplitude data.

Fig. 151 A and **B** show the solutions for strike constraint of 35 +/- 20 deg. and 270 +/- 20 deg. respectively for different values of Qp/Qs in the model. Notice that for the strike constraint of 35 deg. no solution exists for Qp/Qs = 1.3, and for the strike constraint of 270 deg. no solution exists for Qp/Qs greater than 1.5. On the other hand, notice that

both rupture mode angles, slope and strike, are different for different Qp/Qs ratios. In contrast, the solutions in which all S-amplitudes components were used, rake values were practically the same for every Qp/Qs ratio (**Fig. 134**).

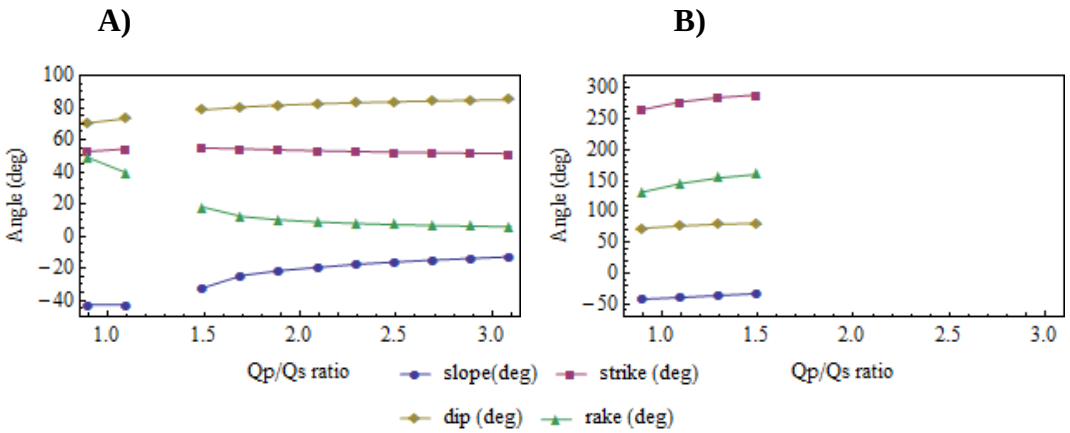

Fig. 151 - Plane solutions for different Qp/Qs in the model A) Plane solutions for a strike constraint of 35 +/- 20 deg. B) Plane solution for a strike constraint of 270 +/- 20 deg. The dip constriant is 80 +/- 10 deg. for both cases and solutions are within +/- 10% of *k* theoretical value. Inversion performed neglecting R and Z components of S-amplitude data.

The inversion performed neglecting R and Z components of S amplitudes provides a possibility to distinguish between the two strike constrained solutions since, for certain cases, both solutions do not exist at the same time. To establish possible solutions, first the less likely ones are discarded. Since intrinsic attenuation is an expected effect because a medium is never perfectly elastic, the solution in which attenuation is not considered in the model is eliminated. Moreover, the simulation results in section 5.4 corroborate that not considering attenuation in the model produces the greatest biases in the plane

solutions. On the other hand, the experimental work of Toksöz et al. (1979) and Johnston and Toksöz (1980) establishes that Qp is greater than Qs for water saturated rocks and oil shales; on this experimental basis, the solutions corresponding to Qp/Qs = 0.9 are also discarded. After discarding these two solutions, both strike constrained solutions still exist for Qp/Qs ratios from 1.1 to 1.5. However, Clouser and Langston (1991) stated that the most reliable Qp/Qs results that they found by applying the spectral ratio method do not conflict with the theoretical relationship given by **Eq.(62)**. Taking this theoretical relationship, the most likely solution for our case would correspond to a Qp/Qs =2.1. Since for Qp/Qs= 2.1 a solution striking 270 +/- 20 deg does not exist, the only possible plane solution is the one striking closer to 35 deg.

6.3.2 Plane Solutions for Additional Microseismic Events

Other six events were processed by fitting amplitude data of rotated seismograms but neglecting S amplitudes from radial and Z components. The preferred plane solution was picked for Qp/Qs =2.1. **Fig. 152** shows the events processed from stages seven and five. The number next to each event represents its relative strength (magnitude) and the color denotes the preferred strike solution. Green events are striking close to 35 deg. and red events are the ones whose preferred strike are not defined since both solutions exist. Note that solutions with preferred strike close to 90 deg. were not found.

Table 32 shows the plane solution results for the events processed from stage seven and five. **Fig. 153** shows the event magnitude and signal noise ratio for stages five and seven. Notice that in general events from stage 5 have a higher magnitude and signal noise ratio. In Addition, events with signal noise ratio below 15 are difficult to process since the P arrival is very noisy.

Finally, notice that the preferred plane solution strongly depends on the selection of Qp/Qs; thus a more accurate knowledge of both Qp and Qs will produce more reliable plane solutions.

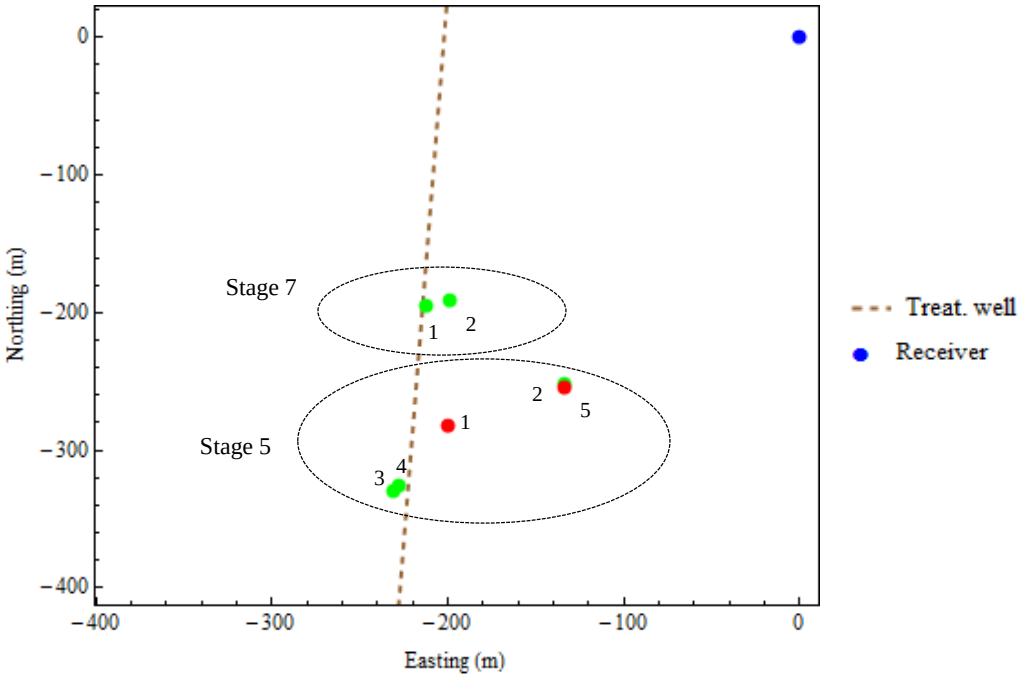

Fig. 152 - Plan view of selected microseismic evenst, receiver array and treatment well. The numbers represent the event relative strength order within the corresponding stage. Green events are striking close to 35 dg., while red events do not have a preferred strike since both solutions are possible.

				Solution 1 (strike = 35 or 215 +/- 20 deg.)				Solution 2 (strike = 90 or 270 +/- 20 deg.)			
Stage	**Event Number**	**Ev strength order**	**Fit error (%)**	**Slope (deg)**	**Strike (deg)**	**Dip (deg)**	**Rake (deg)**	**Slope (deg)**	**Strike (deg)**	**Dip (deg)**	**Rake (deg)**
7	14	*1*	11.42	-19.3	53.2	82.4	8.9				
7	4	*2*	14.60	-22.5	51.9	80.2	9.8				
5	2	*1*	10.79	-39.2	34.7	73.5	36.0	-39.0	255.4	75.2	143.4
5	27	*2*	11.56	11.3	54.3	71.9	-58.2				
5	94	*3*	21.27	-19.5	209.9	85.7	-102.0				
5	93	*4*	17.27	-19.0	40.9	89.1	105.2				
5	126	*5*	12.22	-29.4	233.0	79.2	145.8	-12.0	79.4	74.8	-91.0

Table 32 - Plane solutions for the processed events from stage 7 and 5. Green colored events correspond to solutions with preferred strike close to 35 deg. or 215 deg. Red colored events have no preferred strike solution since both exists.

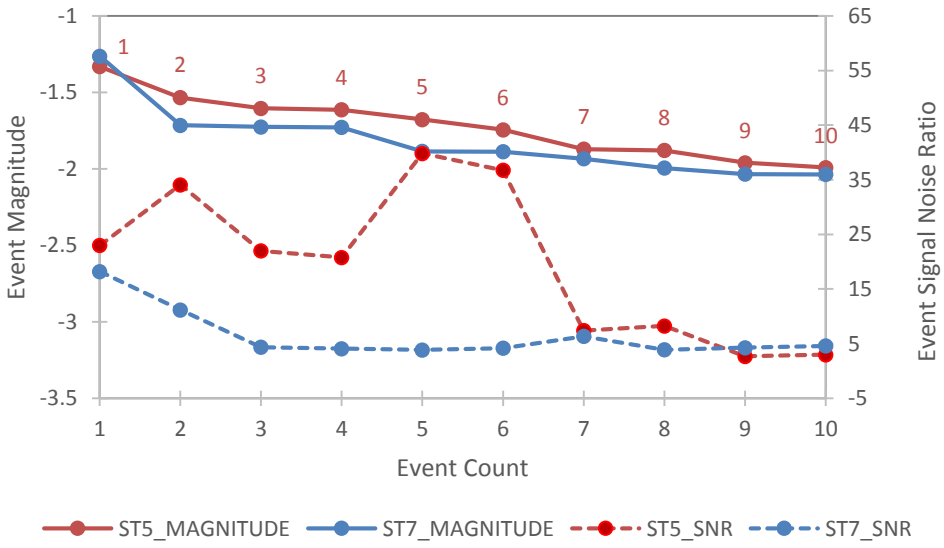

Fig. 153 - Magnitude and Signal noise ratio for events from stages 5 and 7 repectively, the numbers represent, the event relative strength order.

7. DISCRETE FRACTURE NETWORK GENERATION

To create the discrete fracture network (DFN), parameters such as fracture density, length distribution and orientation distribution (strike and dip) are needed. In this chapter, the necessary parameters for the DFN generation will be derived from the reported source details such as location and radius as well as from core data such as spacing frequency and orientation distribution.

The main assumptions considered for the DFN generation are:

- The two sets of fractures are bounded by the horizontal formation bed of constant thickness considered (Lower Spraberry) and both fracture sets fully penetrate the formation bed.
- The dip is constant but different for each fracture set, and the dip for each fracture set is calculated as the average of the reported values in the core analysis.
- For each microseismic location there is a single distinct fracture passing through.
- The shear fracture set is completely mineralized, then the length considered for the DFN generation is derived from the reported source radius.
- The tensile fracture set is completely unmineralized, and the length considered for the DFN generation is derived from a proposed power law distribution.

The DFN generation is semi stochastic. Dip values for each fracture set are fixed as well as the lengths of the shear fractures. However, lengths for the tensile fracture are stochastically generated following a power law distribution, in the same way strikes for

both fracture sets are also stochastically generated following a Fisher distribution. Although, a single fracture passes through a microseismic event, the location of these events are not totally fixed but some uncertainty is introduced. Below, the details about parameters estimation for the DFN generation are explained. An example of a generated DFN corresponding to the stage 5 of the hydraulic treatment in Lower Spraberry is also presented at the end.

7.1 Fracture Location Uncertainty

As discussed, a single fracture is assumed to pass through a microseismic event. However, it is considered that the location of each event has certain uncertainty. This uncertainty is assumed to be associated with the north and east coordinates of the event but not with its vertical coordinates. The depth uncertainty is neglected because for the DFN creation it is assumed that the fractures are fully penetrating the Lower Spraberry formation.

It is assumed that each event location corresponds to a random number with a uniform distribution in north and east coordinates. The limits of the possible values that theses coordinates can take are bounded by an ellipse centered in the reported location of the event, with axes lengths equal to the reported lengths of intermediate and minimum axes of the location error ellipsoid. Furthermore, the minor axis of the considered ellipse is assumed to be parallel to the event back azimuth calculated from the reported event and receivers locations. **Fig. 154** shows the random location of a selected event calculated as explained.

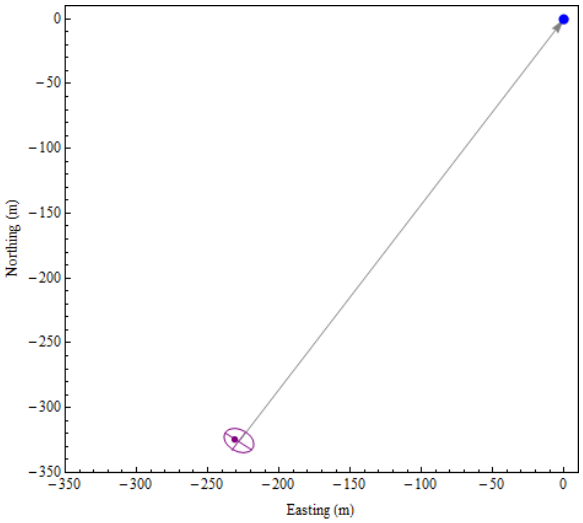

Fig. 154 - Random location (purple dot) with a unform distribution in an elliptical area, receiver location (blue dot) and radial direction of the reported event location (gray arrow). Details are explained in the text.

7.2 Fracture Density

Linear density of each fracture set, average number of fractures per unit length, can be estimated from the core analysis report. The length of the horizontal core can be assumed to be the sampling scanline. However, the direct counting of fractures along the scanline is not an unbiased estimation of linear fracture density because the result depends on the relative orientation of the scanline respect to the fractures (Pointe and Hudson 1985, Priest 1993). Priest (1993) proved that the maximum density along a scanline will be encountered when the orientation of the scanline and the fracture normal are parallel. A trigonometrical correction is required to obtain the right fracture density when the scanline makes a certain angle θ with the fracture normal (Priest 1993):

$$\lambda = \lambda_s / \cos\theta \qquad \textbf{(75)}$$

Where λ and λ_s are the corrected and uncorrected linear fracture density respectively, and θ is the angle between the scaline direction and the fracture normal.

To be able to generate the DFN sets in 2D, we need to find a correspondence between the linear and areal fracture density, where the areal fracture density is the total length of fractures per unit area. Applying a similar approach as for the linear fracture density, the areal fracture density can be estimated. Thus, the areal fracture density will depend on the orientation of the sampling plane, and the maximum density will be obtained when the normal vector of the sampling and the fracture planes are perpendicular to each other. Otherwise the areal density needs to be corrected as follows:

$$\lambda_a = \lambda_{sa} / \sin\gamma \quad \textbf{(76)}$$

Where λ_a and λ_{sa} are the corrected and uncorrected areal fracture density respectively, and γ is the angle between the normal of the fracture plane and the sampling plane.

Furthermore, Mauldon (1994) shown that:

$$\lambda_s / \cos\theta = \lambda_{sa} / \sin\gamma \quad \textbf{(77)}$$

From there we obtain:

$$\lambda_{sa} = \lambda_s \sin\gamma / \cos\theta \quad \textbf{(78)}$$

Eq. (78) can be applied to estimate the areal fracture density for a sampling plane with any orientation using a linear density measurement along an oriented scanline.

An additional aspect to solve is the assignation of microseismic events to one of the two fracture sets according to the fracture areal density. According to Priest (1993), the areal fracture density can be related to the number of fractures in the following way:

$$n = \lambda_{sa} \, \mathrm{S} \frac{1}{L} \quad \textbf{(79)}$$

Where n is the number of fractures sampled, S is the area of the sampling plane and $\bar{L}$ is the mean length of the sampled fractures.

Since a unique sampling plane covering the microseismic area will be used, the ratio of the number of fractures corresponding to each of the two sets can be expressed as:

$$\frac{n_1}{n_2} = \frac{{\lambda_{sa}}^1}{{\lambda_{sa}}^2} \frac{\bar{L}_2}{\bar{L}_1} \quad \textbf{(80)}$$

Where the sub and super indices refer to either fracture set 1 or set 2

An additional equation is needed to find the number of fractures corresponding to either set. This equation simply expresses that the sum of total fractures is equal to the number of microseismic events n_t:

$$n_1 + n_2 = n_t \quad \textbf{(81)}$$

7.3 Fracture Length

Lengths for the two fractures sets will be calculated in different ways. Lengths for the shear fracture set will be assumed to be related to the displacement produced by the induced slip on the fracture planes. Since the shear fracture sets are mostly mineralized, it is reasonable to assume that only the reactivated area has potential to contribute to flow. The reported source radius will be used for the lengths estimations, assuming that the area of a circular fracture, as considered in the microseismic report, is the same as the rectangular fracture. The dipping side of the fracture is assumed to be equal to 2R and the length is calculated as:

$$L = \frac{\pi R}{2} \quad \textbf{(82)}$$

Where L is the fracture length, R is the reported source radius.

Lengths for the tensile fracture set will be sampled from a power law distribution. Since this fracture set is completely unmineralized, the complete length will contribute to flow and not only the stimulated region. The Power law distribution can be expressed as:

$$P(l) = C\, l^{-\alpha} \quad \textbf{(83)}$$

Where $\alpha > 0$ and C is normalization constant.

Assuming that the fracture lengths are bounded between a minimum and maximum value and that the maximum length can be expressed as a multiple of the minimum length, the normalization constant can be found by integrating the power law distribution between these bounds in the following way:

$$\int_{l_{min}}^{t\, l_{min}} P(l)dl = C \int_{l_{min}}^{t\, l_{min}} l^{-\alpha} dl = 1 \quad \textbf{(84)}$$

Where l_{min} is the minimum length in the fracture systmen and $t\, l_{min}$ is the maximum length of the fracture system with $t > 1$. Then the value of the constant C is:

$$C = \frac{-\alpha+1}{l_{min}^{-\alpha+1}\,(t^{-\alpha+1}-1)} \quad \textbf{(85)}$$

A random sample from the power law distribution will be generated by the transformation method (Press et al. 1992):

$$l = l_{min}[t^{-\alpha+1}\, r\, (t^{-\alpha+1}-1)]^{\left(\frac{1}{-\alpha+1}\right)} \quad \textbf{(86)}$$

Where r is random number with uniform distribution and $0 < r < 1$.

7.4 Fracture Orientation

Dip values for each fracture set are equal to the average of the reported values in the cored data analysis inform.

Fracture strike is assumed to follow a Fisher distribution (Priest 1993), which is expressed as:

$$f\ (\beta) = \frac{K\ \sin\beta\ \ e^{K\ \cos\beta}}{e^{K} - e^{-K}} \quad \textbf{(87)}$$

Where β represents the angular deviation from the mean, K is a constant that controls the shape of the distribution, representing the extent of deviation from the mean and can be estimated from the core data.

The angular deviation β can be sampled from the Fisher distribution in the following way:

$$\beta = \cos^{-1}\left[\frac{\ln r}{K} + 1\right] \quad \textbf{(88)}$$

Where r is random number with uniform distribution and $0 < r < 1$.

7.5 DFN Generation Example

As an example, we will generate a DFN based on the microseismic events of stage 5. **Fig. 155** shows the 71 reported microseismic events for stage 5. The 3 events which were already identified as fractures belonging to the set striking 35 deg. are also displayed.

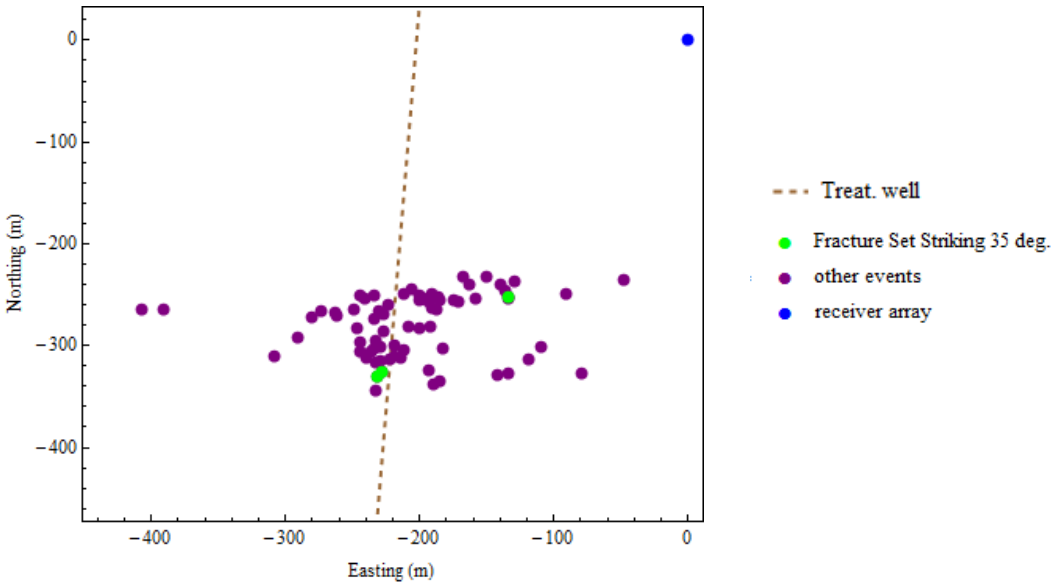

Fig. 155 - Microseismic events for stage 5.

The first step in the DFN generation is to quantify the number of events belonging to either set, shear or tensile, based on the areal density for each fracture set. The areal density is calculated from the apparent linear density provided in the core analysis report. The sampling plane is parallel to the formation bed which is assumed to be horizontal. To

be able to apply **Eq. (78)**, we need to find angles θ and γ. They can be obtained in the following way:

$$\theta = \cos^{-1}\left(\hat{l}.\hat{n}\right) \quad \textbf{(89)}$$

$$\gamma = \cos^{-1}(\hat{s}.\hat{n}) \quad \textbf{(90)}$$

Where $\hat{l}$ is the parallel to the core sample direction (along the horizontal well), $\hat{s}$ is the normal vector of the sampling plane and $\hat{n}$ is the normal vector of the fracture plane.

The normal vector of the fracture plane is calculated as:

$$\hat{n} = (-\sin\bar{\delta}\ \sin\bar{\varphi}, -\sin\bar{\delta}\ \cos\bar{\varphi}, \cos\bar{\varphi}) \quad \textbf{(91)}$$

Where $\bar{\delta}$ and $\bar{\varphi}$ are the average dip and strike for each fracture set calculated from the reported measurements in the core analysis.

To finally obtain the ratio of events belonging to either fracture set, we need to estimate the mean lengths for each fracture set as required by **Eq. (80)**. These mean lengths can be estimated from the corresponding power law distribution for each set. The issue is that the core data does not provide any information about fracture length. However, it is possible to have some intuition about the relative lengths between the fracture sets. According to (Priest 1993) longer fractures have more probability to intersect a sampling scanline. Thus, it is more probable that the fracture set with higher "corrected" linear density exhibit longer fractures than the less dense fracture set. Furthermore, Bonnet et al. (2001) suggested that there is a relationship between the sampling area and fracture minimum length which can be expressed as follows:

$$l_{min} = x\, S^{0.5} \quad \textbf{(92)}$$

Where *x* is a percentage from 0.5 to 25 %

For this case, we assumed that the sampling area S is rectangular and parallel to the sampling plan and equal to 47 061.2 m2 (506 563 ft2), covering all the microseismic events; we also assumed that the minimum length for the shear set is 10% of this area. For the tensile set, we assumed that its minimum length is a fraction of the of the minimum shear fracture length. This fraction is equal to the ratio between the linear fracture density of tensile and shear sets. However, to be able to obtain mean lengths from power law distributions we still need to find the power law exponents and the maximum lengths corresponding to each fracture set. Since no further information is available, these values are assumed.

Table 33 shows the data to create the DFN generation for stage 5. The shear set length distribution based on the power law was only used to find the number of fractures corresponding to this set from the total microseismic events reported, but the actual generated lengths for this set are based in the source radius as per **Eq. (82).**

Fig. 156 shows one realization of the semi-stochastic DFN generation. The natural fractures in black are the ones connected to the hydraulic fracture and the wellbore. The connected natural fractures are 47 of a total of 71.

Fig. 157 shows the frequency histogram of the number of connected natural fractures to the hydraulic fractures and the approximated normal distribution with mean equal to 36.5 and standard deviation of 7.9 after 500 DFN realizations.

Parameter Description	Set 1 (N 35 deg. E)	Set 2 (E-W)
Mean dip ($\bar{\delta}$) - mean strike ($\bar{\varphi}$) (deg.)	78.5 – 35.9	90 - 84.6
Angle between sampling line and mean fracture normal (θ) (deg)	58.4	9
Angle between sampling and fracture normal vectors (γ) (deg)	78.3	90
Corrected linear fracture density (λ)	1.61 m^{-1} (0.49 ft^{-1})	0.17 m^{-1} (0.051 ft^{-1})
Apparent aerial fracture density (λ_{sa})	1.57 m^{-1} (0.48 ft^{-1})	0.17 m^{-1} (0.051 ft^{-1})
Minimum fracture length (l_{min})	21.7 m (71.2 ft)	2.3 m (7.5 ft)
Maximum fracture length ($t\ l_{min}$)	433.9 m (1423.5 ft)	114.6 m (376.1 m)
Power Law exponent (α)	1.5	1.1
Mean fracture length ($\bar{L}$)	98.1 m (322 m)	28 m (91.9 ft)
Number of fractures (n)	52	19
Fisher constant (K)	860	430

Table 33 - Data for DFN generation in stage 5.

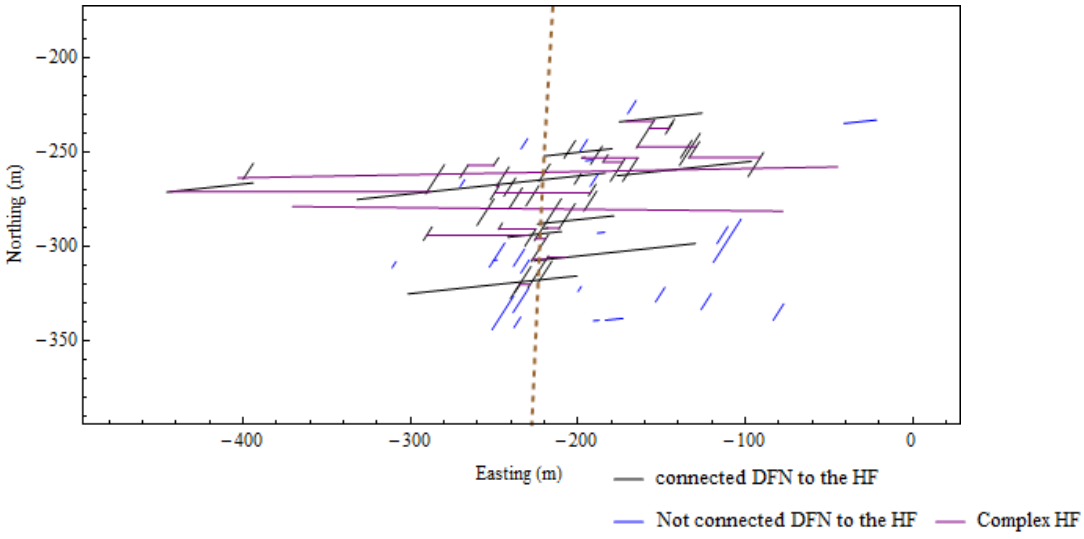

Fig. 156 - One relaization of DFN for stage 5 assuming straight paths of the hydraulic fractures from the two perforation shots.

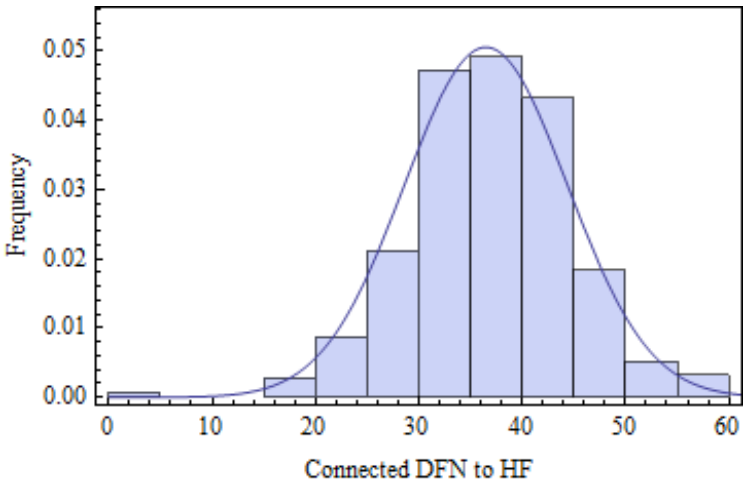

Fig. 157 - Frequenecy histogram of connected natural fractures to the hyfraulic fractures and the approximated Normal pdf with mean = 36.5 and std = 7.9. The histogram was constructed with 500 DFN realizations.

8. CONCLUSIONS

For both natural fracture sets, the mechanicals analysis suggests that normal stress components on the fracture planes are never negative. Thus, the type of rupture expected is compressional shear, however normal stress values close to zero resolved on the tensile set suggest that pure shear rupture mode can also be expected on this set.

The stability analysis, considering the stress field perturbation by the approacing hydraulic fracture tip, suggests that the tensile set is the most favorable oriented for reactivation and that the shear set reactivation strongely depends on its mechanical properties (cohesion and friction coefficient).

The stability analysis, considering the effective stress drop caused by fracturing fluid difussion, also suggests that the tensile natural fracture set is the most favorable oriented for reactivation and that the expected rupture mode is extensional shear. The reactivation of the shear set will also be strongly controlled by its mechanical properties, and in the case of reactivation, the expected rupture mode is compressional shear.

The simulation of constrained solutions indicate that deviatoric assumption produces reliable solutions only when the actual source mechanisms are pure shear. However, the mechanical analysis shows that rupture mechanisms on the natural fractures can vary from extensional shear to compressional shear, undermining the reliability of this type of constrained solutions. Since the most accepted explanation of microseismicity occurrence is the reactivation of plane of weaknesses, it is reasonable to assume that for this field case, the source of microseismicty is the reactivation of natural fractures, thus

dip and strike are known parameters. The simulations shown that strike constraint only can lead to non-unique solutions; in contrast, a combination of strike and dip constraints can provide reliable solutions even in presence of some noisy data. In addition, the solutions should be within a specified tolerance of the k (λ/μ) ratio calculated for the medium

The results of the simulation of uncertainties in source location, in medium velocities and in amplitudes suggest that errors in the velocity model yields the highest errors in source mechanisms solutions with more than 40 deg in rake angle errors when the inaccuracy in Vp or Vs is - 10%. Errors in source mechanisms as consequence of source mislocation is less pronounced, with the greatest solution errors from inaccuracies in the Z location, up to 30 deg in dip angle errors when errors in the Z coordinate are close to 100 m (328.1 ft). The errors in the amplitudes have the least effects on the solution errors, 10 deg as maximum error for every fault plane angle.

The simulation results of attenuation effects suggest that if attenuation factors are neglected, the errors in the plane solutions can be as great as 40 deg. in slope and rake angles.

The studies to establish if it is possible to perform a joint inversion for moment tensor and attenuation factors indicate that explosive sources as perforation shots are not appropiate since they are isotropic sources with P-waves emanating equally in all directions and thus the effect of attenuation is mainly seen in the strength of the source. In principle, for sources with directionality, Qp/Qs ratio can be found by inversion since an appreciable minimum exists

According to the analysis of a perforation shot, it is acceptable to use the homogenous isotropic whole space model when the top most receiver is neglected.

The inversion results from a microseismic event from stage 7 show that it does not exist a distinct minimum for any of Qp/Qs ratios tried in the model and even the solution without considering attenuation show a similar fit error to any of the Qp/Qs cases. In addition, planes solutions for the two strike cases exist for any Qp/Qs ratio, including the case for no attenuation. Thus, it is not possible to distinguish between the two natural fracture sets although additional dip and *k* ratio constrained were imposed. However, an additional inversion attempt neglecting S-amplitudes from radial and Z components was performed. These amplitude components were neglected because theoretically it is still possible to retrieve all the five elements of the moment tensor and because these amplitudes are the most unreliable to pick. The inversion results for the different Qp/Qs ratios do not show a distinct minimum either, but plane solutions for the two strike cases not always exist for every Qp/Qs ratio, which provides a possible way to distinguish the reactivated fracture set. For this case we assumed a preferred theoretical value of Qp/Qs of 2.1 on basis of experimental and field results.

The analysis of seven microseismic events show that it is not always possible to distinghuish the two natural fracture sets present in the Lower Spraberry by strike, dip and *k* ratio constrained inversion. Moroever, these results are heavily dependent on the Qp/Qs value chosen.

REFERENCES

Aki, K., Richards, P. 2002. *Quantitative Seismology.* Second Edition, 11-62. Sausalito, California, University Science Books.

Baig, A., Urbancic, T. 2010. Microseismic Moment Tensors: A Path to Understanding Frac Growth. *The Leading Edge* **29** (3): 320-324.

Bonnet, E., Bour, O., Odling, N. E., Davy, P., Main, I. et al. 2001. Scaling of Fracture Systems in Geological Media. *Reviews of Geophysics* **39** (3): 347-383.

Chiu, H.-C. 1997. Stable Baseline Correction of Digital Strong-Motion Data. *Bulletin of the Seismological Society of America* **87** (4): 932-944.

Cipolla, C. L., Weng, X., Mack, M. G., Ganguly, U., Gu, H. et al. 2011. Integrating Microseismic Mapping and Complex Fracture Modeling to Characterize Hydraulic Fracture Complexity. Paper presented at *SPE Hydraulic Fracturing Technology Conference*, The Woodlands, Texas, USA. SPE-140185-MS.

Clouser, R. H., Langston, C. A. 1991. Qp-Qs Relations in a Sedimentary Basin Using Converted Phases. *Bulletin of the Seismological Society of America* **81** (3): 733-750.

Curtis, J. B. 2002. Fractured Shale-Gas Systems. *AAPG Bulletin* **86** (11): 1921-1938.

Eaton, D. W., Forouhideh, F. 2011. Solid Angles and the Impact of Receiver-Array Geometry on Microseismic Moment-Tensor Inversion. *Geophysics* **76** (6): WC77-WC85.

Engelder, T. 1999. Transitional–Tensile Fracture Propagation: A Status Report. *Journal of Structural Geology* **21** (8–9): 1049-1055.

Farrington, W. B. 1955. Analysis of Stress Conditions in the Upper Spraberry in Western Texas. *Transactions - American Geophysical Union* **36** (1): 139-143.

Fischer, T., Guest, A. 2011. Shear and Tensile Earthquakes Caused by Fluid Injection. *Geophysical Research Letters* **38** (5): L05307.

Fossen, H. 2010. *Structural Geology*. First Edition, 119-140. New York, Cambridge University Press.

Gale, J. F. W., Holder, J. 2010. Natural Fractures in Some US Shales and Their Importance for Gas Production. *Geological Society, London, Petroleum Geology Conference Series* **7**: 1131-1140.

Gale, J. F. W., Reed, R. M., Holder, J. 2007. Natural Fractures in the Barnett Shale and Their Importance for Hydraulic Fracture Treatments. *AAPG Bulletin* **91** (4): 603-622.

Garagash, D., Detournay, E. 1999. The Tip Region of a Fluid-Driven Fracture in an Elastic Medium. *Journal of Applied Mechanics* **67** (1): 183-192.

Ghassemi, A., Zhou, X. X., Rawal, C. 2013. A Three-Dimensional Poroelastic Analysis of Rock Failure around a Hydraulic Fracture. *Journal of Petroleum Science and Engineering* **108**: 118-127.

Godano, M., Regnier, M., Deschamps, A., Bardainne, T., Gaucher, E. 2009. Focal Mechanisms from Sparse Observations by Nonlinear Inversion of Amplitudes:

Method and Tests on Synthetic and Real Data. *Bulletin of the Seismological Society of America* **99** (4): 2243-2264.

Griffith, A. A. The Theory of Fracture. In Proceedings of *The First International Congress of Applied Mechanics,* Delft, The Netherlands, ed. C. B. Biezeno and J. M. Burgers, **1**, 55-63.

Groenenboom, J., van Dam, D. B., de Pater, C. J. 2001. Time-Lapse Ultrasonic Measurements of Laboratory Hydraulic-Fracture Growth: Tip Behavior and Width Profile. *SPE Journal* **6** (1): 14-24.

Gu, H., Weng, X., Lund, J. B., Mack, M. G., Ganguly, U. et al. 2012. Hydraulic Fracture Crossing Natural Fracture at Nonorthogonal Angles: A Criterion and Its Validation. *SPE Production & Operations* **27** (1): 20-26.

H.Gu, X.Weng. 2010. Criterion for Fractures Crossing Frictional Interfaces at Non-Orthogonal Angles. Paper presented at *44th U.S. Rock Mechanics Symposium and 5th U.S.-Canada Rock Mechanics Symposium*, Salt Lake City, Utah,USA. ARMA-10-198.

Horálek, J., Jechumtálová, Z., Dorbath, L., Šílený, J. 2010. Source Mechanisms of Micro-Earthquakes Induced in a Fluid Injection Experiment at the Hdr Site Soultz-Sous-Forêts (Alsace) in 2003 and Their Temporal and Spatial Variations. *Geophysical Journal International* **181** (3): 1547-1565.

Hwang, J., Yun, H., Park, S.-K., Lee, D., Hong, S. 2012. Optimal Methods of Rtk-Gps/Accelerometer Integration to Monitor the Displacement of Structures. *Sensors* **12** (1): 1014-1034.

Jaeger, J. C., Cook, N. G. W., Zimmerman, R. W. 2007. *Fundamentals of Rock Mechanics* Fourth Edition, 97-100. Malden, Massachusetts, Blackwell Publications.

Jechumtálová, Z., Eisner, L. 2008. Seismic Source Mechanism Inversion from a Linear Array of Receivers Reveals Non-Double-Couple Seismic Events Induced by Hydraulic Fracturing in Sedimentary Formation. *Tectonophysics* **460** (1–4): 124-133.

Johnston, D. H., Toksöz, M. N. 1980. Ultrasonic P and S Wave Attenuation in Dry and Saturated Rocks under Pressure. *Journal of Geophysical Research: Solid Earth* **85** (B2): 925-936.

Jost, M. L., Herrmann, R. B. 1989. A Student's Guide to and Review of Moment Tensors. *Seismological Research Letters* **60** (2): 37-57.

Julian, B. R., Miller, A. D., Foulger, G. R. 1998. Non-Double-Couple Earthquakes 1. Theory. *Reviews of Geophysics* **36** (4): 525-549.

Lay, T., Wallace, T. C. 1995. *Modern Global Seismology*. First Edition, 310-346. San Diego, California, Academic Press.

Lorenz, J. C., Sterling, J. L., Schechter, D. S., Whigham, C. L., Jensen, J. L. 2002. Natural Fractures in the Spraberry Formation, Midland Basin, Texas: The Effects of Mechanical Stratigraphy on Fracture Variability and Reservoir Behavior. *AAPG Bulletin* **86** (3): 505-524.

Mauldon, M. 1994. Intersection Probabilities of Impersistent Joints. *International Journal of Rock Mechanics and Mining Sciences & Geomechanics Abstracts* **31** (2): 107-115.

Maxwell, S. C., Cipolla, C. L. 2011. What Does Microseismicity Tell Us About Hydraulic Fracturing? Paper presented at *SPE Annual Technical Conference and Exhibition* Denver, Colorado, USA. SPE-146932-MS.

Maxwell, S. C., Urbancic, T. I. 2005. The Potential Role of Passive Seismic Monitoring for Real-Time 4d Reservoir Characterization. *SPE Reservoir Evaluation & Engineering* **8** (1): 70-76.

Miller, A. D., Foulger, G. R., Julian, B. R. 1998. Non-Double-Couple Earthquakes 2. Observations. *Reviews of Geophysics* **36** (4): 551-568.

Montgomery, S. L., Schechter, D. S., Lorenz, J. 2000. Advanced Reservoir Characterization to Evaluate Carbon Dioxide Flooding, Spraberry Trend, Midland Basin, Texas. *AAPG Bulletin* **84** (9): 1247-1273.

Nolen-Hoeksema, R. C., Ruff, L. J. 2001. Moment Tensor Inversion of Microseisms from the B-Sand Propped Hydrofracture, M-Site, Colorado. *Tectonophysics* **336** (1–4): 163-181.

Ou, G. B. 2008. Seismological Studies for Tensile Faults. *Terrestrial, Atmospheric and Ocean Sciences* **19** (5): 463-471.

Patton, H., Aki, K. 1979. Bias in the Estimate of Seismic Moment Tensor by the Linear Inversion Method. *Geophysical Journal of the Royal Astronomical Society* **59**: 479-495.

Pearson, C. 1981. The Relationship between Microseismicity and High Pore Pressures During Hydraulic Stimulation Experiments in Low Permeability Granitic Rocks. *Journal of Geophysical Research: Solid Earth* **86** (B9): 7855-7864.

Phillips, W. S., Fairbanks, T. D., Rutledge, J. T., Anderson, D. W. 1998. Induced Microearthquake Patterns and Oil-Producing Fracture Systems in the Austin Chalk. *Tectonophysics* **289** (1–3): 153-169.

Pointe, P. R. L., Hudson, J. A. 1985. *Characterization and Interpretation of Rock Mass Joint Patterns.* First Edition, 3-4. Boulder, Colorado, Geological Society of America.

Potluri, N. K., Zhu, D., Hill, A. D. 2005. The Effect of Natural Fractures on Hydraulic Fracture Propagation. Paper presented at *SPE European Formation Damage Conference*, Sheveningen, The Netherlands. SPE-94568-MS.

Press, W. H., Teukolsky, S. A., Vetterling, W. T., Flannery, B. P. 1992. *Numerical Recipes in Fortran : The Art of Scientific Computing.* Second Edition, 277-279. New York, Cambridge University Press.

Priest, S. D. 1993. *Discontinuity Analysis for Rock Engineering*. First Edition, 83-100. New York, Chapman & Hall.

Ramsey, J. M., Chester, F. M. 2004. Hybrid Fracture and the Transition from Extension Fracture to Shear Fracture. *Nature* **428** (6978): 63-66.

Renshaw, C. E., Pollard, D. D. 1995. An Experimentally Verified Criterion for Propagation across Unbounded Frictional Interfaces in Brittle, Linear Elastic Materials. *International Journal of Rock Mechanics and Mining Sciences & Geomechanics Abstracts* **32** (3): 237-249.

Rothert, E., Shapiro, S. 2003. Microseismic Monitoring of Borehole Fluid Injections: Data Modeling and Inversion for Hydraulic Properties of Rocks. *Geophysics* **68** (2): 685-689.

Rutledge, J. T., Phillips, W. S., Mayerhofer, M. J. 2004. Faulting Induced by Forced Fluid Injection and Fluid Flow Forced by Faulting: An Interpretation of Hydraulic-Fracture Microseismicity, Carthage Cotton Valley Gas Field, Texas. *Bulletin of the Seismological Society of America* **94** (5): 1817-1830.

Sasaki, S. 1998. Characteristics of Microseismic Events Induced During Hydraulic Fracturing Experiments at the Hijiori Hot Dry Rock Geothermal Energy Site, Yamagata, Japan. *Tectonophysics* **289** (1–3): 171-188.

Savage, J. C., Mansinha, L. 1963. Radiation from a Tensile Fracture. *Journal of Geophysical Research* **68** (23): 6345-6358.

Shearer, P. M. 2009. *Introduction to Seismology.* Second Edition Edition, 241-245. New York, Cambridge University Press.

Sibson, R. H. 1996. Structural Permeability of Fluid-Driven Fault-Fracture Meshes. *Journal of Structural Geology* **18** (8): 1031-1042.

Sílený, J., Hill, D. P., Eisner, L., Cornet, F. H. 2009. Non-Double-Couple Mechanisms of Microearthquakes Induced by Hydraulic Fracturing. *Journal of Geophyical Research* **114** (B8): B08307.

Sleefe, G. E., Warpinski, N. R., Engler, B. P. 1995. The Use of Broadband Microseisms for Hydraulic Fracture Mapping. *SPE Formation Evaluation* **10** (4): 223-240.

Sneddon, I. N. 1946. The Distribution of Stress in the Neighbourhood of a Crack in an Elastic Solid. *Proceedings of the Royal Society of London. Series A. Mathematical and Physical Sciences* **187** (1009): 229-260.

Snoke, J. A. 2003. Focmec: Focal Mechanism Determinations In *International Handbook of Earthquake and Engineering Seismology Part B*, ed. William H.K. Lee, Chap. 85.12. San Diego, California, Academic Press.

Song, F., Toksöz, M. 2011. Full-Waveform Based Complete Moment Tensor Inversion and Source Parameter Estimation from Downhole Microseismic Data for Hydrofracture Monitoring. *Geophysics* **76** (6): WC103-WC116.

Song, F., Warpinski, N., Toksöz, M. 2014. Full-Waveform Based Microseismic Source Mechanism Studies in the Barnett Shale: Linking Microseismicity to Reservoir Geomechanics. *Geophysics* **79** (2): KS13-KS30.

Stein, S., Wysession, M. 2003. *An Introduction to Seismology, Earthquakes, and Earth Structure*. First Edition, 194-195, 239-247. Malden, Massachusetts, Blackwell Publishing.

Strelitz, R. A. 1978. Moment Tensor Inversions and Source Models. *Geophysical Journal of the Royal Astronomical Society* **52**: 359-364.

Stump, B. W., Johnson, L. R. 1977. The Determination of Source Properties by the Linear Inversion of Seismograms. *Bulletin of the Seismological Society of America* **67** (6): 1489-1502.

Sun, C. T., Jin, Z. H. 2012. The Elastic Stress Field around a Crack Tip. In *Fracture Mechanics*, ed. C. T. Sun and Z. H. Jin, Chap. 3. Boston, Academic Press.

Toksöz, M., Johnston, D., Timur, A. 1979. Attenuation of Seismic Waves in Dry and Saturated Rocks: I. Laboratory Measurements. *Geophysics* **44** (4): 681-690.

Tyler, N., Gholston, J. C., Guevara, E. H. 1997. *Basin Morphological Controls on Submarine-Fan Depositional Trends, Spraberry Sandstone, Permian Basin, Texas* First Edition, 7-20. Austin, Texas, Bureau of Economic Geology.

Udias, A. 1999. *Principles of Seismology*. First Edition, 274-335. New York, Cambridge University Press.

Vavryčuk, V. 2001. Inversion for Parameters of Tensile Earthquakes. *Journal of Geophysical Research* **106** (B8): 16339-16355.

Vavryčuk, V. 2007. On the Retrieval of Moment Tensors from Borehole Data. *Geophysical Prospecting* **55** (3): 381-391.

Vavryčuk, V. 2011. Tensile Earthquakes: Theory, Modeling, and Inversion. *Journal of Geophysical Research* **116** (B12): B12320.

Warpinski, N. R., Mayerhofer, M., Agarwal, K., Du, J. 2013. Hydraulic-Fracture Geomechanics and Microseismic-Source Mechanisms. *SPE Journal* **18** (4): 766 - 780.

Warpinski, N. R., Teufel, L. W. 1987. Influence of Geologic Discontinuities on Hydraulic Fracture Propagation (Includes Associated Papers 17011 and 17074). *Journal of Petroleum Technology* **39** (2): 209-220.

Warpinski, N. R., Wolhart, S. L., Wright, C. A. 2004. Analysis and Prediction of Microseismicity Induced by Hydraulic Fracturing. *SPE Journal* **9** (1): 24-33.

Weng, X., Kresse, O., Cohen, C. E., Wu, R., Gu, H. 2011. Modeling of Hydraulic Fracture Network Propagation in a Naturally Fractured Formation. Paper presented at *SPE Hydraulic Fracturing Technology Conference*, The Woodlands, Texas, USA. SPE-140253-MS.

Williams-Stroud, S. C., Eisner, L. 2010. Stimulated Fractured Reservoir Dfn Models Calibrated with Microseismic Source Mechanisms. Paper presented at *44th U.S. Rock Mechanics Symposium and 5th U.S.-Canada Rock Mechanics Symposium*, Salt Lake City, Utah -US. ARMA-10-520.

Xie, J., Yang, C., Gupta, N., King, M. J., Datta-Gupta, A. 2012. Integration of Shale Gas Production Data and Microseismic for Fracture and Reservoir Properties Using Fast Marching Method. Paper presented at *SPE Eastern Regional Meeting*, Lexington, Kentucky, USA. SPE-161357-MS.